

**Thermal performance of rotating discs  
structured with dimples**

**Thermisches Verhalten von rotierenden,  
mit Dimpeln strukturierten Scheiben**

Der Technischen Fakultät  
der Friedrich-Alexander-Universität  
Erlangen-Nürnberg

zur  
Erlangung des Doktorgrades Dr.-Ing.

vorgelegt von

Julian Gerald Praß

Als Dissertation genehmigt  
von der Technischen Fakultät  
der Friedrich-Alexander-Universität Erlangen-Nürnberg

Tag der mündlichen Prüfung: 25.05.2023

Gutachter: Prof. Dr.-Ing. habil. Stefan Becker  
Prof. Dr.-Ing. Jörg Franke

# Preface

This dissertation was largely written during the time I worked as a research assistant at the Institute for Factory Automation and Production Systems (FAPS) in close cooperation with the Institute of Process Machinery and Systems Engineering (iPAT) and the Institute of Fluid Mechanics (LSTM) at Friedrich-Alexander-Universität Erlangen-Nürnberg.

First, I thank my supervising professors at the two institutes, Prof. Dr.-Ing. habil. Stefan Becker (iPAT,LSTM) and Prof. Dr.-Ing. Jörg Franke (FAPS) for their active support of my research work and the assistance they provided during the dissertation process. Both professors promoted my personal and professional development by assigning me challenging tasks at two completely different research institutes. I particularly thank them for the independence they granted me and the trust they placed in me.

Furthermore, I thank Prof. Dr. Sc. Techn. Philipp Schlatter for supervising the doctoral examination as chairman of the examination committee and Prof. Dr.-Ing. Tobias Günther for taking on the task as further member of the examination committee.

Despite many freedoms and mostly self-determined activities at the institutes, the day-to-day business at the university can be demanding. Special thanks therefore goes to my colleagues at the two institutes, especially my direct office colleagues, who made my time as a research assistant incomparably enriching and unforgettable. These are in particular: Lukas Baier, Thomas M. Braun, Felix Czwielong, Johannes Bürner, Adrian Fehrle, Roman Krusche, Ralf Merkl née Böhm, Katrin Nusser, Andreas Renz, Thomas Uffinger, Florian Wachter, and Johannes Weber. I also thank my research partners and students for their commitment, which contributed to the success of this work.

Sincere appreciation goes to my parents Ulrike and Roland as well as my siblings Tino and Joana, who have provided me with moral support from the very beginning on the path to my doctorate. The largest gratitude, of course, goes to my wonderful wife Aylin and our two children Estelle and Leonard for their understanding consideration and the patience I was permitted to enjoy during the preparation of my thesis.

Roßtal, May 2023

Julian Gerald Praß



# Contents

List of Figures . . . . .	vii
List of Tables . . . . .	xi
Nomenclature . . . . .	xiii
1 Introduction . . . . .	1
1.1 Motivation . . . . .	1
1.2 Aims and objective of this thesis . . . . .	2
1.3 Methodology and structure of this thesis . . . . .	3
2 Analysis of topic-related research . . . . .	5
2.1 Progress in heat transfer enhancement due to dimples . . . . .	5
2.2 Observation of drag reducing effects of dimples . . . . .	11
2.3 Flow and heat transfer of rotating discs . . . . .	13
3 Fundamental theory and governing equations . . . . .	19
3.1 Heat transfer in fluids . . . . .	19
3.2 Principals of fluid dynamics . . . . .	23
3.3 Turbulent flows . . . . .	26
3.4 Boundary layers . . . . .	32
3.5 Rotating discs . . . . .	36
3.6 Numerical modelling of turbulent flows . . . . .	38
4 Investigation of dimpled surfaces in non-rotating flow . . . . .	47
4.1 Turbulent flow in channels and over flat plates . . . . .	47
4.1.1 Setup and validation of turbulent flow simulations . . . . .	48
4.1.2 Vortex-induced formation of ordered flow patterns of the boundary layer . . . . .	52
4.2 Effects of shallow dimples on the flow . . . . .	56
4.2.1 Drag reduction due to shallow dimples on surfaces . . . . .	56
4.2.2 Effects of dimples on the flow velocity . . . . .	60
4.2.3 Effects of dimples on pressure and wall shear stress . . . . .	62
4.2.4 Shallow dimples in channels at low $Re$ . . . . .	64
4.3 Heat transfer enhancement due to dimples . . . . .	67
4.3.1 Simulation setup and validation . . . . .	68
4.3.2 Influences of dimples on local Nusselt number . . . . .	74
4.3.3 Effects of the coverage rate on the heat transfer . . . . .	77

## Contents

5	Influence of noninteracting dimples on rotating discs . . . . .	81
5.1	Numerical setup . . . . .	82
5.2	Validation based on the turbulent flow around smooth, rotating discs . . . . .	88
5.3	Thermal behaviour of single dimples on discs . . . . .	92
5.3.1	Performance of spherical and teardrop-shaped dimples	92
5.3.2	Scale resolved results . . . . .	96
5.3.3	Concluding remarks on the findings from noninteracting dimples on rotating discs . . . . .	98
6	Thermal performance of rotating discs covered with spherical dimples	101
6.1	Problem description and investigated dimple arrangements .	101
6.2	Influences of the cylindrical shaft on the flow and heat transfer	105
6.3	Thermal performance of dimpled discs . . . . .	110
6.3.1	Heat transfer of rotating dimpled disc . . . . .	110
6.3.2	Heat transfer characteristics below the critical rotational velocity . . . . .	113
6.3.3	Thermal behaviour of rotating discs in the transitional region of rotational velocity . . . . .	118
6.3.4	Heat transfer characteristics at high rotational numbers	127
6.3.5	Thermal efficiency of the discs . . . . .	130
6.4	Guidelines for creating application-specific dimple setups . .	131
7	Conclusion . . . . .	133
	Zusammenfassung . . . . .	137
A	Literature Overview . . . . .	143
A.1	Heat Transfer from dimples . . . . .	143
A.2	Drag reduction . . . . .	145
A.3	Rotating discs . . . . .	147
B	visualisation of turbulent structures near the surface . . . . .	151
	Bibliography . . . . .	153

# List of Figures

2.1	Visualisation of dimples (a) and presentation of covered area (b).	6
3.1	Flow quantity $\phi$ of a turbulent flow at a defined physical position $x_i$ over time. . . . .	27
3.2	Schematic representation of the development of a viscous boundary layer and a thermal boundary layer in 2D. . . . .	32
3.3	Dimensionless velocity as a function of dimensionless wall distance. . . . .	34
3.4	Energy cascade for turbulent flows. . . . .	39
3.5	Different meshing approaches for hexahedron elements. . . . .	46
4.1	Validation of the channel flow simulations. . . . .	50
4.2	Schematic representation of longitudinal vortices leading to streaks on flat plates and cross-section of a dimple. . . . .	53
4.3	Schematic representation of the mechanisms leading to the formation of vortices near the surface. . . . .	54
4.4	Streaks near and fluid motion above smooth wall, main flow direction into the viewing plane. . . . .	54
4.5	Effect of streamwise-vortices on the local drag coefficient and the velocity in correlation with the rotation (Simulation data was partly generated within the context of Kalb [SI]). . . . .	55
4.6	Arrangements of Dimples on flat plates, used to determine drag reduction. . . . .	57
4.7	Used computational domains for simulations and corresponding boundary conditions. . . . .	58
4.8	Development of drag coefficient over flows through the domain and local velocity perpendicular to the wall. . . . .	59
4.9	Comparison of pressure and wall shear around dimples for the setups OL and NOL. . . . .	63
4.10	Comparison of the drag coefficient of different dimple shapes. . . . .	66
4.11	Visualisation of the finest mesh with $5.6 \cdot 10^6$ elements. . . . .	70
4.12	Computational domain with dimples and comparison to measurement position of literature data . . . . .	70
4.13	Anisotropy invariant map, showing that the simulated turbulence is physically realisable. . . . .	73
4.14	Increase of Nusselt number due to dimples compared to the smooth channel at constant streamwise position. . . . .	75
4.15	Increase of Nusselt number due to dimples compared to the smooth channel at constant spanwise position. . . . .	76

List of Figures

4.16	Used computational domains for simulations of heat transfer. . .	77
4.17	Dimensionless wall shear along the dimples. . . . .	78
4.18	Thermal performance of different setups at varying $Re_\delta$ . . . . .	79
5.1	Computational domain for the simulations of the discs with dimples.	83
5.2	Setups of investigated cases in order to determine the effects of individual dimples on rotating discs. . . . .	84
5.3	Evaluation of simulation results of a disc structured with five spherical dimples with and without cylindrical shaft. . . . .	89
5.4	Simulation results in comparison with correlations found in literature. . . . .	91
5.5	Thermal performance of spherical and teardrop-shaped dimples on rotating discs. . . . .	93
5.6	Temporal mean heat flux along centre line of dimples. . . . .	95
5.7	Visualisation of the arising vortices in the flow field. . . . .	97
6.1	Investigated arrangements of dimples on rotating discs. . . . .	104
6.2	Evaluation of the simulation quality on the basis of the development of the mean heat flux density at the disc surface and by evaluation of the dominant frequencies. . . . .	106
6.3	Evaluation of the simulation quality on the basis of comparison with literature values. . . . .	109
6.4	Mean ratios of Nusselt numbers for six different setups of dimpled discs as function of $\Gamma$ . . . . .	111
6.5	Time-averaged heat flux density over 100 equidistant circular lines from cylindrical shaft to disc edge for $\Gamma = 1.17$ . . . . .	114
6.6	Snapshots of an arbitrary time $t$ of local heat flux and arising flow structures around a smooth rotating disc. . . . .	115
6.7	Snapshots of an arbitrary time of local heat flux and arising flow structures around a rotating disc patterned with dimples. . . . .	118
6.8	Time-averaged heat flux density over 100 equidistant circular lines from cylindrical shaft to disc edge for $\Gamma = 2.33$ . . . . .	119
6.9	Time-averaged heat flux density over 100 equidistant circular lines from cylindrical shaft to disc edge for $\Gamma = 3.50$ . . . . .	122
6.10	Relative average depth of dimples divided by local circumferential length. . . . .	125
6.11	Correlation of the heat transfer increase of dimpled setups with average dimple depth and local, dimensionless rotational velocity.	126
6.12	Time-averaged heat flux density over 100 equidistant circular lines from cylindrical shaft to disc edge for $\Gamma = 4.66$ . . . . .	128
6.13	Thermal performance parameter of the investigated setups. . . .	131

B.1 Vortex structures at  $y^+ < 150$  visualised by the  $\lambda_2$ -criterion with threshold  $-1.2 \cdot 10^7$  and coloured by wall distance (Simulation data was partly generated within the context of Kalb [SI]). . . . 152



# List of Tables

4.1	Data of the examined setups to investigate the reduction of drag by dimples. . . . .	57
4.2	Validation data for the smooth channel with one heated and one adiabatic surface. . . . .	72
5.1	Metrics of the meshes used for URANS and SAS. . . . .	86
5.2	Material properties of the used medium air. . . . .	86
5.3	Time step lengths and corresponding angle of rotation. . . . .	88
6.1	Overview of the investigated setups including name used, type of arrangement, number of dimples, diameters used and surface coverage rate. . . . .	105
6.2	Characteristic frequency of mean heat flux density and corresponding Strouhal number. . . . .	107
A.1	Selected literature on the heat transfer due to dimples sorted chronologically . . . . .	144
A.2	Selected literature on the drag reduction due to dimples sorted chronologically . . . . .	146
A.3	Selected literature on the flow and heat transfer due to rotating discs chronologically sorted . . . . .	148



# Nomenclature

## Acronyms

AIM	anisotropy invariant map
CFD	computational fluid dynamics
CFL	Courant-Friedrichs-Lewy
DDES	delayed detached eddy simulation
DNS	direct numerical simulation
DSM	dynamic Smagorinsky model
FFT	fast Fourier transformation
LES	large eddy simulation
NOL	not overlapping arrangement of dimples
OL	overlapping arrangement of dimples
PISO	pressure-implicit with splitting of operators
PSD	power spectral density
RANS	Reynolds-averaged Navier-Stokes
REF	reference case
RKE	realizable $k-\epsilon$
RNG	re-normalisation group
SAS	scale-adaptive simulation
SGS	subgrid-scale
SIMPLE	semi-implicit method for pressure linked equations
SM	Smagorinsky model
SST	shear stress transport
URANS	unsteady Reynolds-averaged Navier-Stokes
WALE	wall-adapting local eddy viscosity

## Greek letters

$\alpha^*$	thermal diffusivity as a function of $c_p$
$\alpha_D$	thermal diffusivity as a function of $c_v$
$\alpha_h$	convection heat transfer coefficient
$\alpha_r$	rotation rate
$\beta$	coverage rate
$\gamma$	ratio of Reynolds numbers $Re_{\Omega,1}/Re_u$

## Nomenclature

$\Gamma$	ratio of Reynolds numbers $Re_\Omega/Re_u$
$\delta$	channel half-height
$\delta_0$	inlet boundary layer thickness
$\delta_{99}$	boundary layer thickness
$\delta_\theta$	momentum thickness
$\delta_d$	displacement thickness
$\delta_{ij}$	Kronecker delta
$\delta_T$	thermal boundary layer
$\delta_u$	viscous boundary layer thickness
$\Delta$	filter width
$\Delta t$	time step size
$\Delta T$	characteristic temperature difference
$\Delta x^+$	dimensionless spacing in streamwise direction
$\Delta x_i$	shift in direction of $x_i$
$\Delta z^+$	dimensionless spacing in spanwise direction
$\epsilon$	rate of dissipation of turbulent kinetic energy
$\epsilon_{ijk}$	Levi-Civita symbol
$\epsilon_{\text{rel}}$	relative error
$\zeta$	point in space
$\zeta_G$	term in the Gnielinski correlation
$\eta_K$	Kolmogorov length scale
$\Theta^+$	dimensionless Temperature
$\kappa$	wavenumber
$\kappa_\Theta$	universal constant to calculate $\Theta^+$
$\kappa_c$	von Kármán constant
$\lambda_2$	second largest of the three eigenvalues of $S_{ij}^2 + \Omega_{ij}^2$
$\lambda_m$	mean free path
$\lambda_S$	wave length of streamwise vortices
$\mu$	dynamic viscosity
$\mu_t$	turbulent viscosity
$\nu$	kinematic viscosity
$\nu_t$	eddy viscosity
$\xi$	arbitrary or observation variable
$\xi_c$	calculated value of observation variable on coarse mesh
$\xi_f$	calculated value of observation variable on fine mesh

$\xi_R$	generalized Richardson extrapolation estimate
$\rho$	density
$\rho_0$	constant or reference density
$\sigma$	standard deviation
$\tau_{ij}$	molecular-caused momentum transport
$\tau_{ij}^{SGS}$	subgrid-scale Reynolds stress tensor
$\tau_t$	specific time
$\tau_w$	wall shear stress
$\bar{\tau}_w$	temporal mean wall shear stress
$\bar{\tau}_{w,0}$	reference wall shear stress of a flat plate
$\phi$	flow variable
$\Phi_{ij}$	velocity spectrum tensor
$\chi$	space vector
$\psi$	possible values a considered variable can represent
$\omega$	specific rate of dissipation
$\omega^+$	normalized vorticity
$\omega_u$	vorticity
$\Omega$	angular velocity
$\Omega_{ij}$	antimetric part of the velocity gradient

### Latin letters

$a$	speed of sound
$a_{ij}$	anisotropy tensor
$A$	surface area
$A^+$	van Driest constant
$A_0$	reference or projected area
$A_{tot}$	total area
$b_1$	exponent
$b_2$	exponent
$c_f$	drag coefficient
$c_{f0}$	drag coefficient of a smooth channel or plate
$c_{f\tau}$	drag coefficient formed with $\tau_w$
$c_M$	dimensionless moment coefficient
$c_{M1}$	dimensionless moment coefficient of a rotating disc
$c_{M,d}$	spatial mean moment coefficient of dimpled disc

## Nomenclature

$c_{M,s}$	spatial mean moment coefficient of smooth disc
$c_p$	specific heat capacity at constant pressure
$c_v$	specific heat capacity at constant volume
$C$	constant
$C_1$	integration constant
$C_\Theta$	integration constant
$C_S$	Smagorinsky model constant
$C_W$	WALE constant
$d$	distance to closest wall
$D$	mass diffusivity
$D_0$	reference dimple imprint diameter
$D_c$	diameter of cylindrical shaft
$D_d$	disc diameter
$D_h$	hydraulic diameter
$D_i$	dimple imprint diameter
$D_r$	diameter of rotating domain
$D(y^+)$	van Driest damping function
$e$	inner energy
$E$	energy spectrum function
$f$	frequency
$\bar{f}$	mean frequency
$f_p$	frequency of one period
$f_{\text{res}}$	frequency resolution
$F_R$	total drag force
$\widetilde{g}_{ij}$	subgrid-scale flux
$g_j$	acceleration in $j$ -direction
$G$	energetic potential
$\widetilde{G}$	filter for large eddy simulation
$\widetilde{G}_B$	Box filter
$\widetilde{G}_G$	Gaussian filter
$h$	dimple depth
$H_d$	disc thickness
$i$	index
$II_a$	invariant of the anisotropy tensor $a_{ij}$
$III_a$	invariant of the anisotropy tensor $a_{ij}$
xvi	

$j$	index
$k$	turbulent kinetic energy
$k_t$	thermal conductivity
$l$	local circumferential length
$l_p$	length of a pipe
$l_x$	streamwise distance of dimples
$l_z$	spanwise distance of dimples
$L$	characteristic length
$L_s$	mixing length for subgrid-scales
$L_x$	length of a domain
$L_y$	height of a domain
$L_z$	width of a domain
$\dot{m}_{\text{out}}$	mass flux at outlet
$M$	torque
$n$	normal direction
$n_c$	number of elements of a coarse mesh
$n_f$	number of elements of a fine mesh
$N$	performed rotations of a disc
$N_d$	number of dimples
$o$	order of accuracy of a scheme
$p$	pressure
$\bar{p}$	temporal mean pressure
$p_0$	reference pressure
$p_{\text{in}}$	static pressure at inlet
$p_m$	mean pressure
$q$	heat transfer rate
$\dot{q}$	heat flux density
$\bar{\dot{q}}$	temporal average of $\dot{q}$
$\bar{\dot{q}}^*$	dimensionless temporal average of $\dot{q}$
$\bar{\dot{q}}_d$	temporal mean value of heat flux of a disc with dimples
$q_f$	sum of velocity fluctuations
$\dot{q}_i$	heat flux in $i$ -direction
$\dot{q}_m$	spatial mean heat flux density
$\bar{\dot{q}}_s$	temporal mean value of heat flux of a smooth disc
$Q$	$Q$ -criterion

## Nomenclature

$r$	local radius
$r^*$	dimensionless disc radius
$r_e$	edge radius
$R$	specific gas constant
$R_c$	general correlation coefficient
$R_{ij}$	two-point correlation coefficient
$R_l$	correlation coefficient lengthscale
$R_{\max}$	maximum of correlation coefficient
$R_{\text{RMS}}$	root mean square of correlation coefficient
$R_s$	auto correlation coefficient in space
$R_t$	auto correlation coefficient in time
$R_u$	correlation coefficient of $u$ in main flow direction
$s$	mesh refinement factor
$S_{ij}$	symmetric part of the velocity gradient
$\widetilde{S}_{ij}$	strain rate of calculated velocity field in LES
$S_{ij}^d$	adjusted strain tensor
$t$	time
$t_0$	starting time
$t_i$	duration of input signal
$t_p$	period duration
$\mathfrak{T}$	specified time
$T$	temperature
$T^+$	dimensionless temperature
$T_\tau$	friction temperature
$T_0$	reference temperature
$T_d$	disc temperature
$T_f$	fluid temperature
$T_f^+$	dimensionless fluid temperature
$T_w$	wall temperature
$T_w^+$	dimensionless wall temperature
$u$	component of velocity in $x$ -direction
$u^+$	dimensionless velocity
$u_\infty$	inlet or free stream velocity
$u_\tau$	friction velocity

$u_i$	$i$ -component of velocity
$\overline{u'_i u'_j}$	turbulent stress tensor
$u_r$	circumferencial velocity
$u_{\text{rel}}$	relative velocity
$U$	characteristic velocity
$U_b$	bulk velocity
$U_c$	centerline velocity
$U_e^+$	non dimensional free stream velocity
$v$	component of velocity in $y$ -direction
$\bar{v}$	temporal mean of $v$
$w$	component of velocity in $z$ -direction
$x$	cartesian coordinate representing streamwise direction $x_1$
$x_i$	spatial coordinate in $i$ -direction
$\dot{x}_i$	integration variable in space
$y$	cartesian coordinate representing wall normal direction $x_2$
$y^+$	dimensionless wall distance
$y_m^+$	mean dimensionless wall distance
$y_{\text{max}}^+$	maximum dimensionless wall distance
$z$	cartesian coordinate representing spanwise direction $x_3$
$z_d$	average dimple depth

### Mathematical expressions

$\frac{D\diamond}{Dt}$	substantial derivative of $\diamond$
$\frac{d\diamond}{d\xi}$	derivative of $\diamond$ with respect to $\xi$
$\frac{\partial\diamond}{\partial\xi}$	partial derivative of $\diamond$ with respect to $\xi$
$f(\diamond)$	probability density function of $\diamond$
$\diamond'$	temporal fluctating part of $\diamond$
$\diamond''$	fluctating value of $\diamond$
$\langle\diamond\rangle$	expectation or probability-weighted mean of $\diamond$
$\overline{\diamond}$	temporal average of $\diamond$
$\tilde{\diamond}$	spatial filtering of $\diamond$

### Dimensionless groups

$Kn$	Knudsen number $Kn = \lambda_m/L$
$Ma$	Mach number $Ma = U/a$

## Nomenclature

$Nu$	Nusselt number $Nu = \alpha_h L / k_t$
$Nu_0$	Nusselt number of a smooth channel or plate
$Nu_m$	mean Nusselt number
$Nu_{m,\Omega=0}$	mean Nusselt number of stationary disc
$Nu_{m,d}$	spatial mean Nusselt number of dimpled disc
$Nu_{m,s}$	spatial mean Nusselt number of smooth disc
$Pr$	Prandtl number $Pr = \nu / \alpha^*$
$RAR$	Reynolds analogy ratio
$Re$	Reynolds number $Re = LU / \nu$
$Re_\delta$	Reynolds number based on bulk velocity $Re_\delta = 2\delta U_b / \nu$
$Re_\theta$	Reynolds number based on momentum thickness $Re_\theta = Lu_\tau / \nu$
$Re_\tau$	friction Reynolds number $Re_\tau = u_\tau \delta / \nu$
$Re_\Omega$	rotational Reynolds number $Re_\Omega = \Omega D_d^2 / (4\nu)$
$Re_{\Omega,1}$	local rotational Reynolds number $Re_{\Omega,1} = \Omega r D_d / (2\nu)$
$Re_c$	Reynolds number based on centerline velocity $Re_c = \delta U_c / \nu$
$Re_L$	turbulence Reynolds number $Re_L = k^{1/2} L / \nu = k^2 / (\varepsilon \nu)$
$Re_u$	cross-flow Reynolds number $Re_u = u_\infty D_d / (2\nu)$
$Sc$	Schmidt number $Sc = \nu / D$
$Sh$	Sherwood number $Sh = \alpha_h L / D$
$Sr$	Strouhal number $Sr = fL / U$
$St$	Stanton Number $St = Nu / (PrRe)$
$TPP$	thermal performance parameter

# Introduction

*"As the saying goes, the Stone Age did not end because we ran out of stones; we transitioned to better solutions. The same opportunity lies before us with energy efficiency and clean energy."*

—Chu [36]

## 1.1 Motivation

Due to the increasing scarcity of resources and the arising environmental awareness of people, methods for optimizing efficiency become increasingly important in industry. This opens up new fields of research in both industry-related and fundamental research. Tremendous progress has already been made in many areas in terms of energy and resource efficiency over the last years. Particularly in established processes, the possibilities for further performance increases are often limited. However, potential still exists in a number of fluid mechanical processes. The technically relevant turbulent flows in particular cause losses that are directly responsible for the consumption of several billion tons of fossil oil per year worldwide [70]. At the latest, the effects of the energy crisis of the 1970s, when the oil price doubled for the first time within two years from 1972 to 1974 before more than doubling again from 1977 to 1980 [202], promoted interest in researching scientific solutions for direct drag reduction in all fluid mechanical processes. As described by Gad-el-Hak [70], reducing the overall drag of aircraft would result in over a billion dollars in fuel price savings for US aircraft alone.

Nature proved to be the most important source of inspiration to achieve efficiency in flows, producing drag reduction mechanisms essential for the survival of various species [23]. While promising results have already been achieved with surface texture replication (e. g. [13]), many effects turned out to be not usable until today in most technical flows since they are based on natural mucus (e. g. [45]), renewable surface structures (e. g. [47]), dynamically adaptable surface shapes (e. g. [179]) or a combination of those. All these measures aim to keep the boundary layer laminar. By the research of the mechanisms of action new concepts for lowering drag of bodies exhib-

## 1 Introduction

iting relative motion to contacting fluid are constantly developed (e. g. [82, 147, 238]).

In addition to the drag reductions inspired by nature, other passive and active methods have also been investigated. Active methods, which are characterized by energy input into the fluid, include boundary layer suction (e. g. [7]), boundary layer blow-off (e. g. [177]) or other boundary layer influences such as moving walls (e. g. [35, 38]), as well as general turbulence destabilisation with the aim of relaminarising turbulent flows (e. g. [128]). Passive methods, by contrast, are characterized by the fact that no actuators are necessary to influence the boundary layer. This category includes methods such as grooves (e. g. [126]), tabs (e. g. [176]), protrusions (e. g. [204]), crests (e. g. [P4]), and dimples (e. g. [140, 168, P3]). These methods aim to change the statistics of turbulent motions towards the one-component limit in order to relaminarise the flow [103] or to modify the phenomenon of streak formation [109, 119] by stabilizing coherent structures and generating an energy barrier across which the interaction of small scales is prevented, and thus energy loss is minimized.

Dimples are also well known in the field of thermal efficiency enhancement [144] in addition to their use to increase mechanical efficiency. In this case, deeper dimples are used, for example in cooling channels of gas turbine blades. As such, dimples are used as turbulators, structures that generate vortices when they are subjected to cross-flow [62, 63]. These disturb the thermal boundary layer which increases mixing of the fluid and thus enhances heat transport from surfaces. In contrast to other turbulators such as protrusions, ribs or rods, dimples are characterised by the fact that the vortices are generated inside the dimple, which makes them self-cleaning and prevents the surface from getting polluted. They also do not protrude into the channel, which prevents the channel from being blocked and reduces the weight of the overall construction. Ultimately, the resulting pressure drop is low, which leads to comparably high thermal efficiency of dimples [219]. As noted by Griffith et al. [79], the thermal effects of such dimples have been intensively studied since the work of Schukin et al. [200] in 1995.

## 1.2 Aims and objective of this thesis

With regard to the drag-reducing effect of dimples in channels and on surfaces subjected to cross-flow, contradictory statements still exist in the scientific literature. In addition to the pure effectiveness, the physical mechanism of action is controversially discussed [140, 212]. In this way, different

authors arrive at appreciably different results with relatively similar setups. For this reason, one aim of this work is to model the physical phenomena in detailed numerical flow simulations, to draw conclusions about the effects of the dimples on the flow and thus to close the existing gaps in knowledge with regard to both the thermal and the drag-reducing effects of dimples.

Another aim of this work is to explore the possibilities of energy-efficient heat transfer from rotating discs by using dimples. Examples of such applications include the cooling of brake discs and other rotating components that require cooling during operation, such as turbines or electric motors. As part of the *RegVent* project [59], which was funded by the Bavarian State Ministry of Education, Science and the Arts, rotating discs were used as friction fans. As a result of their positioning in two separate air ducts, the discs in this setup were investigated as room ventilation systems with heat recovery. Despite the frequently studied effects of dimples in rotating cooling channels, there is still a lack of fundamental research into the influences of dimples on rotating discs. In this work, the thermal and hydro-mechanical behaviour of dimples on discs is therefore to be investigated in a structured manner for the first time. The declared aim of this research is to obtain knowledge about parameters that lead to desired effects in the structuring of discs. From this, a design rule is to be derived that enables the heat transfer of rotating discs to be designed with regard to desired objectives through the use of dimples.

## 1.3 Methodology and structure of this thesis

Chapter 2 provides an overview of the most important literature in the three disciplines relevant to this thesis: (i) heat transfer from surfaces with dimples, (ii) drag reduction due to dimples, and (iii) heat transfer from rotating discs. Chapter 3 presents the most important theoretical principles. These are heat transfer in fluids in section 3.1, the general principles of fluid mechanics in section 3.2, the basics of turbulent flows in section 3.3, specific knowledge of boundary layers in section 3.4, special features of rotating discs in section 3.5 and the numerical treatment of turbulent flows in section 3.6.

Chapters 4 to 6 cover the main part of this thesis. In chapter 4, the most important physical phenomena of dimples in plain channel and plate flows are investigated. In section 4.1 the basic phenomena in turbulent flows without dimples are examined and the simulation quality is validated. In the following section 4.2 the impact of flat dimples on the drag behaviour is analysed. In section 4.3 the behaviour of deeper dimples is evaluated. Due to the considerably different geometry of these dimples from flat surfaces and the heat

## *1 Introduction*

transfer involved, these simulations require detailed validations, before the relevant parameters are examined in detail.

In chapter 5, dimples on rotating discs are investigated, which are placed far enough from each other so that the mutual influence of the flow around the dimples is prevented. In sections 5.1 and 5.2, the setup is presented and the quality of the simulations is shown on the basis of available literature data and numerical parameters. Section 5.3 deals with the analysis of the thermal behaviour of the discs with single dimples. Here, the different performance of round and teardrop-shaped dimples is discussed in particular. Furthermore, the findings from scale-adaptive simulations (SAS) are presented.

From the findings concerning the dimple shape and the numerical efficiency of the different solver methods, the interaction of several dimples in different arrangements on rotating discs is analysed within chapter 6. Section 6.1 deals with the methodology according to which the setups were constructed in order to allow for a systematic investigation of the widest possible range of influencing factors. In the following section 6.2, the fluid-mechanical effects of the cylinder, which is used as a support for the discs and is also subjected to flow, are discussed. Subsequently, the findings of the different setups in various flow regimes are presented. The investigations show that there is a critical rotation rate above which some of the effects of the dimples become dominant. Therefore, section 6.3 is structured according to the flow condition in relation to the critical rotation velocity. Here, a distinction is made between a range below the critical rotation velocity as well as a transition range and a state above the critical rotation velocity. In addition to the quantitative thermal effects, the thermal efficiency of the individual setups is also examined. Finally, guidelines are developed in section 6.4, according to which the design of dimples setups on a rotating disc can be carried out with regard to the desired target parameters. The final chapter 7 summarises the most important findings of the work and gives an outlook on promising starting points for further research work.

# Analysis of topic-related research

*"[To] mechanical progress there is apparently no end: for, as in the past so in the future, each step in any direction will remove limits and carry us past barriers which have till then blocked the way in other directions; and so what for the time may appear to be a visible end or practical limit will turn out but a bend in the road."*

—Reynolds [187]

This thesis deals with the use of dimples as a surface structure to increase the convective heat transfer of rotating discs while at the same time limiting the hydrodynamic losses. Therefore, three different fields of research are of major importance for this work. These are firstly the increase of heat transfer from plates subjected to cross-flow by the use of dimples, and secondly the mechanisms of heat transfer at rotating discs. With regard to the use of dimples on plates, there is a third, albeit less wide-ranging, field of research dealing with the phenomenon of drag reduction caused by the use of dimples. This chapter thus presents the already existing scientific work on each of these three research fields.

## 2.1 Progress in heat transfer enhancement due to dimples

Dimples are depressions in surfaces, which are generally used in structured, but less often also in random arrangements. Spherical dimples are the most common shape, but there are also studies on oval, polygonal and teardrop-shaped dimples [144]. Figure 2.1 shows an example of spherical dimples in a structured arrangement on a surface as well as the covered area of the dimples compared to the reference area to calculate coverage ratio  $\beta$ . As outlined by Ligrani [144], serious research into heat transfer on dimples began in 1986. In this year, Gromov et al. [80] published first studies on the flow and heat transfer due to dimples. The authors describe the emergence of symmetric cells in the boundary layer and recirculation flow inside the dimples. In the 1990s, Kesarev & Kozlov [108] investigated the local heat transfer at individual dimples. They found a dependence of the heat transfer on the degree of

## 2 Analysis of topic-related research

turbulence of the flow. Afanasyev et al. [3] investigated both the heat transfer and the drag behaviour of plates structured with dimples. They found up to 30% to 40% increase in heat transfer without significant increase in friction factors.

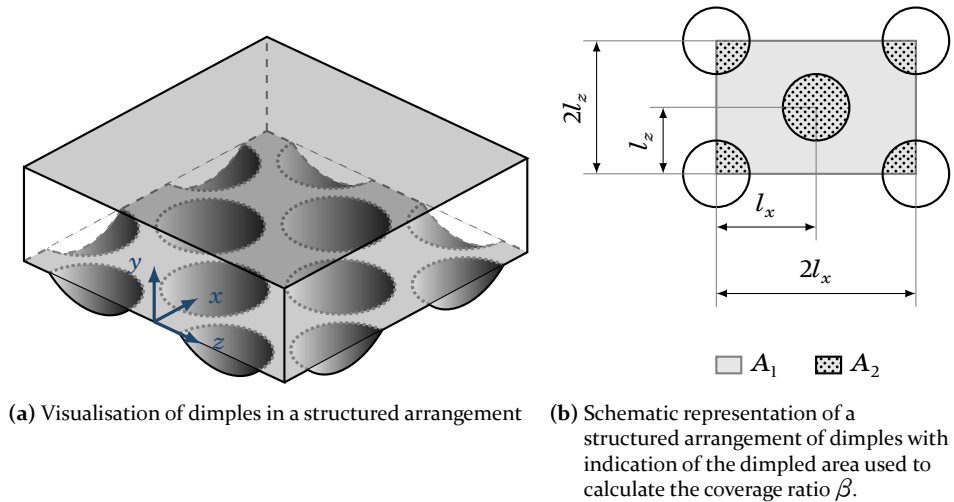


**Figure 2.1:** Visualisation of dimples (a) and presentation of covered area (b).

Schukin et al. [200] presented the first investigations of dimples to be used in gas turbine technology, which is the main field of application and research regarding the heat transfer behaviour of dimples to date. The given measurement results include the average heat transfer coefficient at a heated plate downstream of a single hemispherical cavity in a diffuser and in a nozzle. Kithcart & Klett [118] investigated the influence of dimples and other three-dimensional surface roughness in ducts with respect to thermal efficiency. They used the ratio of Stanton number  $St = Nu/(PrRe)$  increase to drag coefficient increase  $(St/St_0)/(c_f/c_{f0})$  for evaluation and found dimples to be best suited to increase heat transfer without significant losses. Although Gee & Webb [72] showed as early as 1980 that the use of thermal efficiency  $(St/St_0)/(c_f/c_{f0})^{1/3}$  is better suited for judgements about the heat transfer increase, the comparison of increasing heat transfer to increasing drag  $(St/St_0)/(c_f/c_{f0})$  is still used today. However, this value only provides information about how well the Reynolds analogy is suitable for the case under consideration, while the thermal efficiency can be interpreted as a ratio of gain to cost.

Chyu et al. [37] compared spherical and teardrop-shaped dimples with rib turbulators. Their investigations show that the dimples provide similarly

## 2.1 Progress in heat transfer enhancement due to dimples

high heat transfer as the rib turbulators, but with mentionable lower pressure losses. The authors also point out the advantage of weight reduction when using dimples for turbine cooling. Lin et al. [145] showed results of numerical simulations known as computational fluid dynamics (CFD) on the same dimples arrangement regarding the resulting flow structures as well as the heat transfer distribution. Gortyshov et al. [77] investigated the hydrodynamics and heat transfer in ducts with different arrangements of dimples and found both an increase in heat transfer and pressure loss with increasing dimples depth.

Moon et al. [161] experimentally investigated the influence of channel height on heat transfer and drag in dimpled passages. The investigations included channel heights of 37% to 149% of the dimple diameter at Reynolds numbers  $Re$  of 12 000 to 60 000. The authors found no dependence of the heat transfer increase on the duct height. Similarly, no dependence of the heat transfer enhancement ratio on  $Re$  was found. Furthermore, the authors confirmed the high thermal performance of the dimples compared to other turbulators. Chen et al. [27] found very good results for different variants of dimples in investigations of the heat transfer behaviour of dimples in pipes. They were able to demonstrate an increase in heat transfer of up to 84% for the same pumping power compared to smooth tubes. The authors emphasise that despite the comparatively simple design, dimples outperform almost all other known heat transfer enhancement mechanisms.

Mahmood et al. [150] compared the flows for a wide range of  $Re$  and temperature ratios at constant channel height. They identified the detachment of vortex pairs at the dimples and the resulting strong secondary flows as factors influencing the heat transfer. Furthermore, they described shear layer reattachment within the dimples as well as the strong mixing due to the vortices as significant influences. Ligrani et al. [143] deepened the knowledge of this geometry and described that the effects on thermal transport are particularly pronounced near the downstream rims of the dimples and on the smooth surfaces behind and between the dimples. In an investigation concerning the influence of channel height, Mahmood & Ligrani [151] found an intensification of detached vortices with decreasing channel height. They also found a strong correlation of Nusselt number  $Nu$  and temperature difference of fluid temperature and wall temperature.

Ligrani et al. [141] described the transient, dynamic and time-averaged characteristics of the vortex structures formed by dimples in staggered arrangement in channels of different heights  $h/D_1 = 0.25$  to 1.00. They described a primary vortex pair for all channel heights, which periodically sheds from the

## 2 Analysis of topic-related research

centre of the dimples. This detachment causes a constant flow of fluid into the dimples. According to the authors, the frequency of these vortices scales with the mean bulk velocity  $\bar{u}$  and the dimple imprint diameter  $D_i$ , resulting in dimensionless frequencies  $f$  of 2.2 to 3.0 for all channel heights investigated. Furthermore, with decreasing channel height, the authors found more pronounced primary vortices as well as additional, likewise intensifying secondary vortices which arise at the spanwise sides of the dimples. Finally, Ligrani et al. [141] observed a relation between the vortices and the locally prevailing wall shear stress  $\tau_w$ . These investigations were further intensified by Won et al. [237]. Using ensemble-averaged power spectral density profiles, the authors found separation frequencies of primary vortex pairs from 7 Hz to 9 Hz at Reynolds numbers based on channel height  $Re_H$  from 2100 to 20 000.

On setups similar to those studied by Kithcart & Klett [118] in terms of friction factors and some flow structure characteristics, Mahmood et al. [152] and Ligrani et al. [142] conducted intensive studies on heat transfer and flow structures arising in channels with dimples on one wall and protrusions on the opposite wall. The authors found increased vortex activity and thus increased mixing as a result of protrusions, which increases both heat transfer and drag compared to dimpled channels without protrusions. Overall, the protrusions lead to lower thermal performance due to the increased drag. In initial numerical investigations, Isaev et al. [95] were able to determine both large-scale vortex structures and an increase in heat transfer. The authors also found notable increases of drag in these investigations. Their results are in well agreement with the values determined experimentally by Chyu et al. [37].

From the early 2000s, the need for valid results of the effects of turbulators in rotating ducts intensified. Bredberg [15] addressed this challenge by using numerical simulations and explicitly points out the lack of experimental investigations of  $Nu$  in rotating ducts in his investigations. Griffith et al. [79] conducted experiments regarding heat transfer in rotating ducts with dimples and confirmed the considerable influence of rotation on the flow and resulting heat transfer behaviour. Discussions of the paper by Ligrani et al. [142] and Griffith et al. [79] show that the measured factors of heat transfer increase in the literature for similar dimple setups in stationary ducts range from 1.6 to 2.6 and thus – depending on the measurement method used – are likely to be subject to noteworthy measurement uncertainties. A comprehensive literature review by Ligrani et al. [143] underlines the wide dispersion of the measured heat transfer increase and increase of drag for different

## 2.1 Progress in heat transfer enhancement due to dimples

dimple shapes, setups and measurement methods. Other studies, in which rotation was taken into account, delivered partly contradictory results. Some studies show that the rotational effects on the ratio of  $Nu$  are suppressed at high  $Re$ , whereby the heat transfer increase with increasing  $Re$  corresponds more closely to that of the stationary channels [144]. However, this is attributed to the fact that the rotation number decreases with increasing  $Re$  and otherwise constant conditions in the measurement setups. Studies in which  $Re$  was kept constant show a stronger deviation of  $Nu$  increase compared to stationary channels with increasing rotation number [144].

Kim et al. [116] extended the Reynolds number range up to  $Re = 360\,000$  related to the hydraulic diameter of the stationary cooling channel. The investigations confirm the high thermal efficiency of the dimples compared to other, common cooling methods. In the following, the research group including Isaev & Leontiev [94] carried out many numerical investigations on individual dimples using the  $k-\omega$ -SST model proposed by Menter [155], which was by then known to yield good results for such complex, wall-dominated flows [157]. Although these investigations contribute to the understanding of the flow within a dimple, they provide only a limited contribution to the direct applicability of the technology due to the neglect of the often complex interactions that occur when using several dimples.

Burgess & Ligrani [22] examined the influence of dimple depth in more detail and found larger increases in mean Nusselt number  $Nu_m$  for deeper dimples. However, the authors point out that in practice the possible dimple depth is often limited by the wall thickness of the channel. This limitation is also relevant for the present work when the effects of dimples on rotating discs of limited thickness are discussed. The authors note that the local values of  $Nu$  within the dimples are mostly higher than those of the smooth channels. This is consistent with the results of Kesarev & Kozlov [108] and Schukin et al. [200] as mentioned by Ligrani [144].

Kim & Choi [115] and Samad et al. [194] dealt with the numerical optimisation of the arrangement and size of dimples. They found correlations between dimple shape, heat transfer behaviour and drag, enabling rudimentary designs of the surface layout. In direct numerical simulations, Wang et al. [226] found regions of high turbulent intensity above the downstream half of the dimples and along the side edges. These regions match with those where Ligrani et al. [141] found vortex shedding in experiments. The authors also point out the increased drag due to dimples, but the heat transfer and thus the thermal efficiency was not considered. In his dissertation, Elyyan [57] dealt with the influences of the Coriolis force due to rotation on dimpled channels

## 2 Analysis of topic-related research

using large eddy simulations (LES). He found a pronounced dependence of flow and turbulent mixing on the relative direction of rotation, related to the position of the dimples. In agreement with Xiao et al. [239], Elyyan & Tafti [58] pointed out that dimples are no suitable heat transfer amplifiers for steady, laminar flows.

Numerical investigations by Xie et al. [241] regarding the effectiveness of dimples in non-rotating cooling ducts with  $180^\circ$  bends show that dimples are suited to reach heat transfer increases of up to 2.0 with only 5% pressure drop increase. These values were obtained for  $100\,000 \leq Re \leq 600\,000$  and with dimples on the outer side of the  $180^\circ$  bends. In a numerical optimisation using RANS simulations, Kim et al. [110] optimised spherical dimples arranged in a row with respect to heat transfer. They found inclined elliptical dimples to be ideally suited to increase heat transfer by 81.2%, while pressure drop only increased by 31.7%. The investigation of the flow structures showed a pronounced vortex, which was caused by the dimple shape and was also detectable downstream of the dimple. The authors see this as the reason for the improvement in heat transfer. Turnow et al. [218] also confirm the good effectiveness of oval dimples. In time-resolved numerical investigations of the flow around spherical dimples, they also found coherent vortex structures that occur inclined to the main flow. The orientation of these structures varies over time, resulting in oscillations of long period duration. In another publication, Turnow et al. [221] found an optimal dimple depth of  $h/D_i = 0.26$ . With this setup, the heat transfer rate reached over 200% of the smooth channel, which agrees well with the results obtained by Siddique et al. [203].

Chen et al. [28] investigated the influence of shifting the lowest point of the dimples while maintaining the round print shape of the dimple. They found that such asymmetric dimples have better thermal properties than spherical dimples when the lowest point is shifted about 15% downstream. The authors emphasise the positive potentials of asymmetric dimples. V-shaped dimples were investigated by Jordan & Wright [102]. They found comparable thermal efficiency with spherical dimples at low  $Re$ . However, with increasing  $Re$ , the authors observed secondary vortices due to the V-shape, which considerably increased the heat transfer, but only marginally increased the pressure drop. Xie et al. [240] investigated spherical dimples with protrusion structures within the cavity. This shape is also motivated by the need for minimising the recirculation area at the dimple inlet and thus increasing the heat transfer more in proportion to the pressure drop. Depending on the specific location of the protrusion, the authors found ideal shapes for the highest

## 2.2 Observation of drag reducing effects of dimples

heat transfer as well as for the highest thermal efficiency. However, corresponding dimples are more difficult to manufacture than conventional spherical dimples. Rao et al. [183, 184] conducted a comprehensive experimental and numerical study on round, elliptical, inclined elliptical, and teardrop-shaped dimples. The teardrop-shaped dimples turned out to be the most suitable. This shape is also asymmetrical and reduces the recirculation area at the dimple inlet. The teardrop shape leads to a higher surface coverage rate compared to the spherical shape. As a result, teardrop-shaped dimples in ducts achieve appreciable thermal efficiency.

From 2015 onwards, the teardrop shape was researched more intensively. Yoon et al. [243] explored the influence of the length of the upstream half of the dimples. Their results show that small asymmetries up to 20% have hardly any influence on the thermal performance. For 30%, however, the efficiency increases, but does not increase further with increasing asymmetry. Numerical optimisation of the shape and arrangement of the dimples provided further insights into the flow-relevant effects. Li et al. [137] performed a geometric optimisation of the thermal performance of dimples in pipes. They found that for this case, an arrangement of the dimples in rows provides better heat transfer characteristics than staggered arrangements. Furthermore, they found the dimple diameter to have little influence compared to the influence of dimple shape, depth, pitch, and starts. Murata et al. [165] investigated arrangements of teardrop-shaped dimples at different angles to the inflow direction. In their investigations, the film cooling effectiveness remained almost constant at different blowing ratios. They found the highest heat transfer at an angle of 30°.

Rashidi et al. [185] provide a comprehensive overview of the energy saving potentials as well as the mechanisms of dimples in thermal energy systems. They conclude their work with suggestions for future research topics in the field of dimples. They emphasise the need for further research on dimples in rotating systems. They justify this with the increased relevance to applications. This conclusion is in line with the motivation for the present research work. A tabular overview of the research carried out on heat transfer due to dimples is given in the appendix in table A.1.

## 2.2 Observation of drag reducing effects of dimples

In addition to the intensively explored field of application of heat transfer enhancement, a much smaller field of science deals with the reduction of drag of smooth surfaces by dimples. As noted by Lashkov & Samoilova [130]

## 2 Analysis of topic-related research

and Lienhart et al. [140], these are not the effects that occur on round golf balls when using dimples. On golf balls, the dimples lead to a stabilisation of the turbulent boundary layer as well as to defined detachment edges on the surface of the ball. This stabilises the trajectory of the golf ball. Since dimples are spatially discrete indentions whose shape and arrangement on plates vary in spanwise as well as in streamwise direction, the effects on the flow are strongly dependent on the specific geometric design. As a result, different studies come to very different conclusions regarding the effects and effectiveness of drag reduction. However, all studies have in common that drag reductions – if at all – are only found with shallow dimples whose depth  $h$  does not exceed approximately 5% of the imprint diameter  $D_i$ , i. e.  $h/D_i < 5\%$  for a wide range of  $Re$ .

It is therefore not surprising that Lashkov & Samoilova [130], in their investigations of the influence of dimples on the drag of plates with dimple depths  $h/D_i$  between 7% and 15%, only found increases of drag for  $Re = 3 \cdot 10^6$  to  $9 \cdot 10^6$ . Comprehensive numerical and experimental investigations were carried out by Lienhart et al. [140]. They investigated two different setups with  $h/D_i = 4.3\%$  and  $h/D_i = 5\%$  in a channel flow and on a plate. They found only negligible differences of about 1% over the entire range  $Re = 1 \cdot 10^4$  to  $6 \cdot 10^4$  investigated. In the direct numerical simulations, they found that the mean wall shear stress decreased due to the dimples. However, the dimples resulted in a pressure force in flow direction, which amounted to about 5.5% of the total force on the wall. This effect entirely negated the positive influence of the reduced shear force and even lead to a slight net increase of drag.

Tay [212] investigated a very similar setup over a similar range of  $Re$  and found drag increases of up to 2.5% for  $Re = 1 \cdot 10^4$  to  $2 \cdot 10^4$ . However, for  $Re > 3 \cdot 10^4$  he found reductions of about 0.7%. In addition, the author examined the same dimples in a more dense arrangement, increasing the coverage rate  $\beta$  from 40% to 90%. In this case, he found notable drag reductions for  $Re > 3 \cdot 10^4$  as well, reaching up to almost 2% at  $Re \approx 4 \cdot 10^4$ . In further investigations, he explored the formation of flow structures over shallow and deep dimples [213] and investigated the physical effects of drag reduction of shallow dimples [214] as previously suggested by Abdulbari et al. [1]. In this work, he extended the original investigations by a setup with a reduced dimples depth  $h/D_i = 1.5\%$  and a coverage rate of 90%. With this setup, reductions of 1% to 2.5% were achieved over the entire range  $Re = 6 \cdot 10^3$  to  $7.7 \cdot 10^4$ . For  $Re > 3 \cdot 10^4$ , up to 3% reduction could be achieved with the setup of the same coverage rate using deeper dimples of  $h/D_i = 1.5\%$ .

The authors Tay et al. [214] attribute the results to the conclusion that the dimples lead to spanwise flow components near the wall, which suppress the normal energy cascade towards the smaller scales and thus reduce the wall shear stress due to the stabilisation of the flow. Deeper dimples, however, are more likely to lead to flow separation and pressure force components on the wall. As  $Re$  increases, detachments become less likely, suppressing the negative effect of flow separation. The highest drag reductions of up to 6% were found by Tay & Lim [215] with teardrop-shaped dimples.

Van Nesselrooij et al. [168] found reductions of up to 4% for a plate with dimples of depth  $h/D_i = 2.5\%$  at  $Re = 4 \cdot 10^4$ . By varying the distribution of the dimples on the surface, the authors showed that the orientation of the dimples with respect to each other has a decisive influence on the drag reduction. From this, they deduce that the dimples must be placed in such a way that large scale flow structures are created near the wall, which influence the turbulent structures in the boundary layer. This creates a system that is sensitive to disturbances and must be optimally adapted to the respective flow condition in order to generate positive effects with regard to drag. Similar investigations by van Campenhout et al. [25] with a favourable pressure gradient in the inflow boundary layer did not lead to a reduction in drag with otherwise identical setup. A tabular overview of the research carried out on drag reduction due to dimples is given in the appendix in table A.2.

## 2.3 Flow and heat transfer of rotating discs

The first theoretical investigations of laminar and turbulent flow without heat transfer around rotating discs were carried out and published by von Kármán [105], who analytically derived the theoretical boundary layer thickness, the axial velocity and the frictional resistance for the laminar case as well as an approximate solution for the turbulent case of a rotating disc. Theodorsen & Regier [216] carried out measurements at high Mach numbers  $Ma$ , which largely confirmed and expanded von Kármán's considerations. The results also showed that skin friction does not depend on  $Ma$ , but strongly depends on surface roughness and its specific structure. Further investigations of the flow field were carried out by Cochran [40], who improved von Kármán's work and gave the exact solution for the laminar flow field. Schlichting & Truckenbrodt [197] expanded the knowledge by presenting the solution for the axial flow around a rotating disc in the laminar range.

Noteworthy investigations of the heat transfer of rotating discs were published from the 1950's onward by Millsaps & Pohlhausen [158, 159] who cal-

## 2 Analysis of topic-related research

culated the mean heat transfer coefficient for discs of constant temperature in the laminar regime and later by Cobb & Saunders [39], who converted the results given by Millsaps & Pohlhausen [158, 159] into the equation  $Nu = 0.28 \cdot Re^{0.5}$  and stated, that this formula underestimates the results they had found experimentally. As an explanation, they mention that the solution of Millsaps & Pohlhausen [158, 159] applies to incompressible fluids, but due to the density changes of air by thermal effects, the specific heat capacity at constant pressure  $c_p$  would have to be used instead of that at constant volume  $c_v$  in the energy equation. By correcting this they found the correlation to be  $Nu = 0.35 \cdot Re^{0.5}$ , which was much better in agreement with their experimental results and also confirms the results of Wagner [223]. In the turbulent range they found the relationship  $Nu = 0.015 \cdot Re^{0.8}$ , which comes from the friction analogy for turbulent flows, as a limitation of the achievable values. Rotem [190] later stated that the heat transfer of freely rotating discs limited by  $Nu=0.0172 \cdot Re^{0.8}$  in the turbulent range is about 25 % lower for enclosed discs with  $Nu = 0.0131 \cdot Re^{0.8}$ .

Also during this time, a comprehensive investigation of the stability of three-dimensional boundary layers was carried out by Gregory et al. [78], who were the first to use the china-clay evaporation technique [188] on rotating discs [69]. For this method, which was developed during the Second World War, the model is sprayed with a transparent cellulose glue containing powdered kaolin, known as china clay [86]. When the glue dries, the surface of the model turns white. If a liquid with a similar refractive index is sprayed onto the kaolin, the refraction of light in the crystals that make up the layer is inhibited and the layer thus appears transparent. Since the evaporation of the liquid is increased in areas of turbulent flow, these zones lose their transparency earlier than lamellar zones. This flow visualization technique allowed the identification of the beginning of the transition range from laminar to turbulent flow. As drivers of the transition, they identified disturbances leading to waves, that propagate under the influence of the rotation and - with increasing radius and thus increasing  $Re$  - form characteristic vortex cords, which ultimately lose their identity in a fully turbulent flow. In the late 1950's and early 1960's, research in the field of flow around rotating discs focused on the influence of compressibility [175], Prandtl number  $Pr$  [209, 217] and non-uniform surface temperature distribution on the discs under investigation [84, 85, 217]. In addition, more unusual influences, such as that of an axial magnetic field on the flow and heat transfer [208] have also been investigated, giving rise to new fields of studies that will not be examined here in greater extend.

### 2.3 Flow and heat transfer of rotating discs

Kreith et al. [125] investigated the mass and heat transfer from an enclosed rotating disc with and without source flow by means of hot wire, smoke visualization technique, and the china clay method. They derived a dimensionless correlation of Sherwood number  $Sh = \alpha_h L/D$  using mass diffusivity  $D$  for mass transfer from a partially enclosed disc with source flow at Schmidt number  $Sc = \nu/D = 2.4$  with the kinematic viscosity  $\nu$ . In his doctoral thesis published in 1969, the main author Kreith [124] presented the first comprehensive overview of the heat and mass transfer on rotating bodies in both laminar and turbulent regimes, with and without enclosure as well as with and without external flow field.

Due to the rapidly growing computer power [120], which was found to double every one to two years [162, 163] and still does so today [20, 122], numerical investigations became more and more important. On the one hand, science was concerned with increasing the flexibility and efficiency of code for solving fluid mechanical problems (cf. e.g. Schumann [201]). On the other hand, the new field of turbulence models emerged, among which the  $k$ - $\epsilon$  model, developed by Jones & Launder [101] and later reformulated by Launder & Sharma [133] to the *standard*  $k$ - $\epsilon$  model known today, became widely used. They showed that the model is well suited to capture the swirling flow around rotating discs and point out the importance of this model for the calculation of heat transfer of rotating discs.

Nevertheless, the simulations were not used to any significant extent until the 1990s. Ong & Owen [173] simulated the flow and heat transfer of a rotating disc and showed on the basis of several simulations that the method is sufficiently simple, efficient and accurate to answer practical questions. This conclusion is supported by Pilbrow et al. [180], who investigated the heat transfer on a rotating disc with a special enclosure to illustrate the effects in gas turbines. Their simulations show good agreement with the measurements. Furthermore, the simulations gave detailed insights into areas that could not be measured. This possibility is one of the greatest advantages of computational fluid dynamics to date.

Czarny et al. [44] investigated vortex structures in turbulent flows between rotating and stationary discs. Previously, Abrahamson et al. [2] and Humphrey et al. [89] had discovered such structures between co-rotating discs, later vortex instabilities in certain rotor-stator configurations were suspected as the reason for difficult-to-predict flow conditions. Czarny et al. [44] found in their investigations that detectable structures occur over a wide range of flow conditions. In their experiments, the number of vortices decreases with increasing rotational Reynolds number.

## 2 Analysis of topic-related research

Comprehensive numerical work by means of LES as well as measurements in the wind tunnel were carried out by Wiesche [228] from 2002. The work dealt with the heat transfer increase as well as wake instabilities [228], the heat transfer in general [229] and the influence of the disc thickness as well as the angle of attack to the flow [230]. In 2016, Wiesche & Helcig [231] published a comprehensive work concerning the flow and heat transfer phenomena that occur when rotating discs are exposed to flows under different conditions. The authors point out that the numerical effort for simulating the flow around rotating discs using LES is still relatively high today and therefore the use of RANS simulations still remains justified, even if their ability to represent more complex phenomena is limited.

Nguyen & Harmand [169] were able to closely reproduce the heat transfer of rotating discs mounted on a cylinder using RANS simulations. Using more complex LES, they were able to describe the complex vortex formations and the detailed heat transfer behaviour of the disc. They found a close connection between the time-dependent heat transfer at the disc surface in the wake of the cylinder and the vortices in the flow field. They also found half-moon shaped areas of high heat transfer on the flow-facing side of the disc as well as a high correlation between turbulent momentum transport and heat transfer on the disc.

Sardasht et al. [195] investigated seven turbulence models, including four RANS models and three hybrid models, with respect to their suitability for adequately predicting the heat transfer of rotating discs subjected to impinging jets. In their investigations, the delayed detached eddy simulation with realizable  $k$ - $\epsilon$  model (DDES-RKE) was best suited to represent the characteristics of both the flow and the heat transfer. Among the RANS models, the re-normalisation group model ( $k$ - $\epsilon$ -RNG) performed poorest. The shear stress transport model ( $k$ - $\omega$ -SST) performed well in the edge region. The scale adaptive model (SAS) yielded similar results as the  $k$ - $\omega$ -SST model in the stationary case, but achieved slightly better results in the case of rotating conditions. A tabular overview of the research carried out on the flow and heat transfer of rotating discs is given in the appendix in table A.3.

### Conclusions

This overview of the scientific literature about heat transfer due to dimples, drag reduction due to dimples and heat transfer from rotating discs demonstrates the intensive research being done in these three disciplines. In all cases, a number of experimental and numerical investigations have already been carried out. Especially in the case of drag-reducing effect of dimples,

### *2.3 Flow and heat transfer of rotating discs*

there is still no consensus regarding the mode of action and the effective potential of dimples. Information about the effects of dimples on the flow would also affect the research field of thermal effects of dimples. So far, no investigations of the thermal and hydro-mechanical effects of dimples on rotating discs have been carried out. Several authors such as Griffith et al. [79] and Wagner et al. [224] point out the usefulness of investigating the effects of dimples in rotating systems as well. These challenges are therefore addressed in the following of this thesis.



# Fundamental theory and governing equations

*"Les causes primordiales ne nous sont point connues; mais elles sont assujetties à des lois simples et constantes, que l'on peut découvrir par l'observation, et dont l'étude est l'objet de la philosophie naturelle."*<sup>1</sup>

—Fourier [65]

In order to understand the complex fluid-mechanical processes of convective heat transfer in general and on rotating discs in particular, the partial differential equations for the description of the heat transfer as well as those of the underlying fluid dynamics are presented in the following. Subsequently, the principals of turbulent flows are discussed. Special emphasis is then given to boundary layers and the features of the flow around rotating discs are described.

## 3.1 Heat transfer in fluids

In general, heat transfer takes place through one or more of the three basic types *heat conduction*, *convection*, and *heat radiation* [91, 139]. Since heat radiation plays only a subordinate role in the investigations carried out in this thesis, it will not be discussed in detail. Heat conduction and especially convection dominate the heat transfer investigated in this work, hence these are introduced in the following. The explanations are mainly based on the works of Incropera et al. [91] and Lienhard & Lienhard [139].

### Conduction

Heat conduction is the transport of thermal energy between molecules in fluids or solids driven by a temperature gradient. Heat is always transferred from the higher temperature to the lower temperature and is proportional to the

---

<sup>1</sup>The primary causes are not known to us; but they are subject to simple and constant laws, which can be discovered through observation, and whose study is the object of natural philosophy. (*own translation*)

### 3 Fundamental theory and governing equations

temperature gradient. Fourier's law of 1822 [65], given in Equation (3.1), describes stationary heat conduction for the one-dimensional plane wall and shows that the steady heat flux density  $\dot{q}$  in a medium is proportional to the temperature gradient  $dT/dx$  multiplied by the material-specific thermal conductivity  $k_t$ . This effect occurs at the atomic and molecular level and transfers energy in the form of heat from the more energetic to the less energetic particle [91].

$$\dot{q} = -k_t \frac{dT}{dx} \quad (3.1)$$

The heat transfer rate  $dq$  normal to an infinitesimal surface element  $dA$  is determined according to equation (3.2) where  $n$  denotes the normal direction to the surface  $dA$ .

$$dq = -k_t \frac{\partial T}{\partial n} dA \quad (3.2)$$

By using the first law of thermodynamics, the dependent variable  $\dot{q}$  can be eliminated from Fourier's law, resulting in the unsteady heat diffusion equation given in equation (3.3) using the thermal diffusivity  $a_D = k_t/(\rho c_v)$ , where  $\rho$  is the fluid density and  $c_v$  is the specific heat capacity at constant volume.

$$\frac{\partial^2 T}{\partial x_i^2} = \frac{1}{a_D} \frac{\partial T}{\partial t} \quad (3.3)$$

### Convection

In addition to heat diffusion by random molecular motion energy is also transported by macroscopic fluid motion, when fluid moves with a relative velocity  $u_{\text{rel}} \neq 0$  to a solid body while both substances have a different temperature. Convective heat transfer occurs as free or as forced convection. Free convection is exclusively driven by buoyancy forces due to density differences while forced convection occurs when an external energy source such as a pump or fan powers the flow. In the flows considered in this work, the density differences due to temperature gradients are negligible compared to the prevailing inertial effects. Therefore, buoyancy forces can be neglected.

The heat transfer  $\dot{q}_w$  from the wall to the fluid is coupled to the temperature gradient via the convection heat transfer coefficient  $\alpha_h$  as shown in equation (3.4).

$$\dot{q}_w = \alpha_h (T_w - T_f) \quad (3.4)$$

This relationship is known as Newton's law of cooling. The convection heat transfer coefficient  $\alpha_h$  depends on the specific boundary layer, which in turn is influenced by the surface geometry and the prevailing forces and conditions such as surface roughness. Therefore, any investigation of convective heat transfer can ultimately be summed up in the determination of the corresponding  $\alpha_h$ .

In common heat transfer considerations, energy is transferred from a surface of higher temperature  $T_w$  to a fluid of lower temperature  $T_f < T_w$ . Since fluid adheres to the wall, the heat flow at the surface  $y = 0$  can be coupled to the temperature gradient using Fourier's law according to equation (3.5) via the thermal conductivity  $k_t$  of the fluid [91].

$$\dot{q}_w = -k_t \left. \frac{\partial T}{\partial y} \right|_{y=0} \quad (3.5)$$

Accordingly, the convection heat transfer coefficient  $\alpha_h$  can be determined from equations (3.4) and (3.5) as given in equation (3.6).

$$\alpha_h = -\frac{k_t}{T_w - T_f} \left. \frac{\partial T}{\partial y} \right|_{y=0} \quad (3.6)$$

The Nusselt number  $Nu$  is a dimensionless ratio that relates  $\alpha_h$  and a characteristic length  $L$  to the thermal conductivity  $k_t$  as shown in equation (3.7). In this work,  $Nu$  was used for evaluations in chapters 4 to 6.

$$Nu = \frac{\alpha_h L}{k_t} \quad (3.7)$$

As recommended by Turnow [219], the temperature can be represented dimensionless as  $T^+$  via equation (3.8) in order to compare different temperature levels with one another. Here,  $T_0$  is the reference temperature and  $\Delta T$  the characteristic temperature difference.

$$T^+ = \frac{T - T_0}{\Delta T} \quad (3.8)$$

### 3 Fundamental theory and governing equations

Using this,  $\alpha_h$  can be determined from equation (3.6) according to equation (3.9).

$$\alpha_h = -\frac{k_t}{T_w^+ - T_f^+} \left. \frac{\partial T^+}{\partial y} \right|_{y=0} \quad (3.9)$$

When used in equation (3.7),  $Nu$  results as a function of the dimensionless temperature according to equation (3.10).

$$Nu = -\frac{1}{T_w^+ - T_f^+} \left. \frac{\partial T^+}{\partial y} \right|_{y=0} L \quad (3.10)$$

The mean Nusselt number  $Nu_m$  of a surface under consideration is obtained as the integral of the local Nusselt number over the surface, as shown in equation (3.11).

$$Nu_m = \frac{1}{A (T_w^+ - T_f^+)} \int_A Nu (T_w^+ - T_f^+) dA \quad (3.11)$$

In the case of constant wall temperature and constant fluid temperature far from the wall, equation (3.11) simplifies to equation (3.12). Likewise,  $\alpha_h$  is directly proportional to the temperature gradient at the wall  $\partial T^+ / \partial y|_{y=0}$  in this case.

$$Nu_m = \frac{1}{A} \int_A Nu dA \quad (3.12)$$

Using this approach, the total heat transfer rate  $q$  can be determined with  $Nu_m$  using equation (3.13).

$$q = Nu_m \frac{k_t}{L} (T_w - T_f) A \quad (3.13)$$

## 3.2 Principals of fluid dynamics

All calculations used in this work are based on the continuum assumption. This is valid for laminar and turbulent flows when time and length scales are very large compared to the molecular scales. This means that the Knudsen number  $Kn = \lambda_m/L$  must be significantly less than unity, i. e.  $Kn \ll 1$ . Here,  $\lambda_m$  and  $L$  are the mean free path of molecules and the macroscopic characteristic length, respectively. In the present work air is used as medium with a free path length of  $\lambda_m \approx 5 \cdot 10^{-8}$  m to  $6.8 \cdot 10^{-8}$  m [87, 98, 181], depending on temperature, pressure and humidity. The smallest geometric dimensions investigated are in the range of  $1 \cdot 10^{-4}$  m, resulting in  $Kn \approx 5 \cdot 10^{-4}$  to  $6.8 \cdot 10^{-4}$  and thus  $Kn \ll 1$ . The conservation of mass, momentum and energy can therefore be used as the basis of all physical descriptions. The following derivations are based on standard works for fluid dynamics and thermodynamics such as Durst [54], Brodkey [21], Bird et al. [12], Spurk & Aksel [210], White [227], Rotta [192], Böswirth & Bschorer [14] or Herwig & Schmandt [87].

### Continuity equation

The continuity equation, also referred to as mass conservation, states, that the rate of increase of mass per unit volume is equal to the net rate of mass addition per unit volume by convection [12], leading to the general form given in equation (3.14)

$$\frac{\partial \rho}{\partial t} + \frac{\partial(\rho u_i)}{\partial x_i} = \frac{D\rho}{Dt} + \rho \frac{\partial u_i}{\partial x_i} = 0 \quad (3.14)$$

with the fluid density  $\rho$  and the velocity component  $u_i$  in the  $x_i$ -direction. For thermodynamically incompressible flows equation (3.14) simplifies to equation (3.15) [54].

$$\frac{\partial u_i}{\partial x_i} = 0 \quad (3.15)$$

This condition applies in good approximation for many technically relevant flows where it holds for Mach number  $Ma$  as defined in equation (3.16) with the speed of sound  $a$  that  $Ma \lesssim 0.2...0.3$ .

$$Ma = \frac{u}{a} \quad (3.16)$$

As can be seen from equation (3.17) [167] density changes scale linearly with changes of velocity and with  $Ma^2$ , meaning that the changes in density are

### 3 Fundamental theory and governing equations

around 4% of the velocity changes at  $Ma = 0.2$  and around 9% of the velocity changes at  $Ma = 0.3$ .

$$-Ma^2 \frac{du}{u} = \frac{d\rho}{\rho} \quad (3.17)$$

Since temperature gradients are relevant in this work, flows are considered incompressible when the changes in density  $d\rho$  due to variations in pressure  $p$  and temperature  $T$  as given in equation (3.18) are not greater than 5%. Such flows are referred to as incompressible flows, as no significant density changes occur in the flow field. In this sense, incompressibility is to be interpreted as a property of the flow field rather than a fluid property [87].

$$d\rho = \frac{\partial \rho}{\partial p} dp + \frac{\partial \rho}{\partial T} dT \quad (3.18)$$

#### Momentum equation

From Newton's second law the momentum equation for viscous fluids can be derived as shown in e. g. [54] or [21], leading to equation (3.19) with the unknown, symmetric, molecular-caused momentum transport  $\tau_{ij}$  and acceleration  $g_j$ .

$$\rho \left[ \frac{\partial u_j}{\partial t} + u_i \frac{\partial u_j}{\partial x_i} \right] = -\frac{\partial p}{\partial x_j} - \frac{\partial \tau_{ij}}{\partial x_i} + \rho g_j \quad \text{for } j = 1, 2, 3 \quad (3.19)$$

For Newtonian fluids, that are relevant in this work,  $\tau_{ij}$  can be derived from the physics of ideal gases [54], leading to the general form given in equation (3.20)

$$\tau_{ij} = -\mu \left[ \frac{\partial u_j}{\partial x_i} + \frac{\partial u_i}{\partial x_j} \right] + \frac{2}{3} \delta_{ij} \mu \frac{\partial u_k}{\partial x_k} \quad (3.20)$$

Here,  $\delta_{ij} = 1$  for  $i = j$  and 0 for  $i \neq j$  is the Kronecker delta and  $\mu$  stands for dynamic viscosity. For incompressible fluids, the second term on the right side disappears since  $\partial u_k / \partial x_k = 0$  for incompressible fluids as shown in equation (3.15). Applied in equation (3.19) the Navier-Stokes equations follow from the momentum equation, as given in equation (3.21).

$$\rho \left[ \frac{\partial u_j}{\partial t} + u_i \frac{\partial u_j}{\partial x_i} \right] = -\frac{\partial p}{\partial x_j} + \mu \frac{\partial^2 u_j}{\partial x_i^2} + \rho g_j \quad (3.21)$$

Equation (3.21) yields one equation for each spatial direction  $j = 1, 2, 3$ . The resulting system of equations, consisting of the conservation of mass in equation (3.14) and the three equations of conservation of momentum in equation (3.21), is not closed, since the four existing equations need to solve for five unknown scalar quantities  $u_1 = u$ ,  $u_2 = v$ ,  $u_3 = w$ ,  $\rho$  and  $p$ . To solve this problem, an additional equation of state of the form  $p = f(\rho T)$  can be introduced. For ideal gases, the ideal gas law according to equation (3.22) using the specific gas constant  $R$  is usually applied.

$$p = \rho RT \quad (3.22)$$

Using the continuity equation given in equation (3.15) and the Navier-Stokes equations from equation (3.21), flows without thermal impacts can be described using suitable initial and boundary conditions. As soon as thermal effects become relevant, the total energy balance of the fluid needs to be taken into account.

### Energy equation

The total energy is composed of kinetic, potential and internal energy and can be described according to equation (3.23) using inner energy  $e$  and the potential  $G$  as well as the heat flux  $\dot{q}_i$

$$\rho \frac{D}{Dt} \left( \frac{1}{2} u_j^2 + G + e \right) = -\frac{\partial \dot{q}_i}{\partial x_i} - \frac{\partial (p u_j)}{\partial x_j} - \frac{\partial (\tau_{ij} u_j)}{\partial x_i} \quad (3.23)$$

The thermal energy equation given in equation (3.24) follows by subtracting the mechanical part of the energy, which can be obtained from multiplying equation (3.19) by  $u_j$  and is therefore not independent of the momentum equation [54].

$$\rho \frac{De}{Dt} = -\frac{\partial \dot{q}_i}{\partial x_i} - p \frac{\partial u_j}{\partial x_j} - \tau_{ij} \frac{\partial u_j}{\partial x_i} \quad (3.24)$$

From the form of the thermal energy equation shown in equation (3.24), different forms of representation can be derived, depending on the field of application. In fluid mechanics, the change of internal energy is usually replaced by pressure and temperature. This, in conjunction with the Maxwell equations of thermodynamics and using the specific heat capacity at constant volume  $c_v$ , yields the form of the thermal energy equation for ideal gases in equation (3.25).

$$\rho c_v \frac{DT}{Dt} = k_t \frac{\partial^2 T}{\partial x_i^2} - p \frac{\partial u_i}{\partial x_i} - \tau_{ij} \frac{\partial u_j}{\partial x_i} \quad (3.25)$$

Here, the heat flow  $\dot{q}_i$  has been replaced by the thermal conductivity  $k_t$  multiplied by the temperature gradient according to Fourier's law as given in equation (3.1) [91].

## 3.3 Turbulent flows

The characteristics of a flow are largely determined by whether the prevailing inertial forces or the viscous forces of the fluid dominate. The ratio of those forces is thus an important indicator for the behaviour of a flow and is known as the Reynolds number  $Re$  given in equation (3.26), even though Stokes [211] used this concept 30 years before Reynolds [186] popularised its use from 1883 onwards [191].

$$Re = \frac{UL}{\nu} \quad (3.26)$$

$U$  is a characteristic velocity,  $L$  is a characteristic length and  $\nu = \mu/\rho$  is the kinematic viscosity. With increasing  $Re$ , the probability increases that small disturbances in the flow are not damped by the viscosity over time but are further amplified by inertia [8]. In this case the flow turns turbulent in contrast to laminar flow at lower  $Re$ . Most technically relevant flows are turbulent flows. Overall, turbulent flows exhibit some important properties that can be described primarily in qualitative terms. For example, turbulent flows are irregular and disorganised. In addition, turbulence leads to increased diffusion. This results in higher rates of momentum, heat and mass transport, which leads to mixing and accelerated transport processes of scalar quantities such as temperature  $T$ . The increased mixing also leads to increased dissipation. This often results in increased losses that need to be compensated by higher external power in order to maintain the flow.

Other characteristics of turbulent flows are their three-dimensionality and rotation. Due to vortex stretching and tilting, turbulent flows always develop in all three spatial directions. Furthermore, turbulent flows are characterised by the occurrence of different scales, whereby energy is principally transported from the large to the small scales. Nevertheless, all turbulent flows can be described as a continuum, since even the smallest scales are far larger than the molecular scales. The individual movement of a vortex or a particle in a turbulent flow is unpredictable [181], but the probability of future states can be estimated using statistical methods.

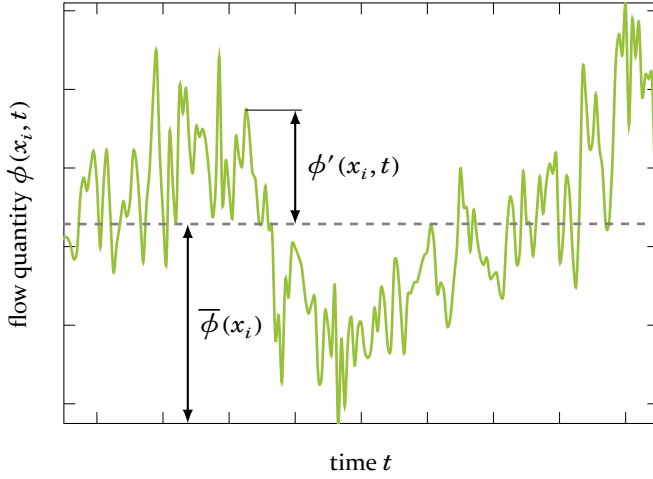


**Figure 3.1:** Flow quantity  $\phi$  of a turbulent flow at a defined physical position  $x_i$  over time with the temporal average  $\bar{\phi}$  from equation (3.28) and the fluctuating part  $\phi'(t)$  based on Durst [54].

### Statistics of turbulent flows

A common approach for the treatment of turbulent flows is the division of the time-dependent variables  $\phi$  such as velocity  $u_i$ , pressure  $p$  or temperature  $T$  into a temporal mean value  $\bar{\phi}$  and a time-dependent fluctuation component  $\phi'$  according to equation (3.27) [54].

$$\phi = \bar{\phi} + \phi' \quad ; \quad u_i = \bar{u}_i + u'_i \quad ; \quad p = \bar{p} + p' \quad ; \quad T = \bar{T} + T' \quad (3.27)$$

The division is visualised in figure 3.1. The calculation of the mean value can be done according to equation (3.28).

$$\bar{\phi}(x_i) = \lim_{\bar{\tau} \rightarrow \infty} \frac{1}{\bar{\tau}} \int_0^{\bar{\tau}} \phi(x_i, t) dt \quad (3.28)$$

Equation (3.27) shows that the turbulent fluctuation  $\phi'$  represents the difference between the instantaneous value  $\phi$  and the temporal mean value  $\bar{\phi}$ . From this definition it follows that the temporal mean value of the fluctuation  $\bar{\phi}'$  is equal to 0 according to equation (3.29).

### 3 Fundamental theory and governing equations

$$\lim_{\bar{x} \rightarrow \infty} \frac{1}{\bar{x}} \int_0^{\bar{x}} \phi'(x_i, t) dt = \overline{\phi'}(x_i) = 0 \quad (3.29)$$

The calculation of the mean value of a local instantaneous flow quantity can also be calculated using the probability density function. The expectation value  $\langle \phi \rangle$  of a random variable  $\phi$  is defined in equation (3.30) [181].

$$\langle \phi \rangle = \int_{-\infty}^{\infty} \psi f(\psi) d\psi \quad (3.30)$$

Here,  $\psi$  represents the possible values that  $\phi$  can take while  $f(\psi)$  is the probability density function.  $\langle \phi \rangle$  is thus the probability-weighted mean of all potential values of  $\phi$ , which is why it can also be considered the mean of  $\phi$ . Therefore,  $\overline{\phi}$  equals  $\langle \phi \rangle$ , as shown in equation (3.31) [54].

$$\overline{\phi}(x_i) = \lim_{\bar{x} \rightarrow \infty} \frac{1}{\bar{x}} \int_0^{\bar{x}} \phi(x_i, t) dt = \int_{-\infty}^{\infty} \psi f(\psi) d\psi = \langle \phi \rangle \quad (3.31)$$

#### Correlated Fluctuations

More detailed information about the structure of turbulence is provided by correlation analysis of the fluctuations, usually the velocity fluctuations. Here, both the temporal variation of a variable at a fixed point in space and the spatial correlation at a given point in time can be considered. The correlation coefficient  $R_c$  for two variables  $\phi_1$  and  $\phi_2$  is defined in equation (3.32) [181].

$$R_c = \frac{\langle \phi'_1 \phi'_2 \rangle}{\sqrt{\langle \phi_1'^2 \rangle \langle \phi_2'^2 \rangle}} \quad (3.32)$$

The normalisation  $\sqrt{\langle \phi_1'^2 \rangle \langle \phi_2'^2 \rangle}$  leads to a limitation of the function to the range of  $-1$  to  $+1$ . The unscaled two-point correlation  $R_{ij}$  of streamwise velocity fluctuation  $u'$  at time  $t$  is given in equation (3.33). In the following equations,  $x_i$  stands for any point in space,  $\Delta x_i$  represents a shift of  $x_i$ , and  $\zeta$  is a specific, fixed position in space. Likewise,  $t$  stands for any point in time,  $\Delta t$  represents a duration of time, and  $\tau_t$  is a specific, fixed point of time.

$$R_{ij} = \langle u'(x_i, t) u'(x_i + \Delta x_i, t) \rangle \quad (3.33)$$

Using this approach, the correlation of the velocity at different points at the same time  $t = \tau_t$  can be derived using equation (3.32). It is called the auto-correlation in space and is given in equation (3.34).

$$R_s = \frac{\langle u'(x_i, \tau_t) u'(x_i + \Delta x_i, \tau_t) \rangle}{\sqrt{\langle u'(x_i, \tau_t)^2 \rangle \langle u'(x_i + \Delta x_i, \tau_t)^2 \rangle}} \quad (3.34)$$

In the same way, the autocorrelation in time for a fixed point  $x_i = \zeta$  can be determined according equation (3.35).

$$R_t = \frac{\langle u'_i(x_k, t) u'_j(x_k, t + \tau_t) \rangle}{\sqrt{\langle u'_i(x_k, t)^2 \rangle \langle u'_j(x_k, t + \tau_t)^2 \rangle}} \quad (3.35)$$

The analysis of the time-averaged autocorrelation of velocity  $u$  in the main flow direction  $x$ , that will be used in this thesis further on, leads to  $R_u$  as defined in equation (3.36) [117] for all positions  $y$  investigated.

$$R_u = \frac{1}{\Delta t L_z} \int_{t_0}^{t_0 + \Delta t} \int_0^{L_z} u'(0, y, z, t) u'(\zeta, y, z, t) dz dt - \bar{u}^2(y) \quad (3.36)$$

Here,  $y$  is the wall-normal direction,  $\zeta$  is the position in streamwise  $x$ -direction,  $z$  is the spanwise direction,  $L_z$  is the width of the domain,  $t$  is the time, and  $t_0$  the chosen starting time. Correlation analysis were used for validations in chapters 4 to 6.

### Length scales

To verify whether computational domains are large enough to resolve the turbulent structures, the integration of the correlation coefficient length scale  $R_l$  according to equation (3.37) is frequently used.

$$R_l = \frac{1}{R_s(x_i = 0, t)} \int_0^\infty R_s(\zeta, t) d\zeta \quad (3.37)$$

A length scale  $L$  characterising the largest eddies in a turbulent flow is given in equation (3.38) as a function of the turbulent kinetic energy  $k$ , and the rate of dissipation of turbulent kinetic energy  $\varepsilon$ . This length corresponds to the characteristic length of the flow problem under investigation.

### 3 Fundamental theory and governing equations

$$L = \frac{k^{3/2}}{\varepsilon} \quad (3.38)$$

The length scale of the smallest structures is given by the Kolmogorov length scale  $\eta_K$  according to equation (3.39) as a function of the kinematic viscosity  $\nu$  and the rate of dissipation of turbulent kinetic energy  $\varepsilon$ .

$$\eta_K = \left( \frac{\nu^3}{\varepsilon} \right)^{1/4} \quad (3.39)$$

With the definition of the turbulence Reynolds number  $Re_L = k^{1/2}L/\nu = k^2/(\varepsilon\nu)$  according to Pope [181], it becomes apparent that the ratio of these scales  $L/\eta_K$  increases with  $Re_L$  according to equation (3.40).

$$\frac{L}{\eta_K} = \frac{k^{3/2}\varepsilon^{1/4}}{\varepsilon\nu^{3/4}} = \frac{k^{3/2}}{\varepsilon^{3/4}\nu^{3/4}} = \left( \frac{k^2}{\varepsilon\nu} \right)^{3/4} = Re_L^{3/4} \quad (3.40)$$

For the numerical consideration of the flow, this implies that with a constant length scale  $L$  of the flow problem, a finer resolution becomes necessary with increasing  $Re$  in order to resolve the same proportion of the energy. This increases both the effort for the calculation and for the post-processing.

#### Anisotropy invariant map

The anisotropy invariant map (AIM) offers the possibility to check the plausibility of numerically simulated turbulence. For this purpose, the anisotropy of the Reynolds stress tensor is represented in an invariant map [61]. This type of analysis was introduced by Lumley [148] and further developed by Jovanović [103]. The anisotropy tensor  $a_{ij}$  is defined according to equation (3.41) [103] where  $\overline{u'_i u'_j}$  denotes the turbulent stress tensor,  $q_f = \overline{u'_k u'_k}$  the turbulence intensity [61] represented by the sum of the velocity fluctuations on the main diagonal, thus the trace of the turbulent stress tensor and  $\delta_{ij}$  the Kronecker delta. From the anisotropy tensor  $a_{ij}$  the invariants  $II_a$  and  $III_a$  can be derived according to equations (3.42) and (3.43).

$$a_{ij} = \frac{\overline{u'_i u'_j}}{q_f} - \frac{1}{3} \delta_{ij} \quad (3.41)$$

$$II_a = a_{ij}a_{ji} \quad (3.42)$$

$$III_a = a_{ij}a_{jk}a_{ki} \quad (3.43)$$

### Identification of vortices

In order to identify vortices in turbulent flows, different approaches have been developed. A very simple way is to use vorticity  $\omega_u = \epsilon_{ijk} \frac{\partial u_j}{\partial x_i}$  in order to identify vortices. A disadvantage of this method is the insufficient identification of vortices in boundary layer flows, since in these a superposition of vortices and shear movements occurs. A differentiation of these is not possible using  $\omega_u$ . The  $Q$ -criterion according to Hunt et al. [90] represents the second invariant of the velocity gradient  $\partial u_i / \partial x_j$  following equation (3.44). Here  $S_{ij}$  according to equation (3.45) and  $\Omega_{ij}$  according to equation (3.46) stand for the symmetric and the antimetric part of the velocity gradient, respectively.

$$Q = \frac{1}{2} (\Omega_{ij}\Omega_{ij} - S_{ij}S_{ij}) \quad (3.44)$$

$$S_{ij} = \frac{1}{2} \left( \frac{\partial u_i}{\partial x_j} + \frac{\partial u_j}{\partial x_i} \right) \quad (3.45)$$

$$\Omega_{ij} = \frac{1}{2} \left( \frac{\partial u_i}{\partial x_j} - \frac{\partial u_j}{\partial x_i} \right) \quad (3.46)$$

For positive values of  $Q$ , the antimetric part and thus the rotation rate  $\Omega_{ij}^2$  dominates the symmetric part, i. e. the strain rate  $S_{ij}^2$ . These areas therefore mark regions in which rotation predominates in the investigated flow.

The  $\lambda_2$  method, which was developed by Jeong & Hussain [99] in 1995, is very well suited for vortex identification in a large number of different flows. In this method, the  $\lambda_2$ -criterion is used to determine for each point in the velocity field whether it is part of a vortex core or not. The starting point for the definition of the  $\lambda_2$  criterion is again the symmetric and the antimetric parts  $S_{ij}$  and  $\Omega_{ij}$  of the velocity gradient  $\partial u_i / \partial x_j$ . From the sum  $S_{ij}^2 + \Omega_{ij}^2$ , the three eigenvalues  $\lambda_1$ ,  $\lambda_2$  and  $\lambda_3$  are calculated, where  $\lambda_1 \geq \lambda_2 \geq \lambda_3$  holds. The  $\lambda_2$  criterion states that a point is part of a vortex for  $\lambda_2 < 0$ .

This criterion identifies local pressure minima, which result exclusively from vortex movements. A vortex structure is visualised by the iso-surface of a chosen  $\lambda_2$  threshold value.

## 3.4 Boundary layers

In the vicinity of solid walls, flows differ fundamentally from a free flow. As a result of the interaction between fluid and wall, boundary layers are created which can influence the entire flow. This is particularly relevant when the wall is covered with macroscopic structures such as dimples [219]. The theory of boundary layers was developed by Prandtl [182], who showed that the flow around a body can be divided into two different areas. These are a very thin layer of low velocity close to the body, in which viscosity dominates, and the main flow far away from the body, where viscosity can be neglected [199]. The formation of a viscous and a thermal boundary layer is shown schematically on an overflowed plate in figure 3.2. Here, the temperature at the wall is higher than that of the fluid.

There are different definitions for the determination of the viscous boundary layer thickness  $\delta_u$ . The conventional definitions have in common the description of the boundary layer thickness as a function of the mean velocity profile which develops perpendicular to the wall. The most basic, rather arbitrary definition sets the boundary layer thickness  $\delta_{99}$  equal to the wall distance at which  $u$  reaches 99% of the free stream velocity  $u_\infty$ . A physically sensible and fluid-mechanically interpretable measure for the boundary layer thickness is the displacement thickness  $\delta_d$  given in equation (3.47). The displacement thickness  $\delta_d$  indicates how far the streamlines of the external flow are displaced by the boundary layer. This thickness is approximately 1/3 of the thickness  $\delta_{99}$ . [199]

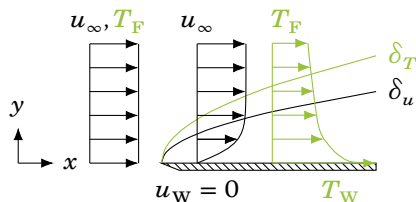


**Figure 3.2:** Schematic representation of the development of a viscous boundary layer and a thermal boundary layer in 2D.

$$\delta_d(x) = \int_0^{\infty} \left(1 - \frac{u}{u_{\infty}}\right) dy \quad (3.47)$$

Another possibility to determine the boundary layer thickness is the momentum thickness  $\delta_{\theta}$ , given in equation (3.48). It is defined by the smallest amount of momentum that flows in the boundary layer relative to that in the inviscid flow [91].

$$\delta_{\theta} = \int_{y=0}^{\infty} \frac{u}{u_{\infty}} \left(1 - \frac{u}{u_{\infty}}\right) dy \quad (3.48)$$

The presence of velocity gradients and thus a boundary layer inevitably leads to a molecular momentum exchange perpendicular to the surface. This results in drag that can be expressed by the drag coefficient  $c_{f\tau}$ , which is defined from the occurring wall shear stress  $\tau_w$  according to equation (3.49).

$$c_{f\tau} = \frac{\tau_w}{\frac{1}{2}\rho u_{\infty}^2} \quad (3.49)$$

In a Newtonian fluid, the wall shear stress  $\tau_w$  is coupled to the velocity gradient at the wall by viscosity  $\mu$  according to equation (3.50).

$$\tau_w = \mu \left. \frac{\partial u}{\partial y} \right|_{y=0} \quad (3.50)$$

In the same way as a velocity boundary layer is caused by different velocities of wall and fluid, a region of temperature gradient is also caused by different temperatures of wall and fluid. The region over which the temperature gradient occurs is called the thermal boundary layer  $\delta_T$  and is defined analogously to the boundary layer  $\delta_{99}$ . The thickness is thus determined by the point at which equation (3.51) applies.

$$\frac{T_w - T}{T_w - T_f} = 0.99 \quad (3.51)$$

### 3 Fundamental theory and governing equations

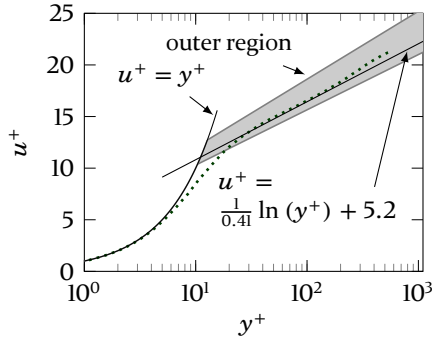


**Figure 3.3:** Dimensionless velocity  $u^+$  as a function of dimensionless wall distance  $y^+$ . The grey area indicates ranges of approximations found in Foken [64], Högström [88] and Pope [181].

#### Similarities

In some flows, the viscous and thermal boundary layers are similar. The Reynolds analogy [106] is based on the assumption that the heat flux  $\dot{q}$  correlates with the momentum flux  $\tau_{ij}$ . It thus links the viscous and the thermal boundary layers with each other. This assumption is approximately valid for gases and smooth surfaces as long as no form drag is present [71]. In this case, it is possible to estimate the heat transfer of a body to a fluid by using the often more easily available information about wall shear stress  $\tau_w$ .

In turbulent flows, the resulting velocity boundary layers are similar for many types of flows. Figure 3.3 shows the course of the dimensionless velocity  $u^+$  according to equation (3.52) over the wall distance  $y^+$  as given in equation (3.53). The friction velocity  $u_\tau$  is derived from the wall shear stress  $\tau_w$  as defined in equation (3.54).

$$u^+ = \frac{u}{u_\tau} \quad (3.52)$$

$$y^+ = \frac{u_\tau y}{\nu} \quad (3.53)$$

$$u_\tau = \sqrt{\frac{\tau_w}{\rho}} \quad (3.54)$$

As shown in figure 3.3,  $u^+ = y^+$  applies in the viscous sublayer in direct vicinity of the wall up to  $y^+ < 5$ . For  $y^+ > 30$ , the boundary layer follows

the logarithmic relationship given in equation (3.55). This region is known as the log-law region. In between is a transition region, the buffer-layer, in which the boundary layer transitions from the linear to the logarithmic relationship.

$$u^+ = \frac{1}{\kappa_c} \ln (y^+) + C_1 \quad (3.55)$$

$\kappa_c$  and  $C_1$  are the von Kármán constant and an integration constant. Depending on the study under consideration, the values for these constants fluctuate in the small percentage range around  $\kappa_c = 0.41$  and  $C_1 = 5.2$  [181]. The uncertainty arising from this variation is indicated in light grey in figure 3.3.

Analogous to  $u_\tau$  and  $u^+$ , a friction temperature  $T_\tau$  as given in equation (3.56) and a dimensionless temperature  $\Theta^+$  as given in equation (3.57) can be defined to consider the dimensionless temperature profile [75].

$$T_\tau = \frac{\bar{q}_w}{\rho c_p u_\tau} \quad (3.56)$$

$$\Theta^+ = \frac{\bar{T} - T_w}{T_\tau} \quad (3.57)$$

Outside the viscous sublayer, this leads to the logarithmic relation in equation (3.58), where  $\kappa_\Theta = 0.47$  [75] is a universal constant. The integration constant  $C_\Theta$  contains a dependency of the Prandtl number  $Pr$  according to equation (3.59) [199].

$$\Theta^+ = \frac{1}{\kappa_\Theta} \ln (y^+) + C_\Theta (Pr) \quad (3.58)$$

$$C_\Theta (Pr) = 13.7Pr^{2/3} - 7.5 \quad (Pr > 0.5) \quad (3.59)$$

$Pr$  represents the ratio of the viscosity  $\nu$  to the thermal diffusivity  $\alpha^*$ , which in turn depends on the thermal conductivity  $k_t$  as given in equation (3.60).

$$Pr = \frac{\nu}{\alpha^*} = \frac{\nu \rho c_p}{k_t} \quad (3.60)$$

### 3.5 Rotating discs

In this work, the heat transfer from rotating discs of constant temperature to fluid with free stream velocity  $u_\infty$  is investigated. Such a setup results in a complex flow interaction, which arises from the superposition of the rotation and the cross-flow. Fluid close to the rotating disc is accelerated in azimuthal direction as a result of the rotation, and at the same time convective transport takes place as a result of the main flow. Heat transfer occurs due to the temperature difference between the disc and the fluid.

The characteristic prevailing velocities are the main flow velocity  $u_\infty$  and the azimuthal velocity at the outermost edge of the disc, which is the product of the angular velocity  $\Omega$  and the disc radius  $D_d/2$ . By using these velocities in equation (3.26) and the disc radius as the characteristic length  $L$ , two Reynolds numbers suitable for describing the flow conditions can be formed. These are the rotational Reynolds number  $Re_\Omega$  in equation (3.61) and the cross-flow Reynolds number  $Re_u$  in equation (3.62) [231].

$$Re_\Omega = \frac{UL}{\nu} = \frac{(\Omega D_d/2)(D_d/2)}{\nu} = \frac{\Omega D_d^2}{4\nu} \quad (3.61)$$

$$Re_u = \frac{UL}{\nu} = \frac{u_\infty (D_d/2)}{\nu} = \frac{u_\infty D_d}{2\nu} \quad (3.62)$$

To characterise the prevailing flow condition at the disc, the ratio  $\Gamma$  of  $Re_\Omega$  to  $Re_u$  according to equation (3.63) was used in chapters 5 and 6.

$$\Gamma = \frac{Re_\Omega}{Re_u} \quad (3.63)$$

For the description of the heat transfer of the rotating disc, the mean Nusselt number  $Nu_m$  averaged over the disc surface according to equation (3.64) is suitable. Here as well, the disc radius  $D_d/2$  is used as characteristic length. The mean convection heat transfer coefficient  $\alpha_h$  is calculated according to equation (3.4) from the quotient of the temporal and spatial mean heat flux at the disc  $\bar{q}_m$  and the temperature difference  $T_w - T_f$ .

$$Nu_m = \frac{\alpha_h D_d}{2k_t} = \frac{\bar{q}_m D_d}{2k_t (T_w - T_f)} \quad (3.64)$$

The dimensionless moment coefficient  $c_{M1}$  of a rotating disc, which is defined for the rotating disc wetted on one side according to equation (3.65) [197, 198, 199], is used to evaluate the drag, using torque  $M$ , density  $\rho$ , angular velocity  $\Omega$ , and disc radius  $D_d/2$ . A more general formulation for  $c_M$  is given in equation (3.66), which replaces the specific, characteristic values of the rotating disc with general characteristic values and summarizes all constants in  $C$ , using a characteristic velocity  $U$ , a characteristic length  $L$ , and a characteristic area represented by  $L^2$ .

$$c_{M1} = \frac{M}{\frac{\rho}{2} \Omega^2 \frac{D_d^5}{32}} \quad (3.65)$$

$$c_M = \frac{M}{\rho U^2 L^3 C} \quad (3.66)$$

Depending on the definition, the values can be converted into one another using the corresponding characteristic values and a constant  $C$  for proportional scaling. By using the cross-flow velocity  $U = u_\infty$  and the disc radius  $L = D_d/2$ ,  $c_M$  can be expressed as given in equation (3.67). The choice of these values can be interpreted as using the disc radius  $D_d/2$  as characteristic length and the projected disc area  $\pi D_d^2/4$  as characteristic area. All constants including  $\pi/8$  resulting from the area of the discs are summarised in  $C$ . From equations (3.61) and (3.62) it follows that  $u_\infty = \Omega D_d/2\Gamma$ . With this definition, the factors  $c_{M1}$  and  $c_M$  can be converted into one another using equation (3.68) and  $C = 2\pi$ .

$$c_M = \frac{M}{\rho u_\infty^2 D_d^3 C} \quad (3.67)$$

$$c_M = \frac{M 4 \Gamma^2}{\rho \Omega^2 D_d^5 \frac{\pi}{32}} = c_{M1} \cdot \frac{\Gamma^2}{2\pi} \quad (3.68)$$

By considering the increase of  $Nu$  on the one hand and the increase of  $c_M$  on the other hand, the thermal efficiency of the setups compared to the smooth disc can be determined. For this purpose, the *Reynolds analogy ratio (RAR)* and the *thermal performance parameter (TPP)*, as shown in equation (3.69) and equation (3.70), were used for evaluations in chapter 6.

$$RAR = \frac{\overline{Nu}_{m,d}/\overline{Nu}_{m,s}}{\overline{c}_{Mm,d}/\overline{c}_{Mm,s}} \quad (3.69)$$

$$TPP = \frac{\overline{Nu}_{m,d}/\overline{Nu}_{m,s}}{(\overline{c}_{Mm,d}/\overline{c}_{Mm,s})^{1/3}} \quad (3.70)$$

To determine  $RAR$ , the increase of the temporal and spatial averaged Nusselt number  $\overline{Nu}_{m,d}$  of the considered setup with dimples in relation to the average Nusselt number of the smooth disc  $\overline{Nu}_{m,s}$  is divided by the ratio of the corresponding moment coefficients  $\overline{c}_{Mm,d}/\overline{c}_{Mm,s}$ . For the calculation of  $TPP$ , both the increase in convective heat transfer and the increase in drag are related to the same mass flow ratio, as originally proposed by Gee & Webb [72] and later confirmed by Liou & Hwang [146]. Thus, this value more realistically reflects the actual, energetic advantages or thermal efficiency of the considered setups.  $RAR$  cannot be used directly as a measure for estimating the efficiency of the investigated setup. Rather, it provides information on how well the Reynolds analogy matches for the compared cases, where a perfect validity would result in  $RAR = 1$ .  $RAR$  is often referred to in the literature as Reynolds analogy performance parameter, e. g. [143, 144]. However, this name is misleading, as this ratio does not allow for evaluation of the performance of a setup in the conventional sense, which suggests a connection to efficiency.

### 3.6 Numerical modelling of turbulent flows

As introduced in section 3.3, the largest structures of a turbulent flow exhibit a length scale  $L$  whose order corresponds to that of the characteristic length of a flow problem. Due to the instability of these structures, they gradually break down into smaller structures. During this process, energy is transported from the large to the small scales. On the smallest scales, which correspond to the Kolmogorov length scale  $\eta_K$ , the energy dissipates into internal energy [121]. To consider this energy transfer, it is helpful to transform the two-point correlation from equation (3.34) into the Fourier space as given in equation (3.71). Here  $\Phi_{ij}$  is the velocity spectrum tensor,  $\chi$  stands for the space vector and  $\kappa$  is the wavenumber, which is the inverse of the length scale.

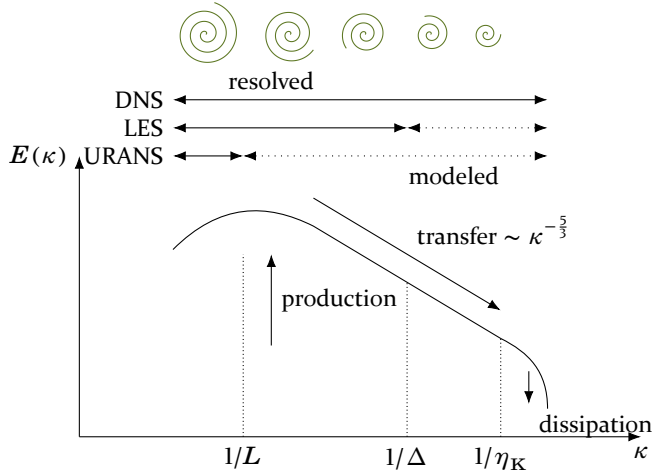


**Figure 3.4:** Schematic distribution of energy over wavenumber  $\kappa$  in a turbulent flow. Different levels of modelling resolve different amounts of the energy. Relevant scales are the characteristic length  $L$ , the filter width  $\Delta$ , and the Kolmogorov length scale  $\eta_K$ .

$$\Phi_{ij}(\kappa, t) = \frac{1}{(2\pi)^3} \iiint_{-\infty}^{\infty} e^{-i\kappa\chi} R_{ij}(\chi, t) \, dx dy dz \quad (3.71)$$

The integration of  $1/2\Phi_{ij}$  over  $\kappa$  yields the energy spectrum function  $E$ . As shown in equation (3.72), the integral of the energy spectrum function  $E$  over all wavenumbers  $\kappa$  yields the kinetic turbulent energy  $k$  [181].

$$\int_0^{\infty} E(\kappa, t) \, d\kappa = \frac{1}{2} R_{ij}(0, t) = \frac{1}{2} (\overline{u'_i u'_i}) = k \quad (3.72)$$

The schematic representation of the energy spectrum  $E$  over the wavenumber  $\kappa$  in figure 3.4 visualises the effect of energy transfer. In this representation, three areas can be distinguished [66]. At low wavenumbers  $0 \leq \kappa \leq 1/L$  the energy is introduced into the flow. This is the energy containing range around the peak of  $E(\kappa, t)$ . In the inertial range  $1/L < \kappa < 1/\eta_K$ , the energy transport takes place towards the smaller scales. In this range, the relation  $E(\kappa, t) \sim \kappa^{-5/3}$  applies. In the dissipation range  $1/\eta_K \leq \kappa$ , the energy dissipates into internal energy.

This universal behaviour applies to flows of high  $Re$  and far from solid walls. Since walls influence the formation and decay of vortices, the effect of viscos-

### 3 Fundamental theory and governing equations

ity on the energy cascade is masked. This results in different energy spectra in the vicinity of walls [III].

#### Different levels of modelling

In order to simulate a turbulent flow domain based on the conservation equations, all occurring scales need to be spatially and temporally resolved. Such an approach is called direct numerical simulation (DNS). The numerical effort for a DNS increases with  $\sim Re^3$ . Therefore, the direct simulation of highly turbulent flows is neither possible nor economically reasonable even on modern high-performance computers. Furthermore, in many technically relevant flows the most important information does not lie in the smallest scales and these can therefore be modelled without considerable loss of information instead of requiring calculation. For this purpose, different modelling approaches exist. In the following, the ones that were used in this work will be presented.

#### Reynolds-averaged Navier-Stokes equations (RANS)

For many engineering applications, the time-averaged flow field and integral quantities such as lift, drag, mean torque and pressure losses are of primary relevance. Therefore, the most rigorous modelling approach to minimise the need for eddy resolution is the calculation of the time average of the flow variables. To achieve this, it is first necessary to decompose the flow variables  $\rho$ ,  $p$ ,  $T$  and  $u_i$  into a time-independent mean value ( $\bar{\phi}$ ) and a time-dependent fluctuation value ( $\phi'$ ), as already shown in section 3.3 as well as in equation (3.73).

$$\rho = \bar{\rho} + \rho' \quad ; \quad p = \bar{p} + p' \quad ; \quad T = \bar{T} + T' \quad ; \quad u_i = \bar{u}_i + u'_i \quad (3.73)$$

This decomposition is introduced into the presented equations for conservation of mass, given in equation (3.15) and conservation of momentum, given in equation (3.21). The equations are then averaged over time. By following the rules for time averaging in equation (3.74), the continuity equation for the mean flow in equation (3.75) and the Reynolds-averaged Navier-Stokes equations using a constant density  $\rho_0$  and neglecting the gravity term as given in equation (3.76) follow.

$$\overline{\bar{\phi}} = \bar{\phi} \quad ; \quad \overline{\phi'} = 0 \quad ; \quad \overline{\phi\phi'} = 0 \quad ; \quad \overline{\phi'\phi'} \neq 0 \quad (3.74)$$

$$\frac{\partial \bar{u}_i}{\partial x_i} = 0 \quad (3.75)$$

$$\rho_0 \left[ \frac{\partial \bar{u}_j}{\partial t} + \frac{\partial \overline{u_i u_j}}{\partial x_i} \right] = -\frac{\partial \bar{p}}{\partial x_j} + \frac{\partial}{\partial x_i} \left[ \mu \frac{\partial \bar{u}_j}{\partial x_i} - \rho_0 \overline{u'_i u'_j} \right] \quad (3.76)$$

The equation for the mean value of a scalar quantity, here temperature, in the flow field is given in equation (3.77) [61].

$$\frac{\partial (\rho_0 \bar{T})}{\partial t} + \frac{\partial}{\partial x_i} (\rho_0 \bar{u}_i \bar{T} + \rho_0 \overline{u'_i T'}) = \frac{\partial}{\partial x_i} \left( \alpha_D \frac{\partial \bar{T}}{\partial x_i} \right) \quad (3.77)$$

The mean value is usually formed as a function of the flow under consideration. If the flow is stationary, any unsteadiness is averaged out over time. In this case, any fluctuation is implicitly assumed to be turbulence. As a result, the mean flow equations are steady, known as Reynolds-averaged Navier-Stokes (RANS) equations. If the flow itself is unsteady, the equations are averaged over statistically identical realizations of the flow. In this case, random fluctuations are also averaged out, but the equations averaged in this way may have a non-stationary mean value originating from coherent structures in the flow. Consequently, the equations are called unsteady RANS (URANS) equations.

Due to the non-linear term in equation (3.21), the term  $\partial (\overline{u'_i u'_j}) / \partial x_i$  arises in equation (3.76). Because of its structural similarity to the momentum transport term, it acts on the flow similarly to an additional stress. Therefore, the term is called Reynolds stress tensor. This tensor is symmetrical and thus introduces six new unknowns into the system of equations. These unknowns are not balanced by equations, which is why the system of equations is no longer closed. This circumstance is known as the closure problem of turbulence and requires the modelling of the Reynolds stress tensor.

To model the influence of turbulence on the averaged flow field, the Boussinesq approximation is the most widely used assumption. Here, analogous to the viscous stress, a turbulent viscosity  $\mu_t$  is formed, which, multiplied by the mean spatial velocity gradient, approximates the Reynolds stress tensor as given in equation (3.78).

$$\rho_0 \overline{u'_i u'_j} = -\mu_t \left( \frac{\partial \bar{u}_j}{\partial x_i} + \frac{\partial \bar{u}_i}{\partial x_j} \right) \quad (3.78)$$

### 3 Fundamental theory and governing equations

As can be seen from equation (3.78), the six unknowns are replaced by an unknown quantity, the turbulent viscosity tensor  $\mu_t$ . In contrast to the dynamic viscosity  $\mu$ , this is not a property of the fluid. In analogy to the dynamic viscosity, many turbulence models are based on the calculation of the turbulent viscosity as a product of a length scale characteristic of the turbulence and a characteristic velocity. Transport equations can be developed to calculate these. Nowadays, two-equation models are widely used because they are numerically efficient and sufficiently adjustable due to the independent equations to be able to represent a large number of different states of turbulence. The best known two-equation models are the  $k$ - $\epsilon$  model of Launder & Sharma [133] and the  $k$ - $\omega$  model of Wilcox [232]. While the  $k$ - $\epsilon$  model adequately represents free shear flows, the  $k$ - $\omega$  model is superior for wall-bounded shear flows. A combination of the two models was presented by Menter [155] as the  $k$ - $\omega$ -SST model. Due to the mentionable improvements of this model compared to the classical two-equation models [157], the  $k$ - $\omega$ -SST model is nowadays a widely used standard in the scientific environment and was also applied in this work.

#### Large eddy simulation

With the help of two-equation models, efficient calculations of several types of flow are possible. By using the URANS formulation, time dependencies in the main flow can also be represented. However, small scale fluctuations in flows caused by turbulence are to a great extent isotropic far from wall. Other, often large-scale variations in flows are not isotropic at all. For this reason, a flow simulation with one – however calibrated – turbulence model to capture all fluctuations is often not suitable for the investigation of more complex flow phenomena such as pronounced vortex shedding or rotation [67]. A better separation of large, anisotropic structures and more homogeneous, isotropic turbulent fluctuation can be achieved with large eddy simulations (LES) as used in this work in chapter 4.

In a LES, large structures are calculated directly, while the resource-intensive calculation of the smallest scales is omitted. This is done by spatial filtering of the conservation equations according to Leonard [135] with a filter  $\tilde{G}$  of filter width  $\Delta$  according to equation (3.79).

$$\tilde{\phi}(x_i, t) = \int_{-\infty}^{+\infty} \tilde{G}(x_i, \dot{x}_i; \Delta) \phi(\dot{x}_i, t) d\dot{x}_i \quad (3.79)$$

Here  $\dot{x}_i$  is the integration variable in space. The filter  $\tilde{G}$  is designed in such a way that  $\int \tilde{G}(x_i) dx_i = 1$  applies. Common and widely used filters are the Gauss filter  $\tilde{G}_G = \sqrt{6/\pi} 1/\Delta \exp(-6x_i^2/\Delta^2)$  and the Box filter, which is defined by  $\tilde{G}_B = 1/\Delta$  for  $|x_i| \leq \Delta/2$  and  $\tilde{G}_B = 0$  elsewhere. More details on different filters and their properties can be found in Fröhlich [68] and Breuer [20]. Since only large structures are to be calculated directly in the LES, the mesh can be coarser than for a DNS. Thus, filtering can take place via the mesh by setting the filter width equal to the mesh size. Filtering the conservation of mass equation (3.15) and conservation of momentum equation (3.21) leads to the filtered equations equation (3.80) and equation (3.81).

$$\frac{\partial \tilde{u}_i}{\partial x_i} = 0 \quad (3.80)$$

$$\rho \left[ \frac{\partial \tilde{u}_j}{\partial t} + \frac{\partial \tilde{u}_i \tilde{u}_j}{\partial x_i} \right] = -\frac{\partial \tilde{p}}{\partial x_j} + \frac{\partial}{\partial x_i} \left[ \mu \left( \frac{\partial \tilde{u}_i}{\partial x_j} + \frac{\partial \tilde{u}_j}{\partial x_i} \right) \right] \quad (3.81)$$

When applying the linear filtering operation on the non-linear term on the left-hand side, a closure problem arises again. This results in a need for modelling this term  $\tau_{ij}^{\text{SGS}}$  as given in equation (3.82) known as subgrid-scale Reynolds stress tensor that represents the impact of the unresolved velocity components on the resolved velocity components [67].

$$\tau_{ij}^{\text{SGS}} = \widetilde{u_i u_j} - \tilde{u}_i \tilde{u}_j \quad (3.82)$$

The main task of the subgrid-scale (SGS) model is to ensure that the energy drain of the LES matches that of the DNS according to the energy cascade shown in figure 3.4. According to Zhiyin [246], the oldest known model is the Smagorinsky model (SM) [205]. As with most SGS models, the concept of an eddy viscosity  $\nu_t = \mu_t/\rho$  is applied, in which the traceless part of the SGS stresses is coupled with the strain rate  $\widetilde{S}_{ij}$  given in equation (3.84) of the calculated velocity field as given in equation (3.83).

$$\tau_{ij}^{\text{SGS}} - \frac{1}{3} \delta_{ij} \tau_{kk}^{\text{SGS}} = 2\rho \nu_t \widetilde{S}_{ij} \quad (3.83)$$

$$\widetilde{S}_{ij} = \frac{1}{2} \left( \frac{\partial \tilde{u}_i}{\partial x_j} + \frac{\partial \tilde{u}_j}{\partial x_i} \right) \quad (3.84)$$

### 3 Fundamental theory and governing equations

The turbulent viscosity can be written according to equation (3.85) using the Smagorinsky model constant  $C_S$ .

$$\nu_t = (C_S \Delta)^2 \sqrt{2\widetilde{S}_{ij}\widetilde{S}_{ij}} \quad (3.85)$$

From the consideration of isotropic turbulence follows  $C_S = 0.18$ . However, this value is too high for most flows, which is why  $C_S = 0.1$  or even lower values are often assumed. In the vicinity of solid walls,  $\nu_t$  must be reduced due to the anisotropy of turbulence. This is usually done by van Driest damping [52], replacing  $C_S$  in equation (3.85) by  $C_S D(y^+)$  with the van Driest damping function  $D(y^+)$  according to equation (3.86) using the van Driest constant  $A^+ = 25$ .

$$D(y^+) = 1 - e^{-y^+/A^+} \quad (3.86)$$

Germano [74] developed the dynamic procedure to calculate the value of  $\nu_t$  from the information available from the resolved scales. Another widely used model is the wall-adapting local eddy-viscosity (WALE) model. One advantage of this model is that it calculates a turbulent viscosity  $\nu_t = 0$  for laminar shear flows. Therefore, laminar regions in the flow are automatically treated correctly from a physical point of view. In the case of the WALE model, the eddy viscosity is calculated according to equation (3.87) which in term uses the mixing length for subgrid-scales  $L_s$  according to equation (3.90), and the adjusted strain tensor  $S_{ij}^d$  according to equation (3.88) using the subgrid-scale flux  $\widetilde{g}_{ij}$  as given in equation (3.89).

$$\nu_t = L_s^2 \frac{(S_{ij}^d S_{ij}^d)^{3/2}}{(\widetilde{S}_{ij}\widetilde{S}_{ij})^{5/2} + (S_{ij}^d S_{ij}^d)^{5/4}} \quad (3.87)$$

$$S_{ij}^d = \frac{1}{2} (\widetilde{g}_{ij}^2 + \widetilde{g}_{ji}^2) - \frac{1}{3} \delta_{ij} \widetilde{g}_{kk}^2 \quad (3.88)$$

$$\widetilde{g}_{ij} = \frac{\partial \widetilde{u}_i}{\partial x_j} \quad (3.89)$$

$$L_s = \min(\kappa_c d, C_W \Delta) \quad (3.90)$$

When calculating the mixing length for subgrid-scales  $L_s$  in equation (3.90),  $\kappa_c$  is the von Kármán constant,  $d$  is the distance to closest wall,  $C_W$  is the

WALE constant and  $\Delta$  is the filter or mesh width. As stated in [6], the value for  $C_W$  is originally 0.5 [170]. In the context of this work, the WALE model was used in the ANSYS® Fluent software in chapter 4. Based on intensive validation work, the value  $C_W = 0.325$  is used as the default value in ANSYS® Fluent [6]. The WALE model is used here in addition to numerical efficiency and correct treatment of laminar flows, as it provides good results especially for wall-bounded flows. Besides RANS and LES formulations, hybrid methods also exist, of which the scale-adaptive simulation (SAS) according to Egorov et al. [56] and Menter & Egorov [156] was applied in chapter 5.

#### Mesh Requirements

The mesh has an influence on the quality of the results in every fluid dynamics simulation. Depending on the solver used, different types of meshes can be applied. For complex geometries, unstructured meshes consisting of polyhedron-shaped elements, which lead to numerical disadvantages, are usually unavoidable. In contrast, greater challenges in meshing arise when hexahedron elements are used. However, these elements are advantageous for the simulation quality and are therefore used throughout this work.

In order to adequately resolve the boundary layer near the wall, a condensation of the mesh nodes in the wall-normal direction is necessary. Mesh compression, as shown in figure 3.5(a), is a suitable method for this purpose. The element quality suffers from this, as the ratio of longest to shortest element edge increases due to the compression. For RANS simulations, in which no small-scale fluctuations are resolved, the distortion of the elements up to a maximum edge length ratio of about 1000 usually does not lead to a considerable loss of quality.

However, this does not apply to scale-resolving simulations such as LES simulations, which were applied in this work. In order to adequately resolve the smallest vortices in all spatial directions, elements with a maximum edge length ratio of less than  $\approx 20$  are required for such simulations. To avoid the detailed resolution of the entire computational domain, it is advisable to use adapted meshes with hanging nodes in this case. For this purpose, elements in defined layers are divided in half in all three spatial directions, whereby one hexahedron is transformed into eight hexahedra in the next layer. This procedure is shown schematically in figure 3.5(b) and was used in all simulations carried out in chapter 4. Corresponding meshes cannot be processed by all solvers. Therefore, the software ANSYS® Fluent, Release 17.1 and Release 19.1 was used for all LES and RANS simulations in chapter 4. RANS, URANS and SAS simulations with lower mesh requirements were carried out with

### 3 Fundamental theory and governing equations

ANSYS® CFX, Release 17.1 and Release 19.1 in chapters 5 and 6 after demonstrating the validity of the approach in chapter 5.

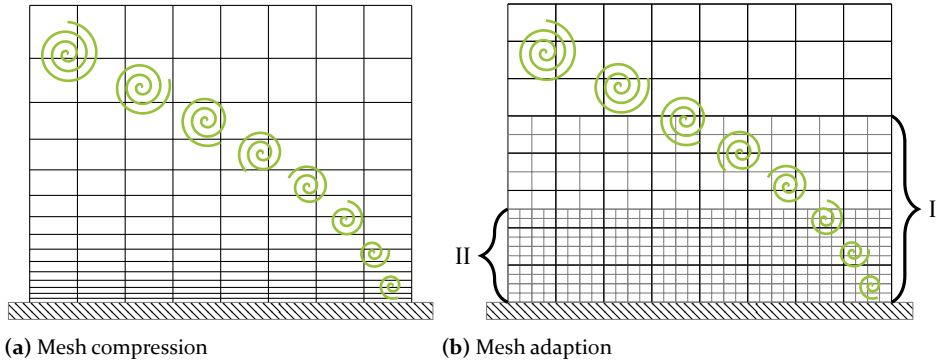


**Figure 3.5:** Visualisation of different meshing approaches for meshes consisting of hexahedron elements. Mesh compression (a) leads to good resolution of the wall-normal flow profile but fails at resolving turbulent structures. This can be achieved using mesh adoption (b), where the size of elements is divided by two in each spatial direction in each level, levels are indicated as I and II. This ensures that the element quality is maintained down to the wall.

# Investigation of dimpled surfaces in non-rotating flow

*"When I meet God, I am going to ask him two questions: Why relativity? And why turbulence? I really believe he will have an answer for the first."*

—Heisenberg, cited by Marshak & Davis [153]

In order to understand the mechanisms of interaction of dimples on rotating discs, these are first explored in stationary channels. The investigation of this simplified case offers a number of advantages. On the one hand, literature values already exist for various setups, which can be used for validation. On the other hand, effects of interest are not masked by the superposition of other mechanisms, which come into play with rotating discs. In addition, there are still inconsistencies and knowledge gaps in the scientific community regarding the effectiveness and the mechanisms of action of dimples on surfaces. The investigations presented in this chapter contribute to closing these gaps. Some of the simulation data used in this chapter was partly generated within the context of [S4].

## 4.1 Turbulent flow in channels and over flat plates

Reference simulations were carried out on smooth plates as well as in infinitely extended smooth channels to obtain reference values for the effects investigated and for further validation of the simulations. Both the flow conditions and the geometric dimensions were chosen according to the cases with dimples. In order to consider the effect of the opposite wall in the case of the channel simulations, the free surface opposite the considered wall was simulated as a wall with no-slip boundary condition. For the physically correct representation of the flow over a free plate, this surface was modelled with a symmetry boundary condition.

### 4.1.1 Setup and validation of turbulent flow simulations

In order to obtain physically meaningful results from a simulation, several restrictions have to be considered, especially in LES. These restrictions concern – among others – the mesh resolution as well as the time step size. Also the physical dimensions of the simulation domain must be sufficiently large to allow for resolving all relevant structures [68]. In the following, the simulation validation is illustrated exemplarily for the domain shown in figure 4.7(a) on page 58 without dimples. As described by Moin & Kim [160] three aspects are essential for mesh generation. These are firstly the total size of the domain, which must be large enough to prevent influences of the boundary conditions on the resulting flow in the region of interest, secondly the spatial mesh resolution, which is determined by the respective size of the individual cells and thirdly the limitation by available computing power.

#### Computational domain and setup

The size of the domain in streamwise  $x$ -direction and spanwise  $z$ -direction should be at least twice as large as the maximum length up to which relevant velocity correlations exist [160] to ensure that the basically non-physical periodic boundary conditions [68] – that are necessary for DNS [117] and also for other transient, scale resolving simulations of channel flow – have no influence on the results [201]. According to the investigations conducted by Comte-Bellot [43], this distance is  $3.2 \delta$  and  $1.6 \delta$  in  $x$ - and  $z$ -direction, respectively, with the channel half-height  $\delta$ . As the resulting structures typically grow bigger for lower  $Re$ , e. g.  $Re_\tau = 180$  [68], many investigations have been carried out on domains of size  $L_x \times L_z \times L_y = 4\pi\delta \times (\frac{4}{3} \dots 2)\pi\delta \times 2\delta$ , such as e. g. Grundestam et al. [81], Kim et al. [114], Kristoffersen & Andersson [127] and Moser et al. [164]. For higher  $Re$ , e. g.  $Re_\tau \geq 395$  [164], and thus smaller eddies domain sizes of  $2\pi\delta \times \pi\delta \times 2\delta$  are common [68].

When plates are overflowed neither the thickness of the boundary layer nor the thickness of the turbulent zone outside the boundary layer are influenced by additional walls. Nevertheless, the flow regions close to the wall are similar, although they can differ in scaling, see for example [9, 46, 164, 207]. For this type of simulations, the dimensions of the domain usually depend on the boundary layer thickness. Inoue [92] used domains  $L_x \times L_y \times L_z = 36\delta_0 \times 4\delta_0 \times 6\delta_0$  based on the inlet boundary layer thickness  $\delta_0$ , to simulate developing boundary layers. In the present simulations of developed boundary layers - and thus without a defined inlet boundary layer thickness  $\delta_0$  - domains of  $L_x \times L_y \times L_z \approx 26\delta_\theta \times 14\delta_\theta \times 15\delta_\theta$  and  $\approx 30\delta_\theta \times 14\delta_\theta \times 13\delta_\theta$

based on momentum thickness  $\delta_\theta$  were used. No considerable dependence of the results on the domain length could be found, which is in accordance with the results of Inoue [92].

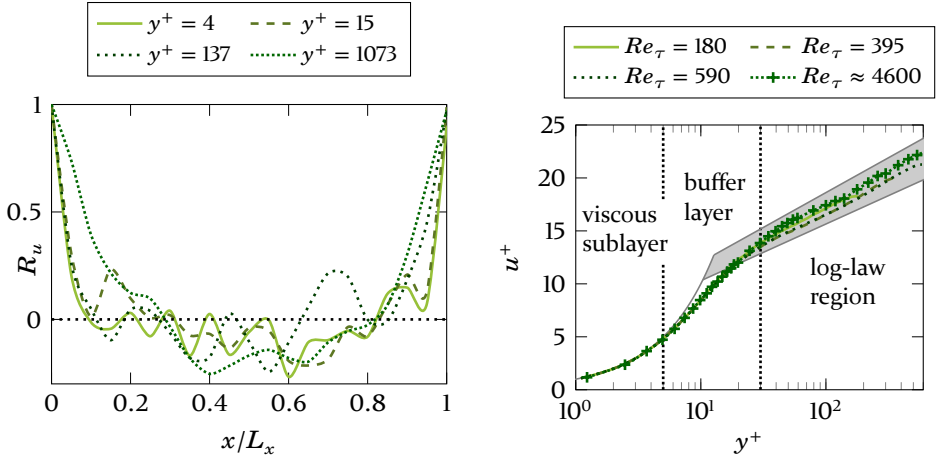
The domain height is much higher in order to minimise non-physical influences of the boundary condition on the flow near the surface of the plate. Furthermore, the domain was chosen large enough to allow for uncorrelated velocity values in main flow direction inside the viscous sublayer up to  $y^+ \leq 5$ , the buffer layer at  $5 < y^+ \leq 30 \dots 50$ , the log-law region at  $30 \dots 50 < y^+ \leq 300 \dots 800$ , and the outer layer which already belongs to the main flow at  $y^+ > 1000$  [181]. These regions are indicated in figure 4.1(b). Since the dimensions of the domain are linked to the condition that geometric periodicity is also guaranteed for the dimpled channel, the length and width were chosen such that a total of four rows of dimples in streamwise and two rows of dimples in spanwise directions were represented, as shown in figure 4.6 on page 57. In these simulations, the friction Reynolds number of  $Re_\tau \approx 4600$  was relatively high compared to most literature values such as [92, 114, 164]. Therefore, further verification measures to ensure the plausibility of the results are to be taken into account.

The verification of sufficiency of the domain sizes used for the simulations was done by correlation analysis as supposed by Herwig & Schmandt [87] of the velocity in main flow direction at different wall distances. As shown in figure 4.1(a), the values over the entire boundary layer are uncorrelated clearly before 40% of the domain length. According to Kiš et al. [117] this result indicates that the chosen domain size is sufficient for the simulations carried out. It can be seen that the values slightly fluctuate around 0 shortly downstream of the boundary condition, which stems from the fact that averaging in spanwise direction was done over five equidistant evaluation lines for each  $y^+ \in \{4, 15, 137, 1073\}$ . The position of these lines as well as the evaluation points located on them are included in figure 4.6(a) on page 57. Due to the periodic boundary conditions, the correlation at the end of the simulation domain naturally rises towards unity again.

Using the resulting momentum thickness  $\delta_\theta$  and the friction velocity  $u_\tau$  yield a Reynolds number based on momentum thickness of  $Re_\theta \approx 9066$  and a non-dimensional free stream velocity  $U_e^+ = U_\infty/u_\tau = \sqrt{2/c_f} = 27.033$ . This is in good agreement with the simulations of Inoue [92]. Österlund [174] and Nagib et al. [166] find similar values  $\kappa_c = 0.384, C = 4.08$  [174] and  $\kappa_c = 0.384, C = 4.127$  [166] for the best fit to their experiments for the adopted formula of Fernholz & Finley [60] by Nagib et al. [166]  $c_f =$

#### 4 Investigation of dimpled surfaces in non-rotating flow

$2 [U_e^+]^{-2} = 2 \left[ \frac{1}{\kappa_c} \ln (Re_\theta) + C \right]^{-2}$ . The results given deviate less than 3% from this correlation, titled Coles Fernholz 2 in [166], which demonstrates the high quality of the simulations carried out.



(a) Correlation coefficient  $R_u$  at different distances of the wall demonstrating the sufficiency of the chosen domain size. (b) Dimensionless velocity profile at the wall of the current LES ( $Re_\tau \approx 4600$ ) in comparison with the data of Moser et al. [164] ( $Re_\tau \in [180, 395 \text{ and } 590]$ ), as well as the possible range of the log-law region found in [64, 88, 181] included in grey.

**Figure 4.1:** Validation of the channel flow simulations. The data were published in a similar way in Praß et al. [P3].

### Boundary conditions and mesh metrics

The boundary conditions correspond to those of the plates with dimples shown in figure 4.7 on page 58. The lower boundary of the domain was modelled as a wall with no-slip condition. The upper boundary of the domain was modelled as a free-slip wall by using a symmetry condition in order to simulate the overflow of a free plate. The side boundaries in the  $z$ - and  $x$ -directions were defined as periodic boundaries, with the main flow velocity adjusted by a pressure gradient in  $x$ -direction as suggested by Deardorff [49] corresponding to  $Re_\tau \approx 4600$ . This method proved to be more robust for the simulations performed here than the constant mass flow method proposed by Benocci & Pinelli [11].

In order to resolve the flow close to the wall on all relevant scales, meshes according to the requirements of Chapman [26] with  $y^+ = 1-2$  as well as dimensionless spacing in  $x$ - and  $z$ -direction  $\Delta x^+ < 100$  and  $\Delta z^+ < 20$  were

used, as these early estimates are still known to be valid today [68]. The growth rate of the cells perpendicular to the wall was also chosen according to the specifications given by Chapman [26]. A mesh independence study finally led to a mesh of resolution  $y^+ = 1.2$ , as well as  $\Delta x^+ < 10$  and  $\Delta z^+ < 10$ . This resulted in a mesh with  $16.7 \cdot 10^6$  elements, which is reasonably consistent with Choi & Moin [34], who estimate the required number of grid points for turbulent boundary layers to scale with  $Re_\tau^{26/11}$  for high  $Re_\tau$  and give a formula for determining the mesh points, which leads to approximately  $20 \cdot 10^6$  elements for the present simulation, based on the assumption that the used power-law curve-fits are valid for  $Re_{\tau, x_0} \approx 5800$ .

As the mesh resolution near the wall is almost as fine as that needed for a DNS, such simulations are sometimes referred to as *well resolved* LES in literature, e. g. Cabot & Moin [24]. Due to the high mesh resolution down to the wall, the flow can be described in detail. The adequate resolution of the boundary layer can be verified by the representation of the dimensionless velocity  $u^+$  as a function of dimensionless wall distance  $y^+$  as shown in figure 4.1(b). All values follow the law of the wall, according to which  $u^+ = y^+$  applies within the viscous sublayer and  $u^+ = 1/\kappa_c \ln(y^+) + C_1$  in the turbulent boundary layer. The marked range includes the values for  $\kappa_c$  reaching from 0.35 to 0.43, and  $C_1 = 5.2 \pm 5\%$ . These values arise from different resources, namely Foken [64], Högström [88] and Pope [181]. This universal course of the boundary layer is maintained even with Reynolds numbers up to  $Re_\tau \approx 5200$  and beyond [134]. In addition to the match with the theory, a negligible deviation to the data derived via DNS by Moser et al. [164] is found. This proves that the physical effects near the wall can be resolved accurately with the present LES. This fact is especially important to emphasise as the flow phenomena in the immediate vicinity of the wall are of major interest when surface structures such as dimples are applied.

All LES were initialized using the results of RANS simulations performed on the same meshes in order to accelerate the development of the fully formed flow. The time step size was set to  $1 \cdot 10^{-6}$  s in order to reach  $CFL < 1$ . Artificial turbulence generated via a spectral synthesizer based on Kraichnan [123] and further developed by Smirnov et al. [206] as given in [6] was superimposed on these to accelerate the formation of physical turbulence, as suggested by Fröhlich [68]. The temporal averaging of the fluctuating values was enabled from the point in time when the average flow velocity and the static pressure on a cross-sectional area perpendicular to the main flow direction fluctuated around a constant value. Such a method of evaluation of the steady state of a simulation, as recommended by Fröhlich [68], was

also applied by Choi & Moin [33], who considered the simulations to be statistically stationary as soon as the wall shear stresses showed quasi-periodic behaviour. Other authors such as Moin & Kim [160] evaluated the quasi-periodic behaviour of the horizontally averaged turbulent stresses in time or the quasi-periodic behaviour of the kinetic energy while maintaining a linear profile of the total shear stress [114]. The method used here is based on the principle of Wille [233], who considered the behaviour of the force necessary to maintain the flow. All these methods lead to comparable points in time, from which the flow can be considered quasi-stationary. In the present simulations this state was reached after 9 to 10.5 flow-through-times. This short simulation time compared to other simulations, e. g. Wille [233], can be attributed to the described initial conditions. The subsequent averaging of the values was performed over the subsequent 7 to 8 flow-through-times.

#### 4.1.2 Vortex-induced formation of ordered flow patterns of the boundary layer

In the previous section, the general, quantifiable evidence for the simulation quality was discussed. In addition, depending on the flow under investigation, there are characteristic features which should also be checked when evaluating the simulation quality. In the immediate proximity of turbulently overflowed surfaces, adjacent areas of strongly differing velocities are formed [119]. These parallel structures, known as streaks, can be observed very clearly in the viscous sublayer, but can also be observed in the buffer layer and in the lower part of the log-law region up to  $y^+ \approx 100$ . Further away from the wall, at  $y^+ \approx 400$ , they are superimposed by turbulent fluctuations and can no longer be clearly identified [119]. The streaks form about 100 wall units apart from each other in spanwise direction and have a length of about 1000 wall units [29]. They are the result of rotating longitudinal vortices caused by velocity gradients in the flow field that are self-sustaining [83, 100, 112] as they draw the necessary energy from the main flow [113]. Due to differently oriented directions of rotation of adjacent vortices, fluid is either transported in the direction of the wall or in the direction of the main flow. The former mechanism is called a *sweep*, the latter *burst*, as schematically shown in figure 4.2(a). There is no doubt that streaks have an influence on the drag of an overflowed body [68, 119], while the exact physical mechanisms of formation have not yet been conclusively explored [30] but are supposed to consist of a combined effect of advection of the mean velocity profile through wall normal motion, mean shear and viscous diffusion [29]. Studies show that areas where burst occurs correspond with local areas of lower shear stress on the

wall [P2, P3]. Likewise, sweep occurs in areas with higher wall shear stress, which can be linked to the higher momentum of the fluid coming from the main flow.

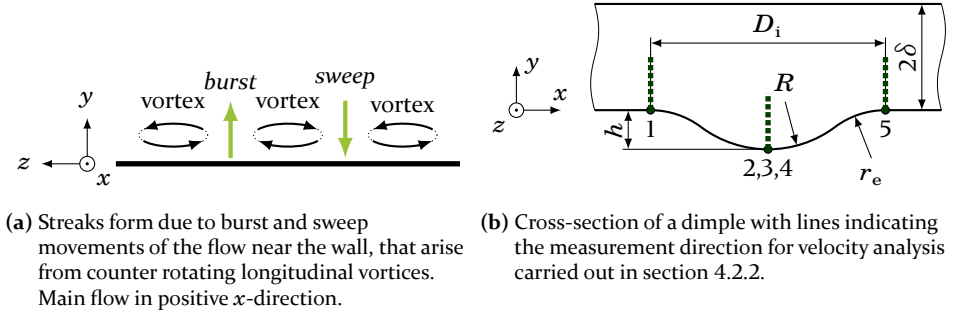


**Figure 4.2:** Schematic representation of longitudinal vortices leading to streaks on flat plates (a) and cross-section of a dimple (b).

Kline et al. [119] describe the occurrence of the streaks in direct proximity to the wall and their interaction with the main flow by gradual lifting of the fluid from the wall. They also describe the process of sudden oscillation and the subsequent bursting and ejection of the fluid. Kim et al. [109] carried out detailed investigations of the influence of the streaks on the turbulence production near the wall. They found that bursting is the key mechanism for turbulence production. In 1985, Allen [4] and Wallace [225] provided visualizations of the formation of streaks and the lifting of the structure from the wall. Modified representations of these are shown in figure 4.3. The representation shows that the gradual lifting of the structure from the wall leads to instability which is caused by the higher momentum content of the main flow. The lifting of the structure first forms a hairpin vortex, which then loses its identity. It is this mechanism that leads to the turbulence production described by Kim et al. [109].

The simulations performed exhibit these same streaks, as exemplarily shown by a snapshot of a sectional plane at  $y^+ = 20$  coloured by velocity magnitude in figure 4.4. The differences in amplitude of velocity between the individual streaks are clearly visible. As described in the literature, the streaks extend in a longitudinal direction and are arranged next to each other as zones of higher and lower velocities. The additional streamlines above the sectional plane further confirm the findings of Kline et al. [119], who state that the streaks are self-sustaining in the flow due to longitudinal vortices, which in turn draw their energy from the main flow [113]. As shown schematically in figure 4.2(a), fluid preferably rises from the wall towards the main flow, where two counter-

#### 4 Investigation of dimpled surfaces in non-rotating flow

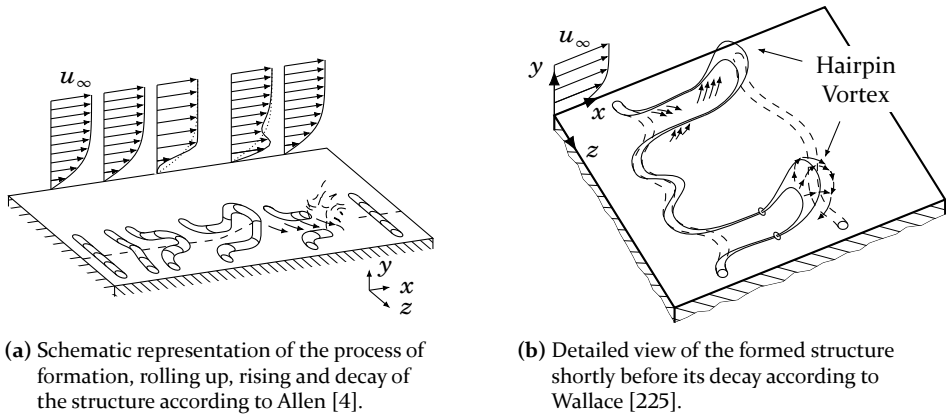


**Figure 4.3:** Schematic representation of the mechanisms leading to the formation of vortices near the surface.

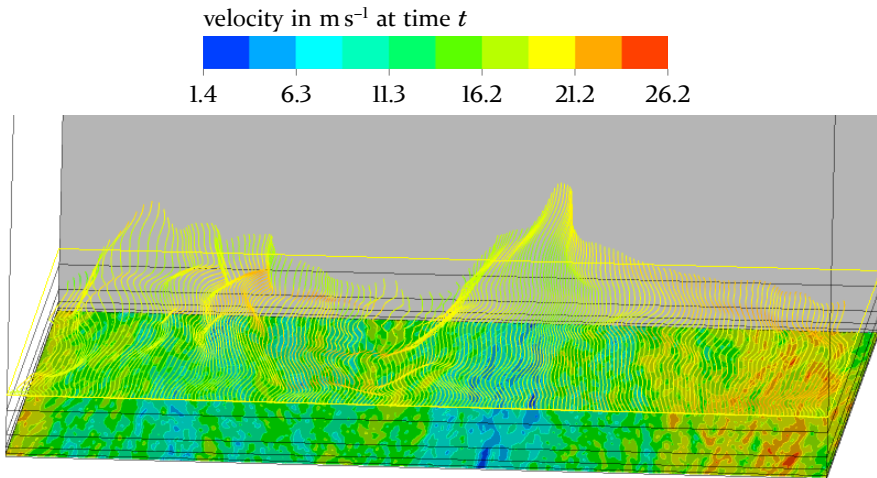


**Figure 4.4:** Streaks near and fluid motion above smooth wall, main flow direction into the viewing plane. Representation taken from Praß et al. [P3].

rotating vortices transport slow fluid close to the wall into the area between them. At these points a streak of slowly flowing fluid is formed on the wall. Likewise, at locations where two counter-rotating vortices transport fast fluid from the main flow towards the wall, streaks of higher velocity arise. Above streaks of lower velocity, the streamlines are thus diverted towards the main flow, while above faster streaks they are bent towards the wall. This behaviour can also be observed in the visualisation in figure 4.4.

To further illustrate this phenomenon, longitudinal vortices close to the wall are visualised in figure 4.5. The vortices are coloured according to the flow velocity  $v$  in the direction perpendicular to the wall. Red represents negative velocity and thus flow towards the wall. Blue, in contrast, visualises positive velocity values and thus flow away from the wall. On the left side of figure 4.5 the wall is coloured according to the local drag coefficient. Brighter colour represents higher resistance coefficients and thus higher wall shear stresses. On the right side of figure 4.5 a plane at the height of  $y^+ = 2$  is coloured according to the velocity  $u$  in the main flow direction. The marked vortex shows exemplarily that the vortex in the area of descending fluid (red area) leads to a higher local drag coefficient. This is due to the higher flow velocity  $u$  in  $x$ -direction, which is caused by the fact that the vortex transports fluid of higher velocity to the wall in this area. On the side where fluid rises from the wall as a result of the vortex (blue area), the drag coefficient is considerably lower. The associated flow velocity in the main flow direction is also lower. This is due to the fact that in this area slowly flowing fluid near the wall rises as a result of the vortex.

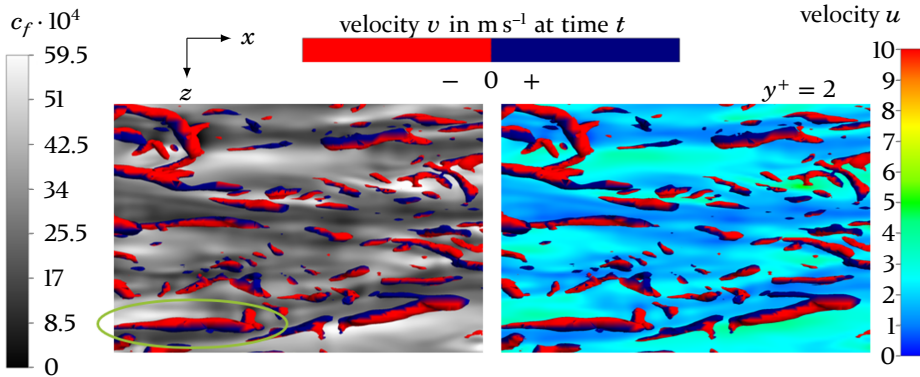


**Figure 4.5:** Effect of streamwise-vortices on the local drag coefficient and the velocity in correlation with the rotation (Simulation data was partly generated within the context of Kalb [SI]).

The measures taken and results obtained show that the simulations are valid and that complex flow phenomena are adequately resolved down to the wall. The appropriate domain size ensures that turbulent structures can propagate without being influenced by the boundary conditions. The high mesh resolution in combination with the selected time step size ensures sufficient resolution of the small-scale structures. The high level of agreement of the velocity profile with literature [64, 88, 164, 181] as well as the presence of the

streaks and the resulting fluid and momentum transport perpendicular to the surface demonstrate the correct modelling of the physical circumstances. The simulation methodology is therefore found suitable for delivering reliable results also for the flow over surfaces with dimples.

## 4.2 Effects of shallow dimples on the flow

Besides the suitability of dimples to increase heat transfer considerably while only slightly increasing hydrodynamic losses, they can – under specific circumstances – be used to reduce drag. For this purpose, the dimples have to exhibit a ratio of depth to diameter in the low, single-digit percentage range. In addition, the result is strongly dependent on the arrangement of the dimples and the existing flow conditions. For example, Lienhart et al. [140] found a slight increase of drag of 2% in a setup with  $h/D_i = 5\%$  and 22.5% coverage rate  $\beta$ , while van Nesselrooij et al. [168] determined a reduction of drag of up to 4% in experimental studies for a very similar setup with a coverage ratio of  $\beta = 33.3\%$  using shallow dimples of  $h/D_i = 2.5\%$ . Tay et al. [214] also found a reduction of net drag of up to 3% for dimples of  $h/D_i = 5\%$ , but with a much higher coverage ratio of 90%. There are still no clear results regarding the actual mechanisms that cause the reduction of drag. It is solely known that the dimples need to be shallow so that the resulting form drag due to the cavity shape is lower than the drag reduction due to the effects of the dimples on the flow [136]. When it comes to increasing heat transfer, deeper dimples achieve better results. This shows that a meaningful increase in heat transfer with a simultaneous reduction of drag is only possible to a limited extent.

### 4.2.1 Drag reduction due to shallow dimples on surfaces

Due to the geometric limitations when using thin discs, the depth of dimples is limited by the disc thickness. Thus, only shallow dimples or dimples of low diameter are suitable for application on thin discs. The separated investigation of the mechanisms regarding the reduction of drag as well as the increased heat transfer due to dimples is necessary to provide the basis for the consideration of the effects on rotating discs.

Five parameters are sufficient to describe a patterned dimple setup on the wall [168]. These are the diameter of the dimples  $D_i$ , the depth of the dimples  $h$ , the edge radius  $r_e$ , the streamwise distance between dimples  $l_x$ , and the spanwise distance between dimples  $l_z$ , as shown in figure 4.6. In this section, two setups were investigated. The parameters for the setups are given

## 4.2 Effects of shallow dimples on the flow

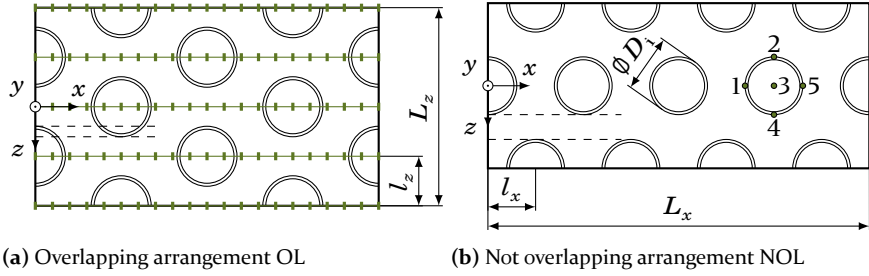


**Figure 4.6:** Arrangements of Dimples on flat plates, used to determine drag reduction. Locations for evaluations are indicated (green lines in (a), points 1-5 in (b)) as well as characteristic parameters to describe the distribution of dimples.

in table 4.1. For the first setup, the dimples were arranged overlapping (OL) in flow direction, for the second setup they were not overlapping (NOL). For the detailed consideration of the resulting drag, the setups already described in section 4.1.1 were used. The solid wall was supplied with dimples in different arrangements, as shown in figure 4.7. Only dimples of the diameter  $D_i = 20$  mm with depth  $h/D_i = 2.5\%$  were used. For these setups experimentally determined data from van Nesselrooij et al. [168] exist, which suggest a noteworthy drag reduction potential for the setup OL. Their results are thus used as reference and for validation. The boundary conditions, mesh resolution and numerical validation were carried out analogously to the simulations without dimples presented in section 4.1.1.

**Table 4.1:** Data of the examined setups to investigate the reduction of drag by dimples.

setup	$D_i/\text{mm}$	$h/D_i/\%$	$l_x/D_i$	$l_z/D_i$	$r_e/D_i$	$L_x$	$L_z$	$\beta/\%$
OL	20	2.5	1.430	0.825	0.5	$4l_x$	$4l_z$	33.3
NOL	20	2.5	0.825	1.430	0.5	$8l_x$	$2l_z$	33.3

When determining the drag of a smooth, parallel plate subjected to parallel cross-flow, only frictional drag occurs. Due to the dimples, however, there are also areas that feature a projected surface perpendicular to the direction of flow. As a result, a component of form drag is added to the frictional drag. For this reason, the total resulting force  $F_R$  in flow direction acting on the surface was always used to determine the corresponding drag coefficient  $c_f$  as given in equation (4.1).

#### 4 Investigation of dimpled surfaces in non-rotating flow

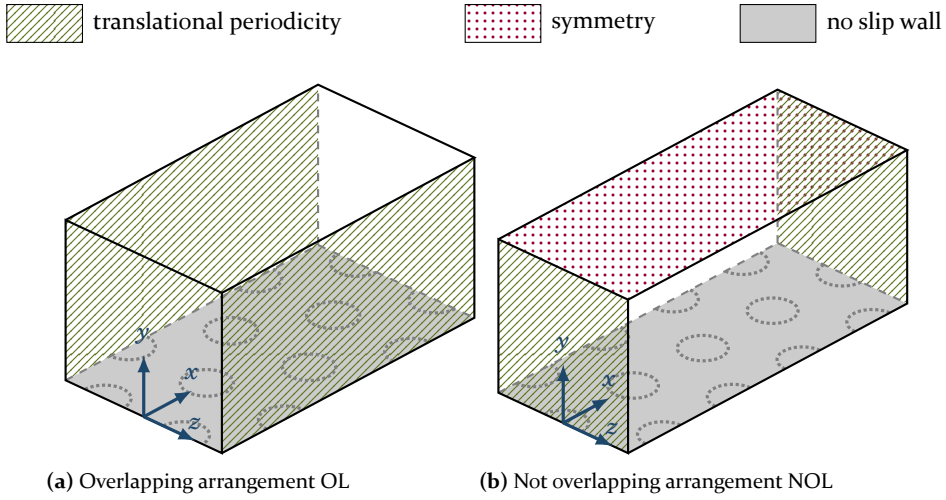


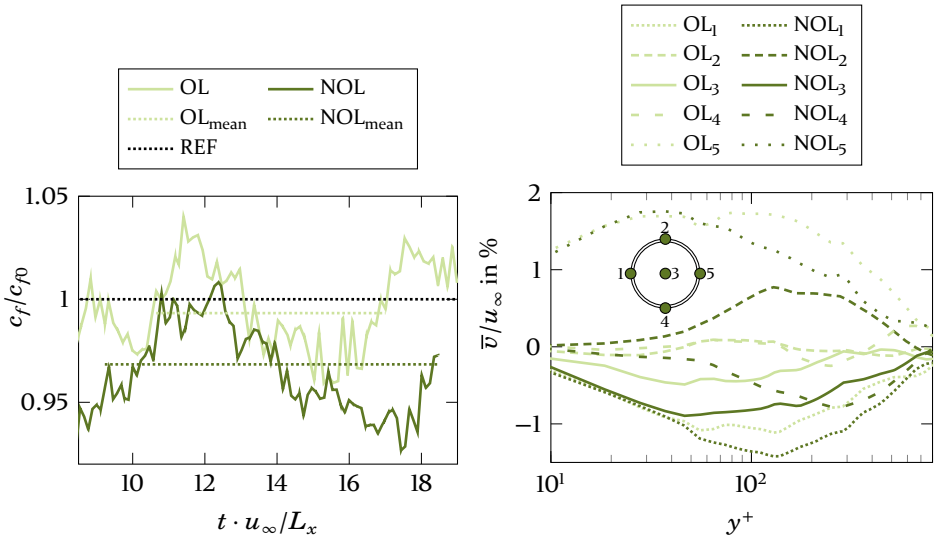
**Figure 4.7:** Used computational domains for simulations and corresponding boundary conditions. Boundaries of translational periodicity in spanwise direction are indicated in (a), boundaries of translational periodicity in streamwise direction and symmetry are indicated in (b) for clear representation.

$$c_f = \frac{2F_R}{\rho u_\infty^2 A} \quad (4.1)$$

The projected surface parallel to the flow direction was used as surface area  $A$ , which in the case of the smooth plate is equal to the wetted surface. The dimples slightly increase the area of the wetted surface. The use of the wetted surface would therefore always lead to lower  $c_f$ . However, the influence of the dimples on a given plate is to be investigated, so that the use of the projected surface allows for a better comparison of the results. In addition, the use of drag force as well as the projected area as a reference surface corresponds to the approach of van Nesselrooij et al. [168], thus ensuring comparability with their data.

The quasi-stationary state was reached for the setup OL after slightly more than 10.5 flow-through-times and for the setup NOL after little more than 9 flow-through-times, which corresponds closely to the simulations without dimples. The subsequent averaging of the values was performed over 6 and 9 flow-through-times for the setups OL and NOL, respectively. The observation of the temporal evolution of  $c_f$  in figure 4.8(a) reveals an oscillation of the values over time. For both setups, this oscillation results in period

durations of  $T_p \approx 6 - 8$  flow-through-times. These low-frequency oscillations have considerably higher period durations than the fluctuations of the mean velocities and the mean pressure, as shown in Praß et al. [P2, P3]. The amplitudes are at maximum 4.14% and 7.21% deviation from the mean value for the setups OL and NOL, respectively. These values are nevertheless higher than the fluctuation of the mean velocity would suggest [P3]. Additionally, both graphs are overlaid by higher frequency fluctuations of lower amplitudes.



**(a)** Temporal progression and mean values of the total drag coefficient for the flat plate without dimples (REF) compared to the progression of the investigated setups OL and NOL. **(b)** Average velocity perpendicular to the wall scaled with bulk velocity in streamwise direction for OL and NOL at different positions near the dimples.

**Figure 4.8:** The development of drag coefficient  $c_f$  as a function of number of flows through the domain (a) shows small drag reductions for both setups OL and NOL. The examination of velocities perpendicular to the wall (b) shows that different vortices form over the dimples. The data were published in a similar way in Praß et al. [P3].

The authors van Nesselrooij et al. [168] found reduction of drag of about 3% for the arrangement OL at  $Re = 35\,000$  compared to the smooth plate. In the LES performed here, the average reduction found was not more than 0.67% and is therefore hardly existent. Better results were obtained with the arrangement NOL, which exhibits a 3.16% lower  $c_f$  than the smooth plate. However, van Nesselrooij et al. [168] could not find a reduction of drag for this setup, but even an increase of drag of slightly more than 2%. At first glance, these results appear to be in direct contrast to each other. However, the ex-

pected and the simulated differences are in the range of single percent-points. In a direct comparison of the measured and simulated values, absolute deviations of only about 3% for the arrangement OL and about 5% for the arrangement NOL are found between the simulations and the experiments. Lienhart et al. [140], for example, obtained absolute deviations of more than 8% with their DNS compared to the corresponding measurements. Even compared to the DNS of Moser et al. [164], the deviation exceeded 2.5%. Moreover, the repeatability of the experiments of van Nesselrooij et al. [168] was reported to be up to 2%. The small effects to be detected as well as the relatively low repetition accuracy of the experiments underpin the relevance of the adequate resolution of the computational domain and the validations of the simulations carried out in section 4.1.1.

#### 4.2.2 Effects of dimples on the flow velocity

In addition to the behaviour of the drag coefficient  $c_f$ , the high-resolution simulations offer the possibility to investigate the local velocity distribution in the immediate vicinity of the dimples with respect to the three spatial dimensions. Of particular interest is the velocity component  $v$  in the direction normal to the wall, which can be seen as a measure for the momentum transport perpendicular to the wall. The velocity at the wall is equal to zero in all directions due to the no-slip condition. The influence of the dimples is restricted to a region close to the wall. Thus, there is a limited area within the boundary layer in which the velocity perpendicular to the wall is influenced by them. This comprises the range  $10 < y^+ < 800$  as shown in figure 4.8(b). The velocity evaluation was performed on five lines perpendicular to the wall. The starting points of the lines represent the entry of the flow into the dimple (1) as well as the centre of the dimple (3) and the exit of the flow from the dimple (5) along the dimple diameter in streamwise direction. In addition, the effects at the outermost dimple edges in spanwise direction (2) and (4) were considered. The data collection was carried out on all dimples represented in the simulations, the results discussed present the average results for each location.

The average velocity perpendicular to the wall in relation to the free stream velocity  $u_\infty$  is shown in figure 4.8(b). All available, statistically meaningful data were used for the time averages shown. Due to the limited simulation duration, the averaging durations are nevertheless short compared to temporal averages from experimental investigations. Here negative values correspond to a flow towards the wall, while positive values represent fluid movement away from the wall in direction of the main flow. For both setups OL and

NOL, the highest negative values of more than  $-1\%$  are found at the dimple inlet (1). Up to  $y^+ \approx 50$  the courses are approximately identical, further away from the wall up to  $y^+ \approx 600$  the flow towards the wall is more pronounced for the setup NOL than for the setup OL. A similar behaviour can also be observed above the dimple centre (3), where the magnitude of velocity towards the wall is about twice as high for setup NOL over the entire region investigated. At the dimple outlet (5) the flow for both setups is directed away from the wall. Here the resulting flow for setup OL for  $y^+ > 60$  reaches higher values than in the setup NOL.

These observations indicate that for the setup NOL over all dimples a stronger flow towards the wall tends to prevail than for the setup OL along the dimple diameter in the direction of flow. According to figure 4.2(a), the dimples in the setup NOL thus favour the formation of a sweep more than the dimples of the setup OL. The observation of the flow at the dimple edges (2) and (4) reveals that the geometric dimensions of the dimples of setup NOL might match the spanwise extension of the longitudinal vortices. This setup produces a net flow away from the wall above (2) and a flow of similar intensity towards the wall at (4). This finding is an indication that structures with a preferred direction of rotation form above the dimples. This suggests that the dimples in the NOL setup maintain longitudinal vortices. Since this setup also exhibits the lowest drag, a connection between the maintenance of the structures and the drag reduction seems plausible. In order to validate this correlation from simulation data an extensive study of long simulation duration of hundreds of flow-through-times on different setups would be needed. This challenge arises in all time resolved flow simulations and will be topic for future studies when computational resources further increase. The available simulation durations are too short which means that the effect could also be merely a temporary phenomenon. It is therefore possible that over longer periods of time, other structures also emerge, similar to the observations of Turnow et al. [220]. For the setup OL, the overlap of positions (2) and (4) in flow direction causes a cancellation of the average flow velocity perpendicular to the wall. No difference in the frequency of occurrence and structure of the vortices is apparent for the plate with dimples and the flat plate as can be seen in appendix B.

From this consideration it follows that the influence of the streaks by dimples is generally possible. The stabilization of corresponding structures can also positively influence  $c_f$ . However, since the actual shape of the streaks is strongly dependent on the prevailing  $Re$  and the influence of dimples on the flow near the wall is strongly connected to their geometry, it is unlikely to

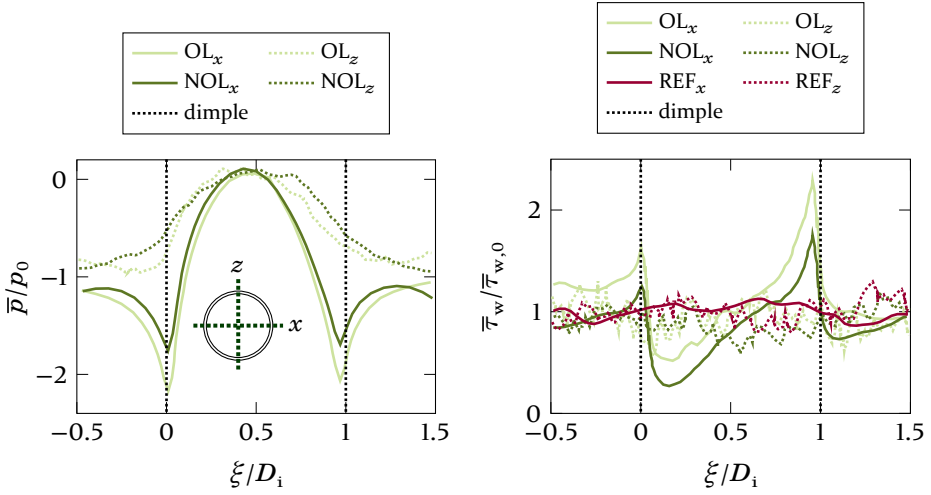
find a dimple setup that yields satisfactory results over a wide range of  $Re$ . This conclusion is in accordance with the results of Lienhart et al. [140], van Nesselrooij et al. [168], Tay et al. [214] and Tay & Lim [215], who found a pronounced Reynolds number dependence of their investigated setups, which cannot be explained exclusively by the Reynolds number dependence of  $c_f$  of smooth plates as described by Coles [42] and Spalart [207] or that of smooth channels as investigated by Dean [48]. However, the investigations show that the adaptation of the dimple geometry and their arrangement, taking into account the expected longitudinal vortices and streaks, offers a high potential concerning drag reduction that has not yet been scientifically investigated.

#### 4.2.3 Effects of dimples on pressure and wall shear stress

In addition to the velocity distribution in the immediate vicinity of the plate, the dimples alter the pressure distribution and also influence the wall shear stresses and thus the local drag. Tay et al. [214] and van Nesselrooij et al. [168] assume that the dimples cause secondary flows, that are responsible for the fluid mechanical effects of the dimples. These in turn are related to characteristic pressure distributions in the vicinity of the dimples. Figure 4.9(a) shows the mean static pressures across all dimples in streamwise direction  $x$  and spanwise direction  $z$  for the two setups OL and NOL. For averaging, the linear pressure loss over the length of the domain was excluded.

The pressure distribution at the dimples is qualitatively and quantitatively comparable for both setups. In flow direction  $x$  the pressure drops initially before the dimple entry. Then a fluid retardation takes place, which causes the pressure to increase considerably. The maximum is reached at about 43 % of the dimple diameter  $D_i$ . During the subsequent acceleration of the fluid towards the dimple outlet, the static pressure decreases. The reasonably symmetrical pressure distribution in flow direction shows that no flow separation occurs at the dimple entrance. This is consistent with the investigations of van Nesselrooij et al. [168]. Lienhart et al. [140], however, found detachments and recirculation areas for similar dimples with  $h/D_i = 5\%$  at much lower  $Re_\tau = 590$ . The pressure distribution in this case shows a clear maximum at about 76 % to 80 % of the dimple diameter. The authors attribute to this phenomenon an influence on the resulting pressure drag of the dimples. This amounted to 5.5 % of the total drag and thus exceeded the drag-reducing effects of the dimples ( $\approx -1.5\%$ ). This observation thus supports the assumption that the integral effects depend strongly on geometry and arrangement of the dimples as well as flow conditions.

## 4.2 Effects of shallow dimples on the flow



(a) Average static pressure at the wall in direct proximity of the dimples. The sketch shows the position of the measurement lines in  $x$ - and  $z$ -direction along the dimples. (b) Wall shear distribution scaled with average wall shear of the flat plate at the wall in direct proximity of the dimples as reference.

**Figure 4.9:** Comparison of pressure and wall shear around dimples for the setups OL and NOL in  $x$ - and  $z$ -direction represented by  $\xi$ . The data were published in a similar way in Praß et al. [P3].

Besides static pressure, it is mainly the shear rate  $\tau$  at the surface that determines the behaviour of drag. Figure 4.9(b) shows the distribution of magnitude of wall shear stress  $\tau_w$  in streamwise ( $x$ ) and spanwise ( $z$ ) direction along the dimples for the investigated arrangements in comparison to the smooth reference channel. The reference data is derived from averaging over one flow-through-time in an area that corresponds to the size of a dimple. When averaging over the entire simulation period as well as over several comparison areas, clearly no variations would be detectable. However, the chosen representation reveals fluctuations which can be attributed to the presence of the streaks. Due to the local and temporal fluctuation of the streaks, no quantitative conclusions about their characteristics should be drawn from the data presented. For both setups OL and NOL a notable local increase of the wall shear stress in streamwise direction can be seen both at the dimple inlet and at the dimple outlet. These local peaks are mainly caused by the predominant geometry changes at these points and are also visible in measurements in experiments, e. g. [142, 150, 151]. In addition, the blocks of the numerical mesh are aligned with these edges. It is a well known fact that such changes inside meshes can result in a local overestimation – and thus an exaggeration – of the actual effects. Since measured values, depending on

#### 4 Investigation of dimpled surfaces in non-rotating flow

the measuring equipment used, represent an integral value over a measuring volume, it is difficult to determine the exact exaggeration experimentally. It follows that corresponding local peaks determined experimentally tend to be too low, whereas numerically determined values – as in this case – tend to overestimate the actual magnitude.

The wall shear stress in  $x$ -direction for the setup OL lies above the course of the setup NOL over the entire dimple. This is consistent with the finding of higher total drag of this setup. The integral of wall shear stress over the considered range is 11 % above the reference value, while for the setup NOL it is 14 % below the reference value. This difference clearly shows the relevance of the central area of the dimples in flow direction on the total drag and the importance of the arrangement of dimples.

The increase of  $\tau_w$  in the inlet area of the dimples is caused by the resulting fluid acceleration, as stated by Isaev et al. [93]. The subsequent decrease results from the inertia of the fluid, due to which the flow cannot directly follow the geometry. However, the fact that the values of  $\tau_w$  remain positive shows that no persistent flow separation from the wall occurs. The steep gradient and the reduction of the wall shear stress by about 50 % give a good impression of how sensitive the surface flow is to changes in geometry, considering the low ratio of  $h/D_1 = 2.5\%$  and the high Reynolds number of  $Re_\theta \approx 9066$ . Flow separations would inevitably lead to local areas of increased pressure and thus form drag, which would cancel out all positive influences of the dimples on the frictional drag, as mentioned by Tay et al. [214]. In  $z$ -direction both setups with dimples show lower average values of  $\tau_w$ . The setup OL lies 6.7 % below the reference value, the setup NOL even 10.4 %. However, there are no considerable differences in the distribution and fluctuation intensity for the investigated setups. Nevertheless, the fluctuations are much more pronounced when compared to those in flow direction. These result from the smaller expansion of the streaks in spanwise direction compared to the expansion in streamwise direction [70].

#### 4.2.4 Shallow dimples in channels at low $Re$

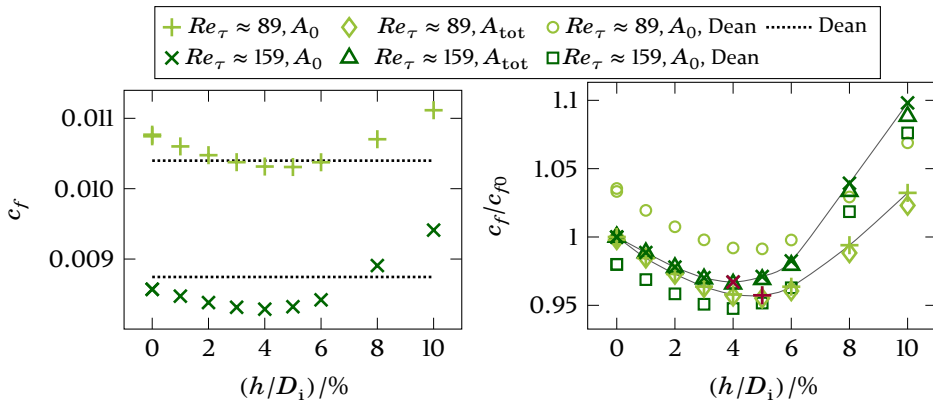
Often the effects of flow over free surfaces differ substantially from those in channels and those in the flow between two parallel plates. In many practical applications the flow is influenced by enclosures or other walls. To evaluate the influence of different dimple depths in such flows, this section analyses the flow between two infinitely extended, parallel plates, of which one is structured with dimples. For the investigations sharp-edged dimples with

edge radius  $r_e = 0$  were used. The height  $h$  of the dimples varied from 1% to 10% of the diameter  $D_i$ . The distribution of the dimples with distances  $l_x/D_i = 1.739$  and  $l_z/D_i = 1.004$  resulted in a coverage rate of  $\beta = 22.5\%$ . The channel height  $2\delta/D_i = 0.417$  was chosen according to the investigations of Tay et al. [214], the distribution was inspired by the investigations of Lienhart et al. [140]. To ensure comparability with other works, the Reynolds number  $Re_\delta$  based on bulk velocity  $U_b$  and channel height  $2\delta$  is also used in addition to  $Re_\tau = u_\tau\delta/\nu$ , as recommended by Pope [181]. Tay et al. [214] form the Reynolds number  $Re_c = U_c\delta/\nu$  with centreline velocity  $U_c$  and the half channel height  $\delta$ , therefore the conversion  $Re_\delta = (1.5625 Re_c)^{1/1.0117}$  is applied. The relation  $U_c/U_b = 1.28 Re_\delta^{-0.0116}$  presented by Dean [48] is used for the conversion.

The investigations of Tay et al. [214] and Lienhart et al. [140] lead to very different results. The investigations carried out differ in dimples setup as well as investigate range of  $Re$  and channel height  $2\delta$ . Lienhart et al. [140] found only increased drag with a channel height of  $2\delta/D_i = 3.33$ , using dimples of depth  $h/D_i = 5\%$  and a coverage rate of  $\beta = 22.5\%$ . Tay et al. [214], however, found up to 3% reduction of drag in channels of height  $2\delta/D_i = 0.4$  with dimples depth  $h/D_i = 5\%$  and coverage rate  $\beta = 90\%$ . The investigations of Tay et al. [214] show that higher coverage rates  $\beta$  lead to better results at higher  $Re$ . However, at lower  $Re$ , lower coverage rates are superior. In addition, dimples of lower depth  $h/D_i = 1.5\%$  provide more constant results over a wider Reynolds number range, while deeper dimples become efficient only at higher  $Re$ . In this context, it remains to be clarified what effect the dimple depth has at lower coverage rates and correspondingly lower  $Re$ . The Reynolds numbers considered here,  $Re_\tau = 89$  ( $Re_\delta = 2430$ ,  $Re_c = 1421$ ) and  $Re_\tau = 159$  ( $Re_\delta = 4860$ ,  $Re_c = 2819$ ) lie below the ranges of  $Re$  considered by Tay et al. [214] and Lienhart et al. [140]. This leads to the possibility to use numerically efficient RANS simulations for the detection of general effects on drag. In order to keep the mesh and calculation errors low, extensive tests and measures were carried out, as published in Praß et al. [PI].

Figure 4.10(a) shows the dependence of  $c_f$  on the dimples depth for the two Reynolds numbers examined. In addition, the corresponding drag coefficients are shown according to Dean's [48] equation  $c_f = 0.073 Re_\delta^{-1/4}$ , which applies to two-dimensional, fully turbulent flows in smooth channels. As stated in this publication, the transition range for this flow extends from about  $Re_\delta = 10^3$  to  $10^4$ . Good results of the approximation can be expected for the range  $6 \cdot 10^3 < Re_\delta < 6 \cdot 10^5$ . The considered flows are thus just

#### 4 Investigation of dimpled surfaces in non-rotating flow



(a) Drag coefficient  $c_f$  for different dimple depths and theoretical values for the flat channels according to Dean [48]. (b) Normalized drag coefficient  $c_f/c_{f0}$  for different dimple depths. Additionally included are values calculated with total, wetted area  $A_{tot}$  of dimpled setups as well as the values calculated with  $c_{f0}$  according to Dean [48].

**Figure 4.10:** Comparison of the drag coefficient of different dimple shapes at two Reynolds numbers (a) and relative consideration of the change using the projected and the total wetted area (b). The data were published in a similar way in Praš et al. [P1].

outside this range, which is why slight deviations can be expected. The magnitude of the deviations of the simulations of the smooth channels, where  $h/D_i = 0$ , are at a maximum of 3.5% and are thus smaller than the existing deviations of the underlying data used by Dean [48], on the basis of which the correlation was determined.

The graphs clearly show that in both cases  $c_f$  is reduced by using flat dimples. This effect results in an optimum at  $h/D_i = 4\%$  to  $5\%$ , which corresponds very well with the literature data. It is noticeable that the reduction of drag decreases with further increasing depth of dimples and is no longer present at  $h/D_i = 7\%$  to  $8\%$ . Deeper dimples result in a increase of drag, which is in accordance with the results of Tay et al. [214]. This finding is illustrated by the presentation of the results in figure 4.10(b), which displays the ratio of the drag coefficient  $c_f$  to the drag coefficient of the smooth channel  $c_{f0}$ . For the purpose of completeness two different calculations of the  $c_f$ -value are visualised. Besides the calculation with the projected or reference area  $A_0$ , the total surface area  $A_{tot}$  enlarged by the dimples was used. Due to the small dimples depth, the difference almost vanishes for shallow dimples with  $h/D_i < 7\%$ . For deeper dimples, the positive bias of the results in terms of drag becomes evident by using the larger area  $A_{tot}$ . Additionally,

### 4.3 Heat transfer enhancement due to dimples

the ratio of  $c_f$  to the theoretical value  $c_{f0}$  according to Dean [48] is shown. The values obtained by the calculation with constant reference area  $A_0$  are to be seen as the most relevant, as the effect compared to the surface  $A_0$  is of major interest. Connecting lines are thus used in the representation for these values in order to simplify their identification. The respective minima lie in the case of  $Re_\tau = 89$  at  $-4.1\%$  and in the case of  $Re_\tau = 159$  at  $-3.3\%$ . For better visibility, they are highlighted in red in figure 4.10(b).

Two further points are evident from the data. First, the highest possible relative decrease of  $c_f$  decreases with increasing  $Re$ . Second, also the relative dimple depth  $h/D_i$ , that leads to the highest reduction of drag, decreases with increasing  $Re$ . Although extrapolations of the results are to be treated with caution, these findings provide a possible explanation why Lienhart et al. [140] did not detect any reduction of drag at the same coverage rate  $\beta$  at considerably higher Reynolds numbers of  $Re_\tau > 550$  using dimples of  $h/D_i = 5\%$ . It is possible that the geometry would be suitable for drag reduction at lower  $Re_\tau$ . Alternatively, a different dimples set-up could have had positive effects at the higher  $Re_\tau$  investigated.

The findings show that a reduction of drag on surfaces and in channels by using dimples is generally possible. However, the achievable effects are in the single digit percentage range and very much dependent on the specific surface design in combination with the prevailing flow conditions. With slightly varying conditions, the positive effect can turn into the opposite and lead to an increase in net drag. Due to this sensitivity, some published results in this area seem contradictory at first sight. The present simulations, however, show where the different findings come from and thus help to close the prevailing knowledge gap in this context.

### 4.3 Heat transfer enhancement due to dimples

As shown in the previous section, flat dimples can reduce drag. However, this can only be achieved when the flow remains attached while the global flow structures near the wall are modified. In contrast, for a considerable increase in heat transfer, it is necessary to increase the momentum exchange perpendicular to the wall. This is achieved by local flow separation, which can be caused by deeper dimples. For the majority of technically relevant flows, dimples with  $h/D_i > 10\%$  are suitable for this purpose.

This section deals with the thermal and physical mechanisms on channels with dimples of geometry and arrangement suitable for efficient heat trans-

fer increase. Data provided by Mahmood & Ligrani [151] serves to validate the simulation of heat transfer in dimpled channels. The simulations were run using a periodic section of the duct geometry. As in the previous section, literature data as well as simulation results of a geometrically identical channel without dimples were used as reference values for quality assurance. The criteria for the mesh resolution were maintained, mesh convergence studies were carried out and the quality of the boundary layer representation was verified.

##### 4.3.1 Simulation setup and validation

As in the previous simulations, the WALE model proposed by Nicoud & Ducros [170] was used as a subgrid-scale model. As Ben-Nasr et al. [10] show, in the case of simulations with heat transfer the WALE model captures the statistical quantities better than a dynamic Smagorinsky model (DSM), which is an improved version of the standard Smagorinsky model (SM). Especially in the determination of the mean temperature profile at the wall, the DSM showed disadvantages compared to the WALE model. The latter is also numerically more efficient. In their simulations, Ben-Nasr et al. [10] achieved almost 25 % savings in computational cost. Similarly, Yuen et al. [244] found clear advantages of the WALE model over the Smagorinsky model in the simulation of compartment fires especially regarding accuracy.

To ensure the best possible comparability of the simulation results with data provided by Mahmood & Ligrani [151], air was used as simulation fluid. The reference temperature was assumed to be  $T_0 = 298.15$  K, the wall with dimples was therefore modelled with a constant wall temperature of  $T_w = 324.08$  K to ensure the ratio  $T_0/T_w = 0.92$  given by Mahmood & Ligrani [151] for the reference case of  $2\delta/D_i = 1$ . The opposite wall was simulated as adiabatic wall. Due to the present range of pressure and temperature, the assumption of an ideal gas can be considered as valid. The values for thermal conductivity  $k_t$  and kinematic viscosity  $\nu$  were calculated as temperature-dependent variables according to the values in [222] by linear interpolation. The numerical settings include a coupled scheme for pressure-velocity coupling, the least squares cell based approach for gradients, second order accuracy for pressure, central differencing for density and momentum, and bounded central differencing for the energy equation.

The validation of the simulation quality was carried out by means of three different observation criteria. These are firstly a mesh convergence study with associated Richardson extrapolation [189], secondly the verification of the

### 4.3 Heat transfer enhancement due to dimples

resulting Nusselt number  $Nu_0$  and drag coefficient  $c_{f0}$  of the smooth channel with literature values and thirdly the consideration of velocity data by means of correlation as well as investigation of the second and third invariants of turbulent fluctuations in an anisotropy invariant map (AIM) as proposed by Lumley & Newman [149] and further developed by Jovanović [103].

The relevance of estimating the discretization error due to too coarse meshing in flow simulations is undisputed [154]. The great advantage of Richardson extrapolation is that it can be applied during post-processing [172] in order to estimate the introduced error. In the present case, three meshes were used with different resolutions of a channel section large enough to represent a total of eight of the dimples used by Mahmood & Ligrani [151] as indicated in figure 4.12(a). The resolutions used were  $8.3 \cdot 10^5$ ,  $2.8 \cdot 10^6$  and  $5.6 \cdot 10^6$  elements. The resulting mesh with the highest resolution is visualized in figure 4.11. The time step size was chosen according to the flow velocity and the smallest cell size in order to fulfil the criterion  $CFL < 1$ . For the Richardson extrapolation, the results of the two finer meshes were used. For the calculations, the generalised Richardson extrapolation as given in equation (4.2) was used. The simulations were performed with second order accuracy ( $o = 2$ ), the mesh refinement factor  $s$  can be derived directly from the number of elements  $n_f$  of the fine and  $n_c$  of the coarse mesh according to equation (4.3).  $Nu_0$  and  $c_{f0}$  were used as observation variables  $\xi$ . These were compared with common literature values.

$$\xi_R = \xi_f + \frac{\xi_f - \xi_c}{s^o - 1} \quad (4.2)$$

In equation (4.2),  $\xi_R$  represents the generalized Richardson extrapolation estimate of the observation variable according to Richardson & Gaunt [189]. It is derived from the calculated value of the observation variable  $\xi$  on the fine mesh  $\xi_f$  and on the coarse mesh  $\xi_c$ , the mesh refinement factor  $s$  as given in equation (4.3) and the order of accuracy of the used scheme  $o$ .

$$s = \sqrt{\frac{n_f}{n_c}} \quad (4.3)$$

For the calculation of  $Nu_0$ , the Gnielinski correlation as given in equation (4.4) [222] was used, which is based on the work of Gnielinski [76] related to the fully developed, turbulent flow through circular pipes. The equation is known to have good validity for non-circular pipes as well [91]. In this case, the calculation is done with the hydraulic diameter  $D_h$ , the length of the

#### 4 Investigation of dimpled surfaces in non-rotating flow

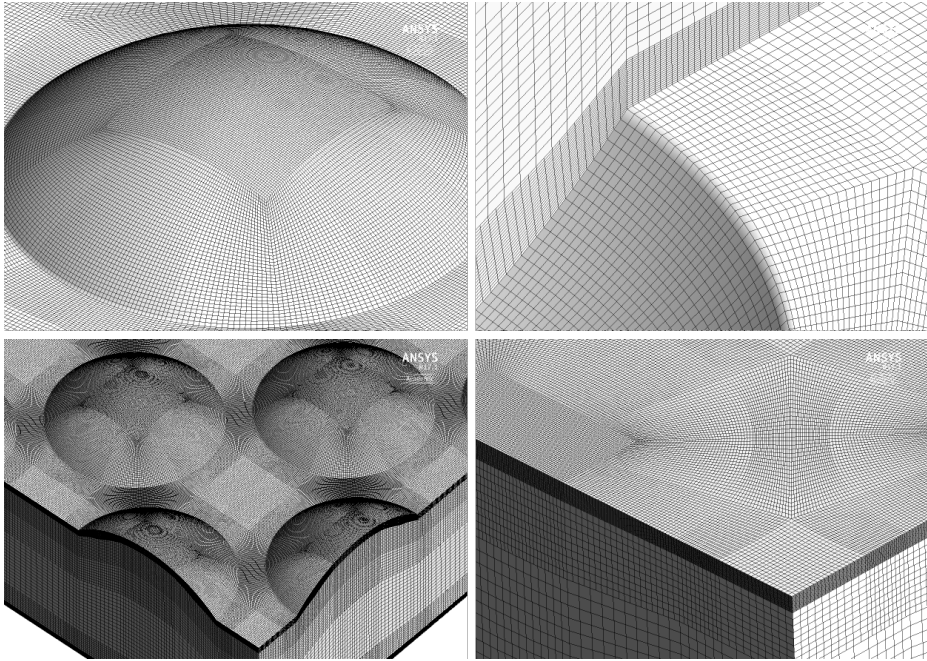
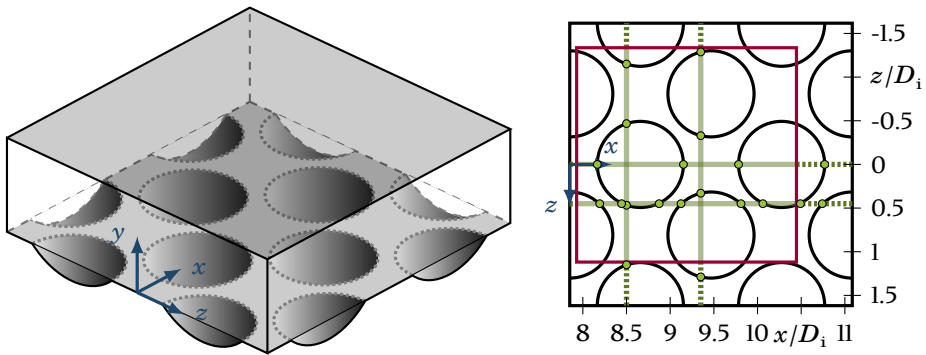


**Figure 4.11:** Visualisation of the finest mesh with  $5.6 \cdot 10^6$  elements.



(a) Computational domain of the channel with dimples of depth  $h/D_i = 20\%$  for investigation of the heat transfer behaviour. (b) Top view with measurement domain of Mahmood & Ligrani [151] in red and sample lines in green.

**Figure 4.12:** Computational domain with dimples (a) and comparison to measurement position of Mahmood & Ligrani [151] (b).

considered pipe  $l_p$ , the Prandtl number  $Pr$  as given in equation (3.60), and the Reynolds number  $Re_\delta$  based on bulk velocity  $U_b$  and channel height  $2\delta$ . This procedure was successfully applied for a similar case by Turnow et al.

[221] and yields similar results to the simpler correlation named after Dittus and Boelter<sup>2</sup> given in equation (4.6).

$$Nu_0 = \frac{(\zeta_G/8) Re_\delta Pr}{1 + 12.7 (\zeta_G/8)^{1/2} (Pr^{2/3} - 1)} \left[ 1 + \left( \frac{D_h}{l_p} \right)^{2/3} \right] \quad (4.4)$$

$$\zeta_G = (1.8 \log_{10} Re_\delta - 1.5)^{-2} \quad (4.5)$$

$$Nu_0 = 0.023 Re_\delta^{0.8} Pr^{0.4} \quad (4.6)$$

For the case of infinitely expanded plates considered here, the hydraulic diameter is  $D_h \approx 4\delta$ , the length  $l_p$  approaches infinity, and thus the term in the square brackets simplifies to 1. With  $Re_\delta = 10\,300$  and  $Pr = 0.7$ , the theoretical  $Nu_0$  according to equation (4.4) is  $Nu_0 = 32.99$ . The Dittus Boelter correlation yields a similar value of  $Nu_0 = 32.36$ . The Gnielinski correlation is valid for  $10^4 < Re_\delta < 10^6$ ,  $0.1 < Pr < 1000$  and  $l_p > D_h$ . For the range of validity, it leads to an accuracy of about 90%, while the Dittus-Boelter correlation achieves about 75% accuracy [91].

The reference drag coefficient  $c_{f0}$  was calculated using three different methods. These are the derivation of the value from Prandtl's one-seventh power law [227], the correlation according to Dean [48], and the correlation of Zanoun et al. [245] based on more recent research results. While according to Prandtl  $c_f$  is a function of  $CRe^{-1/7}$ , Dean [48] and Zanoun et al. [245] find a better fit of the available data with a function of the type  $CRe^{-1/4}$ . The formulas of Dean [48] and Zanoun et al. [245] thus differ only in the constant  $C$ , which Dean [48] gives as 0.073 and Zanoun et al. [245] as 0.0743, which is 1.8% higher.

The Richardson extrapolation given in table 4.2 shows that the discretization error is no longer dominant over other errors for the mesh with  $5.6 \cdot 10^6$  elements. This is evident from the fact that the determined deviation of  $Nu_0$  and  $c_{f0}$  for this mesh is of the same order of magnitude as that of the extrapolated values. Table 4.2 shows that  $Nu_0$  with this mesh deviates from the literature values by about 1%. The extrapolated value in relation to the

<sup>2</sup> This correlation does not appear in the original publication by Dittus & Boelter [51]. Furthermore, according to Winterton [235], it is unclear where the value of the constant 0.023 comes from.

Gnielinski correlation is in the same range, in relation to the Dittus-Boelter correlation the maximum error is almost 3 %.

A very similar picture emerges with regard to drag. Depending on the reference considered,  $c_{f0}$  of the fine mesh lies in the range of less than 3 % to less than 5 %. The extrapolated value agrees with the reference values to less than 4 % to just over 6 %. Since the error of the extrapolated values  $\xi_R$  is in the same order of magnitude as that of the fine mesh, the discretization error is not to be seen as the dominant source of the remaining deviation.

**Table 4.2:** Validation data for the smooth channel with one heated and one adiabatic surface. Nusselt number  $Nu_0$  and drag coefficient  $c_{f0}$  are given for different mesh resolutions together with their relative deviation to literature values. Last column represents the data obtained via Richardson extrapolation.

Correlation		ref.		$8.3 \cdot 10^5$	$2.8 \cdot 10^6$	$5.6 \cdot 10^6$	$\xi_R$
	$Nu_0$			30.50	32.37	32.70	33.26
Dev.	Gnielinski	[222]	/%	-7.56	-1.89	-0.89	0.81
	Dittus-Boelter	[91]	/%	-5.75	0.02	1.04	2.78
	$c_{f0}$	$\cdot 10^3$		14.58	6.64	7.02	7.67
Dev.	Prandtl	[227]	/%	102.14	-7.94	-2.67	6.30
	Dean	[48]	/%	101.21	-8.37	-3.12	5.81
	Zanoun	[245]	/%	97.69	-9.97	-4.82	3.95

The selected domain is large enough to cover all relevant scales of fluid motion. This is verified by the correlation analysis analogous to the procedure in section 4.2.1. From about 20 % of the domain length, the velocity fluctuations in all considered regimes of the boundary layer are uncorrelated.

The simulated turbulence is also physically meaningful, which is a well suited indicator for realistic simulations [61]. It can be illustrated by the invariants  $II_a$  and  $III_a$  as given in equations (3.42) and (3.43) of the anisotropy tensor  $a_{ij}$  given in equation (3.41) at different points along a line perpendicular to the wall. As shown in figure 4.13, all values lie within the limits given by Lumley [148] and scaled according to the notation of Jovanović [103].

The obtained course near the wall agrees very well with the expected trajectory of a turbulent channel flow. It is known that in such flows the trajectories of the invariants are close to the two-component state and the axisymmetric state [103]. Directly at the wall, in the viscous sublayer, the anisotropy

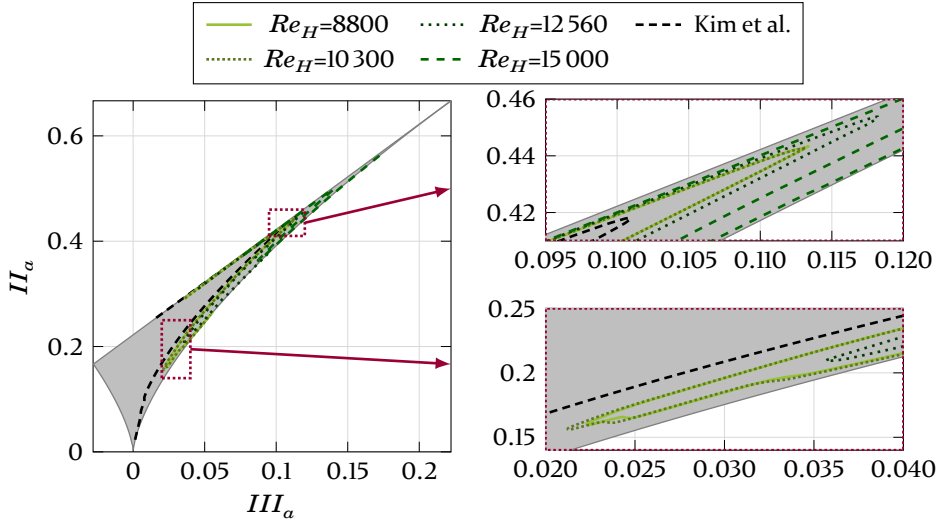


**Figure 4.13:** Anisotropy invariant map, showing that the simulated turbulence is physically realisable. Compared to the DNS data of Kim et al. [114], no isotropic turbulence is found far away from the wall.

increases along the two-component limit towards the one-component turbulence. At the transition from the viscous sublayer to the buffer layer, the invariants reach their maximum and follow the course of the axisymmetric turbulence. Due to the considered range of  $Re$ , the slight shift towards the two-component state is also realistic [103]. In contrast to the data of the DNS from Kim et al. [114], no isotropy is achieved in the region far from the wall in the flows investigated here. This physically implausible behaviour can probably be attributed to the boundary conditions used in streamwise direction. Since in this work the effects close to the wall are of interest and all values are within the described limits, it can be accepted that isotropy of turbulence far from the wall is not achieved.

Based on the simulations in the smooth channel, the necessary resolution to capture the relevant scales is known. However, the relatively high coverage rate of  $\beta = 58.4\%$  and the depth of the dimples of  $h/D_i = 20\%$  lead to a mentionable modulation of the flow characteristics. For this reason, the mesh for the simulations of the dimpled channels was likely to need further refinement and was analysed via the ratio of the Nusselt number of the dimpled channel to the Nusselt number of the smooth channel  $Nu/Nu_0$  by Richardson extrapolation. The investigation shows an estimated discretiz-

ation error of 2.17% for a mesh with  $8.6 \cdot 10^6$  elements and of 1.09% for a mesh with  $12.6 \cdot 10^6$  elements. The finer mesh thus achieves an error of the same order of magnitude as the mesh with  $5.6 \cdot 10^6$  elements for the smooth channel.

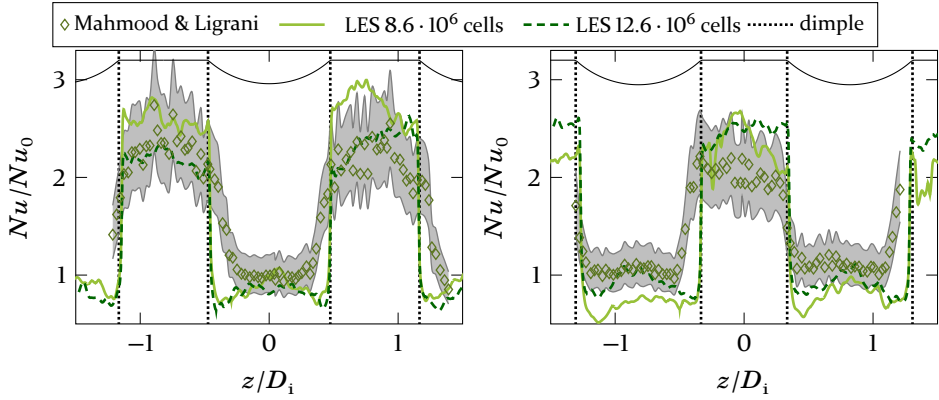
### 4.3.2 Influences of dimples on local Nusselt number

The evaluation of the local heat transfer shows a very good qualitative and quantitative agreement with the data of Mahmood & Ligrani [151] shown in figure 4.14 and figure 4.15. As confirmed in comparable simulations by Sato et al. [196], the highest gradients occur at the edges of the dimples. When looking at the visualisations of Mahmood & Ligrani [151], it seems probable that there is a slight offset between the measured values and the visualised values. For this reason, the results of Mahmood & Ligrani [151] were slightly shifted in the following illustrations compared to the published data in order to improve the comparability of the results. The evaluation was carried out using the sample lines shown in green in figure 4.12(b). The measuring range of the investigations by Mahmood & Ligrani [151] is marked in red. In the following graphs, the respective cross-section of the dimples is shown as a line in the upper area in the correct scale for better comprehension. The respective transition points of dimples and smooth area are projected as dotted lines on the graphs.

The results obtained along lines at constant  $x$  for the case  $Re_\delta = 10300$  shown in figure 4.14 indicate that the heat transfer within the upstream half of the dimples is similar to that of the smooth channel. Within the dimples, at the investigated positions, the relative velocity between fluid and wall is lower due to flow separation. This reduces the shear on the wall, which is a driving force for turbulent mixing. At the same time, the dimple shape and the separation behaviour create new flow structures that increase the mixing. These two effects are more or less balanced in the setup investigated.

Mahmood & Ligrani [151] find very similar values in the centre of the dimples, but the measurements near the edges of the dimple show a much smoother course. This behaviour is generally known, as the averaging period for the measurements is usually considerably longer than for the corresponding simulations ( see e.g. Nusser [171]). Furthermore, the measurement volume over which the average is taken per measurement point is larger than the cell volume of the well-resolved LES. In addition, the convective effects on the wall are time-dependent and thus an averaging over the measuring period

### 4.3 Heat transfer enhancement due to dimples



(a) Measurement along a line with constant  $x/D_i = 8.50$ , i. e. a line located at 80% between two consecutive rows of dimples.

(b) Measurement along a line with constant  $x/D_i = 9.35$ , i. e. a line located at 85% between two consecutive rows of dimples.

**Figure 4.14:** Increase of Nusselt number due to dimples compared to the smooth channel at constant  $x/D_i$ . Measurement uncertainty as given by Mahmood & Ligrani [151] is indicated in grey. Position and shape of the dimples along the intersection line are indicated.

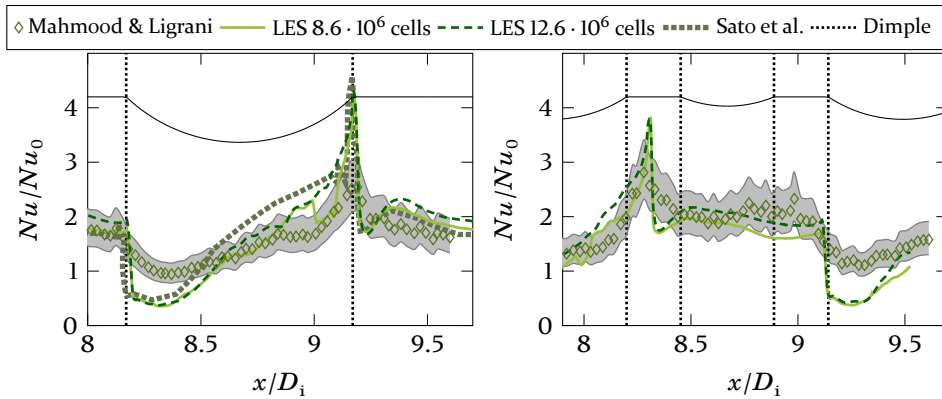
occurs depending on the time-dependent convective effects in the measuring volume, which can be determined only to a limited extent. These influences lead to considerable measurement uncertainties, which are visualised according to the information of Mahmood & Ligrani [151] as grey areas along with the plotted measurement and simulation results. The dimple edges can be represented as perfectly sharp edges in the simulation. This is not possible in the experiment due to manufacturing conditions. As a result, the edge of dimples acts as a defined detachment edge in the simulation much more than is the case in the experiment, leading to higher gradients in these areas.

The increase in heat transfer mainly takes place in the wake of the dimples. With constant  $x/D_i$ , the dimple wake of the previous row corresponds to the area between the intersected dimples. Here the increase of  $Nu$  reaches values above 2. The range of the maximum heat transfer increase in streamwise direction is locally strongly limited and depends on the resulting flow structures in the wake. The line with  $x/D_i = 8.50$  shown in figure 4.14(a) lies about  $0.65D_i$  behind the midpoints of the previous row of dimples. This equals 80% of the distance from one row of dimples to the next. The line with  $x/D_i = 9.35$  shown in figure 4.14(b) lies about  $0.69D_i$  behind the previous row and thus at about 85% of the distance between two consecutive rows. This small difference already gives a 8.6% lower increase in heat trans-

#### 4 Investigation of dimpled surfaces in non-rotating flow

fer according to the data of Mahmood & Ligrani [151] and 11% according to the simulations.

The analysis in flow direction in figure 4.15(a) shows the strong local dependence of the heat transfer across a dimple. At the dimple inlet, the increase of  $Nu$  falls below 1 due to separation. This effect is recorded less distinctly in the measurements. Within the detachment range, the heat transfer remains low. Subsequently,  $Nu$  increases continuously along the length of the dimple. It reaches a maximum at the outlet edge, which is also visible but much less pronounced in the measurements. In the wake of the dimple  $Nu$  initially drops sharply before another local but clearly less pronounced peak follows. After this,  $Nu$  continues to drop moderately up to the next dimple. The course over the dimple corresponds very closely to that found by Sato et al. [196] in comparable simulations.



(a) Nusselt number ratio along a line with constant  $z/D_i = 0.0$ , i. e. through the centreline of a dimple. (b) Nusselt number ratio along a line with constant  $z/D_i = 0.45$ . This line intersects two dimple series at different offsets to the centre.

**Figure 4.15:** Increase of Nusselt number due to dimples compared to the smooth channel at constant  $z/D_i$ . Available data from Sato et al. [196] and Mahmood & Ligrani [151] as well as the reported measurement uncertainty are included.

Outside the centre line of the dimples, the heat transfer behaviour remains qualitatively comparable to a large extent, but the increase compared to the smooth channel is smaller. This can be seen from the plot along the line  $z/D_i = 0.45$  in figure 4.15(b). This line intersects one dimple row off-centre at about  $0.35D_i$  and another at  $0.45D_i$ . At the intersection at  $0.35D_i$ , the drop at the dimple inlet as well as the rise across the dimple and the peak behind the dimple edge are still clearly visible. However, this peak is located further downstream, which results from the fact that the forming structures

are modulated by the shape of the dimple trailing edge. Only at the border of the dimple, i. e. at the intersection at height  $0.45D_i$ , the characteristic is no longer recognisable. Nevertheless, a clear increase in heat transfer remains in this area as  $Nu/Nu_0 \approx 2$ , which can be attributed to the secondary structures created as a result of the dimple edge.

### 4.3.3 Effects of the coverage rate on the heat transfer

In order to use the positive effects regarding the heat transfer of deeper dimples as well as the desirable effects regarding the drag of shallower dimples on rotating discs of limited thickness, compromises are inevitable. Since the absolute depth of the dimples is limited by the disc thickness, dimples with smaller diameter  $D_i$  lead to deeper dimples in relative terms of  $h/D_i$ . The examination of two setups with dimples of the same depth  $h/D_i = 20\%$  but at lower coverage rates  $\beta = 24.7\%$  and  $\beta = 7.2\%$  at  $Re_\delta = 12560$  helps to determine the influence of the coverage rate on a surface. The resulting diameters of the corresponding dimples with unchanged simulation domain related to the previously investigated- reference dimple imprint diameter  $D_0$  are  $D_i/D_0 = 0.65$  and  $D_i/D_0 = 0.35$ , respectively. The domains are visualised in figure 4.16.

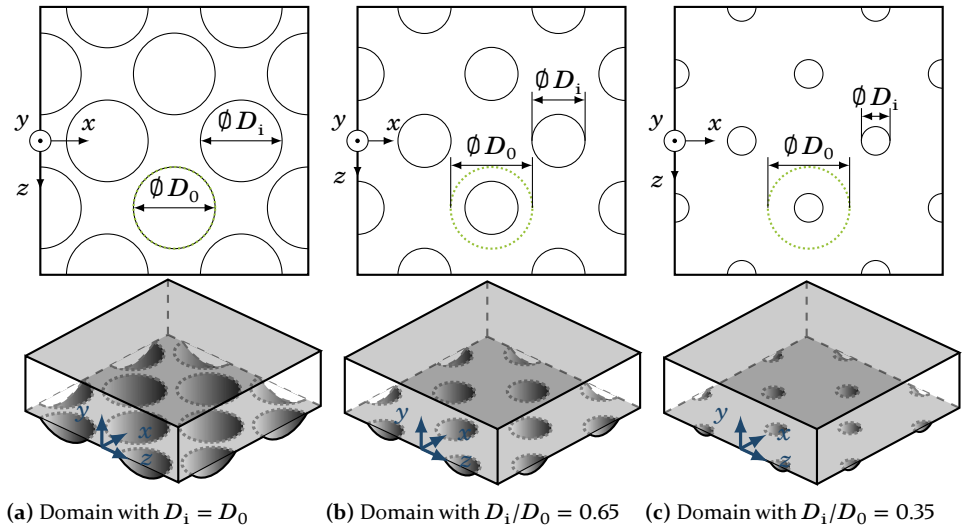
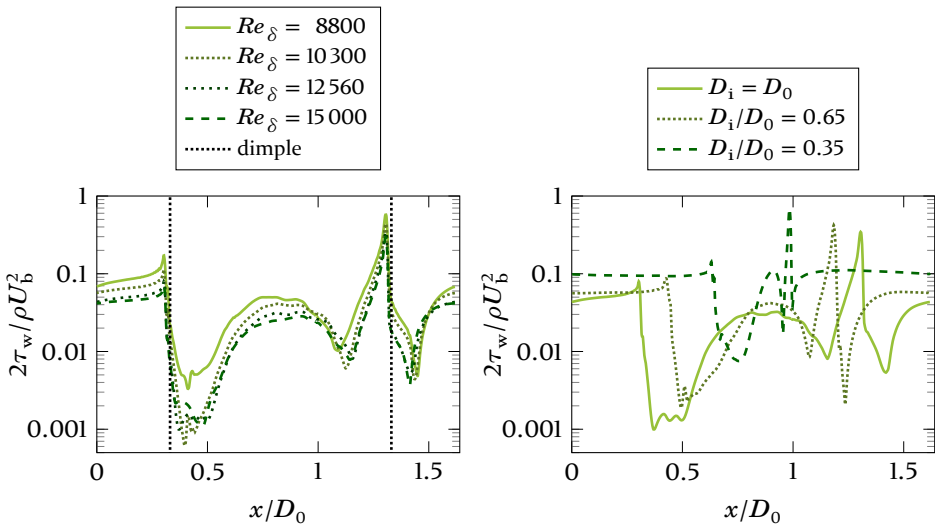


**Figure 4.16:** Used computational domains for simulations of heat transfer. Channels with dimples of reduced imprint diameter  $D_i$ .

In addition to the increase of  $Nu$ , the increase of drag is crucial for the evaluation of thermal efficiency. Improving heat transfer and improving resist-

#### 4 Investigation of dimpled surfaces in non-rotating flow

ance represent opposing optimisation goals. With increasing dimple size at constant  $h/D_i$ , the proportion of pressure drag increases. However, the drag component resulting from the wall shear stress shows a dependence on both  $Re$  and the dimple geometry. Figure 4.17(a) shows the dimensionless wall shear stress for different  $Re_\delta$  and  $D_i/D_0 = 1$ . It can be seen that the wall shear stress decreases with increasing  $Re_\delta$  over the entire course of the dimple. A sharp drop can be found directly at the dimple inlet due to flow separation. Depending on the forming detachment area, the point at which the flow reattaches varies with  $Re$ . The value increases rapidly towards the trailing edge of the dimple. Due to the edge, another, smaller detachment area forms before the wall shear stress increases again towards the next dimple. The characteristic course of the wall shear stress remains even with smaller dimples. In figure 4.17(b), however, it is noticeable that the mean wall shear stress increases with decreasing dimple diameter. This indicates a change of the characteristic of the boundary layer, which is not only local but global in nature in streamwise direction.



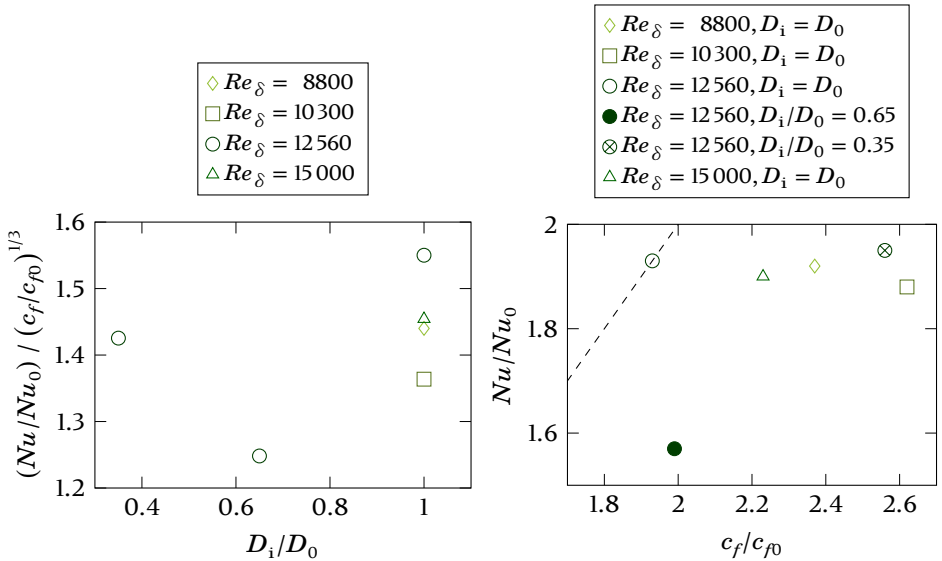
(a) Comparison of dimensionless wall shear stress for different  $Re_\delta$  and constant diameter  $D_i = D_0$  in dependence of the streamwise position at  $z/D_i = 0.0$ . (b) Comparison of dimensionless wall shear stress at fixed  $Re_\delta = 12560$  and varying diameter  $D_i$  in dependence of the streamwise position at  $z/D_i = 0.0$ .

**Figure 4.17:** Dimensionless wall shear along the dimples shows a qualitatively comparable behaviour that is independent of  $Re_\delta$ .

The behaviour resulting from the smaller dimples also leads to a better heat transfer ratio. This results in a higher overall thermal efficiency than for the case with dimples of size  $D_i/D_0 = 0.65$ , as shown in figure 4.18(a). The

### 4.3 Heat transfer enhancement due to dimples

setup with the largest dimples achieves the highest thermal efficiency. There is also no clear trend with regard to  $Re$  observed with this setup. The lowest thermal efficiency results for the setup with large dimples at  $Re_\delta = 10\,300$ . At  $Re_\delta = 8\,800$  and  $Re_\delta = 15\,000$  the setup performs on roughly the same level. This demonstrates the sensitivity of a setup of dimples to deviations of the operating condition from the design point. Due to this, extrapolation of the results is effectively impossible. Even with interpolation, the interpolation space must be chosen small in order to obtain valid statements. This behaviour explains why the literature sometimes contains contradictory statements regarding the effectiveness of similar setups, e. g. [140, 168, 214, 215].



(a) Dependency of thermal efficiency of  $D_i/D_0$  and  $Re_\delta$  for  $h/D_i = 20\%$ . (b) Visualisation of the relation of  $Nu/Nu_0$  and drag force coefficient  $c_f/c_p_0$  for different  $D_i/D_0$  and  $Re_\delta$  for  $h/D_i = 20\%$ . Dashed line represents  $(Nu/Nu_0) / (c_f/c_p_0) = 1$

**Figure 4.18:** Thermal performance of different setups at varying  $Re_\delta$ .

This finding is reinforced by analysing the increase of  $Nu$  compared to the increase of  $c_f$  in figure 4.18(b). This comparison is based on the modified Reynolds analogy [32, 41, 91]. The dashed line indicates where the increase of  $Nu$  is equal to the increase of  $c_f$ . It can be seen that in no case the increase of heat transfer is higher than the increase of drag. Merely the setup with large dimples of  $D_i = D_0$  at  $Re_\delta = 12\,560$  achieves a ratio close to unity. The limited performance of the setup with  $D_i/D_0 = 0.65$  is also reflected

in this observation. The other points of consideration deliver similarly high increases of heat transfer of just under 2. However, the increase of drag due to the generated form drag in the dimples as well as the overall increased frictional drag in the case of the dimples of  $D_1/D_0 = 0.35$  is up to 2.6. This is consistent with the known fact that the Reynolds analogy loses much of its validity in the case of occurring pressure drag [71, 91].

#### **Conclusions on drag reduction and heat transfer due to dimples**

The investigations in channels and on stationary plates with different kinds of dimples show that a reduction of drag is only possible with flat dimples  $h/D_1 \ll 10\%$ . In order to adequately resolve the effects on the wall in numerical simulations, stringent mesh criteria and sufficiently large domains are to be maintained. Flow conditions and dimples setup must be matched within narrow limits to achieve positive effects. However, the studies show that specific manipulation of streaks near the surface by dimples is promising in terms of drag reduction. An increase in heat transfer is possible with dimples of higher depth  $h/D_1 \geq 10\%$ . Moderate efficiency increases are possible regardless of the chosen setup and flow condition, while for higher efficiency increases of  $(Nu/Nu_0) / (c_f/c_{f0})^{1/3} > 1.5$  setup and flow condition have to be matched and maintained very precisely. Away from the design point, the resulting efficiency can't be predicted from extrapolations and is prone to decreasing drastically in some cases. This statement applies to both drag reduction and heat transfer. It was shown that at first sight contradictory results in the literature can be traced back to exactly this circumstance. The investigations presented thus close the previously existing knowledge gap concerning the general question of the effectiveness of dimples with regard to drag reduction and show clear potential with regard to the physically efficient increase in heat transfer through dimples.

# Influence of noninteracting dimples on rotating discs

*"By describing the basic physical mechanisms governing fluid dynamics better, numerical simulation helps us understand, model, and later control these mechanisms."*

—Sagaut [193]

After the effects of dimples on the flow in stationary setups have been considered, this chapter examines the effects of individual dimples on rotating discs subject to transverse flow.

Due to the superposition of the rotational motion, the direction of inflow of the dimples changes continuously. In addition, the transverse flow is displaced by the thickness of the disc in the upstream direction. This results in a global, non-uniform flow over the disc, which does not occur as a result of the rotation. Discs attached to a cylindrical shaft furthermore provoke a wake area, which causes time- and location-dependent fluctuations in velocity and the prevailing pressure. These effects result in a highly complex flow pattern, which causes the relative flow over a dimple to depend not only on its geometry but also on the radial position on the disc and the current angle of rotation of the disc relative to the inflow direction. This chapter discusses the influence of individual, non-interacting dimples on this complex flow field as well as possible increases in efficiency compared to smooth discs. The main effects are sufficiently detectable by unsteady RANS (URANS) simulations. For more detailed considerations, the results of scale adaptive simulations (SAS) are presented for selected operation points. Some of the data shown in this chapter was gathered in Stadler [S3]. A possible application scenario for dimples on rotating discs is the room ventilation system with heat recovery already mentioned in chapter 1, which uses rotating discs to generate two opposing air flows in two separate ducts. This system was investigated as part of the *RegVent* project, which was funded by the Bavarian State Ministry of Education, Science and the Arts.

## 5.1 Numerical setup

So far no published investigations on the thermal behaviour of dimpled discs is available in literature. However, numerous publications on the heat transfer behaviour of rotating, smooth discs subjected to transverse flow have been published. Experimental as well as simulative investigations have already been carried out by various research groups, as presented in section 2.3. This broad database was used to validate the simulations carried out in this work. In order to ensure comparability, the simulations were based on the investigations by Nguyen & Harmand [169].

### *Initial geometry and computational domain*

Rao et al. [183] achieved heat transfer improvements of 55% to 65% with spherical dimples of depth  $h/D_i = 20\%$  in rectangular channels. Other authors such as Turnow et al. [221] and Moon et al. [161] also achieved good results with similarly designed dimples. However, since the present work evaluates dimples on discs of limited thickness, there are restrictions on the maximum depth of the dimples. Furthermore, it has already been shown that the best values regarding drag are achieved with very shallow dimples. For these reasons, the following investigations focus on dimples of depth  $h/D_i = 10\%$ . The examination of discs with five dimples each, evenly distributed on the same radial distance to the centre, allows for the investigation of the effects of individual, non-interacting dimples<sup>3</sup>. The simultaneous simulation of five dimples, however, makes data acquisition much more efficient than for the simulation of a single dimple on the disc.

For validation and as a reference case for the dimple setups, the flow around a smooth disc was also simulated. The computational domain shown in figure 5.1 was used for all investigated cases. As in the work of Nguyen & Harmand [169], the diameter of the cylinder was set to  $D_c = 58$  mm. The attached disc was set to a thickness of  $H_d = 5$  mm and a diameter of  $D_d = 178$  mm, resulting in  $D_d \approx 3.07D_c$ .

The disc and cylinder rotate at angular velocity  $\Omega$  and are simultaneously subjected to a cross-flow of free stream velocity  $u_\infty$ . The geometric extension of the simulation domain is also based on the work of Nguyen & Harmand [169]. Thus the inflow length measures about four disc diameters  $D_d$ , the

---

<sup>3</sup> Preliminary investigations have shown that the mutual interaction is negligible with five evenly distributed dimples.

wake length measures about  $7D_d$ , the total width was set to approximately  $5D_d$  and the height was set to  $1.5D_c$  in each direction.

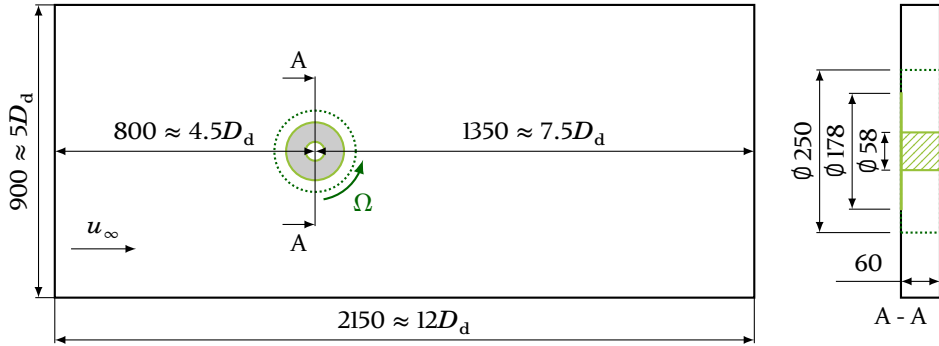


**Figure 5.1:** Computational domain for the simulations of the discs with dimples, absolute lengths are given in mm, and magnified cross section of the rotating disc. Disc and cylinder are shown in light green, the rotating domain is indicated in dark green.

Since the position of the surface structures relative to the upstream flow as well as to the cylinder changes over time in the case of the dimpled, rotating discs, the domain was divided into a rotating and a stationary area. The rotating area with a diameter of  $D_r \approx 1.4 D_d$ , indicated as dotted line in figure 5.1, was kept small enough to minimize the computational effort, but large enough to capture the occurring effects of rotation in the direct vicinity of the disc. The stationary and rotating areas do not overlap and are connected at the cylindrical contact surface by a fluid-fluid interface.

Teardrop-shaped dimples often yield promising results in channels concerning heat transfer increase [183, 184, 242, 243] and have even been investigated for drag reductions [215]. Their effect on rotating discs was therefore also investigated. The geometry of the dimples used was derived from Rao et al. [183]. The geometry of the discs together with the centrally positioned cylinder corresponds to that of the publications by Latour et al. [132] and Nguyen & Harmand [169]. Additionally, a model of a disc without a central cylinder was investigated. For both models – with and without cylinder – the smooth disc without dimples was also investigated.

### Computational mesh

Both domains were meshed with block-structured, hexagonal meshes. For this purpose, the calculation area was divided into geometrically determined

## 5 Influence of noninteracting dimples on rotating discs

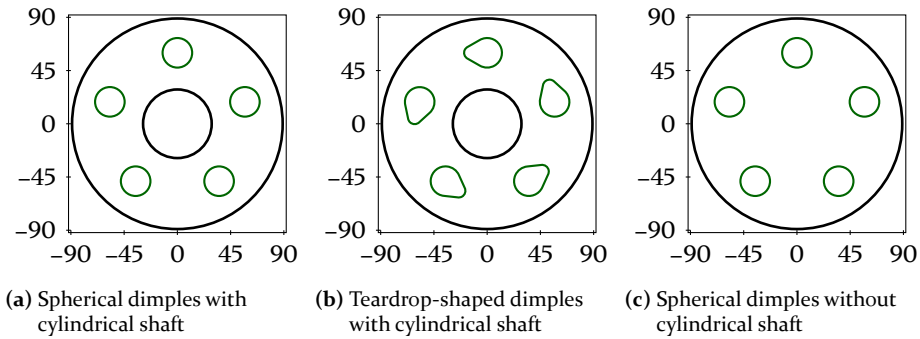


**Figure 5.2:** Setups of investigated cases in order to determine the effects of individual dimples on rotating discs. Discs and cylinders are shown in black, dimples are shown in light green.

blocks, which were meshed separately. In addition to the higher control over the distribution of the grid points, this approach also offers the possibility to resolve areas of interest with a finer mesh. Also, the resulting mesh quality is generally higher than for unstructured meshes as shown in section 3.6, which means that the simulations converge faster or convergence is achieved at all.

In the simulations carried out, the mesh elements were condensed towards the solid walls for detailed boundary layer resolution. Both the dimensionless wall distance  $y^+$  and the growth rate of the elements were controlled to ensure that sufficient elements were placed in the boundary layer. Simulations of rotating discs require larger domains to minimise the influence of boundary conditions on the flow region near the discs. Additionally, no periodicity or symmetry in the flow can be exploited in order to save computational resources. As a result, these simulations require more computing time and numerical effort than the simulations carried out in chapter 4, so that the use of numerically more efficient models – which always imply a loss of accuracy – is unavoidable. As will be shown in section 5.2, URANS simulations are very well suited to represent the heat transfer and the drag behaviour of the discs both with and without dimples. For detailed investigations of the transient flow effects, scale-adaptive simulations were also carried out. A mesh convergence study, similar to that carried out in section 4.1.1, showed that a mesh with a maximum of  $y_{\max}^+ \approx 2.4$  and a mean of  $y_m^+ \approx 1.2$  was suited for valid results of the URANS. The mesh used for SAS yielded  $y_{\max}^+ \approx 1.7$  and  $y_m^+ \approx 0.9$ . Together with a maximum time step size of  $\Delta t = 5 \cdot 10^{-5}$  s for the URANS and  $\Delta t = 1.25 \cdot 10^{-5}$  s in the case of the SAS, mean Cour-

ant–Friedrichs–Lewy (CFL) numbers of 0.8 and 0.4 as well as maximum CFL numbers of 2.7 and 1.4 were obtained.

Due to the rotation of the disc and the constant cross-flow, the highest relative velocities occur in the outer area of the disc. This results in high shear stresses, so that the first grid point requires to be sufficiently close to the wall in order to keep the dimensionless wall distance small. In this case, conventional mesh compression towards the wall results in elements with high aspect ratios and thus low quality. In addition, the dimple structures require a fine surface resolution in both radial and tangential directions in order to reproduce the geometry accurately. For these reasons an adaptive meshing technique similar to that used for the simulations in chapter 4 was chosen in which the refinement is not achieved by compression but by dividing cells into smaller cells as schematically shown in figure 3.5. This approach maintains the aspect ratio of the initial cells and the resulting mesh quality remains high.

As given in table 5.1, the final mesh for URANS simulations consisted of about  $1.2 \cdot 10^7$  elements with a maximum aspect ratio of 17.7, a maximum skewness of 0.546 and a minimum cell quality of 0.756. For the SAS, the resulting mesh consisted of more than twice as many elements with a slightly higher maximum aspect ratio of 21.1. The maximum skewness of 0.582 was also slightly higher than for the URANS mesh. Nevertheless, the minimum cell quality increased to 0.792. In the first adaptation layer on the wall, 16 elements were placed. In each additional adaptation layer, at least six elements were placed in the wall-normal direction in order to meet the recommended minimum requirements for adopted meshes [73] and to ensure that the boundary layer was sufficiently resolved. Since the disc surface was always meshed as a connected topology, these settings were applied to all setups. This ensured that both the resolution and the mesh quality were kept constant in all cases, allowing for better comparability of the results, while simultaneously maintaining the geometrical differences of the setups.

### ***Setup, boundary conditions and initial conditions***

For all URANS simulations the  $k$ - $\omega$ -SST model by Menter [155] was used. The interface between stationary and rotating area was defined as matching interface. As summarised in table 5.2 the simulation medium was air at reference temperature  $T_0 = 20\text{ }^\circ\text{C}$  with corresponding density  $\rho_0 = 1.204\text{ kg m}^{-3}$  and dynamic viscosity  $\mu = 1.825 \cdot 10^{-5}\text{ kg m}^{-1}\text{ s}^{-1}$ , resulting in a kinematic viscosity of  $\nu = \mu/\rho = 1.516 \cdot 10^{-5}\text{ m}^2\text{ s}^{-1}$ .

## 5 Influence of noninteracting dimples on rotating discs

**Table 5.1:** Metrics of the meshes used for URANS and SAS.

	URANS	SAS
elements	12m	32m
max. aspect ratio	17.7	21.1
max. skewness	0.546	0.582
min. cell quality	0.756	0.792

**Table 5.2:** Material properties of the used medium air.

material property	variable	value	unit
density	$\rho_0$	1.204	$\text{kg m}^{-3}$
temperature	$T_0$	20	$^{\circ}\text{C}$
dynamic viscosity	$\mu$	$1.825 \cdot 10^{-5}$	$\text{kg m}^{-1} \text{s}^{-1}$
kinematic viscosity	$\nu$	$1.516 \cdot 10^{-5}$	$\text{m}^2 \text{s}^{-1}$
specific heat capacity	$c_p$	1006.43	$\text{J kg}^{-1} \text{K}^{-1}$
thermal conductivity	$k_t$	0.0242	$\text{W m}^{-1} \text{K}^{-1}$

### Boundary conditions

An inlet velocity of  $u_{\infty} = 4 \text{ m s}^{-1}$  was defined in order to represent the case of a rotating disc with transverse flow. This results in a constant cross-flow Reynolds number according to equation (3.62)  $Re_u = 23\,576$  for all simulations. Different ratios  $\Gamma = Re_{\Omega}/Re_u$  as given in equation (3.63) were realized by the variation of the disc rotational velocity  $\Omega$ , ranging from  $0 \text{ min}^{-1}$  to  $2000 \text{ min}^{-1}$ , resulting in  $Re_{\Omega} \leq 109\,863$  and thus  $\Gamma = Re_{\Omega}/Re_u \leq 4.66$ . The outlet of the stationary domain was defined as pressure outlet with mean pressure  $p_m = 0 \text{ Pa}$ . The disc and the surface of the cylindrical shaft were defined as smooth, rotating walls with no-slip condition and constant temperature  $T_d = 120 \text{ }^{\circ}\text{C}$ . The rotational velocity of the disc was set via the rotating domain, to which the disc exhibits no relative velocity. The boundaries in spanwise and axial direction were defined as symmetry planes. The other boundaries were located sufficiently far from the disc to simulate undisturbed flow without wall influences by using symmetry conditions.

### Initial conditions

All transient simulations were initialized with results of stationary RANS simulations of the respective case under consideration. The resulting initial pressure and velocity fields, which were determined with low computational resource consumption, accelerate the convergence and lead to a much earlier occurrence of the pseudo-stationary state in order to start with the temporal averaging of data of interest [68].

### Solver setup

Solving was done using pressure-based segregated algorithms, the coupling of pressure with velocity was carried out using the semi-implicit method for pressure linked equations (SIMPLE) as originally proposed by Patankar & Spalding [178] and in the transient simulations using pressure-implicit with splitting of operators methods (PISO) with neighbour correction as supposed by Issa [97]. Despite good mesh quality, skewness correction was used in the transient calculations while under-relaxation factors were kept at unity [5].

### Discretization and convergence criteria

Second order methods were used to minimize discretization errors while achieving acceptable computing times. For the spatial discretization of velocities, turbulent quantities and energy, upwind methods were used, while pressure was discretized via central differences. In order to prevent stability problems without reducing the accuracy of the simulation results, a limited implicit second order method was used for the temporal discretization. To ensure sufficient convergence, residuals of  $1 \cdot 10^{-5}$  for the URANS and  $1 \cdot 10^{-6}$  for the SAS were used as convergence criteria.

### Time step size

The time step  $\Delta t$  was selected for all simulations according to the recommendations of the documentation [5]. Thus, an initial time step of  $\Delta t = 1 \cdot 10^{-5}$  s was increased until in each simulation step the convergence criteria of  $1 \cdot 10^{-5}$  were reached within 5 to 10 inner iterations. The time step size was found to depend exclusively on the rotational velocity, independent of the case considered. In table 5.3 the time steps as well as the corresponding angle of rotation per time step for the respective rotational velocities are summarized. One can see that higher rotational velocities require smaller time steps in order to converge. However, the higher rotational velocities result in larger angles of rotation per simulation step, reducing the calculation time per revolution.

## 5 Influence of noninteracting dimples on rotating discs

**Table 5.3:** Time step lengths  $\Delta t$  and corresponding angle of rotation for outer iterations of the investigated ratios  $\Gamma = Re_\Omega/Re_u$ .

$Re_\Omega / -$	$\Gamma / -$	$\Delta t / 10^{-5} \text{ s}$	Angle of rotation per time step / $^\circ$
0	0.00	5	-
27 466	1.17	4	0.12
54 931	2.33	3	0.18
82 397	3.50	3	0.27
109 863	4.66	2	0.24

### Judgement of simulation state

In addition to the judgement of convergence via residuals within the outer iteration steps, it is necessary to run the simulations until a state occurs which is termed as steady state or pseudo-stationary. To determine this state, the mean static pressure  $p_{\text{in}}$  at the inlet, the mass flux  $\dot{m}_{\text{out}}$  at the outlet, as well as the mean heat flux density  $\dot{q}_m$  and the mean wall shear stress  $\tau_w$  at the disc and at the cylindrical shaft were monitored over the simulations. For the later evaluation of the heat transfer behaviour, moment and drag coefficients of all walls were additionally recorded during the simulations. These were calculated using the disc radius  $D_d/2$  and the projected surface  $D_d^2\pi/4$ .

## 5.2 Validation based on the turbulent flow around smooth, rotating discs and numerical characteristics

For the given problem, the validation of numerically obtained data is not a trivial issue. The straight comparison with experimentally determined values contains several potential deviations even with simple flow phenomena, which cannot be prevented, such as geometrical deviations, differing boundary conditions, surface roughness, blockage in the test rig as well as free stream turbulence level [19]. In the flows investigated here, fluctuations in the operating point, temperature deviations, air humidity, density changes and deviations in rotational velocity pose further challenges. In addition, the comparison of the rotational Reynolds number  $Re_\Omega$  and cross-flow Reynolds

## 5.2 Validation based on the turbulent flow around smooth, rotating discs

number  $Re_u$  neglects possible differences in the Mach number  $Ma$  and thickness of the disc, which have a proven influence on the overflow and thus on the fluid dynamical and thermal behaviour of the disc.

The comparison with numerically determined data from similar simulations also shows uncertainties, as the results depend on factors such as the mesh quality, the solver, the discretization, the models used and the stopping criterion. For these reasons, numerical parameters were also used for validation in addition to comparisons with experimentally and numerically determined data. In addition to mesh independence studies, the convergence behaviour and the transient behaviour of the simulations were evaluated.

### Stabilisation of simulation results

Suitable, since for further processing relevant, parameters for determining the pseudo-stationary state are the course of the mean heat flux density  $\dot{q}_m$  and the course of the moment coefficient  $c_M$  at the disc surface. These were therefore monitored for all simulations in each simulation step. The courses of heat flux density and torque over simulated revolutions of the discs  $N$  for the disc with spherical dimples is shown for the case with and without cylindrical shaft in figure 5.3.

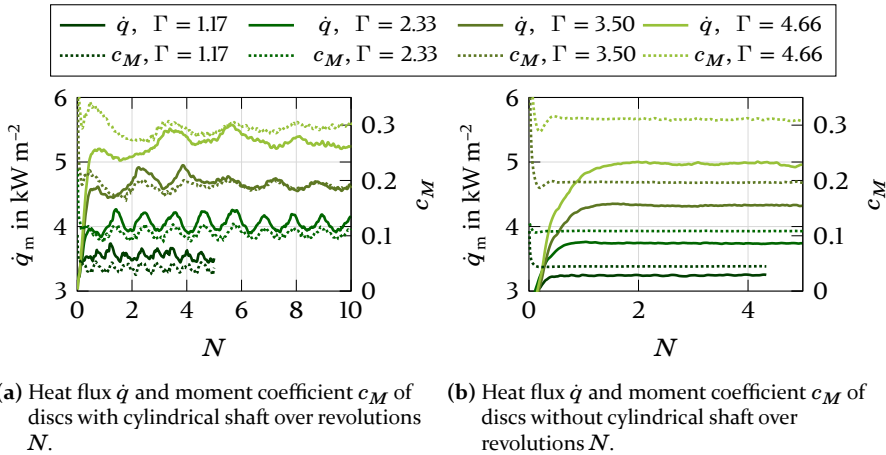


**Figure 5.3:** Evaluation of simulation results of a disc structured with five spherical dimples with (a) and without cylindrical shaft (b). (Simulation data was partly generated within the context of Stadler [S3])

In the case of the simulations with cylinder in figure 5.3(a), the detachment frequency at the cylinder is the dominant source of fluctuations, as

## 5 Influence of noninteracting dimples on rotating discs

can be seen from the comparison with the cases without cylinder represented in figure 5.3(b). The long-term mean value of each case is reached after about two full detachment periods in all simulations, and for  $N > 2$  for the cases without cylinder. As the rotational velocity increases, the characteristic of the flow separation decreases noticeably. This phenomenon is discussed in more detail in chapter 6. In all simulations, the results stabilise after about 1.2 s of simulation time. This corresponds to less than 2 periods of the flow separation on the cylinder. With the higher rotation numbers  $\Gamma \geq 3.50$  the amplitude decreases due to the detachment after the first two fully formed periods. These rotation numbers correspond to a rotation rate  $\alpha_r = \Omega D_d / 2u_\infty = 1.14$  and  $\alpha_r = 1.52$ . The results of Kumar et al. [129] show that for larger  $\alpha_r > 1.95$  even a suppression of the detachment can be expected.

### Validation with data from literature

The necessary mesh resolution was determined using a mesh convergence study as in the previous chapter. Suitable data from Latour et al. [132], Nguyen & Harmand [169] and Wiesche & Helcig [231] exist for validation with literature values. Those authors carried out investigations of heat transfer on rotating discs and derived correlations between the increase of  $Nu$  and  $\Gamma = Re_\Omega / Re_u$ . As a result of different definitions of the dimensionless ratios, some of the papers produced noticeable deviations in the findings. In the following, all results are therefore converted to the variables used in this work.

Figure 5.4 shows the ratio of mean Nusselt number  $Nu_m$  of the rotating discs to mean Nusselt number  $Nu_{m,\Omega=0}$  of the stationary disc plotted over  $\Gamma$ . In addition to the simulation results, the data from Latour et al. [132], Nguyen & Harmand [169] and Wiesche & Helcig [231] are included as literature reference values. Small differences to these data are to be expected as the setups slightly differ in parameters such as the ratio of disc thickness to diameter or the presence of a cylindrical shaft. The correlations found in literature, included in figure 5.4(a), agree very well for the investigated range of  $\Gamma$ . The approximated uncertainty for the correlation of  $\pm 10\%$  given by Latour et al. [132] is indicated in grey. With the exception of the smooth disc at  $\Gamma = 4.66$ , all simulated values lie within this area. Due to slightly different setups and boundary conditions, the correlations found in literature deviate from one another. The URANS simulations performed slightly underestimate the correlations, but accurately reproduce the characteristics and are mostly within the uncertainty range of  $\pm 10\%$  given by Latour et al. [132], which is included in light grey. Only the operating point  $\Gamma = 4.66$  of the smooth disc lies 0.1% outside of this range.

## 5.2 Validation based on the turbulent flow around smooth, rotating discs

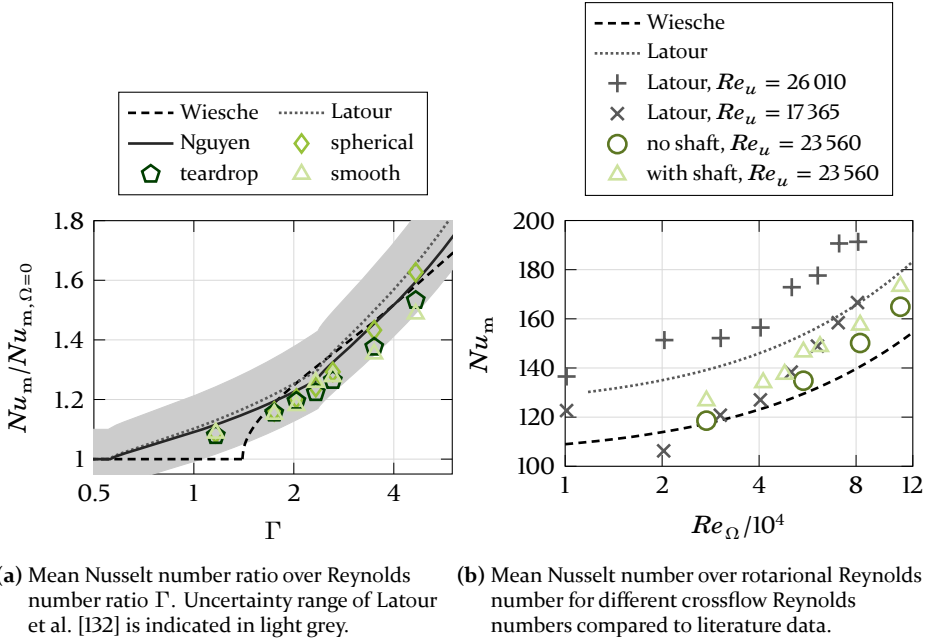


**Figure 5.4:** Simulation results in comparison with correlations given by Latour et al. [132], Nguyen & Harmand [169] and Wiesche & Helzig [231]. (Simulation data was partly generated within the context of Stadler [S3])

In addition to the results of the smooth disc, the increase of  $Nu$  of the discs with spherical and teardrop-shaped dimples is also shown. The dimples have little influence on the heat transfer behaviour in the range  $\Gamma \leq 2.6$ . In this range, the results obtained differ from each other by less than 3%. The influence of the dimples increases with increasing rotational frequency. The teardrop-shaped dimples tend to exhibit lower values in the range of  $\Gamma > 2.6$ , in some cases even lower than the smooth disc. At  $\Gamma = 3.50$  the heat transfer increase of the spherical dimples compared to the smooth disc reaches 5.9%, at  $\Gamma = 4.66$  it exceeds 9%. The teardrop-shaped dimples also produce the highest increase in heat transfer at the highest rotational velocity. Yet it lies no more than 3% above that of the smooth disc.

More detailed insights into the correlation of  $Nu_m$  with the rotational velocity of the disc are provided in figure 5.4(b). The correlation provided by Wiesche & Helzig [231] applies to smooth discs that are not attached to cylinders. The simulation of this case provides very good agreement with the correlation. The maximum deviation in the considered rotational velocity range is slightly above 9%. The implemented data for different  $Re_u$  from Latour et

## 5 Influence of noninteracting dimples on rotating discs

al. [132] illustrate the uncertainty in the given correlations. The simulation results of  $Nu_m$  deviate from the calculated correlation for  $Re_u = 23\,560$  by a maximum of 9% and thus lie below the stated inaccuracy of 10%. Nevertheless, the results tend to match the values of the data for lower  $Re_u = 17\,365$  better than that of  $Re_u = 26\,010$ , despite the fact that the simulated operating point is closer to the higher  $Re_u$ .

The verified mesh quality as well as the stabilising state and the good agreement with literature values suggest a high reliability of the results. No reference values exist in the literature for discs with dimples. Due to the geometric similarity to the smooth discs and the same operating range, the results described in the following are nevertheless considered to be valid.

### 5.3 Thermal behaviour of single dimples on discs

As shown in the previous section, the dimples have a positive effect on the heat transfer increase at higher rotational velocities. This results from the disturbance of the boundary layer, especially in the area of the dimple edges that favours the turbulent momentum transport perpendicular to the surface. However, this effect also causes an increased drag, which in the case of the rotating disc is observed in the behaviour of  $c_M$ . Similar to the observation in ducts and on smooth plates, the ratio of the increase in heat transfer with respect to the increase in the moment coefficient provides information about the thermal efficiency of the setup.

In addition to the thermal performance of the different shapes of dimples as a function of the operating condition, detailed investigations of the heat transfer within the dimples are presented in the following. Furthermore, the results obtained using scale-resolved simulations are examined and the conclusions drawn for further considerations are presented.

#### 5.3.1 Performance of spherical and teardrop-shaped dimples

Figure 5.5 presents the thermal performance of the different shapes of dimples in two ways. In the representation, the index d stands for dimples, while the index s stands for smooth. Figure 5.5(a) shows that over the entire range of rotational velocity the actual heat transfer increase of the teardrop-shaped dimples equals  $95.4\% \pm 0.7\%$  of the corresponding drag increase. In the case of the spherical dimples, this ratio lies about three percentage points lower at  $92.3\% \pm 0.7\%$ . In both cases, the ratio of the increase in heat

### 5.3 Thermal behaviour of single dimples on discs

transfer to the increase of drag is approximately constant, which results in only slight variations in the values over the rotational velocity. Since the changed drag affects the required pumping power for the equivalent mass flow, Gee & Webb [72] suggest taking this effect into account for the evaluation of thermal performance in pipes. Relating the increase of heat transfer as well as the increase of drag to the same mass flow leads to the thermal efficiency  $(Nu_{m,d}/Nu_{m,s}) / (c_{M,d}/c_{M,s})^{1/3}$ . This ratio is shown accordingly for the rotating discs in figure 5.5(b) and shows that the teardrop-shaped dimples provide about 2% performance advantage in the best case. This value is achieved for  $\Gamma = 3.50$  and  $\Gamma = 4.66$ . At lower rotational velocities, no effective advantage of the dimples over the smooth disc can be observed. This is also true for the spherical dimples. However, the efficiency of the spherical dimples exceeds that of the smooth disc for  $\Gamma = 3.50$  by 3.3%, in the case of  $\Gamma = 4.66$  even by 5.5%.

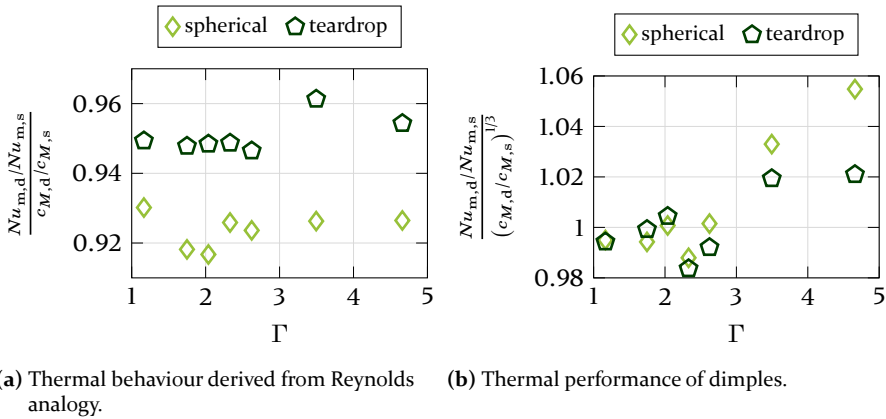


**Figure 5.5:** Thermal performance of spherical and teardrop-shaped dimples on rotating discs. (Simulation data was partly generated within the context of Stadler [S3])

The positive effect of teardrop-shaped dimples that was found in channels cannot be observed for individual dimples on rotating discs. In channels, the main flow is parallel to the central axis of the dimples. In this case, the teardrop shape causes a less abrupt inflow into the dimple than in the case of a spherical dimple. This reduces the edge inflow effect, which is partly responsible for the increase of drag, while the downstream edge, and thus the effects of it on the flow, remains unchanged. The highest, local increase of  $Nu$  takes place at this edge. This interaction results in the observed performance increase of teardrop-shaped dimples in channels.

## 5 Influence of noninteracting dimples on rotating discs

In the case of the rotating disc, the relative flow condition is different. Due to the rotation and the superimposed cross-flow, the relative flow is no longer parallel to the central axis of the dimple. Spherical dimples are robust to this change due to their symmetrical shape. This finding underlines the sensitivity of the used dimples with regard to the prevailing flow condition. To obtain a similar effect on rotating discs, the shape of dimples would have to be matched to the direction of the prevailing relative velocity of the disc to the surrounding fluid. Since this varies in the case of a superimposed cross-flow as a function of  $\Gamma$  and centrifugal forces as well as the current rotation angle of the disc, an optimisation of this shape is not likely to yield satisfactory results.

The differences in heat transfer behaviour become clear when observing the temporal average heat flow  $\bar{q}$  along the centre line of the dimples in the azimuthal direction. These are shown in figure 5.6, where figure 5.6(a) represents the spherical dimples and figure 5.6(b) the teardrop-shaped dimples. In all cases, the data was obtained by averaging over all five simulated dimples on each disc. In addition, the data are represented in dimensionless form in figure 5.6(c) and figure 5.6(d) for both types of dimples. At low rotational velocity  $\Gamma = 1.17$ , the heat flux of spherical dimples drops slightly at the dimple inlet. Up to the centre of the dimple, the heat transfer rises back to the level reached outside the dimple. Afterwards, the heat flux density continues to rise moderately before a peak occurs at the outlet edge. With increasing rotational velocity, the behaviour at  $\Gamma = 2.33$  changes in such a way that the initial drop as well as the following increase of  $\bar{q}$  are more pronounced. This indicates that a recirculation area forms at the inlet of the dimple, which is consistent with the increased drag observed, which is the reason for the thermal behaviour shown in figure 5.5(a). This clear change in characteristics is also evident in the dimensionless representation using  $\bar{q}^*$  given in figure 5.6(c). A similar behaviour can also be observed at the highest rotational velocities  $\Gamma = 3.50$  and  $\Gamma = 4.66$ . Here, the heat flux density downstream the dimple inlet drops in absolute terms to a comparable level of the case  $\Gamma = 2.33$ . The subsequent steep increase leads to a local peak in  $\bar{q}$  at about a quarter of the dimple length as indicated by an arrow in figure 5.6(c). Even after this local peak, the level remains above the heat flux density outside the dimples. The additional increase at the trailing edge of the dimples thus leads to considerably higher average heat flux densities with increasing rotational velocity. As the  $c_f$  increases to the same extent, the spherical dimples show the highest increases of mass flow weighted thermal efficiency in this operation range as discussed in figure 5.5(b).

### 5.3 Thermal behaviour of single dimples on discs

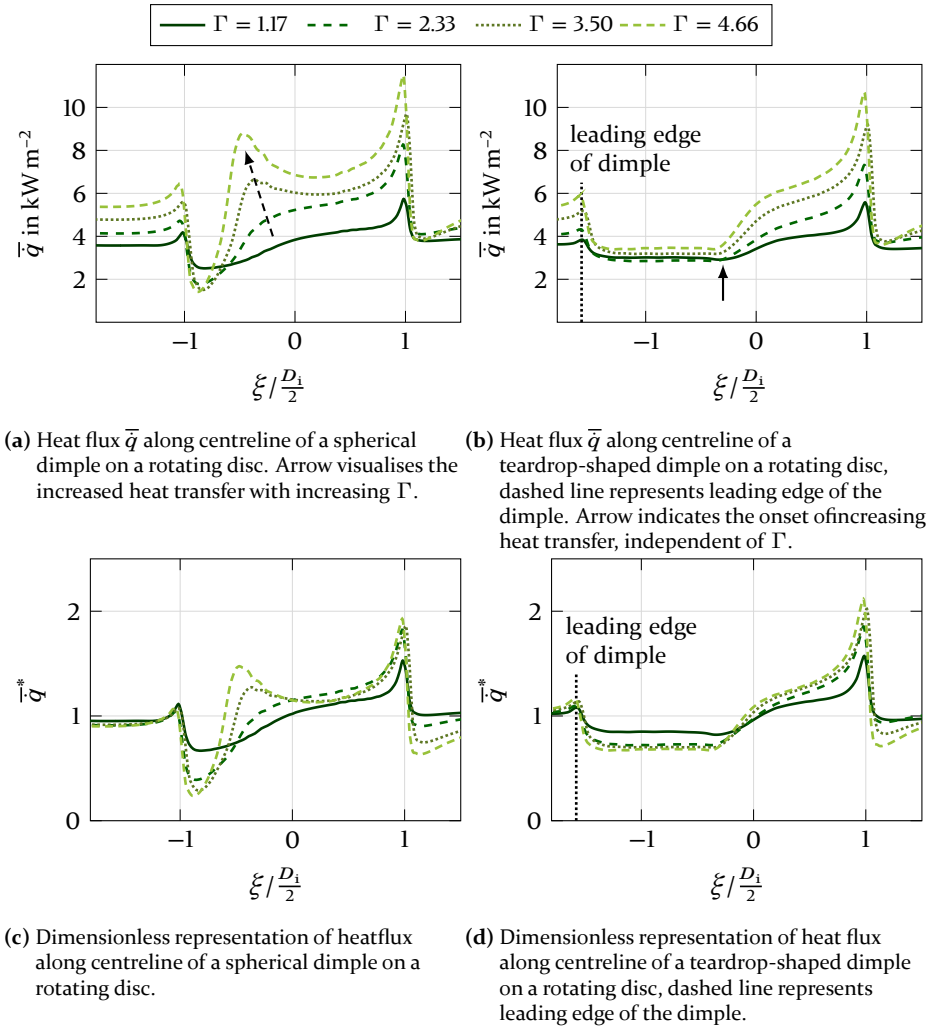


**Figure 5.6:** Temporal mean heat flux along centre line of dimples. Dimensionless values are scaled with the integral mean of the respective setup. (Simulation data was partly generated within the context of Stadler [S3])

The heat flux density along the centre line of the teardrop-shaped dimples in figure 5.6(b) shows a fundamentally different behaviour. Due to the teardrop shape, the dimples are larger in the upstream direction. The inlet edge lies about 58% further away from the lowest point of the dimple and is marked by a dashed line. As with spherical dimples, a reduction of the heat flux density takes place after entering the dimple. However, at all rotational velocities this reduction is less pronounced than in the case of the spherical dimples.

## 5 Influence of noninteracting dimples on rotating discs

Also, no immediate increase of  $\bar{q}$  takes place downstream of this decrease. Instead, the heat flux density remains at a constant level. Only from about  $0.125D_i$  to  $0.175D_i$  upstream the lowest point a renewed increase of the heat flux density occurs as indicated by an arrow in figure 5.6(b). Particularly the dimensionless representation in figure 5.6(d) shows that the characteristic of the heat flux density course is almost independent of the rotational velocity, in contrast to the case of the spherical dimples. The point of onset of this increase is almost independent of the rotational velocity, whereby it tends to start earlier with increasing rotational velocity. Similar to the case of the spherical dimples, the increase towards the downstream edge is more pronounced at higher rotational velocities. However, the slope lies consistently below that of the comparable case with spherical dimples. Also, in no case does a local maximum of the heat flux density occur within the dimples. The maximum  $\bar{q}$  at the downstream edge is quantitatively comparable with that of the spherical dimples in all cases considered.

The course of the heat flux density within the teardrop-shaped dimples suggests that flow separation at the dimple inlet is reduced due to the modified inflow into the dimple. This is consistent with the original purpose of teardrop-shaped dimples used in channels. Due to the reduced detachment, not only the increase in heat transfer but also the increase of drag in the upstream area of the dimples remains moderate. As a result of the comparable behaviour at the trailing edge of the dimple, the teardrop-shaped dimples have a higher overall ratio of heat transfer increase to drag increase. Considering thermal efficiency, however, the teardrop-shaped dimples perform worse than the spherical dimples due to the insufficient increase in heat transfer. This shows that the beneficial effects of teardrop-shaped dimples in ducts cannot be transferred to rotating discs due to the drastically changed inflow conditions of the dimples.

### 5.3.2 Scale resolved results

The URANS simulations delivered acceptable results throughout. Despite the higher numerical effort due to the more complex but also more precise underlying model of the SAS and the finer mesh, the results regarding the thermal behaviour of the discs deviate from those of the URANS simulations by 0.9% to 2.8%. These small deviations prove the high quality of the URANS simulations. One advantage of the SAS, however, lies in the possibility to visualise the resulting flow structures in a higher resolution. In addition to verifying the physical validity, this can also be used to draw conclusions about the behaviour of the flow within the dimples.

### 5.3 Thermal behaviour of single dimples on discs

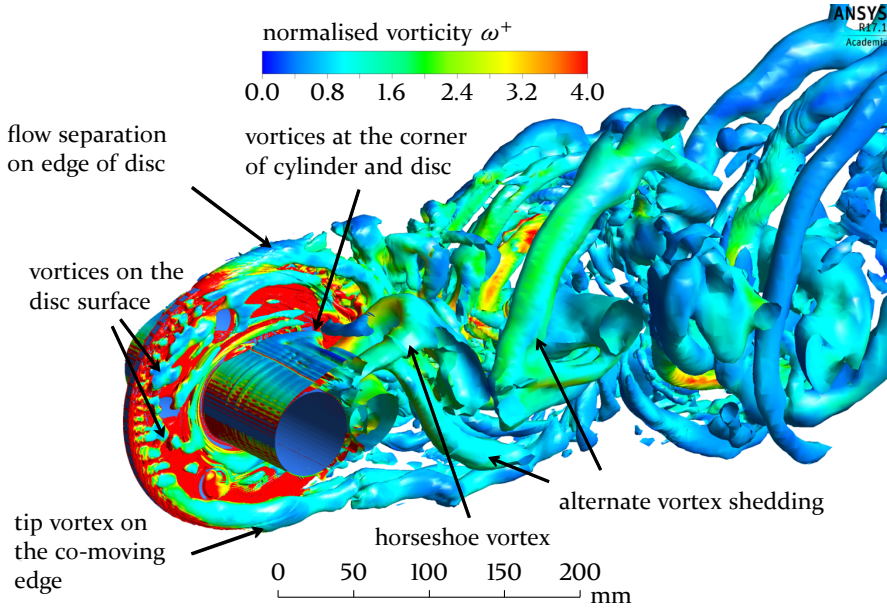


**Figure 5.7:** Visualisation of the arising vortices in the flow field via an isosurface of  $Q = 1000 \text{ s}^{-2}$ , coloured with the normalised vorticity  $\omega^+$ . (Simulation data was partly generated within the context of Stadler [S3])

To visualise the vortex structures at any given time of the statistically evaluable flow, the  $Q$ -criterion is shown in figure 5.7 by means of an isosurface at  $Q = 1000 \text{ s}^{-2}$ . According to the recommendation by Nguyen & Harmand [169], the isosurface is coloured with the normalised vorticity  $\omega^+$  according to equation (5.1). These areas can be visualised and interpreted as coherent vortex structures [53, 90] as shown in figure 5.7.

$$\omega^+ = \frac{\omega_u D_c}{2u_\infty} \quad (5.1)$$

As expected, the highest vorticity occurs near the rotating bodies, therefore the legend is limited to the range  $0 < \omega^+ < 4$  in figure 5.7. At the upper edge of the disc, which rotates counter-clockwise in the indicated representation, the highest flow velocity relative to the cross-flow coming from the left is present. In this area, minor flow detachments occur at the upstream disc edge. These lead to vortex structures that follow the disc geometry due to the prevailing pressure field. The formation of small vortex structures can be seen at the leading edge of the disc. At the lower edge of the disc, the

## 5 Influence of noninteracting dimples on rotating discs

relative velocity is much lower than at the upper edge since the cross-flow is in the direction of rotation. The resulting vortex structures are transported downstream by the cross-flow. The most dominant structures arise in the wake of the cylinder. Here, a periodic detachment as well as typical horseshoe vortices known from the literature can be clearly identified. The structures are transported downstream and develop a distinct vortex street.

The structures identified are in close agreement with those described in literature, such as Nguyen & Harmand [169]. Based on the structures near the dimples, the close connection between the flow state and the current angle of rotation becomes clear. In the wake of the cylinder as well as in the upper region of the disc, the dimples are exposed to large-scale and thus highly energetic structures. These dominate the prevailing flow condition, the influences due to the geometry of the dimple are minimal in these areas. As the disc rotation progresses, the dimple leaves this area, whereupon an interaction with the smaller structures resulting from the detachment at the leading edge occurs. Depending on the prevailing frequency of these structures and the current position of the dimple, both strengthening and weakening interactions with the structures on the dimple occur. In the lower area of the disc, at low or negative relative velocity, the effects of the dimples dominate and determine the prevailing flow pattern.

From these observations it is evident that the combination of dimple shape, radial position of the dimple, rotational Reynolds number  $Re_\Omega$  and cross-flow Reynolds number  $Re_u$  leads to constantly varying flow conditions at the dimples. The spherical dimple shape is the only one that provides the relative flow with an identical leading and trailing edge in every disc position. The optimisation of the dimple shape can therefore only be done for a defined combination of  $Re_\Omega$ ,  $Re_u$  and radial position. The potential for improving the thermal behaviour is higher the more uniform the relative flow conditions are at different angles of rotation. This is generally the case with increasing  $Re_\Omega$  and decreasing  $Re_u$ , thus generally spoken with increasing  $\Gamma$ .

### 5.3.3 Concluding remarks on the findings from noninteracting dimples on rotating discs

The investigations show that teardrop-shaped dimples on rotating discs have no advantages over spherical dimples in the setups considered. The main reason for the better performance of teardrop-shaped dimples in channels lies in the uniform macroscopic flow within a channel. On rotating discs, which are subject to cross-flow, the local flow conditions vary with the angle

### *5.3 Thermal behaviour of single dimples on discs*

of rotation. Adjusting the shape of the dimples with the aim of increasing thermal efficiency requires a high effort in this flow environment, especially since the basic phenomena on spherical dimples have not yet been conclusively studied.

URANS simulations with an appropriately fine mesh resolution are well suited to adequately represent the integral flow effects of the single dimples. The additional numerical effort of SAS, in contrast, is only rewarding for the detailed consideration of flow structures. However, further research into detailed flow has a lower priority than research on the effects of using multiple, interacting dimples on rotating discs.

For these reasons, the effects of different arrangements of spherical dimples on discs are investigated in the following chapter. For this purpose, both structured, uniform arrangements and random distributions of dimples are examined. In addition, dimples of uniform size as well as of different sizes are considered. In all cases, exclusively spherical dimples are examined due to the mentioned findings in this current chapter 5.



# Thermal performance of rotating discs covered with spherical dimples

*"The range of practical applications for disc flow extends to computer memory disc drives [...], centrifuges, cutting discs and saws, gears, and brakes."*

—Childs [31]

The results obtained from chapter 5 show that spherical dimples are well suited for the use on rotating discs due to their inherent directional independence of the inflow. In this chapter, the effects of the distribution of dimples on discs are investigated. The focus is on the dependence of the thermal performance on the arrangement and geometry of the dimples at different Reynolds numbers. For this purpose, the changes of the numerical setup in comparison to that used in chapter 5 are presented first. The validity of the investigations is then verified. The heat transfer and drag behaviour of six different dimple arrangements is subsequently evaluated and discussed in detail. Finally, design rules are derived according to which the distribution of dimples on rotating discs can be determined for given problems. Some of the data shown in this chapter was gathered in [S2].

## 6.1 Problem description and investigated dimple arrangements

So far, neither the influence of regular nor irregular distributions of dimples on rotating discs has been investigated. Therefore, in this chapter, simulations of different arrangements of dimples on rotating discs are evaluated. Unlike in the previous chapter 5, smaller dimples are used for two reasons. Firstly, the number of dimples distributed on the surface can be increased by reducing the size of individual dimples. Secondly, the dimple depth decreases with a constant ratio of  $h/D_1$ , which means that the disc thickness can

be reduced. This decreases the edge effect on the upstream side, reducing a possible source of masking flow effects.

The simulation area used is similar to the one in chapter 5 shown in figure 5.1, but the thickness of the disc is reduced by 60% to  $H_d = 2$  mm. In addition, only one side of the rotating disc was simulated and the height of the domain of  $1.5D_c$  was adjusted following the achievements from investigations of Breuer [18] and Karabelas [104]. Breuer [18] investigated the flow around circular cylinders at different  $Re$  at a domain of height  $\pi D_c$  [16, 17], before investigating the influence of the domain height on the results [18], where he found even better agreement with experiments for some values at domain height  $D_c$  compared to  $\pi D_c$ . Karabelas [104] also refers to these studies and uses a domain of height  $D_c$  in his investigations with which he achieves good results for a rotating cylinder. The investigations of Williamson et al. [234] also show that the wavelength  $\lambda_S$  of the streamwise vortex structures in the wake of a cylinder is approximately  $\lambda_S = 25Re_u^{-0.5}D_c$ . For  $Re_u = 23576$  investigated here, this results in about 16.3% of  $D_c = 58$  mm. In order to increase numerical efficiency and since the three-dimensional, turbulent effects of the cylinder wake are of minor relevance in the present investigations, as well as due to the mentioned results in literature, the computational domain height was reduced to 60 mm, which is approximately the diameter of the cylinder  $D_c$ .

The investigations aim to explore the influence of dimples as a surface structure on rotating discs on fluid and heat transfer behaviour. For this purpose, several parameters such as the rotational frequency, the number of dimples, the geometry of the individual dimples as well as the arrangement of the dimples relative to each other are of particular interest. Six different setups were investigated in order to discover the influences of the arrangement and the size of the dimples. At least three dimples were always arranged next to and behind each other in order to enable interaction of the dimples in both radial and azimuthal directions. From this in conjunction with the dimensions of disc and cylinder, the maximum diameter was determined to be  $D_i = 9$  mm to ensure that a distance between the dimples is always guaranteed. Smaller dimples of imprint diameter  $D_i = 5$  mm to 8 mm were used for the investigation of the effect of this geometrical parameter. The minimum size of the dimples results from the requirement to keep the coverage range  $\beta$  in a range of roughly 10% to 20%. Dimples with a constant depth to diameter ratio of  $h/D_i = 10\%$  were used to ensure that only the influence of the diameter was determined. This value serves as a compromise solution to achieve both significant heat transfer increase, while the required disc thick-

## 6.1 Problem description and investigated dimple arrangements

ness  $H_d$  remains small compared to the disc diameter  $D_d$  and the resulting flow loss remains moderate.

Besides the influence of the diameter, the effects of the distribution of the dimples on the local and global heat transfer of the disc were examined. For this purpose, both mathematically defined, structured arrangements and random distributions of the dimples on the surface were evaluated. Using the identical number and shape of dimples in different arrangements allows for conclusions to be drawn about the impact of the relative position of dimples to each other and on the disc. The heat transfer can be homogenized by random arrangements, while periodic interactions and effects might occur in the structured cases. Finally, different numbers of dimples  $N_d$  for comparable application types were investigated to determine the influence of the coverage rate. Here, the coverage rate is defined as the projected surface of the dimples in relation to the projected surface of the disc.

Six setups were defined from these requirements, which are visualised in figure 6.1. These are three discs with dimples of diameter  $D_i = 9$  mm and three discs with different diameters  $D_i = 5$  mm to 8 mm. In addition to the use of  $N_d = 64$  dimples in patterned and random arrangement, a setup with  $N_d = 56$  dimples of  $D_i = 9$  mm that were arranged in a staggered manner and one with  $N_d = 128$  dimples of diameter  $D_i = 5$  mm to 8 mm arranged in a patterned manner was investigated. In the setups with patterned arrangements, the dimples are organised in four concentric rows. The setups in figure 6.1 are arranged as follows: The first row (a, b, c) shows the setups with dimples of imprint diameter  $D_i = 9$  mm, the second row (d, e, f) shows the arrangements of dimples with  $D_i = 5$  mm, 6 mm, 7 mm and 8 mm. The first column (a, d) represents the patterned arrangements, the second column (b, e) the randomly distributed arrangements. The third column shows the staggered arrangement of 56 dimples (c) and the more densely packed, patterned arrangement with 128 dimples (f). Table 6.1 shows the most important data of the various setups including the names used throughout the chapter and the resulting coverage rate  $\beta$ .

The names of the setups depend on the different parameters. The preceding letter indicates the type of distribution. "P" stands for patterned, "R" for random and "S" for staggered setups. It is followed by the number  $N_d$  of dimples, which is 56, 64 or 128. Finally, the size of the imprint diameter is indicated, which is either 9 mm or 5 mm to 8 mm, denoted by D9 or D5-8, respectively.

## 6 Thermal performance of rotating discs covered with spherical dimples

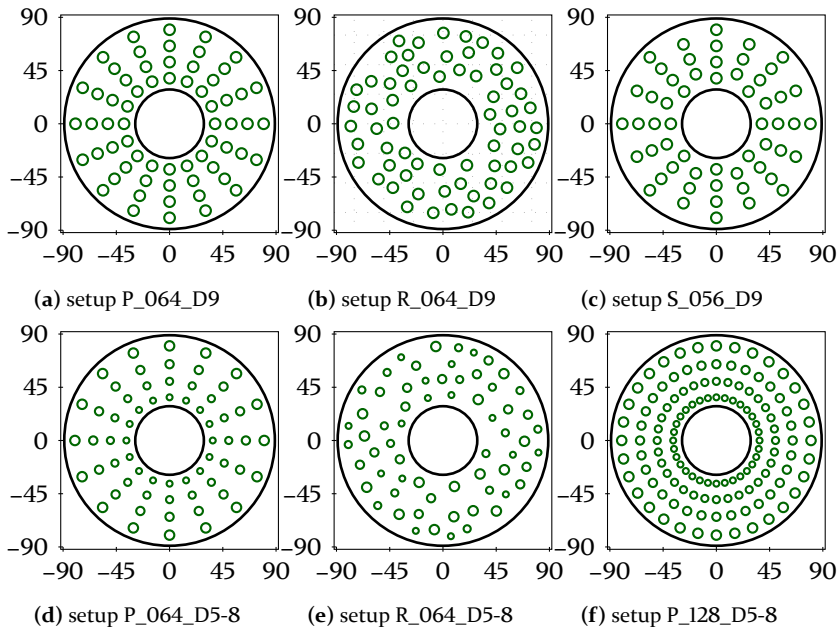


**Figure 6.1:** Investigated arrangements of dimples on rotating discs.

For the patterned setups with varying dimple size, the dimples were arranged in such a way that the dimple diameter increases with increasing disc radius in order to achieve a high packing density. In addition, the radial distance between the dimples was selected equidistantly. This results in rows of four dimples each for patterned cases, with the dimples of the same diameter having the same distance from the axis of rotation. In the staggered arrangement, the distance between the dimples in each row was also kept constant. With the random arrangements, the dimples were placed in descending order according to their size with the aim of increasing the probability of being able to fit all dimples on the disc at a distance of at least 2 mm from one another and 5 mm away from the disc edge and the shaft.

## 6.2 Influences of the cylindrical shaft on the flow and heat transfer

**Table 6.1:** Overview of the investigated setups including name used, type of arrangement, number of dimples, diameters used and surface coverage rate.

setup	arrangement	$N_d$	diameter $D_i$ in mm	coverage rate $\beta$ in %
reference	smooth disc	0	-	0.0
P_064_D9	patterned	64	9	18.3
R_064_D9	random	64	9	18.3
S_056_D9	staggered	56	9	16.0
P_064_D5-8	patterned	64	5, 6, 7, 8	9.8
R_064_D5-8	random	64	5, 6, 7, 8	9.8
P_128_D5-8	patterned	128	5, 6, 7, 8	19.7

### Computational mesh and solver settings

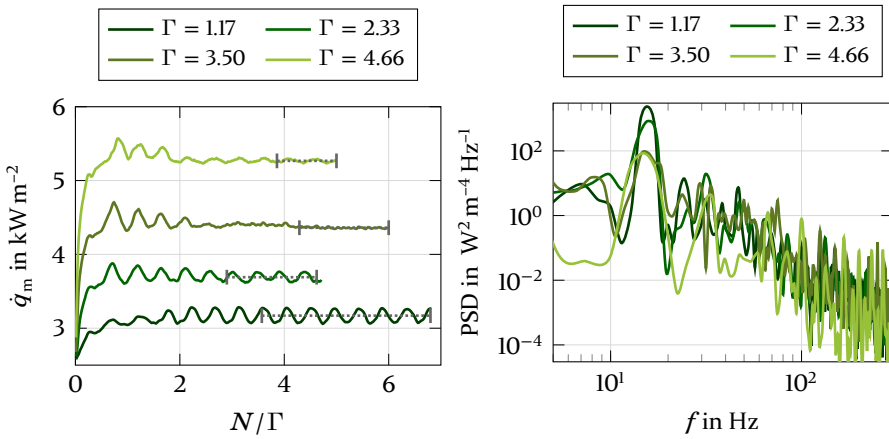
The same mesh criteria, boundary layer resolution and quality assurance mechanisms as in chapter 5 were used in the simulations presented here. Due to the slightly changed geometry, a final mesh with  $y_{\max}^+ \approx 3.0$  and  $y_m^+ \approx 1.7$  was determined to be suited for valid results. The final mesh consisted of about  $10^7$  elements with a maximum aspect ratio of 22.2 and a minimum angularity of  $45.9^\circ$ . The minimum  $2 \times 2 \times 2$  determinant was 0.691, which is well above the minimum requirements for a suitable computational mesh. The material properties as well as the solver settings, discretization schemes, time step sizes, boundary conditions, and initial conditions also correspond to those from chapter 5. The same applies to the evaluation of the quasi-stationary state of the simulations.

## 6.2 Influences of the cylindrical shaft on the flow and heat transfer

As in the previous chapter 5, the heat flux at the disc serves as a suitable parameter to evaluate the transient behaviour of the simulations. The course of heat flux density over the ratio of rotational velocity  $N$  to ratio of Reynolds numbers  $\Gamma$  for the different rotational velocities is shown exemplarily for the case R\_064\_D5-8 in figure 6.2(a). It can be seen that for ratios  $N/\Gamma > 2.4$  all simulations are to be considered as steady state. Only at  $\Gamma = 3.50$  a slight reduction of  $\dot{q}_m$  for  $N/\Gamma > 4$  can be noticed. Even though this decrease is not

## 6 Thermal performance of rotating discs covered with spherical dimples

more than 0.4%, only the range beyond the reduction was used for averaging and for the evaluations in this case. The used ranges for the averages as well as the resulting mean values are indicated in figure 6.2(a) as dotted lines. For this purpose, complete disc revolutions were used in all cases in order to prevent shifts of the mean values caused by non-periodic fractions. The deviation of the calculated mean values from the respective mean value of the first disc rotation of the averaging range was less than 0.4% for all cases, which confirms the assumption of the stabilized state of the simulations.



(a) Stabilization process of the mean heat flux for case R\_064\_D5-8 plotted over the ratio of simulated revolutions  $N$  to  $Re$ -ratio  $\Gamma$ . (b) Power spectral density (PSD) of heat flux for determination of the dominant frequencies, used for deriving the Strouhal number  $Sr$ .

**Figure 6.2:** Evaluation of the simulation quality on the basis of the development of the mean heat flux density at the disc surface (a) and by evaluation of the dominant frequencies (b). (Simulation data was partly generated within the context of Matsche [S2])

From the graphs in figure 6.2(a) it can be seen that the heat flux density periodically oscillates about the mean value. Hereby the amplitude of the fluctuation decreases with increasing  $\Gamma$ , but the frequency remains approximately constant leading to Strouhal numbers  $Sr$  as given in equation (6.1) of  $Sr = 0.215$  to  $0.223$  as shown in table 6.2. This range fits well with the known relationship for long, non-rotating cylinders given in literature as  $Sr \approx 0.2$  for  $10^3 < Re < 2 \cdot 10^5$  [107] or  $Sr = 0.22$  [50]. The Strouhal number  $Sr$  relates the frequency  $f$  of a periodic flow phenomenon with the characteristic length  $L$  to the characteristic flow velocity  $U$  and can thus be interpreted as the dimensionless frequency of this flow phenomenon. For the calculations of the mean frequencies  $\bar{f}$  shown in table 6.2, at least six full periods of the main oscillation were used in each case, which are denoted as *full periods*. The

## 6.2 Influences of the cylindrical shaft on the flow and heat transfer

determined mean frequencies  $\bar{f}$  result from the evaluation of low pass filtering of the signal. From this, the period  $t_p$  of each fundamental oscillation was determined and the inverse value was calculated for obtaining the corresponding frequencies  $f_p = 1/t_p$ . From these, the mean values  $\bar{f}$  and the standard deviations  $\sigma$  were calculated to determine the coefficients of variation  $\sigma/\bar{f}$ . The additionally given frequencies  $f$  follow directly from the fast Fourier transformation (FFT) of the heat flux densities over the given number of disc revolutions. For the case  $\Gamma = 3.50$  the low-pass filtering of the simulation data shown in figure 6.2(b) does not lead to sufficient significance for the value of the determined mean frequency  $\bar{f}$ . Therefore, the indication of this value and thus also the value for  $\sigma/\bar{f}$  in table 6.2 is omitted.

$$Sr = \frac{fL}{U} = \frac{fD_c}{u_\infty} \quad (6.1)$$

As shown in figure 6.2(a), the main oscillation is dominant even before the pseudo-stationary state persists for all cases investigated. As the frequency resolution  $f_{res} = 1/t_i$  depends on the duration  $t_i$  of the input signal the longest possible number of revolutions for these calculations were used and are denoted as *revolutions*. These frequencies were also used to calculate the Strouhal numbers  $Sr$ . Due to the different time step sizes as well as number of simulated time steps for the different Reynolds number ratios  $\Gamma = 1.17, 2.33, 3.50$  and  $4.66$  the calculated frequency bands become  $f_{res} = 1.43, 1.95, 1.32$  and  $2.48$ , respectively, which contribute to a slight inaccuracy concerning the calculation of  $Sr$ .

**Table 6.2:** Characteristic frequency of mean heat flux density  $\dot{q}_m$  and corresponding Strouhal number  $Sr$  for different ratios of Reynolds numbers  $\Gamma$ .

$\Gamma$	full periods	$\bar{f}$ / Hz	$\sigma/\bar{f}$	revolutions	$f$ / Hz	$Sr$
1.17	10	15.54	5.26 %	6	15.68	0.227
2.33	6	15.88	6.42 %	9	15.62	0.227
3.50	8	-	-	19	15.78	0.229
4.66	6	14.75	4.25 %	14	14.85	0.215

The dominant frequency of all cases is found to be around 15 Hz, while further local peaks occur in the range of the rotational frequency of the disc for all cases. In the case  $\Gamma = 2.33$  the rotational frequency of the disc approximately matches that of the Kármán vortex street downstream of the cylindrical shaft.

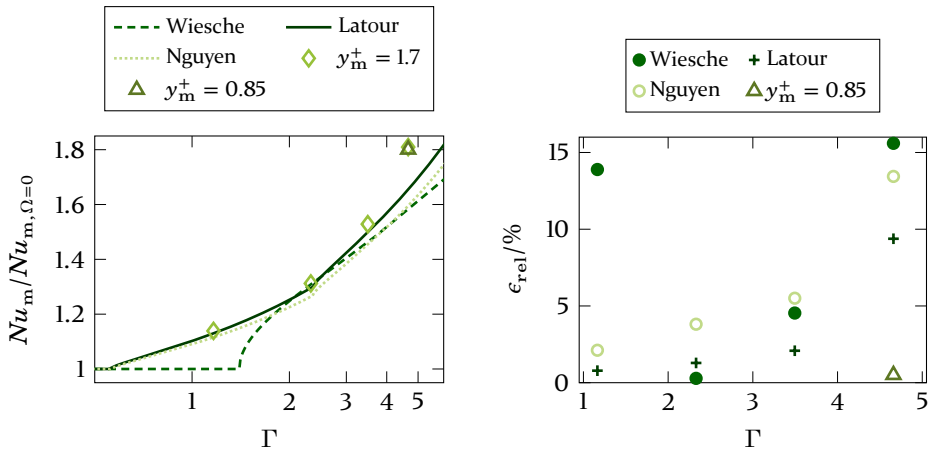
In the case of  $\Gamma = 1.17$  the detachment frequency is twice as high as the rotational frequency, while in the case of  $\Gamma = 4.66$  the rotational frequency is twice as high as the detachment frequency. Only in the case of  $\Gamma = 3.50$ , where the rotational frequency of the disc is 25 Hz, there is no corresponding relationship which would favour a resonance-like behaviour, which explains the slightly different characteristics of the resulting course of  $\dot{q}_m$  over  $N/\Gamma$ .

### Influences of grid point distribution

The necessary mesh resolution was investigated in chapter 5. This part therefore only deals with the determination of the appropriate grid point distribution for the correct representation of the fluid mechanical phenomena of interest. For this purpose two meshes with almost  $10^7$  elements were created, which differ in the compression of the elements towards the fixed walls. The critical case of  $\Gamma = 4.66$  regarding the mesh quality and occurring gradients was used for the comparison of the meshes. The mesh with lower compression leads to a mean and a maximum dimensionless wall distance of  $y_m^+ \approx 1.7$  and  $y_{\max}^+ \approx 3.0$ , respectively while the mesh with higher compression yields  $y_m^+ \approx 0.85$  and  $y_{\max}^+ \approx 2.3$ . Due to the increased compression rate, the element quality decreased which resulted in the time step size for this simulation being reduced by a factor of two in order to prevent divergence. Figure 6.3 shows the increase of  $Nu$  of the rotating discs compared to the stationary disc plotted over  $\Gamma$ . In addition to the simulation results, the data from Latour et al. [132], Nguyen & Harmand [169], and Wiesche & Helcig [231] are included as literature reference values.

The comparison with literature values illustrates three different points. First, the simulation results best match the correlation of Latour et al. [132]. As shown in figure 6.3(b), the relative error related to these values is up to  $\Gamma = 3.50$  smaller than 2.1% and in case of  $\Gamma = 4.66$  still below 10%. Second, the deviation is highest in relation to Wiesche's values, at  $\Gamma = 1.17$  it is with almost 14% clearly above the differences in relation to the other cases, which can be attributed to the fact that Wiesche & Helcig [231] have not determined any increase in heat transfer in this range. This is probably due to the differences in the setup used by Wiesche & Helcig [231]. Third, the simulation continuously overestimates the heat transfer increase and the error tends to increase with increasing  $\Gamma$ . This is due to the fact that with increasing rotational velocity also the maximum velocities and thus the largest velocity gradients occur in the flow field. This results in small-scale patterns, which are not resolved by the URANS, but are taken into account to a certain extent in the LES carried out by Wiesche & Helcig [231] and Nguyen & Harmand [169]. In the experiments carried out by Latour et al. [132], these effects are

## 6.2 Influences of the cylindrical shaft on the flow and heat transfer



(a) Comparison of current URANS simulations of a smooth disc on meshes consisting of  $10^7$  elements with correlations found in literature.

(b) Relative error of the simulated ratios  $Nu_m/Nu_{m, \Omega=0}$  for the mesh with  $y^+ = 1.7$  to the given results in literature.

**Figure 6.3:** Evaluation of the simulation quality on the basis of comparison with values given by Latour et al. [132], Nguyen & Harmand [169], and Wiesche & Helcig [231]. (Simulation data was partly generated within the context of Matsche [S2])

considered automatically. Nevertheless, the overall deviation is acceptable, as the correlations between the two types of data given in literature show deviations of the same magnitude. Two main difference between the investigations of Wiesche & Helcig [231] and those of Latour et al. [132], Nguyen & Harmand [169] and the simulations carried out here are present. These are the absence of a cylindrical shaft and the significantly higher disc thickness in relation to the disc radius in the works of Wiesche & Helcig [231], which are very likely to contribute considerably to the observed deviations.

The comparison of the simulations with different grid point distributions and boundary layer resolution in figure 6.3 shows that the finer resolution does not lead to further quality improvement of the obtained results. The result obtained by the simulation with  $y_m^+ = 1.7$  deviates by 0.5% of that obtained with  $y_m^+ = 0.85$ . This result supports the assumption that the main deviation is generated by the modelling used and not by an insufficient resolution of the boundary layer. Also, the results in comparison with those from chapter 5 show that the disc thickness has a considerable influence. The thinner discs cause a change in flow separation at the upstream edge for both the rotating and the stationary discs. This structure, known as a separation bubble, has a

decisive influence on heat transfer [231], as can also be seen from the results presented.

Altogether, the arising deviations of the simulations are found to be acceptable. The same applies to the boundary layer resolution of the mesh with  $y_m^+ = 1.7$  in case of  $\Gamma = 4.66$ . For further investigations on the discs with dimples, meshes with this grid point distribution were therefore used. Since the velocity gradient in the boundary layer decreases at lower rotational velocities, the  $y^+$  value also decreases, which improves the boundary layer resolution in the cases of lower  $\Gamma$ . The deviations shown can therefore be considered as maximum occurring errors.

### 6.3 Thermal performance of dimpled discs

The most important parameter regarding the heat transfer increase due to dimples on the discs is the ratio of spatial and temporal mean Nusselt numbers  $\overline{Nu}_{m,d}/\overline{Nu}_{m,s}$  from dimpled disc  $\overline{Nu}_{m,d}$  to smooth disc  $\overline{Nu}_{m,s}$ . This ratio provides information about the heat transfer increase, which is essential for the intended functionality in many practical applications. Since this is associated with losses, the heat transfer and the flow losses of the different dimple configurations are evaluated and the thermal efficiency of the discs is examined more closely in this section.

#### 6.3.1 Heat transfer of rotating dimpled disc

Figure 6.4(a) shows the effectiveness of the individual setups in terms of increasing heat transfer. In all cases considered, heat transfer is increased by the use of dimples at all investigated operating points  $\Gamma$ , leading to values of  $\overline{Nu}_{m,d}/\overline{Nu}_{m,s} > 1$ . The improvement compared to the smooth disc increases with increasing rotational velocity. The positive influence of rotation on heat transfer, which has already been observed in the case of smooth discs, is thus further enhanced by the use of dimples.

The results of the different arrangements and dimple shapes shows that larger dimples with a diameter of 9 mm generally lead to higher heat transfer increases than dimples with 5 mm to 8 mm, reaching a maximum improvement of more than 13 % compared to the smooth disc. On average, the setups achieve increases of 3 % to 7.5 % percent over the range of  $Re$  considered. The setup R\_064\_D5-8 achieves the lowest and the setup P\_064\_D9 the highest

### 6.3 Thermal performance of dimpled discs

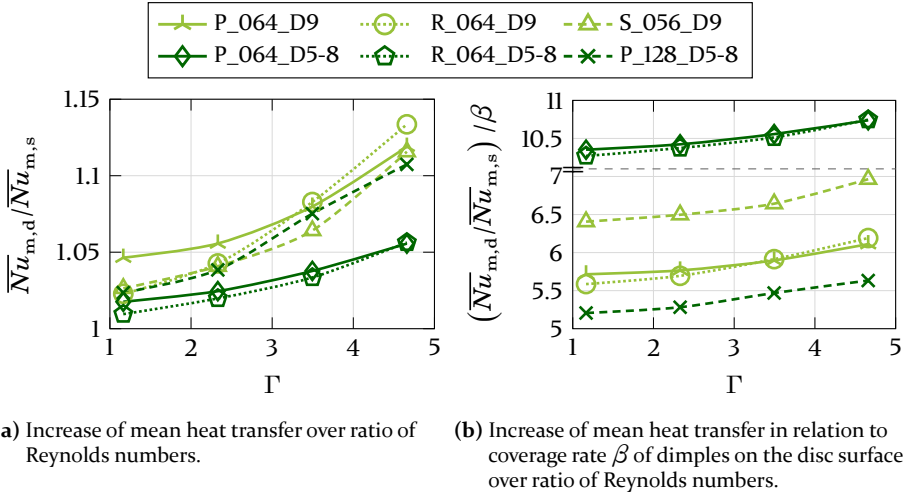


**Figure 6.4:** Mean ratios of Nusselt numbers for six different setups of dimpled disc as function of  $\Gamma$ . The range of 7.2 to 10.2 on the ordinate axis was excluded in (b) in favour of a more compact representation. (Simulation data was partly generated within the context of Matsche [S2])

average increase of  $Nu$ . With the same dimple shape and number, the patterned setups tend to perform better than the unstructured arrangements. It is noteworthy that the differences are higher at lower rotational velocities. Using the smaller dimples there is hardly any difference between patterned and random distribution at  $\Gamma = 4.66$ , as both increase the heat transfer rate by slightly more than 5.5%. For the larger dimples, the random distribution even exceeds the performance of the patterned distribution from  $\Gamma = 3.50$  on, though only by a maximum of 1.4 percentage points. The staggered setup of 56 dimples and the patterned setup of 128 dimples perform comparably over the entire range of rotational velocity, but reach slightly lower heat transfer rates than the setups with 64 large dimples. It turns out that the doubling from 64 to 128 dimples of different size leads to an improvement, which is small in the low rotational velocity range. From  $\Gamma = 2.33$  the difference is about 1.5 percentage points, at  $\Gamma = 3.50$  about 4 percentage points, and at  $\Gamma = 4.66$  over 5.1 percentage points. Thus, at higher numbers of revolutions the positive effect of the increased number of dimples becomes stronger.

These results show that higher heat transfer rates are possible with larger dimples, which agrees with the results found by Isaev et al. [96] and Samad et al. [194], who also found higher heat transfer increase for larger dimples in non-rotating channel flow. Furthermore, higher heat transfer rates occur with higher numbers of dimples. Both, larger dimples of equal number as

## 6 Thermal performance of rotating discs covered with spherical dimples

well as higher amounts of dimples of the same size, result in a higher coverage rate  $\beta$  of dimples on the disc surface. From this, the assumption can be derived, that the achieved heat transfer correlates not only with the rotational velocity but also with the coverage rate  $\beta$  of the discs with dimples.

To investigate such a correlation, figure 6.4(b) shows the heat transfer in relation to the coverage rate of the individual setups, as shown in table 6.1. The comparison clearly shows that the coverage rate is not a direct factor influencing the heat transfer. The setup with 128 Dimples exhibits the largest coverage rate  $\beta = 19.66\%$ . Since the heat transfer increase is not correspondingly high, however, the ratio  $(\overline{Nu}_{m,d}/\overline{Nu}_{m,s})/\beta$  of 5.2 to 5.6 is comparatively low. As the setup with 56 large dimples has similarly high heat transfer increases as the setups with 64 dimples of the same size, a satisfactory ratio of 6.4 to 7.0 results for this case. By far the highest values related to the coverage rate of of 10.2 to 10.7 are achieved by the setups with 64 small dimples.

Since the patterned setups of 64 dimples only differ in the size of dimples, and the setup with 128 dimples has a similar coverage rate as the setup with 64 large dimples, it becomes apparent that larger dimples have a clearly positive effect on the increase of heat transfer in the area of the centre of the disc. Furthermore, it can be seen that the staggered setup of 56 dimples in the low rotational velocity range behaves similar to the random setup of 64 dimples, whereas at higher  $\Gamma$  it behaves similar to the patterned setup. Due to the lower coverage rate, this setup achieves the highest relative heat transfer increases among the larger dimples, reaching up to 7.0 at  $\Gamma = 4.66$ .

Overall, the results show that neither the size of the dimples, nor the number, nor the total coverage rate exclusively explain the increase in heat transfer, even though the dimple size is found to be the most influential factor among these three. Furthermore, the radial position of the dimples on the disc considerably influences the heat transfer characteristic. Smooth discs exhibit varying heat flux characteristics over the radius, thus the effects of dimple distribution in radial dimension interact with these. This effect is additionally superimposed by the shape and position of the dimples in relation to each other, resulting in a highly complex mechanism of action influencing the heat transfer from the disc. In order to explore this mechanism, the heat flux on 100 equally spaced, concentric circular lines was examined for the considered setups. Each  $360^\circ$  line consists of 1000 measurement points from which the mean heat flux  $\overline{q}$  per circular line was calculated.

In the following figures 6.5, 6.8, 6.9 and 6.12 the values of mean heat flux of the different setups over the dimensionless radius  $r^*$  as given in equa-

tion (6.2) with the local radius  $r$ , the diameter of the cylindrical shaft  $D_c$  and the disc radius  $D_d/2$  are shown. The dimensionless radius  $r^*$  represents the radial position on the disc between the outer part of the cylindrical shaft where  $r^* = 0$  and the outer edge of the disc where  $r^* = 1$ . At the secondary ordinate axis, the heat flux is converted into the resulting Nusselt number  $Nu$ . When displaying the patterned arrangements, the positions and size of the dimples are additionally indicated in the following representations via error bars in direction of the abscissa axis. These positions correspond to four rows of dimples, whereby these rows are addressed in ascending numbering according to their respective position  $r^*$ .

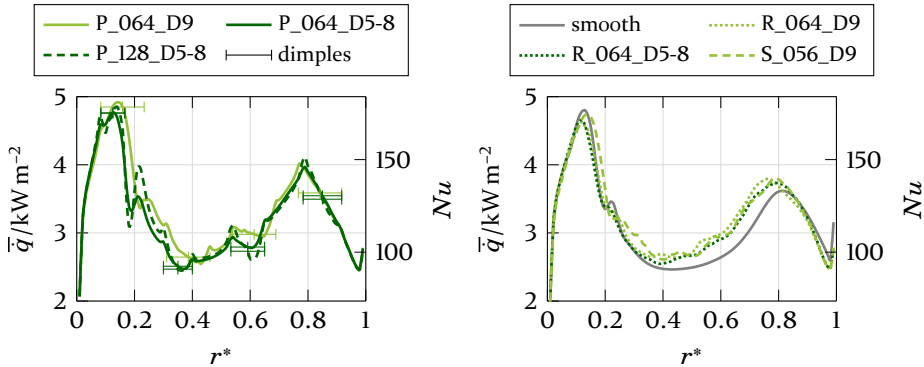
$$r^* = \left( \frac{r - \frac{D_c}{2}}{\frac{D_d}{2} - \frac{D_c}{2}} \right) = \left( \frac{2r - D_c}{D_d - D_c} \right) \quad (6.2)$$

### 6.3.2 Heat transfer characteristics below the critical rotational velocity

At  $\Gamma = 1.17$  the local effects of dimples are not relevant, but are masked by the global effects of the rotating disc. This can be seen in figure 6.5, that shows the heat flux densities averaged over time and space, along each circular line, for the patterned (a) as well as for the smooth disc, the random distributions, and the staggered distribution (b) at  $\Gamma = 1.17$ . Qualitatively and quantitatively the progressions of all graphs are very similar. In both sub-figures two distinct local maxima at about 15% and 80% of the dimensionless radius  $r^*$  are clearly visible. In the case of patterned arrangements, the radial position of the first dimples falls into this area. As these maxima also occur at random arrangements as well as for the smooth disc, the dimples themselves are not to be seen as the cause to this effect. This is also indicated by the fact that the second and third rows of dimples are positioned in the area of local minima of the heat flux density.

In comparison the smooth disc exhibits the lowest heat transfer in the range of  $r^* \approx 0.4$  to  $0.6$ . The local minimum at  $r^* \approx 0.35$  to  $0.45$  which can be observed at all setups results in the fact that at  $\Gamma = 1.17$  the rotational velocity and thus also the relative velocity between fluid and disc are comparatively low. In addition, the influence of the vortex upstream the cylindrical shaft can't be found within this area. With increasing  $r^*$  also the circumferential velocity  $u_r = \Omega \cdot r$  increases, whereby the shear stress  $\tau_w$  at the disc surface rises and thus, according to the Reynolds analogy, also the heat transfer increases. The maximum local heat transfer is reached at  $r^* \approx 0.8$ .

## 6 Thermal performance of rotating discs covered with spherical dimples



(a) Time-averaged heat flux density at  $\Gamma = 1.17$  of patterned setups. (b) Time-averaged heat flux density at  $\Gamma = 1.17$  of random setups, staggered setup and smooth disc.

**Figure 6.5:** Time-averaged heat flux density over 100 equidistant circular lines from cylindrical shaft to disc edge for  $\Gamma = 1.17$ . (Simulation data was partly generated within the context of Matsche [S2])

For  $r^* \gtrsim 0.8$  a decrease of mean heat flux  $\bar{q}$  can be observed. This is due to a separation bubble forming at the upstream edge as a result of the overflow, in which fluid of low mixing and low velocity circulates, as shown in figure 6.6(b), where vortex structures are visualised using the  $\lambda_2$ -criterion proposed by Jeong & Hussain [99]. This results in low temperature gradients and low shear stresses, which is why the heat transfer is moderate. The local, strong peak directly at the edge of the disc is partially due to the sharp edge of the model and can therefore be regarded as a singularity of the simulation, which would not occur in a real disc with a rounded edge.

The patterned setups in figure 6.5(a) show further, less pronounced local maxima on the sides of the first row of dimples that are not apparent with the random arrangements and are particularly pronounced at P\_128\_D5-8. For the staggered setup, corresponding fluctuations in the heat flux density can be detected, but due to the overlapping of the dimples rows in azimuthal direction these cannot be explicitly associated with dimples positions. Since an increased heat transfer is usually related to a higher relative velocity from fluid to disc or to a higher fluid mixing in the corresponding area, the local maxima at the sides of the dimples indicate that the local boundary layer influence due to the dimples leads to an increased mixing, which transports colder fluid near the dimples in the direction of the disc. This indicates vortex structures, which are caused by the dimples in combination with disc rotation and whose axis of revolution follows an azimuthal direction. The fact that

this effect is most pronounced at the innermost and thus first row of dimples indicates that these structures lose their identity at higher inertial forces due to higher relative velocity between fluid and disc. Another indication for this is that the effect is less pronounced or no longer detectable at higher disc rotational velocities, as will be shown later on.

Furthermore, a local maximum at about 20% of the radius can also be seen on the smooth disc in figure 6.5(b), the origin of which is explained in the following. Due to the temporal averaging as well as to the averaging of the values over  $360^\circ$  local and time-dependent effects may not be observed in the chosen representation. However, by considering the current heat flux density on the disc surface at any given time  $t$ , time- and location-dependent phenomena become observable. Due to the rotationally symmetrical geometry, a qualitatively similar situation is obtained at any point in time, allowing for the observation time to be arbitrarily chosen. Quantitative differences result from periodic effects such as the detachments in the wake of the cylindrical shaft as well as random, turbulent fluctuations. Figure 6.6(a) therefore shows the current  $Nu$  at a time  $t$  after reaching the pseudo-stationary state. This type of examination, which is widespread in the literature (e.g. [169, 228, 229]), clearly shows two half-moon-shaped areas of increased heat flux density on the side of the disc directed towards the inflow. The first of these areas is located shortly behind the edge of the disc and results from the separation of the flow at the sharp edge. As a result of the reattachment the heat flux density increases [231], as the turbulent mixing in this area is increased [132, 169].

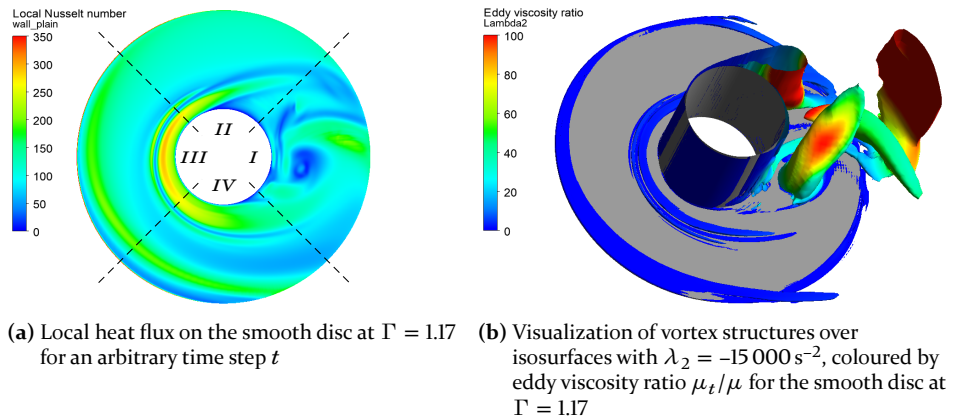


**Figure 6.6:** Snapshots of an arbitrary time  $t$  of local heat flux and arising flow structures around a smooth rotating disc. (Simulation data was partly generated within the context of Matsche [S2])

## 6 Thermal performance of rotating discs covered with spherical dimples

The second area is located just upstream of the cylindrical shaft. At the connection of disc and shaft the flow stagnates, resulting in reverse flow and the formation of a vortex [55], which separates from the disc behind the cylindrical shaft but is maintained in front of the shaft by the succeeding flow. This large-scaled vortex leads to a much smaller counter-rotating vortex, which is located further upstream and is still reasonably stable at the low rotational velocity considered. This vortex also causes an area of increased heat flux.

By averaging the heat flux over the entire circumference of the disc, the half moon-shaped areas lead to global maxima of heat flux density. These thus dominate the heat transfer and are only slightly modulated by the dimples. The smaller, counter-rotating vortex leads to the observed local maximum of  $Nu$  on the smooth disc. Since this maximum is located in the area of the first row of dimples of the patterned setups, the side effects of the dimples produce a similar structure, which amplifies the effect. In the case of the randomly arranged dimples, however, the irregular interaction of the dimples with the flow prevents the formation of a corresponding stable structure, which is why no local increase in heat transfer can be observed.

In general the dimples have a positive influence on heat transfer especially in the range  $r^* = 0.3$  to  $0.8$ . This is due to the fact that the surface structures disrupt the boundary layer even at low relative velocity and lead to increased momentum exchange perpendicular to the disc surface. The local influences of the dimples can be observed particularly well in the patterned setups. In addition to the previously discussed local peaks at the edges of the first row of dimples, this effect also occurs in a less pronounced manner at the edges of the second row of dimples. In the third row, the characteristic changes to the effect that the heat transfer is higher at smaller  $r^*$  and reaches a minimum between 50 % to 70 % of the dimple size before increasing again towards the dimple edge. To explain this phenomenon it has to be kept in mind that due to the rotation of the disc in combination with the constant cross-flow a very inhomogeneous flow pattern occurs in the immediate vicinity of a dimple over one revolution of the disc. This results in four distinct sectors: first, the chaotic wake behind the shaft (*I*); second, the sector of the highest relative velocity above the shaft (*II*); third, the cross-flow facing sector (*III*); and fourth, the sector of lowest relative velocity (*IV*). These sectors are included in figures 6.6(a) and 6.7(a).

The snapshot of the heat flux on the rotating disc with patterned dimples P\_064\_D9 in figure 6.7(a) shows the prevailing situation at dimples in each of these sectors. The resulting vortex structures are visualised in figure 6.7(b)

using the  $\lambda_2$ -criterion, the colour indicates the intensity of turbulent viscosity  $\mu_t$  compared to dynamic viscosity  $\mu$ . In the wake of the shaft in sector *I*, local heat flux is dominated by the large scale vortex structures due to flow detachment. As dimples move further into sector *II* due to rotation, a uniform and homogeneous heat flux profile over  $r^*$  occurs. The inhomogeneity over the azimuth is not visible in the averaging over the circumference. The direction of movement is opposite to the cross-flow direction in this area, which explains the low variations of heat flux density in the radial direction. In section *III*, the main direction of rotation is perpendicular to the cross-flow. The region of increased heat transfer at the rear of the dimple is thus shifted in the direction of the shaft due to the changed relative movement. When averaging the values over the circumference this leads to the observed increase of the dimple range closer to the shaft. In sector *IV*, the mean circumferential velocity of the third row of dimples at  $\Gamma = 1.17$  corresponds to about 85 % of the cross-flow velocity. The resulting relative velocity on the disc surface is equivalent to a cross-flow Reynolds number of  $Re_u \approx 5894$ , which results in lower wall shear stresses  $\tau_w$  and lower inertial effects relative to viscous effects. This leads to homogenization of the heat flux in this area and in turn the influence of dimples is less pronounced. Finally, the third row of dimples is located outside the already mentioned half-moon-shaped areas of increased heat flux density, whereby the rotational and cross-flow effects dominate in that radial area.

Altogether, the average heat transfer is homogeneous in the wake of the shaft over  $r^*$  due to the superposition of the occurring large-scale structures. Due to the alignment perpendicular to the inflow velocity, the heat flux is also homogeneous over  $r^*$  in the sectors of highest (*II*) and lowest (*IV*) relative velocity. Only in sector *III* the heat transfer gradient in radial direction is strongly influenced by the cross-flow. As the radial coordinate is aligned with the cross-flow the region of highest heat flux density is shifted towards the axis of rotation. This region is thus decisively responsible for the observed heat transfer characteristics of the third row of dimples.

Another remarkable characteristic occurs at the patterned arrangements in the fourth row of dimples. The local maximum of the heat flux density at  $r^* \approx 0.8$  is about 8 % higher than that of the randomly arranged setups and about 13 % higher than that of the smooth disc. In all patterned setups the local maximum is situated just behind the dimple edge facing the shaft of the fourth row. This inner edge of the dimples is located clearly within the range of the half-moon-shaped area of increased heat flux density facing towards the cross-flow. By this, the effects already observed in the third row are addi-

## 6 Thermal performance of rotating discs covered with spherical dimples

tionally amplified and the local maximum near the inner edge of the dimples becomes even more pronounced.

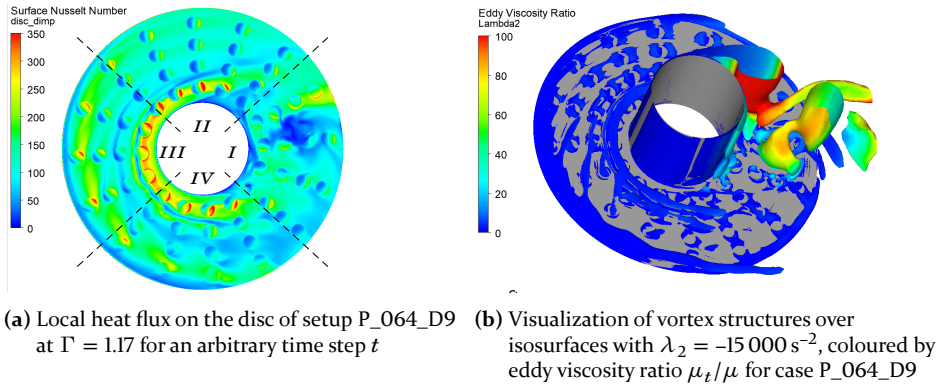


**Figure 6.7:** Snapshots of an arbitrary time  $t$  of local heat flux and arising flow structures around a rotating disc patterned with 64 dimples of diameter 9 mm. (Simulation data was partly generated within the context of Matsche [S2])

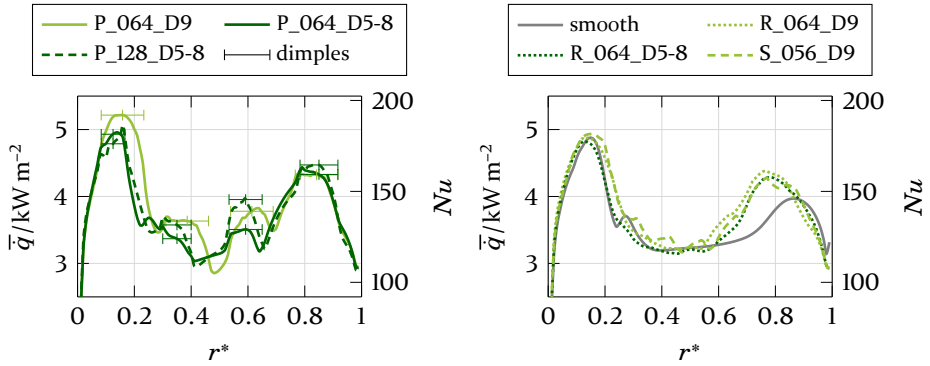
### 6.3.3 Thermal behaviour of rotating discs in the transitional region of rotational velocity

The influence of the rotational velocity on the heat transfer behaviour of rotating discs becomes apparent only when a local, critical threshold value of the rotational velocity in relation to the cross-flow velocity is exceeded. Wisesche & Helcig [231] describe this phenomenon for discs with a high ratio of thickness to diameter  $H_d/D_d = 0.06$ . When using dimples, a comparable phenomenon occurs, which depends on the actual distribution and geometry of the dimples on the disc. In this section, two rotational velocities are considered at which this transition point is located at about 25% and at about 60% of the dimensionless disc radius  $r^*$ .

#### Heat transfer characteristics at $\Gamma = 2.33$

The mean heat flux density at the disc surface for the different setups at  $\Gamma = 2.33$  depending on  $r^*$  is shown in figure 6.8. Similar to figure 6.5, figure 6.8(a) shows the patterned setups, figure 6.8(b) the other setups and the smooth disc. As in the case of  $\Gamma = 1.17$ , two areas of local heat flux increase are visible at  $r^* \approx 0.18$  and again at  $r^* \approx 0.8$ . The first area is thus located a little further away from the axis of rotation compared to the case of  $\Gamma = 1.17$  where this maximum occurred at  $r^* \approx 0.15$ . The second local maximum

covers a broader area and is thus less focused, especially for the patterned setups.



(a) Time-averaged heat flux density at  $\Gamma = 2.33$  of patterned setups. (b) Time-averaged heat flux density at  $\Gamma = 2.33$  of random setups, staggered setup and smooth disc.

**Figure 6.8:** Time-averaged heat flux density over 100 equidistant circular lines from cylindrical shaft to disc edge for  $\Gamma = 2.33$ . (Simulation data was partly generated within the context of Matsche [S2])

Local maxima at the second and third rows of dimples, which are more dominant than in the case of  $\Gamma = 1.17$ , are also prominent in figure 6.8(a). A detailed examination of the individual rows of dimples also shows that the heat flux density of the first row of dimples is increased, especially in the case of the dimples of diameter 9 mm, which is very similar to the behaviour at  $\Gamma = 1.17$ . However, the effect is much more evident at  $\Gamma = 2.33$ , where the maximum value lies 7% above the maximum value of the smooth disc. For the second row of dimples with  $D_i = 6$  mm, a local maximum at the dimple edge facing the axis is observable for both the cases with 64 and 128 dimples in total. The heat flux density drops towards the edge facing away from the axis. The smooth disc also shows a local maximum in this area, before the heat flux density decreases further with increasing  $r^*$ . This is due to the previously described large scale vortex arising in the area of the stagnation flow in front of the shaft. The smaller dimples of the second rows influence this effect only slightly. The situation is different with the larger dimples of  $D_i = 9$  mm. Here, a noticeable shift of the local maximum away from the axis can be observed, which clearly indicates a strong interaction of the dimples with the outer region of the large scale vortex. The increased value remains almost constant even beyond the centre of the dimples. After that, the heat flux density drops rapidly until beyond the outer dimple edge. The resulting local minimum lies about 11% below the value of the smooth disc.

## 6 Thermal performance of rotating discs covered with spherical dimples

In the third row, the two setups with dimples of  $D_i = 7$  mm show a qualitatively very similar behaviour. In both investigated setups the heat transfer increases strongly close to the dimples. Reaching the edge of the dimples, it increases moderately until the centre of the dimples, before it decreases rapidly towards the outer edge of the dimples. Quantitatively, the heat transfer of the setup with 128 dimples outperforms that of the setup using 64 dimples by 13%. The patterned setup with dimples of diameter  $D_i = 9$  mm shows a slightly different behaviour. Here the heat transfer increases strongly just before the dimples and continues to raise beyond the middle of the dimples. Then it drops to a local minimum in the area of the outer dimple edge. In terms of magnitude, the heat transfer lies between the two setups with smaller dimples. A pronounced interaction of the flow between the second and the third row of dimples is thus observed in the case of the  $D_i = 9$  mm, which is not observable with the corresponding 6 mm and 7 mm dimples, neither for the setup with 64 nor for the setup with 128 dimples. This clearly shows that the size of the dimples as well as the radial distance of the individual rows to each other influences the qualitative course of the heat transfer much stronger than the number of azimuthally successive dimples.

At the outermost row of dimples at  $\Gamma = 2.33$  there are no significant differences within the patterned setups. The dimples in this row have approximately the same size, 8 mm and 9 mm, respectively. The doubling from 64 to 128 dimples shows only a slight increase in heat transfer. The local maximum lies in all cases near the centre of the dimples. Additionally, a strong increase in heat transfer from the side of the axis of rotation is noticeable. It is remarkable, however, that the characteristic differs greatly from that of the smooth disc. Here, the general course of the heat flux density is considerably lower towards the outer edge of the disc. The local maximum lies at  $r^* \approx 0.86$ , which corresponds to the centre of the dimples. Nevertheless, the patterned setups exceed the heat transfer of the smooth disc in the range of this maximum by 9% to 13%.

From the shaft to  $r^* \approx 0.6$ , the setups investigated in figure 6.8(b) exhibit no noteworthy deviation from the smooth disc. Only the staggered setup shows some weakly pronounced minima and maxima, which can be assigned to the position of the dimples. However, the differences are much smaller than for the patterned setups due to the radial overlapping of the individual dimple rows. For  $r^* > 0.6$  the increase of heat transfer for the discs with dimples is much more pronounced than that of the smooth disc. The size as well as the number of dimples are of minor relevance here, which becomes obvious from the relatively similar courses of the different setups. This behaviour suggests

that with dimple arrangements that are not patterned, the local influence of the boundary layer on the disc is mainly decisive for increasing the heat transfer. Obviously, however, a minimum relative velocity between disc and fluid is required for this effect to take place.

Since the circumferential velocity increases linearly with the radius  $r$  and the rotational velocity  $\Omega$ , the ratio  $\gamma$  of the local rotational Reynolds number  $Re_{\Omega,1}$  formed with local circumferential velocity  $\Omega r$  instead of maximum circumferential velocity  $\Omega D_d/2$  as characteristic velocity  $U$  in equation (3.61) on page 36 to  $Re_u$  can be calculated directly from  $\gamma = 2\Gamma r/D_d$ . This value represents the dimensionless ratio of local circumferential velocity to cross-flow velocity. The critical value of this local ratio  $\gamma$  can therefore be calculated to  $\gamma \approx 1.7$ . Since  $\gamma = \Gamma$  applies for  $r = D_d/2$ ,  $\Gamma$  represents the maximum value that  $\gamma$  can reach. This explains the absence of a corresponding influence of the unstructured dimples at  $\Gamma = 1.17$ . The setups with dimples outperform the smooth disc by 8% to 10% in terms of maximum heat transfer at the outermost part of the disc.

To conclude, it becomes evident that the size of the dimples affects the heat transfer behaviour more than the number of dimples positioned one after the other, especially at low relative velocities. It is also evident that from a certain relative velocity onwards, the disturbance of the boundary layer by dimples - irrespective of the specific arrangement - is decisive for the increase in heat transfer. This effect is masked in the patterned setups due to the strong order of the dimples, but is clearly noticeable in the more homogeneous, random distributions and the staggered arrangement.

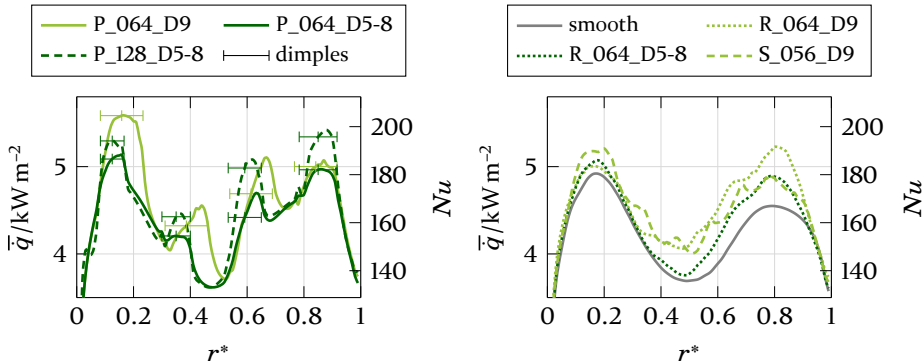
### Heat transfer characteristics at $\Gamma = 3.50$

As the ratio of azimuthal to cross-flow velocity increases, the influence of the dimples on the heat transfer behaviour of the disc increases as well. This is especially true for the patterned setups as shown in figure 6.9(a). Clearly pronounced local maxima in the area of the dimple rows arise at  $\Gamma = 3.50$ . The influence of the large scale flow structures due to the flow around the rotating disc is still evident at  $r^* \approx 0.15$  and  $r^* \approx 0.85$ . However, the dimples of the third row, i. e. at  $r^* \approx 0.6$  lead to increases in the heat flux of comparably high magnitude.

The patterned setup with large dimples, i. e. P\_064\_D9, shows, as at lower rotational velocities, the highest local heat flux density near the cylindrical shaft. The maximum lies 13% above that of the smooth disc and 9% above that of the setup with 64 dimples of smaller size. Similar to the lower rotational velocities, the local maximum for the setups with 64 dimples and for

## 6 Thermal performance of rotating discs covered with spherical dimples

the smooth disc is situated at  $r^* = 0.16$  to  $0.18$ . This shows that the position of the large scale vortex is not considerably influenced by the dimples. However, the size of the dimples is crucial in influencing the intensity of the heat transfer increase. The setup with 128 dimples shows a slightly different characteristic. Here the maximum of the heat flux density lies exactly in the centre of the first dimples row at  $r^* = 0.12$ . Nevertheless, this setup also exhibits a distinct secondary maximum at  $r^* = 0.17$  which matches the location of the outer edge of the first row of dimples. This shows that the influence of the large scale vortex is still present in this setup. In addition, the increased number of dimples causes an increase in the heat flux density in this area. Since in the patterned setup with dimples of the size  $D_i = 9$  mm the centre of the dimples of the first row corresponds to the position of the macroscopic vortex, the influence of the position of the dimples cannot be separated from the influence of the vortex itself. Due to the pronounced increase in heat transfer as a result of this setup, the combination of position, size and number of dimples can nevertheless be identified as an influential criterion for heat transfer behaviour.



(a) Time-averaged heat flux density at  $\Gamma = 3.50$  of patterned setups. (b) Time-averaged heat flux density at  $\Gamma = 3.50$  of random setups, staggered setup and smooth disc.

**Figure 6.9:** Time-averaged heat flux density over 100 equidistant circular lines from cylindrical shaft to disc edge for  $\Gamma = 3.50$ . (Simulation data was partly generated within the context of Matsche [S2])

The second row of dimples, as before at lower rotational velocities, provokes an increase in heat transfer compared to the smooth disc. However, at  $\Gamma = 3.50$  the effect is much more pronounced than for  $\Gamma = 2.33$  and  $\Gamma = 1.17$ . The effect is smallest at the setup with 64 smaller dimples. Here, the maximum heat flux density exceeds that of the smooth disc at the same radial position by only 2%. In the case of 128 dimples, this maximum is about 12% higher. The

effect is strongest with the larger dimples. The local maximum of the heat flux in this setup is approximately in the radial range of the local minimum of the smooth disc. This qualitative observation suggests that the dimples have a strong influence on the heat transfer behaviour of the discs. In quantitative terms, this results in an increase of almost 22%. The inner dimple edges of the dimples with  $D_i = 6$  mm are located at  $r^* = 0.3$ . This results in a local velocity ratio of  $\gamma = 2.2$ , which is above the previously determined threshold value of  $\gamma \approx 1.7$ . The considerable increase of the heat transfer of the dimples of the second row thus confirms the finding of this threshold.

In the third row, twice the number of smaller dimples results in approximately the same increase in heat transfer as half the number of larger dimples. Due to the slightly different radial position of the centres, the maximum of 128 dimples is shifted slightly further in the direction of the axis of rotation. In the case of 64 smaller dimples, a distinct local maximum is also formed. Due to the larger proportion of the disc surface without dimples in this case compared to the setup with 128 dimples, the maximum is shifted a little further towards the disc edge. In all three cases the effect of the heat transfer increase in this area that can be observed at the smooth disc is amplified by the dimples.

In the outermost row of dimples, the effect of the number of consecutive dimples is emphasized even more due to the higher velocity ratio  $\gamma$  in this area. The differences in size of the dimples are small with  $D_i = 8$  mm and  $D_i = 9$  mm, but due to the large radius  $r^*$ , the density of dimples for the setups is much lower with only 64 dimples. Thus the effects of the dimples are less pronounced in relation to the effects of rotation, as they occur similarly on the smooth disc. As a result, the heat transfer increase is most pronounced for the case with 128 dimples. The local maximum outperforms that of the smooth disc by 19%. Both setups with 64 dimples show a very similar behaviour. They outperform the smooth disc by about 10% at the maximum.

Two facts become apparent from the observed behaviour. First, the dimples investigated here have no global influence on the flow field, the influence in radial direction is locally limited to the immediate vicinity of the dimples. Second, it becomes clear that in the inner area of the disc, the size of the dimples has a noteworthy influence on the increase in heat transfer, whereas with increasing velocity ratio  $\gamma$  the number of consecutive dimples becomes decisive.

## 6 Thermal performance of rotating discs covered with spherical dimples

The unstructured setups in figure 6.9(b) all increase the heat transfer compared to the smooth disc. In contrast to the lower rotational velocities, the effect can already be seen at smaller disc radii. The threshold value of  $\gamma = 1.7$  is reached at  $r^* \approx 0.24$ . Nevertheless, the setup of randomly distributed smaller dimples shows hardly any considerable improvement compared to the smooth disc up to about  $r^* = 0.5$ . This is caused by the small number of larger dimples in the inner area of the disc. Due to the spherical shape of the dimples, the average depth over the respective disc radius can be used as a measure for the local dimple density. The disc surface lies at  $z_d = 0$ , for visualization purposes indentations are shown as positive values of  $z_d$ . The average depth is made dimensionless with the length of the corresponding circular ring  $l = 2\pi r^*$ . As a result, the mean depth is weighted with the corresponding proportion of the smooth disc as shown in figure 6.10.

When considering the unstructured setups in figure 6.10(b), it can be seen that the setup with randomly distributed, small dimples exhibits considerably lower maximum values than the other setups, especially near the cylindrical shaft. Thus the behaviour of the smooth disc dominates in this area compared to the other setups. The number and size of the dimples in this area is thus not sufficient to disturb the boundary layer over the entire circumference severely enough to ensure noticeable increases in heat transfer. This shows that not only the local, dimensionless rotational velocity  $\gamma$  is decisive for increasing the heat transfer. There is also a threshold value for the strength of the disturbance of the flow, which must occur in combination with  $\gamma > 1.7$  to cause an increase in heat transfer compared to the smooth disc.

The correlation analyses shown in figure 6.11 confirm this assumption. The diagram shows the values and the absolute maximum values of the root mean square correlation coefficient  $R_c$ , denoted as  $R_{\text{RMS}}$  and  $R_{\text{max}}$ , respectively. They are calculated for the correlation of the heat transfer increase of the different setups  $\bar{q}_d/\bar{q}_s$  with different orders  $b_1$  and  $b_2$  of  $(z_d/l)^{b_1}\gamma^{b_2}$ . Here,  $\bar{q}_d$  stands for the temporal mean value of heat flux of a disc with dimples,  $\bar{q}_s$  stands for the temporal mean value of heat flux of the smooth disc. Three points become apparent here. First, as expected  $\gamma$  by its own is not suited to explain the increase of heat transfer as the resulting correlation of  $\gamma$  and  $\bar{q}_d/\bar{q}_s$  is low. Second, the heat transfer correlates much better with the dimensionless portion of dimpled area per circle segment  $z_d/l$ . Third, the strongest correlation is shown for  $z_d/l \cdot \gamma^2$ , which slightly increases with  $\Gamma$  up to  $\Gamma = 3.50$  and exceeds the linear combination of correlation of both values separately. This confirms the assumption that there is a threshold for

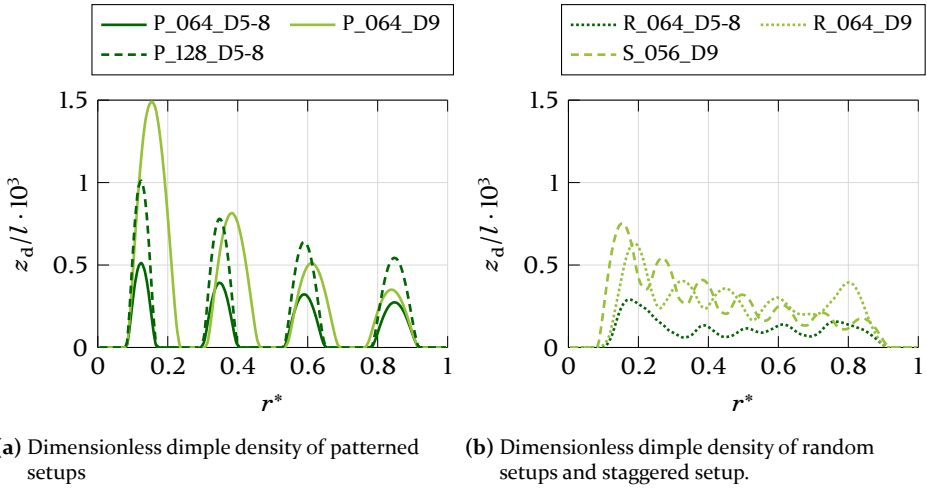


**Figure 6.10:** Relative average depth of dimples divided by local circumferential length.

$\gamma$  at which the effects start to occur, comparable to the transition to turbulent flow when a threshold of  $Re$  is exceeded.

As this threshold value was determined in the range of  $\gamma \approx 1.7$  at  $\Gamma = 2.33$ , figures 6.11(c) and 6.11(d) show the correlation coefficients only for the ranges  $\gamma > 1.7$ . Since at the lowest examined rotational velocity of the discs this value is not reached even at the outer edge of the disc, no corresponding values exist for  $\Gamma = 1.17$ . In addition to the strong correlation of  $z_d/l \cdot \gamma^2$  already found, the correlation of the heat transfer increase with the mean dimensionless dimple depth  $z_d/l$  is of particular interest in this examination, as a correlation would strongly support the hypothesis of a necessary threshold value  $\gamma > 1.7$  in order to increase the heat transfer. Especially in the case of  $\Gamma = 2.33$ , where  $\gamma = 1.7$  is reached at  $r^* \approx 0.6$ , the correlation is clearly increased with all considered conditions. The dimensionless dimple depth seems to be dominant here, with a maximum value of  $R_{\max} \approx 0.8$ . Also for  $\Gamma = 3.50$  the correlation increases noticeably, which supports the hypothesis of the threshold value. In the case of  $\Gamma = 4.66$ , the transition point lies at  $r^* \approx 0.07$ , which means that almost the entire disc exhibits values of  $\gamma > 1.7$ . Consequently, the comparatively high levels of correlation shown in figures 6.11(a) and 6.11(b) are not further increased considerably.

However, it can be seen that especially for the dimple depth  $z_d/l$  the correlation for the condition  $\gamma > 1.7$  is considerably better than for the entire disc. Nevertheless, the correlation does not reach unity for any of the combinations of  $(z_d/l)^{b_1} \cdot \gamma^{b_2}$  studied, which suggests that other parameters do also

6 Thermal performance of rotating discs covered with spherical dimples

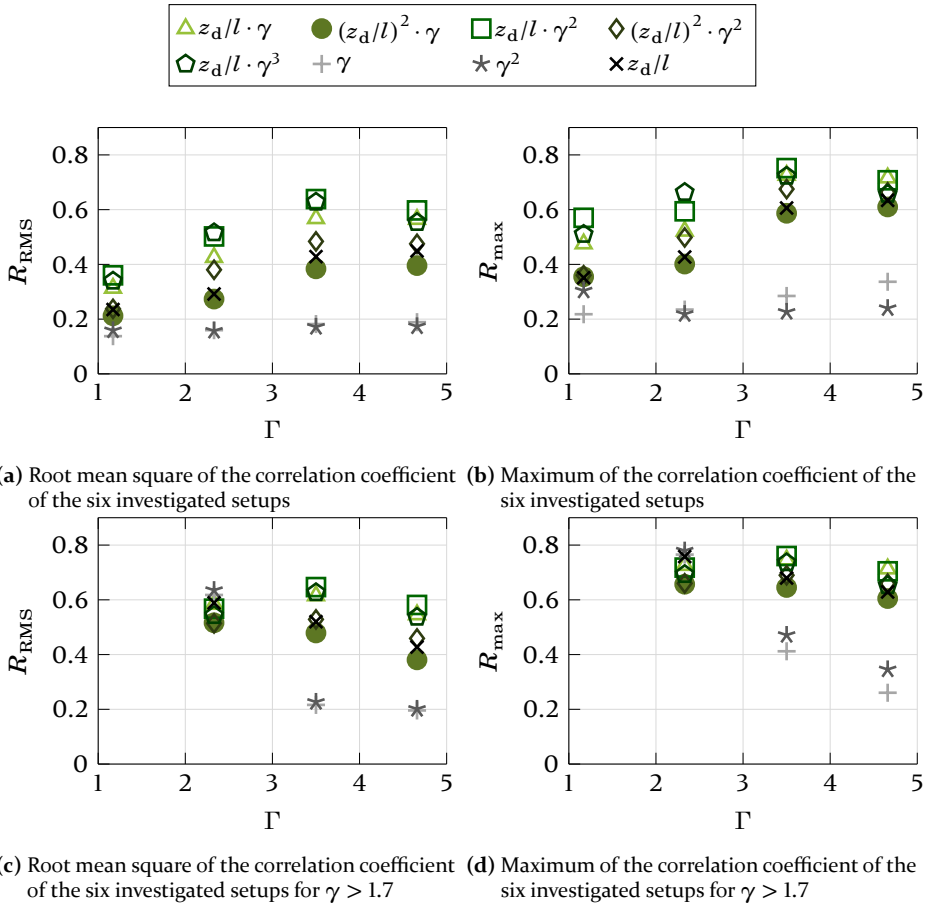


**Figure 6.11:** Correlation of the heat transfer increase of dimpled setups compared to the smooth disc with combinations of different order of the product of relative, average dimple depth  $z_d/l$  and local, dimensionless rotational velocity  $\gamma$ .

influence the heat transfer increase. It is very likely that the distribution of dimples in azimuthal position is one of them. Across all setups and rotational velocities, the disc with 128 patterned dimples shows the highest correlation values. In this setup, the average distances between the dimples in azimuthal direction are the smallest and moreover uniform. This is not taken into account when considering the average dimple depth  $z_d/l$ . Thus, in order to increase heat transfer efficiently, in addition to the depth and radial position, the azimuthal distance and the local rotational velocity in relation to the inflow velocity are likely to be of mentionable importance.

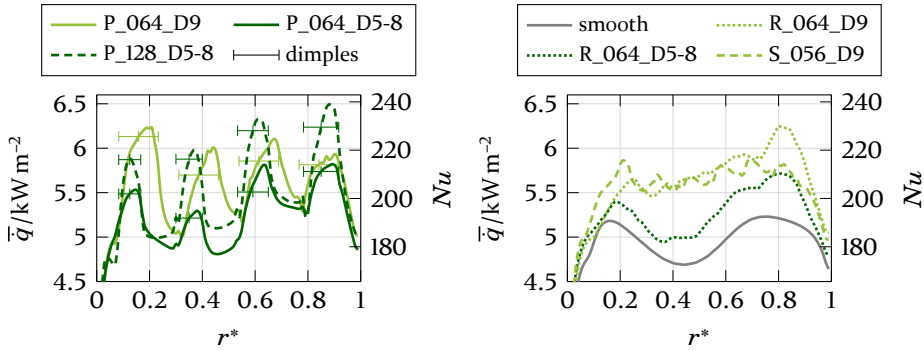
### 6.3.4 Heat transfer characteristics at high rotational numbers

At  $\Gamma = 4.66$ , both the characteristics and the magnitude of heat transfer are dominated by the dimples. In the patterned setups from figure 6.1 (a), (d), and (f) the original heat transfer characteristic of the smooth disc is no longer visible as the influence of the individual rows of dimples masks it for all setups as shown in figure 6.12(a). With 20 %, the increase in heat transfer is again strongest for dimples with a diameter of  $D_1 = 9$  mm. The setups with smaller dimples lead to increases of 13 % and about 7 % for 128 and 64 dimples, respectively.

It is noticeable that in the case of the 128 smaller dimples, the local maximum of heat transfer occurs at the centre of the dimples, whereas in the cases with 64 dimples it is shifted further towards the outer edge of the disc. Due to the high rotational velocity, considerable centrifugal forces are already present on the disc surface at the comparatively small disc radius  $r^*$  of the first row of dimples. The resulting acceleration of the fluid outwards of the axis of rotation leads to zones of increased heat transfer in the wake of the dimples, which are not located exactly azimuthally behind the dimples but are shifted radially outwards. As the areas behind the dimples are smooth in the case of setups with 64 dimples, these structures are clearly visible. For the setup with 128 dimples, the azimuthal distances between the dimples are smaller, which prevents the formation of corresponding zones of increased heat transfer in the wake of dimples. Inside the dimples, the zone of highest heat transfer is located in the middle of the downstream part of the dimples, resulting in the local maximum being located at the height of the dimple centres.

The dimples of the second row exhibit comparable characteristics regardless of their number and size. The local maximum for all three setups lies outside the centreline of the dimples. The reason for this is the combination of a further increased rotational velocity and the increased distance between the dimples in azimuthal direction. As a result, a pronounced, radially outwardly deflected wake area is formed on the smooth part of the disc even for the setup with 128 dimples, in which the heat transfer is increased. However, there is a remarkable difference in the behaviour of the setups among one another. The local maximum of heat transfer of the second row in the case of the setups with 64 dimples is below the maximum of the first row. This behaviour was observed for all setups at lower rotational velocities. The reason for this was the dominance of the large scale vortex in the shaft area. However, the setup with 128 dimples shows a higher heat transfer in the second

## 6 Thermal performance of rotating discs covered with spherical dimples



(a) Time-averaged heat flux density at  $\Gamma = 4.66$  of patterned setups. (b) Time-averaged heat flux density at  $\Gamma = 4.66$  of random setups, staggered setup and smooth disc.

**Figure 6.12:** Time-averaged heat flux density over 100 equidistant circular lines from cylindrical shaft to disc edge for  $\Gamma = 4.66$ . (Simulation data was partly generated within the context of Matsche [S2])

row. This demonstrates that in this case the influence of the large scale vortex already falls behind the influence of the surface structures.

The setups with 128 small and 64 large dimples cause approximately the same maximum heat transfer rate in the second row of dimples, which is 13 % higher than that of the setup with 64 small dimples. The smooth disc exhibits again a local decrease of heat transfer in this area, which causes the relative increase of heat transfer for all setups to be over 11 %. For the setup with 64 large dimples, the position of the local maximum of the second row lies at  $r^* = 0.44$ , which corresponds exactly to the position of the local minimum of the smooth disc. Thus this setup causes a relative increase in heat transfer of 28 %. In addition, this observation emphasizes that the characteristics of the smooth disc with respect to heat transfer at high rotational velocities can be modified tremendously by the use of dimples.

However, the influence of the dimples is still spatially limited, as can be shown by examining the area between the second and third row of smaller dimples. The local minimum of the smooth disc is located in this area. In both setups, with 64 and 128 dimples, a pronounced decrease of the heat transfer can be observed. The radial positions of the local minima are approximately the same as for the smooth disc. With less than 8.8 % with 128 dimples and 2.5 % with 64 dimples the heat transfer in these areas is hardly increased.

In the third and fourth row, the higher number of dimples exhibits the most pronounced influence on the heat transfer behaviour due to the high relative

velocity. In the setups with 64 dimples, no further increase in heat transfer can be observed in the outermost row compared to the third row of dimples. In the case of the dimples of diameter  $D_1 = 9$  mm, even a slight decrease of the maximum heat transfer can be observed. It is noteworthy that pronounced local maxima occur at the inner edges of the dimples. These indicate vortices that form at the examined range of rotational velocity and increase the heat transfer locally in a considerable extent.

With 13% increase, the variant with 64 larger dimples shows the highest mean heat transfer increase of the non-structured setups in figure 6.12(b). It also exhibits the highest local heat transfer increase, located at  $r^* \approx 0.8$  reaching more than 19%. The setup with 64 smaller dimples shows an almost uniform heat transfer increase over the entire disc radius, leading to an average increase of just below 6%. The setup with the staggered dimples is associated with a considerable increase of more than 12% as well as an almost constantly distributed heat transfer over the entire disc radius. The characteristic of the smooth disc is no longer visible. The local maxima at the inner edges of the dimples, which had already been noticeable in the patterned setups, are also visible and contribute to an additional homogenization of the heat transfer.

Overall, the examination of the heat transfer of discs with dimples shows that the influence of the dimples depends strongly on the ratio of Reynolds numbers  $\Gamma = Re_\Omega / Re_u$  as well as on the position, size and arrangement of the dimples themselves. At low rotational velocities, the influence of the dimples - regardless of their size and position - is low while the behaviour of the smooth disc dominates the heat transfer characteristic. A positive influence on the heat transfer is primarily possible with large dimples close to the cylindrical shaft. In general, the influence of the dimples does not influence the global heat transfer behaviour but is locally limited. Even at high rotational numbers, the smooth areas of the discs with dimples behave very similar to the corresponding smooth disc. Due to this, a homogeneous heat transfer over the entire surface of the disc is possible by an even and circumferentially overlapping distribution of larger dimples. To achieve this, it is also necessary to position the dimples in such a way that as the radius of the disc increases, the uniform density of dimples decreases in inverse proportion to the radius.

### 6.3.5 Thermal efficiency of the discs

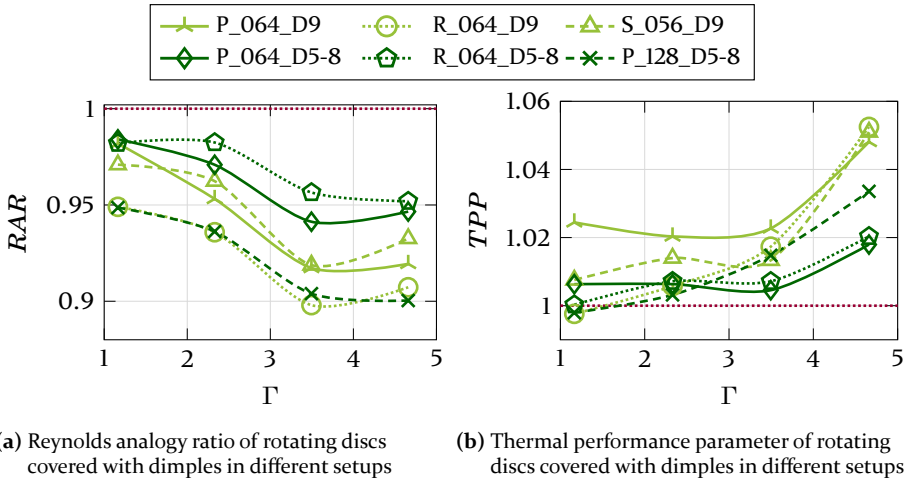
In addition to the mere effectiveness of the dimples regarding increase of heat transfer, their actual efficiency is also important for the evaluation of performance. Due to the increased momentum transfer perpendicular to the disc surface as a result of the dimples, the drag of the disc also increases besides the heat transfer.

Figure 6.13(a) shows the Reynolds analogy factor  $RAR$  as given in equation (3.69) on page 38 for the different examined setups over  $\Gamma$ . In all cases, the value tends to decrease with increasing rotational velocity. In this case an increasing rotational velocity is always accompanied by a rise of the moment coefficient  $c_M$ . Thus, this result is consistent with the well-known phenomenon that  $RAR$  decreases with increasing loss coefficient and thus in general with increasing  $Re$ . This behaviour has been observed in square channels with all kinds of turbulators [144] as well as in round tubes roughened with dimples [138]. As mentioned in section 3.5, this merely indicates that  $Nu$  increases slower than  $c_M$  as  $Re$  increases. It can be seen that the Reynolds analogy has the best validity over the considered operating point range for the setup with 64 small, randomly distributed dimples, reaching values over 95%. The second highest values are achieved by the setup with the identical dimples, positioned in a patterned manner. These setups showed consistently low heat transfer increases and thus behaved similar to the smooth disc. The high  $RAR$  values show that  $c_M$  also increases only moderately. With 89% to 95% the setups with 64 large, randomly distributed and 128 patterned dimples show the lowest values. These setups achieved large increases in heat transfer. This shows that the increase in heat transfer is always accompanied by increased drag. In addition,  $c_M$  increases stronger than  $Nu$ , so  $RAR$  decreases with increasing heat transfer.

To consider the actual thermal efficiency of the individual setups, the thermal performance parameter  $TPP$  as given in equation (3.70) on page 38 is shown in figure 6.13(b). Here, a different characteristic compared to  $RAR$  is evident. The values tend to increase for all setups with increasing rotational velocity. Furthermore, most values are greater than unity, which means that the investigated setups are reasonable from an energetic point of view at the considered operating points in addition to their mere ability to increase heat transfer.

Overall, the use of setups with larger dimples leads to favourable values. In a direct comparison of the setups with 64 dimples positioned in a patterned manner, a similar qualitative progression of  $TPP$  over  $\Gamma$  can be observed for both dimple sizes used. However, the setup with larger dimples constantly

## 6.4 Guidelines for creating application-specific dimple setups



**Figure 6.13:** Thermal performance parameter of the investigated setups. Red line indicates unity for better readability. (Simulation data was partly generated within the context of Matsche [S2])

lies 1.4 to 3 percentage points above that using smaller dimples. Over the observed rotational velocity range, the setup with 56 dimples is generally more efficient than the setup with 128 dimples. The setups with 64 small dimples achieve the lowest performance overall. All setups achieve the highest efficiency at  $\Gamma = 4.66$ . All arrangements using larger dimples achieve a  $TPP$  of about 1.05 at this operating point. Higher values might be achieved with deeper dimples on thicker discs as well as with optimised arrangements.

## 6.4 Guidelines for creating application-specific dimple setups

From the setups and operating points investigated, general rules can be derived which are applicable to the design of heat transfer optimisation of rotating discs. First of all, it should be noted that all investigated setups increased the heat transfer. With a higher rotation ratio  $\Gamma$ , the positive effect of the dimples on heat transfer also increases. From an energetic point of view, all setups are efficient for  $\Gamma \geq 2.33$ . Due to the diversity of considered setups with respect to the distribution of dimples, it is therefore unlikely to find thermally inefficient setups of corresponding dimples in the considered range of coverage rate  $9.8\% < \beta < 19.7\%$ . However, the coverage rate with dimples is not a suitable design parameter for heat transfer increase. Instead,

## 6 Thermal performance of rotating discs covered with spherical dimples

the investigations showed that the combination of dimple size and position together with local rotation ratio is crucial to modulate heat transfer.

The results revealed that the highest correlation values of heat transfer exist with the combination of relative dimple depth  $z_d/l$  with the square of the local rotation number  $\gamma^2$ . This correlation is particularly significant for  $\gamma > 1.7$ . For a design of a defined operating point and thus given ratio  $\Gamma = Re_\Omega/Re_u$ , the desired distribution of the heat flux  $\bar{q}$  can thus be approximated via the relation  $z_d/l \cdot \gamma^2$ . The local rotation ratio  $\gamma$  as well as the circumferential length  $l$  are linear over the radius of the disc. Thus, the dimple depth  $z_d$  can be determined for each radius  $r$  of the disc via the ratio  $\bar{q}/(r\Omega^2)$ .

For a homogeneous distribution of the heat flux over the radius of the disc, a higher concentration of dimples in the area of the cylindrical shaft and a lower dimple density in the outer area of the disc are the result. The setup S\_056\_D9 exhibits a similar distribution, as can be seen in figure 6.10(b). In fact, this setup leads to a homogenisation of the heat flux  $\bar{q}$  over the radius of the disc at high rotational velocities  $\Omega$ , where  $\gamma > 1.7$  is valid on a large part of the disc. This behaviour can be observed in figure 6.12(b), underlining the adequacy of the design rule.

# Conclusion

Efficient heat transfer in rotating systems defines the performance limit and the highest, technically feasible efficiency in many applications nowadays. These include gas turbines and electric motors, for example. While dimples are already used in the field of gas turbines to increase the cooling efficiency in the blade channel, there is still no widespread application despite the existing potential in other areas. One reason for this is that both the mechanisms of action of the dimples themselves and the specific effects in rotating systems have not yet been sufficiently explored. Therefore, the motivation for this work, in addition to expanding the physical understanding of the flow around dimples, was to investigate the influences on a simplified, rotating system. Through this consideration, design rules could be derived in a defined initial system for modulating the heat transfer of rotating discs.

## Methodology

Research into the physical processes on dimples was carried out with regard to the mechanisms of action of drag reduction on overflowed plates. Literature values of van Nesselrooij et al. [168] and Mahmood & Ligrani [151] served as reference values to prove the validity of the simulations. For the study of the increase in heat transfer, investigations were carried out on the flow through channels. The data was validated with and compared to data given by Mahmood & Ligrani [151] and Sato et al. [196]. Due to the high influence of comparatively small geometric changes, special attention was paid to the sufficient spatial and temporal resolution of the simulations.

For the original investigations of the effects of dimples on rotating discs, no published reference values exist. Therefore, the simulations were validated using smooth discs with data of Latour et al. [132], Nguyen & Harmand [169], and Wiesche & Helcig [231]. Simulations with non-interacting spherical and teardrop-shaped dimples were used to evaluate the influence of rotation on the effects at the dimples. The complex interaction of the flow around dimple arrangements was investigated in six setups, which were designed to reveal the differences in the arrangement of the dimples on the disc and the influence of the coverage rate.

### Physical effects in non-rotating systems

The effects of the drag reduction show a strong dependence on Reynolds number  $Re$  as well as the concrete geometric design of the dimple setups. This is due to the influence of streaks near the surface, which can be modulated and thus stabilised by the dimples under certain circumstances. However, this requires precise coordination of the geometric arrangement and the operating condition. A deviation leads to a negative influence on the flow structures, whereby the positive effect of drag reduction turns into drag increase. For dimple depths of  $h/D_i \gtrsim 6\%$  the generated pressure drag becomes dominant, whereby drag reductions in the investigated range of  $Re$  can no longer be achieved. In addition, the influences of individual parameters are not linear and cannot be extrapolated. The data clearly show that seemingly contradictory results in literature regarding the effectiveness of dimples for drag reduction can be attributed to the mentioned, small differences in setups and operating points of the different studies.

While deeper dimples are known to result in higher heat transfer gains, the actual thermal efficiency of a defined setup is not robust to operating point changes. Likewise, the influences of geometric parameters cannot be interpolated linearly. The results show that smaller dimples lead to higher average wall shear stresses, indicating that the boundary layer is globally influenced despite the local nature of the dimples. However, this influence is superimposed by the local influences, resulting in a complex interaction of different effects, making interpolation or extrapolation prone to considerable errors.

### Shape of dimples on rotating discs

The advantages of teardrop-shaped dimples in non-rotating setups do not come into play on rotating discs. In ducts, the relative flow of the dimples does not change over time. Compared to spherical dimples, the teardrop shape causes the flow to enter the dimples more gradually. This minimises losses, while the heat transfer remains comparable to that of spherical dimples due to the shape of the trailing edge.

In the rotating system, the relative inflow depends on the current position of the disc. This means that the advantages of the modified inlet and outlet of the flow at the dimples do not act. Due to the rotational symmetry, spherical dimples are more robust against changes in the incoming flow and therefore provide more advantageous results overall. Optimising the geometry of the dimples on rotating discs would therefore only be possible to a very limited extent for a defined operating point.

## **Influence of individual parameters on the effects of interacting dimples**

The investigation of size, number and arrangement of spherical dimples on discs showed a clear dependence of the influences on the respective operating condition. The influence of the dimples tends to increase with increasing rotational numbers, while the pure effects of the rotating disc dominate at lower rotational numbers. The results show that the size of the dimples and the radial spacing of individual rows of dimples have a stronger influence on the qualitative course of heat transfer than the number of azimuthally consecutive dimples. For local rotation numbers above  $\gamma \approx 1.7$ , in the case of unstructured arrangements of the dimples on the disc, the local influence of the boundary layer is decisive for heat transfer increases. A detailed examination of the distribution of the relative depth of the dimples along the radius shows that larger dimples closer to the rotation axis lead to higher heat transfer rates. This is due to the interaction of the dimples in this area with the stagnation flow in front of the cylindrical shaft.

Overall, up to very high rotation numbers, the effects of the dimples were found to act rather locally. From this it follows that a uniform heat transfer increase on rotating discs can be achieved by radially and azimuthally overlapping rows of dimples. The size of the dimples needs to be adapted to the radial position in such a way that the resulting effective depth of the dimples is inversely proportional to the radius. With regard to the thermal efficiency, increases of up to 5% could be achieved in the investigated rotation number range. A clear positive correlation between efficiency and rotation number was found, especially for the setups with larger dimples.

### **Outlook**

As part of the work, a design-rule was developed with the help of which it is possible to specifically influence the heat transfer behaviour of rotating discs by the placement of dimples. This design rule states that for local rotation numbers  $\gamma > 1.7$  the heat flux  $\dot{q}$  is approximately proportional to  $\gamma^2$  multiplied by the relative dimple depth  $z_d/l$ . This can be used to investigate different scenarios regarding the increase in heat transfer. Based on the investigated setups, the rule is valid for  $1.17 \leq \Gamma \leq 4.66$  for discs and dimples corresponding to the investigated proportions. Extrapolation to other relative dimple sizes has not been tested.

Extending the range of validity by varying the dimples geometry in terms of diameter, depth and resulting arrangement is the next logical step in the research. Additionally, in the investigations of heat transfer enhancement,

## 7 Conclusion

the greatest correlation was shown with the relative dimples depth in the radial direction  $z_d/l$  and the square of the local rotation number  $\gamma^2$ . Although the correlation is clear, it is likely that other parameters such as the relative dimples depth in the azimuthal direction have an influence on the heat transfer behaviour. Detailed investigations of such influences could further refine the model and lead to even better predictive power.

Increasing the heat transfer while minimising the drag increase is an optimisation problem with opposing optimisation objectives. Automatic optimisation methods such as the conjugate gradient method can be used in this context. In fluid mechanics, artificial intelligence methods are also being used more and more frequently due to broader availability of data, which can also be used in the future to further increase the efficiency of dimple setups on rotating discs.

Exclusively numerical investigations were carried out in this work. Due to the ensured simulation quality, these provide detailed, spatially highly resolved information about the entire flow field. Geometric variations can also be implemented well in the model. However, different operating points of a setup require separate simulations, which increases the numerical effort. In this case, experiments on selected geometries would be a suitable means of obtaining a wide range of data on the behaviour of certain setups over different operating points. Significantly longer measurement durations can also be implemented considerably faster than in numerical high-resolution simulations.

# Zusammenfassung

Effiziente Wärmeübertragung in rotierenden Systemen definiert heute in vielen Anwendungen die Leistungsgrenze und den höchsten, technisch realisierbaren Wirkungsgrad. Hierzu zählen beispielsweise Gasturbinen sowie Elektromotoren. Während Dimpel im Bereich der Gasturbinen bereits zur effizienten Kühlung im Schaufelkanal eingesetzt werden, gibt es in anderen Bereichen trotz des vorhandenen Potenzials noch keine breite Anwendung dieser Technologie. Ein Grund hierfür ist, dass sowohl die Wirkmechanismen der Dimpel an sich als auch die spezifischen Effekte in rotierenden Systemen noch nicht ausreichend erforscht sind. Die Motivation für diese Arbeit war daher, neben der Erweiterung des physikalischen Verständnisses der Umströmung von Dimpeln, die Einflüsse dieser auf ein vereinfachtes, rotierendes Strömungssystem zu untersuchen. Durch diese Betrachtung konnten in einem definierten Ausgangssystem Gestaltungsregeln für die Modulation des Wärmeübergangs von rotierenden Scheiben abgeleitet werden.

## Methodik

An überströmten, mit Dimpeln strukturierten Platten wurden die physikalischen Effekte in Bezug auf die Wirkmechanismen zur Widerstandsreduktion von Oberflächen untersucht. Literaturwerte von Mahmood & Ligrani [151] und van Nesselrooij u. a. [168] dienen als Referenzwerte, um die Gültigkeit und Güte der Simulationen zu belegen. Die simulationsbasierten Untersuchungen hinsichtlich der Erhöhung des Wärmeübergangs wurden an durchströmten Kanälen durchgeführt und mit Daten von Mahmood & Ligrani [151] sowie Sato u. a. [196] verglichen. Aufgrund des hohen Einflusses vergleichsweise kleiner geometrischer Änderungen wurde besonderes Augenmerk auf eine ausreichende räumliche und zeitliche Auflösung der Simulationen gelegt.

Für die erstmaligen Untersuchungen der Effekte von Dimpeln auf rotierenden Scheiben existieren keine publizierten Referenzwerte. Daher wurden die hierfür durchgeführten Simulationen anhand glatter Scheiben mit Daten von Latour u. a. [132], Nguyen & Harmand [169] sowie Wiesche & Helcig [231] validiert. Simulationen mit nicht interagierenden runden und tropfenförmigen Dimpeln dienten der Evaluation des Einflusses der Rotation auf die Effekte an den Dimpeln. Die Erforschung der komplexen Interaktion der Umströmung von Dimpel-Anordnungen erfolgte an sechs unterschiedlichen Setups. Die

Setups wurden so gewählt, dass Unterschiede hinsichtlich der Anordnung der Dimpel auf der Scheibe sowie der Bedeckungsrate zum Tragen kamen.

### **Physikalische Effekte in nicht rotierenden Systemen**

Die Effekte der Widerstandsreduktion zeigen eine starke Abhängigkeit der Reynolds-Zahl  $Re$  sowie der konkreten geometrischen Gestaltung der Dimpel-Setups. Dies ist auf die Beeinflussung oberflächennaher Streaks zurückzuführen, welche durch die Dimpel moduliert und dadurch stabilisiert werden können. Diese Beeinflussung erfordert eine genaue Abstimmung der geometrischen Anordnung sowie des Betriebszustandes. Bereits verhältnismäßig kleine Abweichungen führen zu negativer Beeinflussung der Strömungsstrukturen, wodurch der positive Effekt der Widerstandsreduktion in Widerstandserhöhung umschlägt. Für Dimpel-Tiefen von  $h/D_i \gtrsim 6\%$  wird der erzeugte Druckwiderstand dominant, wodurch Widerstandsreduktionen im untersuchten Reynoldszahlbereich nicht mehr erreicht werden können. Zudem wurde gezeigt, dass die Einflüsse einzelner Parameter nicht linear sind und somit nicht extrapoliert werden können. Die Daten zeigen deutlich, dass scheinbar widersprüchliche Ergebnisse in der Literatur bezüglich der Wirksamkeit von Dimpeln zur Widerstandsreduzierung auf die erwähnten, geringen Unterschiede in den Aufbauten und Betriebspunkten der verschiedenen Studien zurückzuführen sind.

Während tiefere Dimpel bekanntermaßen zu höheren Steigerungen des Wärmeübertrags führen, ist die tatsächliche thermische Effizienz eines definierten Setups nicht robust gegenüber Betriebspunktänderungen. Ebenso können die Einflüsse der geometrischen Parameter aufgrund komplexer Abhängigkeiten nicht linear interpoliert werden. Die Ergebnisse zeigen, dass kleinere Dimpel zu höheren durchschnittlichen Wandschubspannungen führen, was darauf hin deutet, dass die Grenzschicht trotz der lokalen Natur der Dimpel global beeinflusst wird. Diese Beeinflussung wird jedoch durch die lokalen Einflüsse überlagert, wodurch eine komplexe Interaktion unterschiedlicher Effekte entsteht, welche sowohl Interpolation als auch Extrapolation fehleranfällig macht.

### **Einfluss der Form von Dimpeln auf rotierenden Scheiben**

Die Vorteile tropfenförmiger Dimpel in nicht rotierenden Setups kommen auf rotierenden Scheiben nicht zum Tragen. In Kanälen ändert sich die relative Anströmung der Dimpel über die Zeit nicht. Im Vergleich zu runden Dimpeln führt die Tropfenform dazu, dass der Einlauf der Strömung in die Dimpel modifiziert wird. Hierdurch werden Verluste minimiert, während die

Wärmeübertragung aufgrund der Hinterkantenform mit jener der runden Dimpel vergleichbar bleibt.

Im rotierenden System hängt die relative Anströmung hingegen von der aktuellen Position der Scheibe ab. Hierdurch kommen die Vorteile des modifizierten Ein- und Auslaufs der Strömung an den Dimpeln nicht zum Tragen. Runde Dimpel sind aufgrund der Rotationsymmetrie robuster gegenüber den Änderungen der Anströmung und liefern daher insgesamt vorteilhaftere Ergebnisse. Eine Optimierung der Geometrie der Dimpel auf rotierenden Scheiben wäre daher nur für einen definierten Betriebspunkt in sehr eingeschränktem Maße möglich.

### **Einfluss einzelner Parameter auf die Auswirkungen interagierender Dimpel**

Die Untersuchung von Größe, Anzahl und Anordnung von runden Dimpeln auf Scheiben zeigte eine deutliche Abhängigkeit der Einflüsse vom jeweiligen Betriebszustand. Der Einfluss der Dimpel nimmt mit steigendem Verhältnis von Rotationsgeschwindigkeit zu Querstromgeschwindigkeit tendenziell zu, während bei niedrigeren Rotationsgeschwindigkeiten die reinen Effekte der rotierenden Scheibe dominieren. Die Ergebnisse zeigen, dass die Größe der Dimpel und der radiale Abstand einzelner Dimpel-Reihen einen stärkeren Einfluss auf den qualitativen Verlauf des Wärmeübergangs haben als die Anzahl der azimuthal aufeinanderfolgenden Dimpel. Für lokale Rotationszahlen oberhalb von  $\gamma \approx 1.7$  ist bei unstrukturierter Anordnung der Dimpel auf der Scheibe der lokale Einfluss der Grenzschicht ausschlaggebend für die Wärmeübergangssteigerung. Eine detaillierte Betrachtung der Verteilung der relativen Tiefe der Dimpel entlang des Radius zeigt, dass größere Dimpel näher an der Rotationsachse zu höheren Wärmeübertragungsraten führen. Dies ist auf die Wechselwirkung der Dimpel in diesem Bereich mit der Staupunktströmung vor der zylindrischen Welle zurückzuführen.

Insgesamt wurde gezeigt, dass die Wirkung der Dimpel bis zu sehr hohen Drehzahlen tendenziell lokal begrenzt ist. Daraus folgt, dass eine gleichmäßige Wärmeübergangssteigerung an rotierenden Scheiben durch radial und azimuthal überlappende Dimpel-Reihen erreicht werden kann. Die Größe der Dimpel muss dabei so an die radiale Position angepasst werden, dass die resultierende effektive Tiefe der Dimpel umgekehrt proportional zum Radius ist. Hinsichtlich des thermischen Wirkungsgrades konnten im untersuchten Drehzahlenbereich Steigerungen von maximal 5 % erreicht werden. Es wurde eine deutliche positive Korrelation zwischen Wirkungsgrad und Rotationszahl festgestellt, insbesondere bei den Versuchen mit größeren Dimpeln.

### Ausblick

Im Rahmen der Arbeit wurde eine Designregel entwickelt, mit deren Hilfe es möglich ist, das Wärmeübergangsverhalten von rotierenden Scheiben durch die Platzierung von Dimpeln gezielt zu beeinflussen. Diese Designregel gibt an, dass für lokale Rotationszahlen  $\gamma > 1.7$  der Wärmefluss  $\dot{q}$  näherungsweise proportional zu  $\gamma^2$  multipliziert mit der relativen Dimpel-Tiefe  $z_d/l$  ist. Damit lassen sich verschiedene Szenarien hinsichtlich der Steigerung des Wärmeübergangs untersuchen. Ausgehend von den betrachteten Setups gilt die Designregel für  $1, 17 \leq \Gamma \leq 4, 66$  für Scheiben und Dimpel entsprechend den untersuchten Verhältnissen. Eine Extrapolation auf andere Dimpel wurde nicht getestet.

Die Erweiterung des Gültigkeitsbereiches durch Variation der Geometrie der Dimpel hinsichtlich Durchmesser, Tiefe und aus der Designregel resultierender Anordnung ist der nächste Schritt für künftige Forschung. Bei den Untersuchungen zur Verbesserung des Wärmeübergangs wurde außerdem die größte Korrelation mit der relativen Tiefe der Dimpel in radialer Richtung  $z_d/l$  und dem Quadrat der lokalen Rotationszahl  $\gamma^2$  festgestellt. Obwohl die Korrelation sehr deutlich ist, ist es wahrscheinlich, dass andere Parameter wie die relative Tiefe der Dimpel in azimuthaler Richtung einen Einfluss auf das Wärmeübertragungsverhalten haben. Detaillierte Untersuchungen solcher Einflüsse könnten das Modell weiter verfeinern und zu einer weiter besseren Vorhersagekraft führen.

Die Steigerung des Wärmeübertrags bei gleichzeitiger Minimierung der Widerstandserhöhung stellt ein Optimierungsproblem mit gegensätzlichen Optimierungszielen dar. Hierfür können automatische Optimierungsverfahren wie das Verfahren der konjugierten Gradienten verwendet werden. Auch werden in der Strömungsmechanik durch breitere verfügbare Datengrundlagen immer öfter Methodiken der künstlichen Intelligenz verwendet, welche künftig auch für die weitere Steigerung der Effizienz von Dimpel-Setups auf rotierenden Scheiben herangezogen werden können.

In dieser Arbeit wurden ausschließlich numerische Untersuchungen durchgeführt. Diese liefern aufgrund der sichergestellten Simulationsqualität detaillierte, örtlich hochauflösende Informationen über das gesamte Strömungsfeld. Auch sind geometrische Varianten im Modell gut umsetzbar. Allerdings erfordern unterschiedliche Betriebspunkte eines Setups eigene Simulationen, was den numerischen Aufwand in die Höhe treibt. Hier wären Experimente an ausgewählten Geometrien ein geeignetes Mittel, um gezielt breite

Datengrundlagen über das Verhalten bestimmter Setups über verschiedene Betriebspunkte zu erhalten. Auch können deutlich längere Messdauern wesentlich einfacher umgesetzt werden als in numerisch hochauflösenden Simulationen.





# A

## Literature Overview

### **A.1 Heat Transfer from dimples**

An overview of the historical development of research on the heat transfer due to dimples is given in table A.1. The publications are sorted chronologically and the focus of investigation is marked. A distinction is made according to whether single dimples or multiple dimples were observed. Furthermore, a distinction is made between round dimples and other shapes such as oval, polygonal or teardrop-shaped dimples. Finally it is indicated whether experimentally determined results (exp) or numerical investigations (num) were presented.

**Table A.1:** Selected literature on the heat transfer due to dimples sorted chronologically

source	year	single	multiple	round	other shape	exp	num
Afanasyev et al. [3]	1993		■	■		■	
Schukin et al. [200]	1995	■		■		■	
Chyu et al. [37]	1997		■	■	■	■	
Lin et al. [145]	1999		■	■			■
Moon et al. [161]	2000		■	■		■	
Mahmood et al. [150]	2001		■	■		■	
Ligrani et al. [141]	2001		■	■		■	
Isaev et al. [95]	2002		■	■			■
Mahmood & Ligrani [151]	2002		■	■		■	
Isaev & Leontiev [94]	2003	■		■			■
Won & Ligrani [236]	2004		■	■			■
Kim & Choi [115]	2005	■		■	■		■
Won et al. [237]	2005		■	■		■	
Wang et al. [226]	2006		■	■			■
Samad et al. [194]	2008		■	■			■
Turnow et al. [218]	2011		■	■	■		■
Kim et al. [110]	2011		■		■		■
Xie et al. [240]	2013	■		■			■
Yoon et al. [243]	2015	■		■	■		■
Isaev et al. [96]	2016	■		■			■
Murata et al. [165]	2017		■		■	■	

Concluded

## A.2 Drag reduction

An overview of the historical development of research on the possible drag reduction due to dimples is given in table A.2. The publications are sorted chronologically and the focus of investigation is marked. A distinction is made according to whether shallow dimples ( $h/D_i \leq 5\%$ ) or deep dimples ( $h/D_i > 5\%$ ) were observed and the coverage ratio  $\beta$  is given. Furthermore, it is shown whether drag reduction (red) or drag increase (inc) was found in the study. Finally it is indicated whether experimentally determined results (exp) or numerical investigations (num) were presented.

**Table A.2:** Selected literature on the drag reduction due to dimples sorted chronologically

source	year	shallow	deep	$\beta$	red	inc	exp	num
Lashkov & Samoilova [130]	2002		■	48% to 68%		■	■	
Lienhart et al. [140]	2008	■		22.5%		■	■	■
Tay [212]	2011	■		40% and 90%	■	■	■	
Tay et al. [214]	2015	■		40% and 90%	■	■	■	
van Nesselrooij et al. [168]	2016	■		33.3% and 90%	■	■	■	
Tay & Lim [215]	2018	■		84% <sup>4</sup>	■	■	■	
Concluded								

<sup>4</sup> Teardrop shaped dimples were used in this study.

## A.3 Rotating discs

An overview of the historical development of research on the flow and heat transfer of rotating discs is given in table A.3. The publications are sorted chronologically and the focus of investigation is marked. The distinction is made according to whether laminar (lam) or turbulent (turb) flow around a single disc (SD) or between two discs (TD) was observed. Furthermore, it is noted whether or not axial flow (AF), crossflow (CF) or heat transfer (HT) were included at the investigations. In addition, a distinction is made between theoretical solutions (TS), experimentally determined results (exp) and numerical investigations (num). Here, *numerical investigations* refers to the use of computational fluid dynamics (CFD) rather than numerical integration of analytical equations.

Table A.3: Selected literature on the flow and heat transfer due to rotating discs chronologically sorted

source	year	lam	turb	SD	TD	AF	CF	HT	TS	exp	num
von Kármán [105]	1921	■	■	■				■	■		
Cochran [40]	1934	■		■				■	■		
Theodorsen & Regier [216]	1944		■	■						■	
Wagner [223]	1948	■		■				■	■		
Schlichting & Truckenbrodt [197]	1951	■		■		■		■	■		
Millsaps & Pohlhausen [159]	1952	■		■				■	■		
Gregory et al. [78]	1955	■	■	■				■	■	■	
Cobb & Saunders [39]	1956	■	■	■				■	■	■	
Rotem [190]	1958		■	■				■	■	■	
Ostrach & Thornton [175]	1958	■		■				■	■		
Sparrow & Gregg [209]	1960	■		■				■	■		
Hartnett & Deland [84]	1961	■		■				■	■		
Kreith et al. [125]	1963	■	■	■		■		■	■	■	
Tien & Tsuji [217]	1964	■		■		■		■	■		
Hartnett et al. [85]	1965		■	■				■	■		
Kreith [124]	1969	■	■	■		■		■	■	■	
Ong & Owen [173]	1991		■	■				■	■		■
Pilbrow et al. [180]	1999		■	■				■	■		■
Czarny et al. [44]	2002		■		■					■	
aus der Wiesche [229]	2007		■	■				■	■		■
Latour et al. [131]	2010	■	■	■				■	■		■

Continued on next page

Table A.3 Continued from previous page

source	year	lam	turb	SD	TD	AF	CF	HT	TS	exp	num
aus der Wiesche [230]	2010		■	■		■	■	■		■	
Latour et al. [132]	2011		■		■		■	■		■	
Nguyen & Harmand [169]	2013		■				■	■		■	■
aus der Wiesche & Helcig [231]	2016	■	■	■		■	■	■	■	■	■
Sardasht et al. [195]	2017		■	■		■	■	■		■	■
Concluded											



# B

## visualisation of turbulent structures near the surface

This appendix discusses near-wall streamwise vortices on plates with flat dimples, as studied in chapter 4 for the flat plate and the setups OL and NOL. Streamwise vortices occur in all investigated turbulent flows in the near-wall region. The average length and the average distance of the structures to each other depends strongly on the value of  $\lambda_2$  for which the vortices are investigated. No difference in the frequency of occurrence and structure of the vortices is apparent for the plates with dimples and the flat plate. Only at the leading and trailing edges of the dimples an influence of the vortex structures is recognizable. At the same threshold value of  $\lambda_2$ , the vortices of the plate with dimples protrude to greater distances from the wall than in the case of the flat plate. These lose orientation in the  $x$ -direction with increasing  $y^+$  and eventually form new vortex structures. Figure B.1 shows the vortex structures with a  $\lambda_2$  threshold of  $-1.2 \cdot 10^7$ . The isosurfaces are coloured according to the  $y^+$  value related to the height of the wall surface. The vortices coloured in dark blue are thus located within the dimples and therefore lie below the average wall level.

*Appendix B visualisation of turbulent structures near the surface*

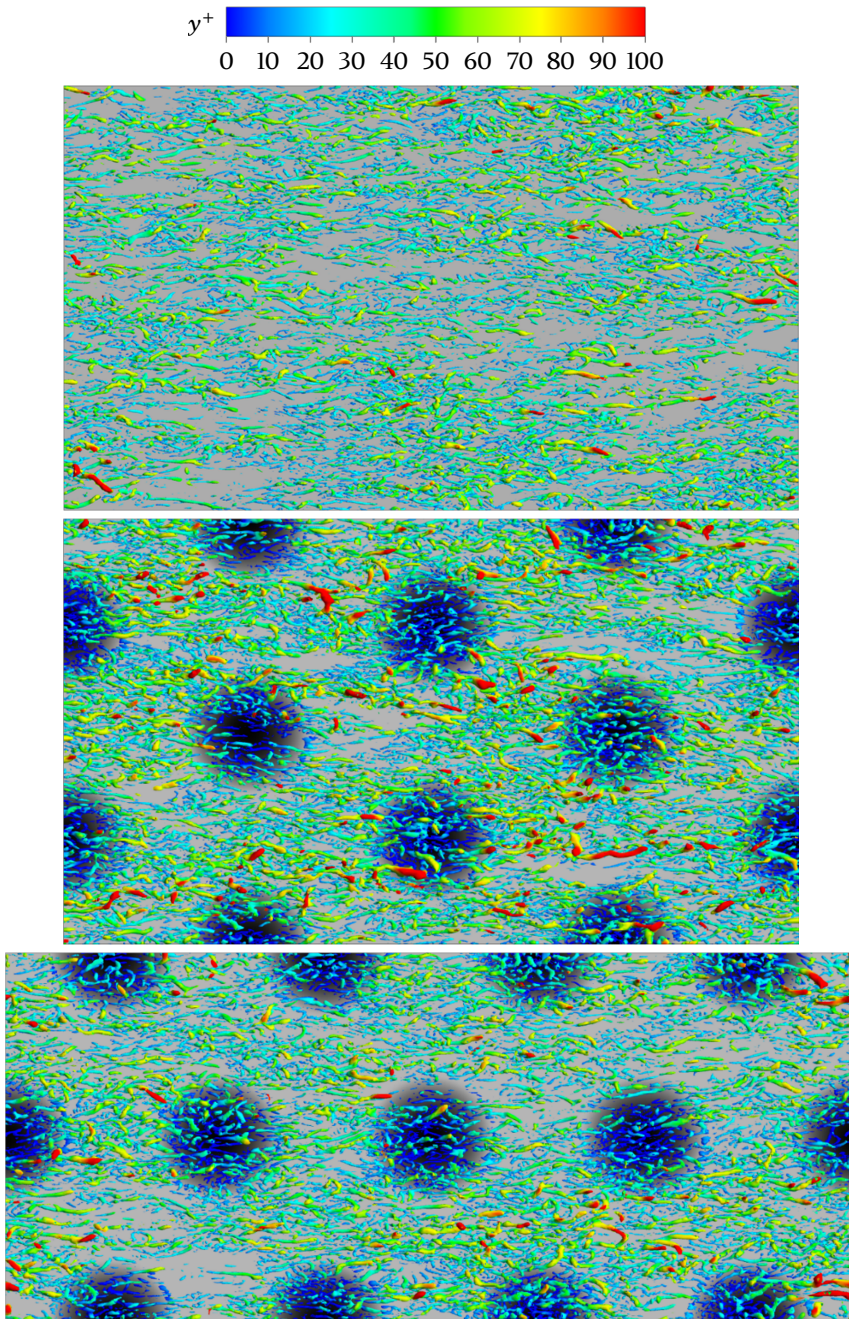


**Figure B.1:** Vortex structures at  $y^+ < 150$  visualised by the  $\lambda_2$ -criterion with threshold  $-1.2 \cdot 10^7$  and coloured by wall distance (Simulation data was partly generated within the context of Kalb [SI]).

# Bibliography

- [1] Abdulbari, H. A., R. M. Yunus, N. H. Abdurahman & A. Charles. Going against the flow—A review of non-additive means of drag reduction. In: *Journal of Industrial and Engineering Chemistry* 19.1 (2013-01), pp. 27–36. ISSN: 1226-086X. DOI: 10.1016/j.jiec.2012.07.023.
- [2] Abrahamson, S. D., J. K. Eaton & D. J. Koga. The flow between shrouded corotating disks. In: *Physics of Fluids A: Fluid Dynamics* 1.2 (1989-02), pp. 241–251. ISSN: 1070-6631. DOI: 10.1063/1.857494.
- [3] Afanasyev, V. N., Y. P. Chudnovsky, A. I. Leontiev & P. S. Roganov. Turbulent flow friction and heat transfer characteristics for spherical cavities on a flat plate. In: *Experimental Thermal and Fluid Science* 7.1 (1993-07), pp. 1–8. ISSN: 0894-1777. DOI: 10.1016/0894-1777(93)90075-T.
- [4] Allen, J. Principles of Physical Sedimentology. Chapman & Hall, 1985. ISBN: 978-1-4613-2545-1.
- [5] ANSYS, Inc. ANSYS® Fluent release 17.2, User’s Guide. 2016-08.
- [6] ANSYS, Inc. ANSYS® Fluent, Release 17.2, Theory Guide. 2016-08.
- [7] Antonia, R. A., P. R. Spalart & P. Mariani. Effect of suction on the near-wall anisotropy of a turbulent boundary layer. In: *Physics of Fluids* 6.1 (1994-01), pp. 430–432. ISSN: 1070-6631. DOI: 10.1063/1.868043.
- [8] Avila, K., D. Moxey, A. de Lozar, M. Avila, D. Barkley & B. Hof. The Onset of Turbulence in Pipe Flow. In: *Science* 333.6039 (2011-07), pp. 192–196. ISSN: 1095-9203. DOI: 10.1126/science.1203223.
- [9] Barenblatt, G. I., A. J. Chorin & V. M. Prostokishin. Scaling Laws for Fully Developed Turbulent Flow in Pipes. In: *Applied Mechanics Reviews* 50.7 (1997-07), pp. 413–429. ISSN: 0003-6900. DOI: 10.1115/1.3101726.
- [10] Ben-Nasr, O., A. Hadjadj, A. Chaudhuri & M. S. Shadloo. Assessment of subgrid-scale modeling for large-eddy simulation of a spatially-evolving compressible turbulent boundary layer. In: *Computers & Fluids* 151 (2017-06), pp. 144–158. ISSN: 0045-7930. DOI: 10.1016/j.compfluid.2016.07.004.
- [11] Benocci, C. & A. Pinelli. The role of the forcing term in the large eddy simulation of equilibrium channel flow. In: *Proceedings of the International Symposium on Engineering Turbulence Modeling and Measurements*. Ed. by W. Rodi. Dubrovnik, Yugoslavia: Elsevier, 1990-09, pp. 287–296. ISBN: 0-444-01563-9.
- [12] Bird, R. B., E. S. Warren & E. N. Lightfoot. Transport Phenomena. Ed. by W. Anderson. Second Edition. New York: John Wiley & Sons, inc., 2002. ISBN: 0-471-41077-2.

## Bibliography

- [13] Bixler, G. D. & B. Bhushan. Bioinspired micro/nanostructured surfaces for oil drag reduction in closed channel flow. In: *Soft Matter* 9.5 (2013), pp. 1620–1635. ISSN: 1744-6848. DOI: 10.1039/C2SM27070F.
- [14] Böswirth, L. & S. Bschorer. Technische Strömungslehre. 10th ed. Springer Fachmedien Wiesbaden, 2014. ISBN: 978-3-658-05667-4. DOI: 10.1007/978-3-658-05668-1.
- [15] Bredberg, J. Turbulence Modelling for Internal Cooling of Gas-Turbine Blades. PhD thesis. Göteborg, Sweden, 2002.
- [16] Breuer, M. Large eddy simulation of the subcritical flow past a circular cylinder: numerical and modeling aspects. In: *International Journal for Numerical Methods in Fluids* 29.9 (1998-12), pp. 1281–1302. ISSN: 1097-0363. DOI: 10.1002/(SICI)1097-0363(19981215)28:9<1281::AID-FLD759>3.0.CO;2-#.
- [17] Breuer, M. Numerical and modeling influences on large eddy simulations for the flow past a circular cylinder. In: *International Journal of Heat and Fluid Flow* 19.5 (1998-10), pp. 512–521. ISSN: 0142-727X. DOI: 10.1016/S0142-727X(98)10015-2.
- [18] Breuer, M. Large eddy simulation of high Reynolds number circular cylinder flow. In: *Industrial and Environmental Applications of Direct and Large-Eddy Simulation*. Ed. by S. Biringen, H. Örs, A. Tezel & J. H. Ferziger. Vol. 529. Lecture Notes in Physics. Springer Berlin Heidelberg, 1999-08, pp. 176–189. DOI: 10.1007/BFb0106102.
- [19] Breuer, M. A challenging test case for large eddy simulation: high Reynolds number circular cylinder flow. In: *International Journal of Heat and Fluid Flow* 21.5 (2000-10), pp. 648–654. ISSN: 0142-727X. DOI: 10.1016/S0142-727X(00)00056-4.
- [20] Breuer, M. Direkte Numerische Simulation und Large-Eddy Simulation turbulenter Strömungen auf Hochleistungsrechnern. habilitation. 2002.
- [21] Brodkey, R. S. The Phenomena of Fluid Motions. 4th ed. Dover Publications Inc., 1995-09. ISBN: 978-0486686059.
- [22] Burgess, N. K. & P. M. Ligrani. Effects Of Dimple Depth on Channel Nusselt Numbers and Friction Factors. In: *Journal of Heat Transfer* 127.8 (2005-08), pp. 839–847. ISSN: 0022-1481. DOI: 10.1115/1.1994880.
- [23] Bushnell, D. M. & K. J. Moore. Drag reduction in nature. In: *Annual Review of Fluid Mechanics* 23 (1991-01), pp. 65–79. ISSN: 1545-4479. DOI: 10.1146/annurev.fl.23.010191.000433.
- [24] Cabot, W. & P. Moin. Approximate Wall Boundary Conditions in the Large-Eddy Simulation of High Reynolds Number Flow. In: *Flow, Turbulence and Combustion* 63 (2000), pp. 269–291. ISSN: 1386-6184. DOI: 10.1023/A:1009958917113.

- [25] Campenhout, O. W. van, M. van Nesselrooij, L. L. Veldhuis, B. van Oudheusden & F. Schrijer. An experimental investigation into the flow mechanics of dimpled surfaces in turbulent boundary layers. In: *2018 AIAA Aerospace Sciences Meeting*. American Institute of Aeronautics and Astronautics, 2018-01. DOI: 10.2514/6.2018-2062.
- [26] Chapman, D. R. Computational Aerodynamics Development and Outlook. In: *AIAA Journal* 17.12 (1979-12), pp. 1293-1313. DOI: 10.2514/3.61311.
- [27] Chen, J., H. Müller-Steinhagen & G. G. Duffy. Heat transfer enhancement in dimpled tubes. In: *Applied Thermal Engineering* 21.5 (2001-04), pp. 535-547. ISSN: 1359-4311. DOI: 10.1016/S1359-4311(00)00067-3.
- [28] Chen, Y., Y. T. Chew & B. C. Khoo. Enhancement of heat transfer in turbulent channel flow over dimpled surface. In: *International Journal of Heat and Mass Transfer* 55.25-26 (2012-12), pp. 8100-8121. ISSN: 0017-9310. DOI: 10.1016/j.ijheatmasstransfer.2012.08.043.
- [29] Chernyshenko, S. I. & M. F. Baig. Streaks and vortices in near-wall turbulence. In: *Philosophical Transactions of the Royal Society A: Mathematical, Physical and Engineering Sciences* 363.1830 (2005-05), pp. 1097-1107. ISSN: 1471-2962. DOI: 10.1098/rsta.2005.1552.
- [30] Chernyshenko, S. I. & M. F. Baig. The mechanism of streak formation in near-wall turbulence. In: *Journal of Fluid Mechanics* 544 (2005-11), pp. 99-131. ISSN: 0022-1120. DOI: 10.1017/S0022112005006506.
- [31] Childs, P. R. N. *Rotating Flow*. Vol. 1. Elsevier Inc., 2011. ISBN: 978-0-12-382098-3.
- [32] Chilton, T. H. & A. P. Colburn. Mass Transfer (Absorption) Coefficients Prediction from Data on Heat Transfer and Fluid Friction. In: *Industrial & Engineering Chemistry* 26.11 (1934-11), pp. 1183-1187. DOI: 10.1021/ie50299a012.
- [33] Choi, H. & P. Moin. Effects of the Computational Time Step on Numerical Solutions of Turbulent Flow. In: *Journal of Computational Physics* 113.1 (1994-07), pp. 1-4. ISSN: 0021-9991. DOI: 10.1006/jcph.1994.1112.
- [34] Choi, H. & P. Moin. Grid-point requirements for large eddy simulation: Chapman's estimates revisited. In: *Physics of Fluids* 24.1 (2012-01), p. 011702. ISSN: 1070-6631. DOI: 10.1063/1.3676783.
- [35] Choi, H., P. Moin & J. Kim. Active turbulence control for drag reduction in wall-bounded flows. In: *Journal of Fluid Mechanics* 262 (1994-10), pp. 75-110. ISSN: 0022-1120. DOI: 10.1017/S0022112094000431.
- [36] Chu, S. Letter from Secretary Steven Chu to Energy Department Employees. Online. 2013-02.

## Bibliography

- [37] Chyu, M. K., Y. Yu, H. Ding, J. P. Downs & F. O. Soechting. Concavity Enhanced Heat Transfer in an Internal Cooling Passage. In: *Volume 3: Heat Transfer; Electric Power; Industrial and Cogeneration*. American Society of Mechanical Engineers, 1997-06. DOI: 10.1115/97-GT-437.
- [38] Cimarelli, A., B. Frohnäpfel, Y. Hasgawa, E. de Angelis & M. Quadrio. Prediction of turbulence control for arbitrary periodic spanwise wall movement. In: *Physics of Fluids* 25.075102 (2013-07), pp. 1-11. ISSN: 1089-7666. DOI: 10.1063/1.4813807.
- [39] Cobb, E. C. & O. A. Saunders. Heat Transfer from a Rotating Disk. In: *Proceedings of the Royal Society A: Mathematical, Physical and Engineering Sciences* 236.1206 (1956-08), pp. 343-351. ISSN: 1364-5021. DOI: 10.1098/rspa.1956.0141.
- [40] Cochran, W. G. The flow due to a rotating disc. In: *Mathematical Proceedings of the Cambridge Philosophical Society* 30.03 (1934-07), pp. 365-375. DOI: 10.1017/S0305004100012561.
- [41] Colburn, A. P. A method of correlating forced convection heat-transfer data and a comparison with fluid friction. In: *International Journal of Heat and Mass Transfer* 7.12 (1964-12), pp. 1359-1384. ISSN: 0017-9310. DOI: 10.1016/0017-9310(64)90125-5.
- [42] Coles, D. The Turbulent Boundary Layer in a Compressible Fluid. In: *Physics of Fluids* 7.9 (1964), p. 1403. ISSN: 1070-6631. DOI: 10.1063/1.1711395.
- [43] Comte-Bellot, G. Contribution a l'étude de la turbulence de conduite. PhD thesis. 1963.
- [44] Czarny, O., H. Iacovides & B. Launder. In: *Flow, Turbulence and Combustion* 69.1 (2002), pp. 51-61. ISSN: 1386-6184. DOI: 10.1023/A:1022471329506.
- [45] Daniel, T. L. Fish Mucus: In Situ Measurements of Polymer Drag Reduction. In: *Biological Bulletin* 160.3 (1981-06), pp. 376-382. ISSN: 0006-3185. DOI: 10.2307/1540846.
- [46] De Graaff, D. B. & J. K. Eaton. Reynolds-number scaling of the flat-plate turbulent boundary layer. In: *Journal of Fluid Mechanics* 422 (2000-11), pp. 319-346. ISSN: 0022-1120. DOI: 10.1017/S0022112000001713.
- [47] Dean, B. & B. Bhushan. Shark-skin surfaces for fluid-drag reduction in turbulent flow: a review. In: *Philosophical Transactions of the Royal Society A: Mathematical, Physical and Engineering Sciences* 368.1929 (2010-10), pp. 4775-4806. ISSN: 1471-2962. DOI: 10.1098/rsta.2010.0201.
- [48] Dean, R. B. Reynolds Number Dependence of Skin Friction and Other Bulk Flow Variables in Two-Dimensional Rectangular Duct Flow. In: *Journal of Fluids Engineering* 100.2 (1978-06), pp. 215-223. ISSN: 0098-2202. DOI: 10.1115/1.3448633.

- [49] Deardorff, J. W. A numerical study of three-dimensional turbulent channel flow at large Reynolds numbers. In: *Journal of Fluid Mechanics* 41.2 (1970-04), pp. 453–480. ISSN: 0022-1120. DOI: 10.1017/S0022112070000691.
- [50] Den Hartog, J. P. Mechanical Vibrations. Fourth. Dover Publications, Inc., 1985. ISBN: 0-486-64785-4.
- [51] Dittus, F. W. & L. M. K. Boelter. Heat transfer in automobile radiators of the tubular type. In: *University of California publications in engineering* 2.13 (1930).
- [52] Driest, E. R. van. On Turbulent Flow Near a Wall. In: *Journal of the Aeronautical Sciences* 23.11 (1956-11), pp. 1007–1011. ISSN: 1936-9956. DOI: 10.2514/8.3713.
- [53] Dubief, Y. & F. Delcayre. On coherent-vortex identification in turbulence. In: *Journal of Turbulence* 1 (2000-01), N11. ISSN: 1468-5248. DOI: 10.1088/1468-5248/1/1/011.
- [54] Durst, F. Fluid Mechanics - An Introduction to the Theory of Fluid Flows. Springer-Verlag Berlin Heidelberg, 2008. ISBN: 978-3-540-71342-5. DOI: 10.1007/978-3-540-71343-2.
- [55] Eckerle, W. A. & L. S. Langston. Horseshoe Vortex Formation Around a Cylinder. In: *Proceedings of the International Gas Turbine Conference and Exhibit*. ASME. 1986-06.
- [56] Egorov, Y., F. R. Menter, R. Lechner & D. Cokljat. The Scale-Adaptive Simulation Method for Unsteady Turbulent Flow Predictions. Part 2: Application to Complex Flows. In: *Flow, Turbulence and Combustion* 85.1 (2010-06), pp. 139–165. ISSN: 1386-6184. DOI: 10.1007/s10494-010-9265-4.
- [57] Elyyan, M. A. Heat Transfer Augmentation Surfaces Using Modified Dimples/Protrusions. PhD thesis. 2008.
- [58] Elyyan, M. A. & D. K. Tafti. Large Eddy Simulation Investigation of Flow and Heat Transfer in a Channel With Dimples and Protrusions. In: *Journal of Turbomachinery* 130.4 (2008-08). ISSN: 0889-504X. DOI: 10.1115/1.2812412.
- [59] FAPS. RegVent. German. FAPS. 2015-06. URL: <https://www.faps.fau.de/curforsch/regvent/>.
- [60] Fernholz, H. H. & P. J. Finley. The incompressible zero-pressure-gradient turbulent boundary layer: An assessment of the data. In: *Progress in Aerospace Sciences* 32.4 (1996-08), pp. 245–311. ISSN: 0376-0421. DOI: 10.1016/0376-0421(95)00007-0.
- [61] Ferziger, J. H., M. Perić & R. L. Street. Computational Methods for Fluid Dynamics. Fourth Edition. Springer-Verlag GmbH, 2020-10. ISBN: 978-3-319-99691-2. DOI: 10.1007/978-3-319-99693-6.

## Bibliography

- [62] Fiebig, M. Embedded vortices in internal flow: heat transfer and pressure loss enhancement. In: *International Journal of Heat and Fluid Flow* 16.5 (1995-10), pp. 376–388. ISSN: 0142-727X. DOI: 10.1016/0142-727X(95)00043-P.
- [63] Fiebig, M. Vortices, Generators and Heat Transfer. In: *Chemical Engineering Research and Design* 76.2 (1998-02), pp. 108–123. ISSN: 0263-8762. DOI: 10.1205/026387698524686.
- [64] Foken, T. 50 Years of the Monin–Obukhov Similarity Theory. In: *Boundary-Layer Meteorology* 119.3 (2006-06), pp. 431–447. ISSN: 0006-8314. DOI: 10.1007/s10546-006-9048-6.
- [65] Fourier, J. *Théorie Analytique de la Chaleur*. Ed. by p. e. f. Firmin Didot. Éditions Jacques Gabay, 1988. ISBN: 2-87647-046-2.
- [66] Fox, R. O. *Computational Models for Turbulent Reacting Flows*. Cambridge, U.K. New York: Cambridge University Press, 2003-10. ISBN: 978-0-511-07452-3. DOI: 10.1017/CB09780511610103.
- [67] Fröhlich, J. & W. Rodi. Introduction to Large Eddy Simulation of Turbulent Flows. In: *Closure Strategies for Turbulent and Transitional Flows*. Ed. by B. E. Launder & N. D. Sandham. Vol. 1. Cambridge University Press, 2002. Chap. 8, pp. 267–298. ISBN: 0-521-79208-8.
- [68] Fröhlich, J. *Large Eddy Simulation turbulenter Strömungen*. Vol. 1. Vieweg+Teubner Verlag, 2006-09. ISBN: 978-3-8351-0104-3.
- [69] Gad-el-Hak, M. *Advances in Fluid Mechanics Measurements*. Ed. by C. A. Brebbia & S. A. Orszag. Vol. 45. Lecture Notes in Engineering. Springer Berlin Heidelberg, 1989. ISBN: 978-3-540-51136-6. DOI: 10.1007/978-3-642-83787-6.
- [70] Gad-el-Hak, M. *Flow Control*. Cambridge University Press, 2006. ISBN: 978-0-521-03671-9.
- [71] Geankoplis, C. J. *Transport Processes and Unit Operators*. 3rd ed. Prentice-Hall International, Inc., 1993. ISBN: 0-13-045253-X.
- [72] Gee, D. L. & R. L. Webb. Forced convection heat transfer in helically rib-roughened tubes. In: *International Journal of Heat and Mass Transfer* 23.8 (1980-08), pp. 1127–1136. ISSN: 0017-9310. DOI: 10.1016/0017-9310(80)90177-5.
- [73] Gerasimov, A. *Quick guide to setting up LES-type simulations*. ANSYS, Inc. 2016-05.
- [74] Germano, M. Turbulence: the filtering approach. In: *Journal of Fluid Mechanics* 238 (1992-05), pp. 325–336. ISSN: 0022-1120. DOI: 10.1017/S0022112092001733.
- [75] Gersten, K. & H. Herwig. *Strömungsmechanik*. Vieweg+Teubner Verlag, 1992. ISBN: 978-3-322-93971-5.

- [76] Gnielinski, V. Neue Gleichungen für den Wärme- und den Stoffübergang in turbulent durchströmten Rohren und Kanälen. In: *Forschung im Ingenieurwesen* 41.1 (1975-01), pp. 8–16. ISSN: 0015-7899. DOI: 10.1007/BF02559682.
- [77] Gortyshov, Y. F., I. A. Popov, R. D. Amirkhanov & K. E. Gulitsky. Studies of Hydrodynamics and Heat Exchange in Channels with various Types of Intesifiers. In: *Proceeding of International Heat Transfer Conference II*. Begellhouse, 1998-08, pp. 83–88. DOI: 10.1615/ihetc11.1350.
- [78] Gregory, N., J. T. Stuart & W. S. Walker. On the stability of three-dimensional boundary layers with application to the flow due to a rotating disk. In: *Philosophical Transactions of the Royal Society of London A: Mathematical, Physical and Engineering Sciences* 248.943 (1955-07), pp. 155–199. ISSN: 0080-4614. DOI: 10.1098/rsta.1955.0013. eprint: <http://rsta.royalsocietypublishing.org/content/248/943/155.full.pdf>.
- [79] Griffith, T. S., L. Al-Hadhrami & J.-C. Han. Heat Transfer in Rotating Rectangular Cooling Channels (AR=4) With Dimples. In: *Journal of Turbomachinery* 125 (2003-07), pp. 555–564. ISSN: 0889-504X. DOI: 10.1115/1.1571850.
- [80] Gromov, P. R., A. B. Zobnin, M. I. Rabinovich & M. M. Sushchik. Formation of solitary vortices in flow over small spherical depressions. In: *Pis'ma v Zhurnal Tekhnicheskoi Fiziki* 12 (1986-II), pp. 1323–1328. ISSN: 0320-0016.
- [81] Grundestam, O., S. Wallin & A. V. Johansson. Direct numerical simulations of rotating turbulent channel flow. In: *Journal of Fluid Mechanics* 598 (2008-02), pp. 177–199. ISSN: 0022-1120. DOI: 10.1017/S0022112007000122.
- [82] Gyr, A. & H.-W. Bewersdorff. Drag Reduction of Turbulent Flows by Additives. Ed. by R. Moreau. Vol. 32. Springer-Science+Business Media B.V., 1995. ISBN: 978-94-017-1295-8.
- [83] Hamilton, J. M., J. Kim & F. Waleffe. Regeneration mechanisms of near-wall turbulence structures. In: *Journal of Fluid Mechanics* 287 (1995-03), p. 317. ISSN: 0022-1120. DOI: 10.1017/S0022112095000978.
- [84] Hartnett, J. P. & E. C. Deland. The Influence of Prandtl Number on the Heat Transfer From Rotating Nonisothermal Disks and Cones. In: *Journal of Heat Transfer* 83.1 (1961-02), pp. 95–96. ISSN: 0022-1481. DOI: 10.1115/1.3680479.
- [85] Hartnett, J. P., S.-H. Tsai & H. N. Jantscher. Heat Transfer to a Nonisothermal Rotating Disk With a Turbulent Boundary Layer. In: *Journal of Heat Transfer* 87.3 (1965-08), pp. 362–368. ISSN: 0022-1481. DOI: 10.1115/1.3689117.
- [86] Helicopters & Aircrafts. The china clay method. website. 2016-04.

## Bibliography

- [87] Herwig, H. & B. Schmandt. *Strömungsmechanik*. Springer Berlin Heidelberg, 2015. ISBN: 978-3-662-45068-0. DOI: 10.1007/978-3-662-45069-7.
- [88] Högström, U. A field study of the turbulent fluxes of heat, water vapour and momentum at a 'typical' agricultural site. In: *Quarterly Journal of the Royal Meteorological Society* 100.426 (1974-10), pp. 624–639. ISSN: 1477-870X. DOI: 10.1002/qj.49710042610.
- [89] Humphrey, J. A. C., C. A. Schuler & D. R. Webster. Unsteady laminar flow between a pair of disks corotating in a fixed cylindrical enclosure. In: *Physics of Fluids* 7.6 (1995-06), pp. 1225–1240. ISSN: 1070-6631. DOI: 10.1063/1.868753.
- [90] Hunt, J. C. R., A. A. Wray & P. Moin. Eddies, streams, and convergence zones in turbulent flows. In: *Studying Turbulence Using Numerical Simulation Databases, 2. Proceedings of the 1988 Summer Program*. 1988-12, pp. 193–208.
- [91] Incropera, F. P., D. P. DeWitt, T. L. Bergman & A. S. Lavine. *Fundamentals of Heat and Mass Transfer*. Ed. by J. Hayton. 6th ed. John Wiley & Sons, Inc., 2007. ISBN: 978-0-471-45728-2.
- [92] Inoue, M. Large-Eddy Simulation of the Flat-plate Turbulent Boundary Layer at High Reynolds numbers. PhD thesis. California Institute of Technology, Pasadena, California, 2012.
- [93] Isaev, S. A., N. V. Kornev, A. I. Leontiev & E. Hassel. Influence of the Reynolds number and the spherical dimple depth on turbulent heat transfer and hydraulic loss in a narrow channel. In: *International Journal of Heat and Mass Transfer* 53.1-3 (2010-01), pp. 178–197. ISSN: 0017-9310. DOI: 10.1016/j.ijheatmasstransfer.2009.09.042.
- [94] Isaev, S. A. & A. I. Leontiev. Numerical simulation of vortex enhancement of heat transfer under conditions of turbulent flow past a spherical dimple on the wall of a narrow channel. In: *High Temperature* 41.5 (2003), pp. 665–679. DOI: 10.1023/A:1026100913269.
- [95] Isaev, S. A., A. I. Leontiev, P. A. Baranov, I. A. Pyshnyi & A. E. Usachov. Numerical analysis of the vortex intensification of heat transfer in a channel with a set of deep spherical dimples on one of the walls. In: *Doklady Physics* 47.10 (2002-10), pp. 755–757. DOI: 10.1134/1.1519324.
- [96] Isaev, S. A., A. V. Schelchikov, A. I. Leontiev, P. A. Baranov & M. E. Gulcova. Numerical simulation of the turbulent air flow in the narrow channel with a heated wall and a spherical dimple placed on it for vortex heat transfer enhancement depending on the dimple depth. In: *International Journal of Heat and Mass Transfer* 94 (2016-03), pp. 426–448. ISSN: 0017-9310. DOI: 10.1016/j.ijheatmasstransfer.2015.11.002.
- [97] Issa, R. I. Solution of the implicitly discretised fluid flow equations by operator-splitting. In: *Journal of Computational Physics* 62.1 (1986-01), pp. 40–65. ISSN: 0021-9991. DOI: 10.1016/0021-9991(86)90099-9.

- [98] Jennings, S. G. The mean free path in air. In: *Journal of Aerosol Science* 19.2 (1988-04), pp. 159–166. ISSN: 0021-8502. DOI: 10.1016/0021-8502(88)90219-4.
- [99] Jeong, J. & F. Hussain. On the identification of a vortex. In: *Journal of Fluid Mechanics* 285 (1995-02), pp. 69–94. ISSN: 0022-1120. DOI: 10.1017/s0022112095000462.
- [100] Jiménez, J. & A. Pinelli. The autonomous cycle of near-wall turbulence. In: *Journal of Fluid Mechanics* 389 (1999-06), pp. 335–359. ISSN: 0022-1120. DOI: 10.1017/S0022112099005066.
- [101] Jones, W. P. & B. E. Launder. The prediction of laminarization with a two-equation model of turbulence. In: *International Journal of Heat and Mass Transfer* 15 (1972), pp. 301–314.
- [102] Jordan, C. N. & L. M. Wright. Heat Transfer Enhancement in a Rectangular (AR=3:1) Channel With V-Shaped Dimples. In: *Journal of Turbomachinery* 135.1 (2013-10). ISSN: 0889-504X. DOI: 10.1115/1.4006422.
- [103] Jovanović, J. *The Statistical Dynamics of Turbulence*. First. Springer-Verlag Berlin Heidelberg GmbH, 2004. ISBN: 978-3-642-05793-9. DOI: 10.1007/978-3-662-10411-8.
- [104] Karabelas, S. J. Large Eddy Simulation of high-Reynolds number flow past a rotating cylinder. In: *International Journal of Heat and Fluid Flow* 31.4 (2010-08), pp. 518–527. ISSN: 0142-727X. DOI: 10.1016/j.ijheatfluidflow.2010.02.010.
- [105] Kármán, T. von. Über laminare und turbulente Reibung. In: *ZAMM - Zeitschrift für Angewandte Mathematik und Mechanik* 1.4 (1921-08), pp. 233–252. ISSN: 1521-4001. DOI: 10.1002/zamm.19210010401.
- [106] Kays, W. M. & M. E. Crawford. *Convective Heat and Mass Transfer*. Ed. by J. J. Corrigán & J. M. Morriss. 3rd ed. McGraw-Hill, Inc., 1993. ISBN: 0-07-033721-7.
- [107] Kelly, S. G. *Mechanical Vibrations*. Ed. by R. Adams. SI Edition. Cengage Learning, 2012. ISBN: 978-1-4390-6214-2.
- [108] Kesarev, V. S. & A. Kozlov. Convective heat transfer in turbulized flow past a hemispherical cavity. In: *Heat Transfer Research* 25.2 (1993), pp. 156–160. ISSN: 1064-2285.
- [109] Kim, H. T., S. J. Kline & W. C. Reynolds. The production of turbulence near a smooth wall in a turbulent boundary layer. In: *Journal of Fluid Mechanics* 50.01 (1971-11), p. 133. ISSN: 0022-1120. DOI: 10.1017/S0022112071002490.
- [110] Kim, H.-M., M.-A. Moon & K.-Y. Kim. Shape Optimization of Inclined Elliptic Dimples in a Cooling Channel. In: *Journal of Thermophysics and Heat Transfer* 25.3 (2011-07), pp. 472–476. ISSN: 0887-8722. DOI: 10.2514/1.T3674.

## Bibliography

- [111] Kim, J. On the structure of pressure fluctuations in simulated turbulent channel flow. In: *Journal of Fluid Mechanics* 205.-1 (1989-08), p. 421. ISSN: 0022-1120. DOI: 10.1017/S0022112089002090.
- [112] Kim, J. Control of turbulent boundary layers. In: *Physics of Fluids* 15.5 (2003-05), pp. 1093–1105. ISSN: 1070-6631. DOI: 10.1063/1.1564095.
- [113] Kim, J. Physics and control of wall turbulence for drag reduction. In: *Philosophical Transactions of the Royal Society A: Mathematical, Physical and Engineering Sciences* 369.1940 (2011-03), pp. 1396–1411. ISSN: 1471-2962. DOI: 10.1098/rsta.2010.0360.
- [114] Kim, J., P. Moin & R. Moser. Turbulence statistics in fully developed channel flow at low Reynolds number. In: *Journal of Fluid Mechanics* 177 (1987-04), pp. 133–166. ISSN: 0022-1120. DOI: 10.1017/S0022112087000892.
- [115] Kim, K.-Y. & J.-Y. Choi. Shape Optimization of a Dimpled Channel to Enhance Turbulent Heat Transfer. In: *Numerical Heat Transfer, Part A: Applications* 48.9 (2005-12), pp. 901–915. ISSN: 1040-7782. DOI: 10.1080/10407780500226571.
- [116] Kim, Y. W., L. Arellano, M. Vardakas, H.-K. Moon & K. O. Smith. Comparison of Trip-Strip/Impingement/Dimple Cooling Concepts at High Reynolds Numbers. In: *Volume 5: Turbo Expo 2003, Parts A and B*. ASMEDC, 2003-01. DOI: 10.1115/GT2003-38935.
- [117] Kiš, P., Y. Jin & H. Herwig. The physics of stripe patterns in turbulent channel flow determined by DNS results. In: *ArXiv e-prints* (2015-11).
- [118] Kithcart, M. E. & D. E. Klett. Heat Transfer and Skin Friction Comparison of Dimpled Versus Protrusion Roughness. In: *Journal of Enhanced Heat Transfer* 3.4 (1996), pp. 273–280. DOI: 10.1615/JEnhHeatTransf.v3.i4.30.
- [119] Kline, S. J., W. C. Reynolds, F. A. Schraub & P. W. Runstadler. The structure of turbulent boundary layers. In: *Journal of Fluid Mechanics* 30.04 (1967-12), pp. 741–773. ISSN: 0022-1120. DOI: 10.1017/S0022112067001740.
- [120] Knight, K. E. Evolving Computer Performance 1963-1967. In: *Datamation* (1968-01).
- [121] Kolmogorov, A. N. The local structure of turbulence in incompressible viscous fluid for very large Reynolds numbers. In: *Proceedings of the Royal Society of London. Series A: Mathematical and Physical Sciences* 434.1890 (1941-07), pp. 9–13. ISSN: 0962-8444. DOI: 10.1098/rspa.1991.0075.
- [122] Koomey, J. G., S. Berard, M. Sanchez & H. Wong. Assessing trends in the electrical efficiency of computation over time. Tech. rep. Lawrence Berkeley National Laboratory, Stanford University, Microsoft Corporation and Intel Corporation, 2009-08.

- [123] Kraichnan, R. H. Diffusion by a Random Velocity Field. In: *Physics of Fluids* 13.1 (1970), p. 22. ISSN: 1070-6631. DOI: 10.1063/1.1692799.
- [124] Kreith, F. Convection Heat Transfer in Rotating Systems. PhD thesis. 1969.
- [125] Kreith, F., E. Doughman & H. Kozłowski. Mass and Heat Transfer From an Enclosed Rotating Disk With and Without Source Flow. In: *Journal of Heat Transfer* 85.2 (1963-05), pp. 153–162. ISSN: 0022-1481. DOI: 10.1115/1.3686038.
- [126] Krieger, V., R. Perić, J. Jovanović, H. Lienhart & A. Delgado. Toward design of the antiturbulence surface exhibiting maximum drag reduction effect. In: *Journal of Fluid Mechanics* 850 (2018-07), pp. 262–303. ISSN: 0022-1120. DOI: 10.1017/jfm.2018.423.
- [127] Kristoffersen, R. & H. I. Andersson. Direct simulations of low-Reynolds-number turbulent flow in a rotating channel. In: *Journal of Fluid Mechanics* 256 (1993-11), pp. 163–197. ISSN: 0022-1120. DOI: 10.1017/S0022112093002757.
- [128] Kühnen, J., B. Song, D. Scarselli, N. B. Budanur, M. Riedl, A. P. Willis, M. Avila & B. Hof. Destabilizing turbulence in pipe flow. In: *Nature Physics* 14 (2018-04), pp. 386–390. ISSN: 1745-2481. DOI: 10.1038/s41567-017-0018-3.
- [129] Kumar, S., C. Cantu & B. Gonzalez. Flow Past a Rotating Cylinder at Low and High Rotation Rates. In: *Journal of Fluids Engineering* 133.4 (2011-04), p. 041201. ISSN: 0098-2202. DOI: 10.1115/1.4003984.
- [130] Lashkov, Y. A. & N. V. Samoilova. On the Viscous Drag of a Plate with Spherical Recesses. In: *Fluid Dynamics* 37.2 (2002), pp. 231–236. DOI: 10.1023/A:1015806332333.
- [131] Latour, B., P. Bouvier & S. Harmand. Convective Heat Transfer on a Rotating Disk With Transverse Air Crossflow. In: *Journal of Heat Transfer* 133.2 (2010-11). ISSN: 0022-1481. DOI: 10.1115/1.4002603.
- [132] Latour, B., P. Bouvier & S. Harmand. Convective Heat Transfer on a Rotating Disk With Transverse Air Crossflow. In: *Journal of Heat Transfer* 133.2 (2011-02), p. 021702. ISSN: 0022-1481. DOI: 10.1115/1.4002603.
- [133] Launder, B. E. & B. I. Sharma. Application of the energy-dissipation model of turbulence to the calculation of flow near a spinning disc. In: *Letters in Heat and Mass Transfer* 1.2 (1974-11), pp. 131–137. ISSN: 0094-4548. DOI: 10.1016/0094-4548(74)90150-7.
- [134] Lee, M. & R. D. Moser. Direct numerical simulation of turbulent channel flow up to  $Re_\tau \approx 5200$ . In: *Journal of Fluid Mechanics* 774 (2015-06), pp. 395–415. ISSN: 0022-1120. DOI: 10.1017/jfm.2015.268.
- [135] Leonard, A. Energy Cascade in Large-Eddy Simulations of Turbulent Fluid Flows. In: 18 (1975), pp. 237–248. ISSN: 0065-2687. DOI: 10.1016/S0065-2687(08)60464-1.

## Bibliography

- [136] Leontiev, A. I., N. A. Kiselev, Y. A. Vinogradov, M. M. Strongin, A. G. Zditovets & S. A. Burtsev. Experimental investigation of heat transfer and drag on surfaces coated with dimples of different shape. In: *International Journal of Thermal Sciences* 118 (2017-08), pp. 152–167. ISSN: 1290-0729. DOI: 10.1016/j.ijthermalsci.2017.04.027.
- [137] Li, M., T. S. Khan, E. Al Hajri & Z. H. Ayub. Geometric optimization for thermal–hydraulic performance of dimpled enhanced tubes for single phase flow. In: *Applied Thermal Engineering* 103 (2016-06), pp. 639–650. ISSN: 1359-4311. DOI: 10.1016/j.applthermaleng.2016.04.141.
- [138] Li, R., Y.-L. He, Y. G. Lei, Y. B. Tao & P. Chu. A Numerical Study on Fluid Flow and Heat Transfer Performance of Internally Roughened Tubes with Dimples. In: *Journal of Enhanced Heat Transfer* 16.3 (2009), pp. 267–285. ISSN: 1065-5131. DOI: 10.1615/JEnhHeatTransf.v16.i3.40.
- [139] Lienhard, J. H. V. & J. H. V. Lienhard. A Heat Transfer Textbook. 4th ed. Phlogiston Press, 2017.
- [140] Lienhart, H., M. Breuer & C. Köksoy. Drag reduction by dimples? – A complementary experimental/numerical investigation. In: *International Journal of Heat and Fluid Flow* 29.3 (2008-06), pp. 783–791. DOI: 10.1016/j.ijheatfluidflow.2008.02.001.
- [141] Ligrani, P. M., J. L. Harrison, G. I. Mahmmod & M. L. Hill. Flow structure due to dimple depressions on a channel surface. In: *Physics of Fluids* 13.11 (2001-11), pp. 3442–3451. ISSN: 1070-6631. DOI: 10.1063/1.1404139.
- [142] Ligrani, P. M., G. I. Mahmood, J. L. Harrison, C. M. Clayton & D. L. Nelson. Flow structure and local Nusselt number variations in a channel with dimples and protrusions on opposite walls. In: *International Journal of Heat and Mass Transfer* 44.23 (2001-12), pp. 4413–4425. ISSN: 0017-9310. DOI: 10.1016/S0017-9310(01)00101-6.
- [143] Ligrani, P. M., M. M. Oliveira & T. Blaskovich. Comparison of Heat Transfer Augmentation Techniques. In: *AIAA Journal* 41.3 (2003-03), pp. 337–362. ISSN: 1533-385X. DOI: 10.2514/2.1964.
- [144] Ligrani, P. Heat Transfer Augmentation Technologies for Internal Cooling of Turbine Components of Gas Turbine Engines. In: *International Journal of Rotating Machinery* 2013 (2013), pp. 1–32. DOI: 10.1155/2013/275653.
- [145] Lin, Y.-L., T. I.-P. Shih & M. K. Chyu. Computations of Flow and Heat Transfer in a Channel With Rows of Hemispherical Cavities. In: *Volume 3: Heat Transfer; Electric Power; Industrial and Cogeneration*. American Society of Mechanical Engineers, 1999-06. DOI: 10.1115/99-GT-263.
- [146] Liou, T.-M. & J.-J. Hwang. Effect of ridge shapes on turbulent heat transfer and friction in a rectangular channel. In: *International Journal of Heat and Mass Transfer* 36.4 (1993-03), pp. 931–940. ISSN: 0017-9310. DOI: 10.1016/S0017-9310(05)80277-7.

- [147] Liu, E., L. Li, G. Wang, Z. Zeng, W. Zhao & Q. Xue. Drag reduction through self-texturing compliant bionic materials. In: *Scientific Reports* 7.40038 (2017-01). ISSN: 2045-2322. DOI: 10.1038/srep40038.
- [148] Lumley, J. L. Computational Modeling of Turbulent Flows. In: *Advances in Applied Mechanics* 18 (1979), pp. 123–176. ISSN: 0065-2156. DOI: 10.1016/S0065-2156(08)70266-7.
- [149] Lumley, J. L. & G. R. Newman. The return to isotropy of homogeneous turbulence. In: *Journal of Fluid Mechanics* 82.1 (1977-08), pp. 161–178. ISSN: 0022-1120. DOI: 10.1017/S0022112077000585.
- [150] Mahmood, G. I., M. L. Hill, D. L. Nelson, P. M. Ligrani, H.-K. Moon & B. Glezer. Local Heat Transfer and Flow Structure on and Above a Dimpled Surface in a Channel. In: *Journal of Turbomachinery* 123.1 (2001-02), pp. 115–123. ISSN: 0889-504X. DOI: 10.1115/1.1333694.
- [151] Mahmood, G. I. & P. M. Ligrani. Heat transfer in a dimpled channel: combined influences of aspect ratio, temperature ratio, Reynolds number, and flow structure. In: *International Journal of Heat and Mass Transfer* 45.10 (2002-05), pp. 2011–2020. ISSN: 0017-9310. DOI: 10.1016/S0017-9310(01)00314-3.
- [152] Mahmood, G. I., M. Z. Sabbagh & P. M. Ligrani. Heat Transfer in a Channel with Dimples and Protrusions on Opposite Walls. In: *Journal of Thermophysics and Heat Transfer* 15.3 (2001-07), pp. 275–283. ISSN: 1533-6808. DOI: 10.2514/2.6623.
- [153] Marshak, A. & A. Davis. 3D Radiative Transfer in Cloudy Atmospheres. Ed. by R. Guzzi, D. Imboden, L. Lanzerotti & U. Platt. Springer-Verlag Berlin Heidelberg, 2005. ISBN: 978-3-540-23958-1. DOI: 10.1007/3-540-28519-9.
- [154] Meana-Fernández, A., J. M. Fernández Oro, K. M. Argüelles Díaz, M. Galdo-Vega & S. Velarde-Suárez. Application of Richardson extrapolation method to the CFD simulation of vertical-axis wind turbines and analysis of the flow field. In: *Engineering Applications of Computational Fluid Mechanics* 13.1 (2019-01), pp. 359–376. ISSN: 1994-2060. DOI: 10.1080/19942060.2019.1596160.
- [155] Menter, F. R. Two-equation eddy-viscosity turbulence models for engineering applications. In: *AIAA Journal* 32.8 (1994-08), pp. 1598–1605. ISSN: 1533-385X. DOI: 10.2514/3.12149.
- [156] Menter, F. R. & Y. Egorov. The Scale-Adaptive Simulation Method for Unsteady Turbulent Flow Predictions. Part I: Theory and Model Description. In: *Flow, Turbulence and Combustion* 85.1 (2010-06), pp. 113–138. ISSN: 1386-6184. DOI: 10.1007/s10494-010-9264-5.

## Bibliography

- [157] Menter, F. R., M. Kuntz & R. Langtry. Ten Years of Industrial Experience with the SST Turbulence Model. In: *Proceedings of the Fourth International Symposium on Turbulence, Heat and Mass Transfer*. Ed. by K. Hanjalić, Y. Nagano & M. J. Tummers. International Symposium on Turbulence, Heat and Mass Transfer. Antalya: Begell House, 2003.
- [158] Millsaps, K. & K. Pohlhausen. Heat Transfer by Laminar Flow from a Rotating Plate. In: *Journal of the Aeronautical Sciences* 18.5 (1951-05), pp. 354–355. ISSN: 0095-9812. DOI: 10.2514/8.1955.
- [159] Millsaps, K. & K. Pohlhausen. Heat Transfer by Laminar Flow from a Rotating Plate. In: *Journal of Aeronautical Sciences* 19.2 (1952-02), pp. 120–126. ISSN: 0095-9812. DOI: 10.2514/8.2175.
- [160] Moin, P. & J. Kim. Numerical investigation of turbulent channel flow. In: *Journal of Fluid Mechanics* 118 (1982-05), pp. 341–377. ISSN: 0022-1120. DOI: 10.1017/S0022112082001116.
- [161] Moon, H. K., T. O’Connell & B. Glezer. Channel Height Effect on Heat Transfer and Friction in a Dimpled Passage. In: *Journal of Engineering for Gas Turbines and Power* 122.2 (2000-01), pp. 307–313. ISSN: 0742-4795. DOI: 10.1115/1.483208.
- [162] Moore, G. E. Cramming more components onto integrated circuits. In: *Electronics* 38.8 (1965-04).
- [163] Moore, G. E. Progress in digital integrated electronics. In: *International Electron Devices Meeting*. 1975, pp. 11–13.
- [164] Moser, R. D., J. Kim & N. N. Mansour. Direct numerical simulation of turbulent channel flow up to  $Re_\tau=590$ . In: *Physics of Fluids* 11.4 (1999-04), pp. 943–945. ISSN: 1070-6631. DOI: 10.1063/1.869966.
- [165] Murata, A., K. Yano, M. Hanai, H. Saito & K. Iwamoto. Arrangement effects of inclined teardrop-shaped dimples on film cooling performance of dimpled cutback surface at airfoil trailing edge. In: *International Journal of Heat and Mass Transfer* 107 (2017-04), pp. 761–770. ISSN: 0017-9310. DOI: 10.1016/j.ijheatmasstransfer.2016.11.081.
- [166] Nagib, H. M., K. A. Chauhan & P. A. Monkewitz. Approach to an asymptotic state for zero pressure gradient turbulent boundary layers. In: *Philosophical Transactions of the Royal Society A: Mathematical, Physical and Engineering Sciences* 365.1852 (2007-01), pp. 755–770. ISSN: 1471-2962. DOI: 10.1098/rsta.2006.1948.
- [167] NASA. Mach Number Role in Compressible Flows. 2015-05. URL: <https://www.grc.nasa.gov/www/k-12/airplane/machrole.html>.
- [168] Nesselrooij, M. van, L. L. M. Veldhuis, B. W. van Oudheusden & F. F. J. Schrijer. Drag reduction by means of dimpled surfaces in turbulent boundary layers. In: *Experiments in Fluids* 57.142 (2016-08), pp. 1–14. ISSN: 1432-1114. DOI: 10.1007/s00348-016-2230-9.

- [169] Nguyen, T. D. & S. Harmand. Heat transfer and vortical structures around a rotating cylinder with a spanwise disk and low-velocity crossflow. In: *International Journal of Heat and Mass Transfer* 64 (2013-09), pp. 1014–1030. ISSN: 0017-9310. DOI: 10.1016/j.ijheatmasstransfer.2013.05.037.
- [170] Nicoud, F. & F. Ducros. Subgrid-Scale Stress Modelling Based on the Square of the Velocity Gradient Tensor. In: *Flow, Turbulence and Combustion* 62.3 (1999-09), pp. 183–200. ISSN: 1386-6184. DOI: 10.1023/A:1009995426001.
- [171] Nusser, K. Investigation of the Fluid-Structure-Acoustics Interaction on a Simplified Car Model. PhD thesis. 2019.
- [172] Oberkampf, W. L. & C. J. Roy. Verification and Validation in Scientific Computing. Cambridge University Press, 2010. ISBN: 978-0-521-11360-1. DOI: 10.1017/CB09780511760396.
- [173] Ong, C. L. & J. M. Owen. Computation of the flow and heat transfer due to a rotating disc. In: *International Journal of Heat and Fluid Flow* 12.2 (1991-06), pp. 106–115. ISSN: 0142-727X. DOI: 10.1016/0142-727X(91)90036-U.
- [174] Österlund, J. M. Experimental Studies of Zero Pressure-Gradient Turbulent Boundary-Layer Flow. Tech. rep. Royal Institute of Technology, Department of Mechanics, SE-100 44 Stockholm, Sweden, 1999.
- [175] Ostrach, S. & P. R. Thornton. Compressible laminar flow and heat transfer about a rotating isothermal disk. Tech. rep. National advisory committee for aeronautics, 1958-08.
- [176] Park, H., D. Lee, W.-P. Jeong, S. Hahn, J. Kim, J. Kim, J. Choi & H. Choi. Drag reduction in flow over a two-dimensional bluff body with a blunt trailing edge using a new passive device. In: *Journal of Fluid Mechanics* 563 (2006-09), pp. 389–414. ISSN: 0022-1120. DOI: 10.1017/s0022112006001364.
- [177] Park, J. & H. Choi. Effects of uniform blowing or suction from a spanwise slot on a turbulent boundary layer flow. In: *Physics of Fluids* 11.10 (1999-10), pp. 3095–3105. ISSN: 1070-6631. DOI: 10.1063/1.870167.
- [178] Patankar, S. V. & D. B. Spalding. A calculation procedure for heat, mass and momentum transfer in three-dimensional parabolic flows. In: *International Journal of Heat and Mass Transfer* 15.10 (1972-10), pp. 1787–1806. DOI: 10.1016/0017-9310(72)90054-3.
- [179] Pavlov, V. V. Dolphin skin as a natural anisotropic compliant wall. In: *Bioinspiration & Biomimetics* 1.2 (2006-06), pp. 31–40. ISSN: 1748-3190. DOI: 10.1088/1748-3182/1/2/001.
- [180] Pilbrow, R., H. Karabay, M. Wilson & J. M. Owen. Heat Transfer in a “Cover-Plate” Preswirl Rotating-Disk System. In: *Journal of Turbomachinery* 121.2 (1999-04), pp. 249–256. ISSN: 0889-504X. DOI: 10.1115/1.2841308.

## Bibliography

- [181] Pope, S. B. *Turbulent Flows*. 8th ed. Cambridge University Press, 2011. ISBN: 978-0-521-59886-6.
- [182] Prandtl, L. Über Flüssigkeitsbewegung bei sehr kleiner Reibung. In: *Verhandlungen des III. Internationalen Mathematiker-Kongresses* (1904).
- [183] Rao, Y., Y. Feng, B. Li & B. Weigand. Experimental and Numerical Study of Heat Transfer and Flow Friction in Channels With Dimples of Different Shapes. In: *Journal of Heat Transfer* 137.3 (2015-03). ISSN: 0022-1481. DOI: 10.1115/1.4029036.
- [184] Rao, Y., B. Li & Y. Feng. Heat transfer of turbulent flow over surfaces with spherical dimples and teardrop dimples. In: *Experimental Thermal and Fluid Science* 61 (2015-02), pp. 201–209. ISSN: 0894-1777. DOI: 10.1016/j.expthermflusci.2014.10.030.
- [185] Rashidi, S., F. Hormozi, B. Sundén & O. Mahian. Energy saving in thermal energy systems using dimpled surface technology – A review on mechanisms and applications. In: *Applied Energy* 250 (2019-09), pp. 1491–1547. ISSN: 0306-2619. DOI: 10.1016/j.apenergy.2019.04.168.
- [186] Reynolds, O. XXIX. An experimental investigation of the circumstances which determine whether the motion of water shall be direct or sinuous, and of the law of resistance in parallel channels. In: *Philosophical Transactions of the Royal Society of London* 174 (1883-12), pp. 935–982. ISSN: 0261-0523. DOI: 10.1098/rstl.1883.0029.
- [187] Reynolds, O. Section G - Mechanical Science - Opening Address by Prof. Osborne Reynolds, M.A., LL.D., F.R.S., M.Inst.C.E., President of the Section. In: *Nature* 36.933 (1887-09), pp. 472–475. ISSN: 1476-4687. DOI: 10.1038/036462a0.
- [188] Richards, E. J. & F. H. Burstall. The "China Clay" Method of Indicating Transition. A.R.C. technical report 2126. H.M. Stationery Office, 1945.
- [189] Richardson, L. F. & J. A. Gaunt. The deferred approach to the limit. In: *Philosophical Transactions of the Royal Society of London. Series A, Containing Papers of a Mathematical or Physical Character* 226.636-646 (1927-01), pp. 299–361. ISSN: 0264-3952. DOI: 10.1098/rsta.1927.0008.
- [190] Rotem, Z. Heat Transfer from Rotating Discs. In: *The Journal of the Royal Aeronautical Society* 62.568 (1958-04), pp. 303–303. ISSN: 0001-9240. DOI: 10.1017/S0368393100068590.
- [191] Rott, N. Note on the History of the Reynolds Number. In: *Annual Review of Fluid Mechanics* 22 (1990), pp. I–II. DOI: 10.1146/ANNUREV.FL.22.010190.000245.
- [192] Rotta, J. C. *Turbulente Strömungen - Eine Einführung in die Theorie und ihre Anwendung*. Ed. by A. Dillmann. Universitätsverlag Göttingen, 2010.
- [193] Sagaut, P. *Large Eddy Simulation for Incompressible Flows*. 3rd ed. Springer-Verlag Berlin Heidelberg, 2006. ISBN: 978-3-540-26344-9. DOI: 10.1007/b137536.

- [194] Samad, A., K.-D. Lee & K.-Y. Kim. Multi-objective optimization of a dimpled channel for heat transfer augmentation. In: *Heat and Mass Transfer* 45.2 (2008-07), pp. 207–217. ISSN: 0947-7411. DOI: 10.1007/s00231-008-0420-6.
- [195] Sardasht, M. T., R. Hosseini & E. Amani. An analysis of turbulence models for prediction of forced convection of air stream impingement on rotating disks at different angles. In: *International Journal of Thermal Sciences* 118 (2017-08), pp. 139–151. ISSN: 1290-0729. DOI: 10.1016/j.ijthermalsci.2017.04.021.
- [196] Sato, N., M. Inagaki, K. Kaneda, N. Horinouchi & A. Ota. Numerical investigation of the effect of Prandtl number on heat transfer in a dimpled-channel flow. In: *International Journal of Heat and Fluid Flow* 68 (2017-12), pp. 139–150. ISSN: 0142-727X. DOI: 10.1016/j.ijheatfluidflow.2017.10.005.
- [197] Schlichting, H. & E. Truckenbrodt. The Flow Around a Rotating Disc in a Uniform Stream. In: *Journal of the Aeronautical Sciences* 18.9 (1951-09), pp. 639–640. ISSN: 0095-9812. DOI: 10.2514/8.2061.
- [198] Schlichting, H. & E. Truckenbrodt. Die Strömung an einer angeblasenen rotierenden Scheibe. In: *ZAMM - Zeitschrift für Angewandte Mathematik und Mechanik* 32.4-5 (1952-04), pp. 97–111. ISSN: 0044-2267. DOI: 10.1002/zamm.19520320402.
- [199] Schlichting, H. & K. Gersten. *Boundary-Layer Theory*. Ninth. Springer-Verlag Berlin Heidelberg, 2017. ISBN: 978-3-662-52917-1. DOI: 10.1007/978-3-662-52919-5.
- [200] Schukin, A. V., A. P. Kozlov & R. S. Agachev. Study and Application of Hemispherical Cavities for Surface Heat Transfer Augmentation. In: *ASME 1995 International Gas Turbine and Aeroengine Congress and Exposition*. Vol. 4. ASME. Houston, Texas, USA: ASME, 1995-06. DOI: 10.1115/95-GT-059.
- [201] Schumann, U. Ein Verfahren zur direkten numerischen Simulation turbulenter Strömungen in Platten- und Ringspaltkanälen und über seine Anwendung zur Untersuchung von Turbulenzmodellen. PhD thesis. 1973.
- [202] Seiferlein, K. E. Annual Energy Review 2006. Research rep. Office of Energy Markets and End Use, U.S. Department of Energy, Washington, DC 20585: Energy Information Administration, 2007-06.
- [203] Siddique, W., N. A. Khan & I. Haq. Analysis of numerical results for two-pass trapezoidal channel with different cooling configurations of trailing edge: The effect of dimples. In: *Applied Thermal Engineering* 89 (2015-10), pp. 763–771. ISSN: 1359-4311. DOI: 10.1016/j.applthermaleng.2015.06.067.
- [204] Sirovich, L. & S. Karlsson. Turbulent drag reduction by passive mechanisms. In: *Nature* 388 (1997-08), pp. 753–755. ISSN: 1476-4687. DOI: 10.1038/41966.

## Bibliography

- [205] Smagorinsky, J. General circulation experiments with the primitive equations. In: *Monthly Weather Review* 91.3 (1963-03), pp. 99–164. ISSN: 0027-0644. DOI: 10.1175/1520-0493(1963)091<0099:GCEWTP>2.3.CO;2.
- [206] Smirnov, A., S. Shi & I. Celik. Random Flow Generation Technique for Large Eddy Simulations and Particle-Dynamics Modeling. In: *Journal of Fluids Engineering* 123.2 (2001-02), pp. 359–371. ISSN: 0098-2202. DOI: 10.1115/1.1369598.
- [207] Spalart, P. R. Direct simulation of a turbulent boundary layer up to  $R_{\Theta} = 1410$ . In: *Journal of Fluid Mechanics* 187 (1988-02), pp. 61–98. ISSN: 0022-1120. DOI: 10.1017/S0022112088000345.
- [208] Sparrow, E. M. & R. D. Cess. Magnetohydrodynamic Flow and Heat Transfer About a Rotating Disk. In: *Journal of Applied Mechanics* 29.1 (1962-03), pp. 181–187. ISSN: 0021-8936. DOI: 10.1115/1.3636454.
- [209] Sparrow, E. M. & J. L. Gregg. Mass Transfer, Flow, and Heat Transfer About a Rotating Disk. In: *Journal of Heat Transfer* 82.4 (1960-11), pp. 294–302. ISSN: 0022-1481. DOI: 10.1115/1.3679937.
- [210] Spurk, H. J. & N. Aksel. Fluid Mechanics. 2nd ed. Springer, Berlin, Heidelberg, 2008. ISBN: 978-3-540-73536-6. DOI: 10.1007/978-3-540-73537-3.
- [211] Stokes, G. G. On the Effect of the Internal Friction of Fluids on the Motion of Pendulums. In: *Transactions of the Cambridge Philosophical Society* (1851), pp. 1–10. DOI: 10.1017/CB09780511702266.002.
- [212] Tay, C. M. Determining the Effect of Dimples on Drag in a Turbulent Channel Flow. In: *49th AIAA Aerospace Sciences Meeting including the New Horizons Forum and Aerospace Exposition*. American Institute of Aeronautics and Astronautics, 2011-01. DOI: 10.2514/6.2011-682.
- [213] Tay, C. M., Y. T. Chew, B. C. Khoo & J. B. Zhao. Development of flow structures over dimples. In: *Experimental Thermal and Fluid Science* 52.- (2014), pp. 278–287. ISSN: 0894-1777. DOI: 10.1016/j.expthermusci.2013.10.001.
- [214] Tay, C. M. J., B. C. Khoo & Y. T. Chew. Mechanics of drag reduction by shallow dimples in channel flow. In: *Physics of Fluids* 27.035109 (2015-03), pp. 1–22. ISSN: 1089-7666. DOI: 10.1063/1.4915069.
- [215] Tay, J. & T. T. Lim. Drag Reduction with Teardrop-shaped Dimples. In: *2018 Flow Control Conference*. American Institute of Aeronautics and Astronautics, 2018-06. DOI: 10.2514/6.2018-3528.
- [216] Theodorsen, T. & A. Regier. Experiments on drag of revolving disks, cylinders, and streamline rods at high speeds. Tech. rep. 20050241738. National Advisory Committee for Aeronautics; Washington, DC, United States: NACA, 1944-01.

- [217] Tien, C. L. & J. Tsuji. Heat transfer by laminar forced flow against a non-isothermal rotating disk. In: *International Journal of Heat and Mass Transfer* 7.2 (1964-02), pp. 247–252. ISSN: 0017-9310. DOI: 10.1016/0017-9310(64)90089-4.
- [218] Turnow, J., N. Kornev, S. Isaev & E. Hassel. Vortex mechanism of heat transfer enhancement in a channel with spherical and oval dimples. In: *Heat and Mass Transfer* 47.3 (2011-11), pp. 301–313. ISSN: 0947-7411. DOI: 10.1007/s00231-010-0720-5.
- [219] Turnow, J. Flow Structures And Heat Transfer on Dimpled Surfaces. PhD thesis. 2012.
- [220] Turnow, J., R. Kasper & N. Kornev. Flow structures and heat transfer over a single dimple using hybrid URANS-LES methods. In: *Computers and Fluids* 172 (2018-02), pp. 720–727. ISSN: 0045-7930. DOI: 10.1016/j.compuid.2018.01.014.
- [221] Turnow, J., N. Kornev, V. Zhdanov & E. Hassel. Flow structures and heat transfer on dimples in a staggered arrangement. In: *International Journal of Heat and Fluid Flow* 35 (2012-06), pp. 168–175. ISSN: 0142-727X. DOI: 10.1016/j.ijheatfluidflow.2012.01.002.
- [222] Verein Deutscher Ingenieure VDI-Gesellschaft Verfahrenstechnik und Chemieingenieurwesen (GVC), ed. VDI-Wärmeatlas. 11th ed. Berlin, Heidelberg: Springer Berlin Heidelberg, 2013. ISBN: 978-3-642-19980-6.
- [223] Wagner, C. Heat Transfer from a Rotating Disk to Ambient Air. In: *Journal of Applied Physics* 19.9 (1948-09), pp. 837–839. ISSN: 0021-8979. DOI: 10.1063/1.1698216.
- [224] Wagner, J. H., B. V. Johnson & T. J. Hajek. Heat Transfer in Rotating Passages With Smooth Walls and Radial Outward Flow. In: *Journal of Turbomachinery* 113.1 (1991-01), pp. 42–51. ISSN: 0889-504X. DOI: 10.1115/1.2927736.
- [225] Wallace, J. M. The vortical structure of bounded turbulent shear flow. In: *Flow of Real Fluids*. Ed. by G. E. A. Meier & F. Obermeier. Vol. 235. Lecture Notes in Physics. Springer Berlin Heidelberg, 1985, pp. 253–268. ISBN: 978-3-540-39690-1. DOI: 10.1007/3-540-15989-4\_89.
- [226] Wang, Z., K. S. Yeo & B. C. Khoo. DNS of low Reynolds number turbulent flows in dimpled channels. In: *Journal of Turbulence* 7.37 (2006-01), pp. 1–29. ISSN: 1468-5248. DOI: 10.1080/14685240600595735.
- [227] White, F. M. Fluid Mechanics. Ed. by M. Lange. 7th ed. New York: McGraw-Hill, 2008. ISBN: 978-0-07-352934-9.
- [228] Wiesche, S. aus der. LES study of heat transfer augmentation and wake instabilities of a rotating disk in a planar stream of air. In: *Heat and Mass Transfer* 40.3-4 (2002-12), pp. 271–284. ISSN: 0947-7411. DOI: 10.1007/s00231-002-0368-x.

## Bibliography

- [229] Wiesche, S. aus der. Heat transfer from a rotating disk in a parallel air crossflow. In: *International Journal of Thermal Sciences* 46.8 (2007-08), pp. 745–754. ISSN: 1290-0729. DOI: 10.1016/j.ijthermalsci.2006.10.013.
- [230] Wiesche, S. aus der. Heat transfer from rotating discs with finite thickness subjected to outer air streams. In: *Proceedings of the 14th International Heat Transfer Conference*. Vol. 2. ASME. 2010-08.
- [231] Wiesche, S. aus der & C. Helcig. Convective Heat Transfer From Rotating Disks Subjected To Streams Of Air. Ed. by F. A. Kulacki. SpringerBriefs in Applied Sciences and Technology. Springer International Publishing, 2016. ISBN: 978-3-319-20166-5. DOI: 10.1007/978-3-319-20167-2.
- [232] Wilcox, D. C. Reassessment of the scale-determining equation for advanced turbulence models. In: *AIAA Journal* 26.11 (1988-II), pp. 1299–1310. ISSN: 1533-385X. DOI: 10.2514/3.10041.
- [233] Wille, M. K. W. Large Eddy Simulation of jets in cross flows. PhD thesis. 1997.
- [234] Williamson, C. H. K., J. Wu & J. Sheridan. Scaling of streamwise vortices in wakes. In: *Physics of Fluids* 7.10 (1995-10), pp. 2307–2309. ISSN: 1070-6631. DOI: 10.1063/1.868744.
- [235] Winterton, R. H. S. Where did the Dittus and Boelter equation come from? In: *International Journal of Heat and Mass Transfer* 41.4 (1998-02), pp. 809–810. ISSN: 0017-9310. DOI: 10.1016/S0017-9310(97)00177-4.
- [236] Won, S. Y. & P. M. Ligrani. Numerical Predictions of Flow Structure and local Nusselt Number Ratios along and above Dimpled Surfaces with different Dimple Depths in a Channel. In: *Numerical Heat Transfer, Part A: Applications* 46.6 (2004-10), pp. 549–570. ISSN: 1040-7782. DOI: 10.1080/10407780490487830.
- [237] Won, S. Y., Q. Zhang & P. M. Ligrani. Comparisons of flow structure above dimpled surfaces with different dimple depths in a channel. In: *Physics of Fluids* 17.4 (2005-04), p. 045105. ISSN: 1070-6631. DOI: 10.1063/1.1872073.
- [238] Wu, L., Z. Jiao, Y. Song, C. Liu, H. Wang & Y. Yan. Experimental investigations on drag-reduction characteristics of bionic surface with water-trapping microstructures of fish scales. In: *Scientific Reports* 8.12186 (2018-08). ISSN: 2045-2322. DOI: 10.1038/s41598-018-30490-x.
- [239] Xiao, N., Q. Zhang, P. M. Ligrani & R. Mongia. Thermal performance of dimpled surfaces in laminar flows. In: *International Journal of Heat and Mass Transfer* 52.7-8 (2009-03), pp. 2009–2017. ISSN: 0017-9310. DOI: 10.1016/j.ijheatmasstransfer.2008.11.006.

- [240] Xie, G., J. Liu, P. M. Ligrani & W. Zhang. Numerical analysis of flow structure and heat transfer characteristics in square channels with different internal-protruded dimple geometrics. In: *International Journal of Heat and Mass Transfer* 67 (2013-12), pp. 81–97. ISSN: 0017-9310. DOI: 10.1016/j.ijheatmasstransfer.2013.07.094.
- [241] Xie, G., B. Sundén & Q. Wang. Predictions of Enhanced Heat Transfer of an Internal Blade Tip-Wall With Hemispherical Dimples or Protrusions. In: *Journal of Turbomachinery* 133.4 (2011-04). ISSN: 0889-504X. DOI: 10.1115/1.4002963.
- [242] Xie, Y., H. Qu & D. Zhang. Numerical investigation of flow and heat transfer in rectangular channel with teardrop dimple/protrusion. In: *International Journal of Heat and Mass Transfer* 84 (2015-05), pp. 486–496. ISSN: 0017-9310. DOI: 10.1016/j.ijheatmasstransfer.2015.01.055.
- [243] Yoon, H. S., S. H. Park, C. Choi & M. Y. Ha. Numerical study on characteristics of flow and heat transfer in a cooling passage with a tear-drop dimple surface. In: *International Journal of Thermal Sciences* 89 (2015-03), pp. 121–135. ISSN: 1290-0729. DOI: 10.1016/j.ijthermalsci.2014.11.002.
- [244] Yuen, A. C. Y., G. H. Yeoh, V. Timchenko, S. C. P. Cheung & T. Chen. Study of three LES subgrid-scale turbulence models for predictions of heat and mass transfer in large-scale compartment fires. In: *Numerical Heat Transfer, Part A: Applications* 69.11 (2016-05), pp. 1223–1241. ISSN: 1040-7782. DOI: 10.1080/10407782.2016.1139903.
- [245] Zanon, E. S., H. M. Nagib & F. Durst. Refined  $c_f$  relation for turbulent channels and consequences for high- $Re$  experiments. In: *Fluid Dynamics Research* 41.2 (2009-03), p. 021405. ISSN: 0169-5983. DOI: 10.1088/0169-5983/41/2/021405.
- [246] Zhiyin, Y. Large-eddy simulation: Past, present and the future. In: *Chinese Journal of Aeronautics* 28.1 (2015-02), pp. 11–24. ISSN: 1000-9361. DOI: 10.1016/j.cja.2014.12.007.

## List of own publications related to this thesis

- [P1] Praß, J., J. Franke & S. Becker. Investigation of drag reduction due to dimpled surfaces in narrow channels by means of flow simulations. In: *Applied Mechanics and Materials* 871 (2017), pp. 244–251. ISSN: 1662-7482. DOI: 10.4028/www.scientific.net/AMM.871.244.
- [P2] Praß, J., H. Wannemacher, J. Franke & S. Becker. Investigation of the influence of dimples on the resistance of overflowed plates. In: *Proceedings of Conference on Modelling Fluid Flow (CMFF'18)*. 2018. ISBN: 978-963313297-5.

## Bibliography

- [P3] Praß, J., H. Wannemacher, J. Franke & S. Becker. The Influence of Different Arrangements of Shallow Dimples on the Resistance of Plates Subjected to Relative Fluid Motion. In: *Technische Mechanik* 39.1 (2019-02), pp. 39–50. ISSN: 0232-3869. DOI: 10.24352/UB.OVGU-2019-005.
- [P4] Wachter, F., A. Metelkin, J. Jovanović, J. Praß & S. Becker. Numerical investigation of the effect of convex transverse curvature and concave grooves on the turbulent boundary layer along a cylinder in axial flow. In: *International Journal of Heat and Fluid Flow* 92 (2021-12), p. 108855. ISSN: 0142-727X. DOI: 10.1016/j.ijheatfluidflow.2021.108855.

## List of student works related to this thesis

- [S1] Kalb, S. Numerische Optimierung der Gefahrenstoffabsaugung an Galvanikanlagen und Analyse turbulenter Grenzschichtstrukturen. MA thesis. 2021.
- [S2] Matsche, F. Numerische Simulation des Wärmeübertrags einer mit Dimplen strukturierten, rotierenden Scheibe. MA thesis. 2019.
- [S3] Stadler, R. Numerische Simulation der Umströmung und des konvektiven Wärmeübergangs an rotierenden Scheiben mit gedimpelten Oberflächen. MA thesis. 2018.
- [S4] Wannemacher, H. Numerische Untersuchung der Auswirkung flacher Dimple und deren Anordnung auf den Strömungswiderstand einer turbulent überströmten Platte. MA thesis. 2017.

## Publication list of the author

- [A1] Böhm, R., J. Praß, J. Bürner & J. Franke. Neue Ansätze für Energiemanagement und Energieeffizienz in der Produktion. In: *Umwelt-Technologie und Energie in Bayern* (2018), pp. 40–41.
- [A2] Braun, T., R. Böhm, J. Praß, U. Baierl, D. Hahn & J. Franke. Investigation of Alternative Applications of Electrically Functionalized Surfaces Using the Plasma-Coating-Technology. In: *Advances in Production Research - Proceedings of the 8th Congress of the German Academic Association for Production Technology (WGP), Aachen, November 19–20, 2018*. 2018.
- [A3] Braun, T., J. Weber, M. Brüstle, P. Wössner, J. Praß & J. Franke. Active Wind Turbine Deicing-Systems Produced via Plasma-Coating Technology. In: *Advanced Materials Research*. Ed. by J. P. Wulfsberg. Vol. 1140. Pfaffikon, Switzerland: Trans Tech Publications, 2016, pp. 320–327.
- [A4] Bürner, J., J. Praß & J. Franke. Identification of demand side management potentials within the sector of domestic living. In: *Environment and Energy in Bavaria* (2018).

- [A5] Bürner, J., J. Praß & J. Franke. Identifikation von Lastmanagementpotenzialen im Umfeld des privaten Wohnens. In: *Umwelt-Technologie und Energie in Bayern* (2018), pp. 42–43.
- [A6] Ebell, N., A. Bott, T. Beck, J. Bürner, J. Praß & J. Franke. Model of a Power-to-Gas System with Fuel Cell in a Mixed Integer Linear Program for the Energy Supply of Residential and Commercial Buildings. In: *Applied Mechanics and Materials* 871 (2017), pp. 11–19. ISSN: 1662-7482. DOI: 10.4028/www.scientific.net/amm.871.11.
- [A7] Hefner, F., J. Praß, P. Kirchner & J. Franke. Design of process parameters for the manufacturing of wrapped connections with single solid round wires using the explicit finite element analysis. In: *Procedia CIRP* 91 (2020), pp. 684–689. ISSN: 2212-8271. DOI: 10.1016/j.procir.2020.02.225.
- [A8] Hoffmann, C., J. Praß, T. Uhlemann & J. Franke. Improving the energy efficiency of industrial drying processes: a computational fluid dynamics approach. In: *Procedia Manufacturing* 33 (2019), pp. 422–429. ISSN: 2351-9789. DOI: 10.1016/j.promfg.2019.04.052.
- [A9] Praß, J. Untersuchung einer dezentralen Raumbelüftungsanlage mit Wärmerückgewinnung mittels zweifach teilbeaufschlagtem, mehrflutigem Querstrom-Reibungsventilator. In: *Tagungsband zum 2. Green Factory Bavaria Kolloquium 2015*. Ed. by J. Franke, S. Kreitlein & A. Höft. 2015, pp. 420–429. ISBN: 978-3-00-050523-2.
- [A10] Praß, J., J. Bürner & J. Franke. Energieeffiziente Raumbelüftung mit Wärmerückgewinnung unter Verwendung eines neuartigen Wirkprinzips. In: *Umwelt-Technologie und Energie in Bayern* (2018), pp. 46–47.
- [A11] Praß, J., J. Bürner & J. Franke. Energy-efficient room ventilation with heat recovery using a novel concept. In: *Environment and Energy in Bavaria* (2018), pp. 29–30.
- [A12] Praß, J. & J. Franke. Numerische Untersuchung eines Reibungsventilators - Einfluss des Nebenverhältnisses auf den Druckaufbau. In: *Tagungsband zum 1. E-Home-Symposium 2016*. Ed. by J. Franke, M. Michl, J. Bauer & R. Böhm. 2016, pp. 11–17.
- [A13] Praß, J., J. Franke & S. Becker. Investigation of drag reduction due to dimpled surfaces in narrow channels by means of flow simulations. In: *Applied Mechanics and Materials* 871 (2017), pp. 244–251. ISSN: 1662-7482. DOI: 10.4028/www.scientific.net/AMM.871.244.
- [A14] Praß, J., M. Reinelt, J. Franke & S. Becker. Numerical Evaluation of Heat Transfer from Rotating Discs Separated by Sealing Elements. In: *Applied Mechanics and Materials* 871 (2017-10), pp. 252–261. ISSN: 1662-7482. DOI: 10.4028/www.scientific.net/amm.871.252.

## Bibliography

- [A15] Praß, J., A. Renz, J. Franke, J. Weber & S. Becker. Numerical Investigation of a Friction Ventilator for Different Geometrical Setups. In: *Advanced Engineering Forum* 19 (2016-10), pp. 35–42. ISSN: 2234-991X. DOI: 10.4028/www.scientific.net/aef.19.35.
- [A16] Praß, J., J. Riedel, A. Renz, J. Franke & S. Becker. Numerical Representation of the Operating Behavior of a Crossflow Friction Turbomachine. In: *Chemical Engineering & Technology* 42.9 (2019-06), pp. 1853–1860. ISSN: 1521-4125. DOI: 10.1002/ceat.201800655.
- [A17] Praß, J., J. Riedel, A. Renz, J. Franke & S. Becker. Featured Highlight: Numerical Representation of the Operating Behavior of a Crossflow Friction Turbomachine. eng. online. 2020.
- [A18] Praß, J., H. Wannemacher, J. Franke & S. Becker. Investigation of the influence of dimples on the resistance of overflowed plates. In: *Proceedings of Conference on Modelling Fluid Flow (CMFF'18)*. 2018. ISBN: 978-963313297-5.
- [A19] Praß, J., H. Wannemacher, J. Franke & S. Becker. The Influence of Different Arrangements of Shallow Dimples on the Resistance of Plates Subjected to Relative Fluid Motion. In: *Technische Mechanik* 39.1 (2019-02), pp. 39–50. ISSN: 0232-3869. DOI: 10.24352/UB.0VGU-2019-005.
- [A20] Praß, J., J. Weber, S. Staub, J. Bürner, R. Böhm, T. Braun, M. Hein, M. Michl, M. Beck & J. Franke. Smart Energy and Grid: Novel Approaches for the Efficient Generation, Storage, and Usage of Energy in the Smart Home and the Smart Grid Linkup: Foundations, Principles, and Applications. In: *Smart Cities: Foundations, Principles, and Applications*. Ed. by H. Song, R. Srinivasan, T. Sookoor & S. Jeschke. Wiley, 2017-07. Chap. 20, pp. 575–604. ISBN: 978-1-119-22639-0. DOI: 10.1002/9781119226444.ch20.
- [A21] Renz, A., J. Praß, J. Riedel, O. Nadler & S. Becker. Numerical and Experimental Investigation of the Velocity Field in Friction Ventilators. In: *International Conference on Fan Noise, Aerodynamics, Applications and Systems*. 2018-04.
- [A22] Renz, A., J. Praß, J. Weber & S. Becker. Experimental Investigation of a Friction Ventilator. In: *Advanced Engineering Forum* 19 (2016), pp. 43–49. ISSN: 2234-991X. DOI: 10.4028/www.scientific.net/AEF.19.43.
- [A23] Teske, F., A. Fehrle, J. Prass & J. Franke. Adapted pricing scheme for the integration of vehicle-to-grid into the energy system. In: *2021 11th International Electric Drives Production Conference (EDPC)*. IEEE, 2021-12. DOI: 10.1109/edpc53547.2021.9684223.
- [A24] Wachter, F., A. Metelkin, J. Jovanović, J. Praß & S. Becker. Numerical investigation of the effect of convex transverse curvature and concave grooves on the turbulent boundary layer along a cylinder in axial flow. In: *International Journal of Heat and Fluid Flow* 92 (2021-12), p. 108855. ISSN: 0142-727X. DOI: 10.1016/j.ijheatfluidflow.2021.108855.

- [A25] Weber, J., S. Riedel, J. Praß, A. Renz, S. Becker & J. Franke. Effect of Boundary Layer Tripping on the Aeroacoustics of Small Vertical Axis Wind Turbines. In: *Advanced Engineering Forum* 19 (2016), pp. 3–9. ISSN: 2234-991X. DOI: 10.4028/www.scientific.net/AEF.19.3.